

NASA TECHNICAL
TRANSLATION



NASA TT F-798

27

(NASA-TT-F-798) SPACE ICONICS (Scientific
Translation Service) 289 p HC \$8.75

CSSL 14C

N75-11419

THRU

N75-11445

Unclas

H1/43 53028

SPACE ICONICS



*Edited by B. N. Rodionov, Ya. L. Ziman, A. A. Izotov,
V. I. Pavlov, T. P. Popova, and Yu. M. Chesnokov*

*Nauka" Press
Moscow, 1973*



NATIONAL AERONAUTICS AND SPACE ADMINISTRATION • WASHINGTON, D. C. • SEPTEMBER 1974

ANNOTATION

This collection of papers covers a broad range of questions of space iconics and iconology, beginning with methodological questions and the definitions of these terms.

The articles reflecting practical iconics examine phototelevision methods, automatic photochemical processing under spaceflight conditions, the questions of determining the instrumental properties of spaceborne photographic, phototelevision, and scanning television equipment. Theoretical iconics is represented by discussions of the technique for reducing blurring on photographs, studies of light propagation in planetary atmospheres, evaluation of the optical properties of the atmosphere and surface of Venus. The papers on iconology examine the questions of determining spacecraft orientation, techniques and equipment for transforming and correlating television and IR pictures of the earth, geological, geophysical, and geographical interpretation of pictures taken from space, questions of machine interpretation of cloud images obtained from space.

Papers reflecting the questions of geodesic study and topographical mapping of the Moon round out the volume.

FOREWORD

The methods and equipment for obtaining images (iconics) and the methods and equipment for interpreting images (iconology) occupy one of the most important positions in studying the planets from space vehicles. The practical application of these techniques began in 1959, when the Soviet automatic interplanetary station Luna 3 photographed the backside of our natural satellite and transmitted its television image to the Earth. It is difficult to describe fully the contribution made by iconics and iconology to science and engineering during the years since 1959. We shall cite only the most impressive contributions.

/3*

The global pictures of the Moon (Luna 2, Zond 3, Lunar Orbiter) have made it possible to obtain a complete cartographic model of the Moon and to establish the significant difference in the topographical and geological structure of the visible and invisible hemispheres. The images transmitted directly from the lunar surface (Luna 9) made it possible to detect previously unknown formations, such as rocks, and discover the extensive pitting of the soil by craters of different sizes. All this overturned our concepts of lunar mantle genesis.

* Numbers in the margin indicate pagination in the original foreign text.

The global pictures of the Earth (Tiros, Meteor, and so on) led to the creation of a permanent space weather system which transmits television and IR pictures of the cloud cover to ground stations. The interpretation of these images along with other weather data has improved weather predictions significantly.

Transmission to the Earth of detailed pictures of Mars (Mariner) led to entirely new data on the nature of this planet. Formations on its surface, similar to lunar craters, were discovered. This made possible a new step forward in the development of comparative planetology.

The images of the Earth's surface obtained in various segments of the spectrum (Vostok, Voskhod, Gemini, and so on) showed that pictures taken from space are an effective method for studying the nature of the Earth for national economic purposes. Special space-borne systems (ERTS, Skylab) are being created, whose primary task will be to obtain images for national economic interpretation.

Serious studies and developments are being carried out both in the USSR and abroad in the space imaging field. In the USSR, these studies have already developed to the point where a space section was organized at the 10th Inter-Agency Conference on Aerial Imaging held in Leningrad in November, 1969. The reports recommended by this section for publication constitute the major portion of the present volume (these articles are indicated by an asterisk in the table of contents). The volume also includes articles recommended for publication by a seminar of the Division of Cosmometry and Iconics of the Institute of Space Studies of the USSR.

/4

The present collection is the first systematized publication of studies on space iconics and iconology. It includes a wide range of theoretical and practical subjects. For reader convenience, the material is grouped with regard to subject matter. The initial papers are concerned with practical and theoretical iconics; then follow articles on several trends in iconology.

This volume does not in any way pretend to provide complete coverage of all the problems of space imaging and interpretation of its results. The objective is to show at least partially the great variety of these problems, and at the same time show how intimately they are interrelated by the specific nature of space studies. It is difficult in a publication of this type to achieve uniformity and even quality of the papers, which is clearly a drawback. However, the publication of this collection of papers is useful in that it provides a consolidation of theoretical and practical developments in the field of space iconics and iconology, shows the present level of these developments, and points out to a certain degree the directions of future studies.

While the collection was being prepared for publication, space imaging developed still further. Extensive imaging information was provided by Lunokhod 1. The heroic crew of the first orbital station Salyut carried out a very interesting photographic survey. Mars was photographed from the Mariner 9 and Mars-2 and Mars-3 artificial satellites, and definite progress was achieved in machine processing of space pictures and their interpretation.

TABLE OF CONTENTS

Annotation	iii
Foreword	v
Iconics and Iconology. B. N. Rodionov	1
Prospects for the Development of Phototelevision Methods in Space Studies. A. S. Selivanov	21
Future Development of IR Thermovision Weather Satellite Equipment. A. V. Listratov	29
Determining Iconometric Parameters of Imaging Devices Using a Wide-Angle Collimator. Ya. L. Ziman	41
Geometric Distortions of Autocollimation Type Scanners. M. K. Narayeva	48
Geometric Distortions of Opticomechanical Panoramic Tele- vision Systems. C. M. Govorov	51
Film Processing in Scientific Spacecraft Television Systems. G. M. Aleshin	59
Reduction of Image Blurring on Individual Aerial Photo- graphs. Yu. I. Fivenskiy and Yu. L. Viryukov	67
Applicability of the Diffusion Approximation. Yu. L. Biryukov, L. G. Titarchuk, and Yu. M. Chesnokov	75
Scattering of Light in a Spherical Multilayer Atmosphere. L. G. Titarchuk	85
Estimates of the Venus Atmosphere Optical Characteristics with Application to the Problem of Photographing its Clouds and Surface. Yu. L. Biryukov, A. S. Fanfilov, and L. G. Titarchuk	121
Determining Spacecraft and Airplane Angular Orientation from Star Photographs. K. I. Elbakyan	136
Geographic Correlation of Television Pictures Obtained from Weather Satellites. A. V. Bushuev	143
Geographical Correlation of TV and IR Images Obtained from Weather Satellites. Ya. L. Ziman, B. V. Nepoklonov	146

System for Electronic Transformation and Geographic Correlation of Satellite Television Information. V. P. Dubenskiy, B. L. Nemkovskiy, B. N. Rodionov	155
Geographical Correlation of Earth Cloud Cover Pictures Obtained from Unoriented Satellites. V. I. Solov'ev	165
Geological and Geophysical Studies from Space and Prospects for Their Development. G. B. Gonin, A. I. Vinogradova, B. V. Shilin, N. A. Yakovlev	174
Experience in Integrated Geological and Geographical Interpretation of Space Photographs Obtained in the USSR. B. V. Vinogradov, A. A. Grigor'yev	182
Use of TV Pictures Obtained from Weather Satellites to Study the Geological Structure of the Earth. I. I. Bashilova	190
Global Small-Scale Lunar Cartography. Yu. N. Lipskiy, Yu. P. Pskovskiy, Zh. F. Rodionova, V. V. Shevchenko, V. I. Chikmachey, and L. I. Volchkova	195
Identification Characteristics of Certain Lunar Relief Forms on Pictures Obtained from Spacecraft. V. I. Kravtsova	205
On the Determination of Certain Astronomical, Selenodesic, and Gravitational Parameters of the Moon. Ye. P. Aleksashin, Ya. L. Ziman, I. V. Isavnina, V. A. Krasikov, B. V. Nepoklonov, B. N. Rodionov, A. P. Tishchenko	215
Evaluating the Accuracy of Selenodesic Reference Grids. A. A. Koptev	231
Determination of Dynamic Corrections to Point Coordinates of Photographs Obtained by the Zond 6 and Zond 8 Spacecraft. V. V. Kiselev, B. N. Rodionov	245
Refinement of the Goloseyev Catalog Point Coordinates in the Limb Zone and Determination of Point Coordinates on the Back Side of the Moon. V. A. Krasikov	257
Determination of Selenographic Coordinates of Lunar Surface Points from Single Pictures Obtained from Zond 6. Ya. L. Ziman, V. F. Baratova, I. V. Isavnina	272

ICONICS AND ICONOLOGY

B. N. Rodionov

It has been suggested that the complex of methods and equipment for obtaining images, integrated on a common methodological basis, be termed iconics (from the Greek word εἰκων, meaning image). The concept of iconics combines such methods and equipment for obtaining images as photography, television, phototelevision, thermovision, radar, and so on. /5

The term iconics has been used previously, but in a narrower sense, as the name for the theory of image reproduction systems, primarily in the sense of their optimization [1]. It appears to us that iconics must include two branches: theoretical and practical. Then the system optimization problem takes its place in theoretical iconics along with its other problems.

We propose that the complex of image interpretation methods and equipment be termed iconology.

Methodological generalization of the various methods and equipment for obtaining images is particularly necessary for space studies, where simultaneous pictures are taken in various parts of the electromagnetic wave spectrum. These pictures yield the best results in

the case of integrated interpretation of their results. Integrated interpretation, particularly machine interpretation, is most effective when using common imaging methodology.

Methodological generalizations are inevitably associated with reformulation of familiar concepts. Here, it is necessary to analyze and systematize many ideas and concepts which have been considered obvious. Prior to examining the iconics and iconology problems proper, we must present some concepts and definitions.

The image and its properties. The high information content of human sight has forced man to develop a whole arsenal of methods and equipment with the aid of which extremely varied information on the external world is converted into forms convenient for perception by the eyes. Such forms include texts, tables, graphs, diagrams, sketches, drawings, pictures (images).

The visualized forms of information can be classified on the /6
basis of various criteria. Probably the most natural classification is that based on the degree of similarity of a particular form with its original — the information source in the conventional generally accepted sense. This approach was reflected in the sequence listed above of transition from the visualized form having zero similarity (text) to the form whose similarity with the original can be so great (picture) that the visual associations caused by it are equivalent to the associations arising when examining the original.

Psychologically, association equivalence is the most universal basis for human perception of the information present in visualized forms. Picture language is most accessible for wide ranges of information users. Therefore, pictures stand out among the other visualized forms. The high degree of similarity and equivalence of visual associations are the characteristics on the basis of which particular visualized forms can be associated with the picture class.

The picture class is extensive. It may be divided into two subclasses: graphic art products and pictures obtained by technical

means, such as the photographs, television, thermovision, and radar mentioned above. In this listing, there are technical means used to construct pictures for both the visible and invisible electromagnetic radiation bands. The perception adequacy mentioned above is obvious for the visible-band devices. With regard to the invisible band, we can speak of some equivalent adequacy. In the invisible (X-ray, UV, IR, RF) spectral regions, the observation results are represented in a visualized form which is as close as possible to what the original would be if the human eye were sensitive to radiation in the given bands. Such forms create visual associations corresponding to those which would arise with artificial broadening of the spectral sensitivity of the eye. This makes it possible to relate the forms to the picture class, since they have a high degree of similarity in the sense mentioned above.

The use of the expression "picture" creates terminological inconveniences, since it usually relates to graphic art products. While retaining this term in application to the class as a whole, it is advisable to use a different term for the pictures belonging to the second subclass.

We shall use the term images for the visualized information forms obtained by technical means which create visual associations equivalent to the associations arising when examining the original and having, in the generally accepted sense, a high degree of similarity to its original. The term image is often used as a synonym for picture, but it is sometimes given a different sense, for example, we say that a particular graph is the image of some function. However, we shall use this term only in accord with our definition. /7

The process of obtaining images by technical means is usually called imaging. We shall use as a synonym for denoting such means the term "imaging systems".

The unified methodology for obtaining and interpreting images must obviously be based on certain singular and invariant properties of the images. We shall try to formulate these properties.

In the language of mathematics, the concept of similarity is a variety of isomorphism. We recall that an isomorphism is the property of mutually single-valued mapping of the mathematical models M and M' , consisting, respectively, of the elements $a, b, \dots, a', b', \dots$ and the operations $O, P, \dots; O', P', \dots$, the results $O(a, b, \dots), P(a, b, \dots), \dots; O'(a', b', \dots), P'(a', b', \dots), \dots$ of which are also elements of the models M and M' . If there exists the mapping $a \rightarrow a'$ of the set of elements of model M into the set of elements of model M' and, conversely, $a' \rightarrow a$, where $O(a, b, \dots) \rightarrow O'(a', b', \dots), O'(a', b', \dots) \rightarrow O(a, b, \dots)$ also, then M and M' are isomorphic.

By definition, an image is an isomorphic model of the original. The similarity is based on the fact that when examining the image, its elements are replaced in the human consciousness by the elements of the original. For this purpose, when constructing the image, the elements of the original must be replaced by the elements of the former. We usually say that the elements of the original correspond to definite elements of the image, and vice versa.

The type of correspondence should be that which exists between the elements of the object being examined and the optical image in the human eye. Only under this condition can we speak of adequacy of the visual associations. The mathematical model of the eye is a central projection system. The correspondence between the original and the image in the eye is a projective correspondence. It is precisely this type of correspondence which is necessary in order that the image and the original be similar to one another in the generally accepted sense.

In speaking of projective correspondence, we usually have in mind geometric models and originals. The concept of projectivity in its broad sense, when the projective space is formed by objects characterized by both geometric and physical parameters, and when both types of parameters are subject to representation, is applicable to images.

The representation of geometric parameters on pictures is described quite completely by the particular form of projective correspondence termed perspective. It reflects the geometric essence of the image construction process.

/8

Our natural sense of similarity has been developed for a world where the perspective correspondence of visual models is invariant. This is associated with the geometry of radiant energy propagation (rectilinearity). The objects surrounding man are perceived visually by man primarily as geometric models constructed following the laws of linear perspective. These forms are very stable, since the perception of perspective is practically independent of illumination, color, and object contrast, provided these characteristics are above the threshold sensitivity of the eye. Violation of perspective correspondence affects similarity and causes difficulties in identifying the image with the original.

Deviation from perspective correspondence produces an impression on the human of geometric distortions. Within certain limits we adapt to such distortions. For example, curvature of lines on panoramic photographs which are rectilinear in actuality disturb us very little when we examine the photographs as a whole. This is explained by the fact that the deviation of the panoramic projection from perspective in small zones is slight, and the similarity of individual details is retained. However, if perspective is strongly disrupted for individual details as well, then simple identification of the pictures with the originals becomes impossible. We encounter this phenomenon, for example, when using certain radar images. Thus, at the edge of the airplane panoramic radar screen, the projection of details is nearly perspective and they are easily identified with the terrain features. However, in the center of the screen, where the projection differs markedly from perspective, the details are not similar to their originals.

This situation obviously leads to the conclusion that perspective correspondence is an important condition of similarity.

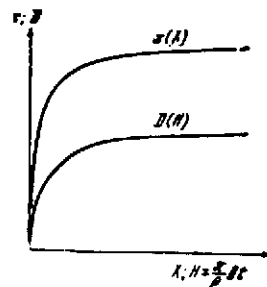
The laws of perspective in accordance with which geometric models are constructed are invariant with respect to the radiation bands. Satisfaction of these laws is imperative for all methods and technical means for obtaining images. Hence follows the validity of considering as images those visualized forms of the invisible band which have the properties of perspective correspondence within the limits of natural adaptation of man.

The physical parameters of the details of the original are represented on images as a result of action on the imaging system sensitive apparatus of the energy radiated by these details. In order that these parameters be represented in a similar fashion, the form of the picture details must correspond with the radiation.

For the entire visible band, integral correspondence involves the fact that details radiating a larger amount of energy must be imaged more brightly. We shall term this brightness correspondence. Here similarity is associated with the natural capability of man to react to external stimuli. This capability is invariant to stimulus type and its nature is the same for tactile, aural, and optical sensations; the larger the stimulus energy, the more significant the reaction of the organism. /9

We shall show that brightness correspondence can be expressed by projective correspondence.

The figure shows a typical photoemulsion characteristic curve $D(H)$ [2] (D is the photographic density; $H = (\pi/\rho)Bt$; ρ is the coefficient of diffuse scattering; B is the brightness; t is the exposure) and a typical $x(X)$ curve, the x -coordinates of the points of which are projectively connected with the X coordinates. It is obvious that the nature of the curves is the same.



By altering the projection parameters, we can select the function $x(X)$ so that it will approximate the photoemulsion characteristic curve. Consequently, D and B are in projective correspondence and the mapping $B \rightarrow D$ is a projective transformation. In preparing the positive, the transformation $D \rightarrow D_n$ takes place, where D_n are the densities of the details of the positive. In principle, this transformation is analogous to $B \rightarrow D$, i.e., it is also a projective transformation. In the final analysis, $B \rightarrow D \rightarrow D_n$, so that there is projective correspondence between D_n and B . The apparent brightness B_n of the details of the positive is inversely proportional to their photographic density. Consequently, there exists the transformation $B \rightarrow B_n$, which is also a projective transformation.

The high degree of similarity of the positive photoimage to the original is well known. Therefore, we can state that the brightness correspondence of the image and the original, which is necessary for similarity, actually is a projective correspondence.

Another correspondence which is necessary for similarity is color correspondence. Within the limits of narrow spectral zones of the visible band, the correspondence between the radiant energies and the apparent color brightness of a detail of the image must have the same nature as in the case of integral brightness correspondence. However, for the entire visible band it is different: the apparent image brightness will depend not only on the amount of energy radiated by the details of the original, but also on the spectral sensitivity /10 of the eye. It can be shown that over the entire visible band, color correspondence is also described by a projective correspondence if we use a particular form of the latter — affine transformations. For simplicity we shall term the combination of brightness and color projective correspondences tonal correspondence. It reflects the energetic essence of image construction.

When examining images, man adapts to deviations from the natural tonal correspondence within still larger limits than to perspective distortions. Color and brightness correspondences may even be

entirely lacking. Thus, similarity of the image and the original is maintained on black-and-white and single-color photographs. In the limiting case, similarity is maintained even without brightness correspondence — the case of the contour image*. More detailed examination of this question leads to discussion of the role of image detail contrast. Considering that the latter is a function of detail brightness, we shall leave this question aside, since we have clarified the nature of the brightness correspondence necessary for similarity.

The tonal correspondence of images obtained using invisible radiation (which is necessary for similarity) is, in principle, the same as for brightness correspondence.

In addition to perspective and tonal correspondences, an important similarity condition is image sharpness. On a blurred image it is difficult to identify its details with those of the original. We shall show that the concept of sharpness is associated in a definite fashion with the projective transformations of radiant energy in imaging systems.

It is well known that image sharpness depends on how the radiant energy passing through the elements of the imaging system is transformed. As a result of the transformation, the amplitude and phase of the signal at the system output differ from the amplitude and phase of the input signal. For the visible band, we consider [3] that if the original is a sinusoidal grid in which the energy distribution is expressed by the law

$$E(x) = a_0 + a \cos(2\pi Nx), \quad (1)$$

then this grid is transformed by the imaging system into an image having light energy distribution following the law

* Here we see that perspective correspondence plays the primary role in ensuring similarity, since only with this correspondence will the contour image be similar to the original. However, this example shows that there is no sharp boundary between the class of pictures and the neighboring class of drawings (see above).

$$E'(x) = a_0 + aF(N)\cos[2\pi Nx - \varphi(N)]. \quad (2)$$

In (1), (2): a_0 is the average value of the energy over the entire original grid; a is the amplitude, and N the period of the sinusoid; x is the coordinate of some point of the grid; $F(N)$ is the contrast-frequency characteristic (CFC); $\varphi(N)$ is the phase-frequency characteristic (PFC).

We denote

$$E'(x) - a_0 = \delta E'(x), \quad a\cos(2\pi Nx) = \delta E(x)$$

and transform (2) with account for this expression,

$$\frac{\delta E'(x)}{\delta E(x)} = F(N)[\cos \varphi(N) + \operatorname{tg}(2\pi Nx) \sin \varphi(N)]. \quad (3)$$

The quantities $\delta E'(x)$ and $\delta E(x)$ are variable components of the energy variation in the grid image and original. The sharpness depends on their ratio: the closer this ratio is to unity, the greater the similarity of the image to the original. This ratio characterizes the energy transformation scale in the imaging system.

We denote $F(N) = \tilde{f}$; $\varphi(N) = \tilde{\alpha}$; $\operatorname{tg}(2\pi Nx) = -\tilde{y}/\tilde{f}$, and rewrite (3) in the form

$$\delta E'(x)/\delta E(x) = \tilde{f}\cos\tilde{\alpha} - (\tilde{y}/\tilde{f})\sin\tilde{\alpha}. \quad (4)$$

This expression shows that the nature of the ratio $\delta E'(x)/\delta E(x)$ is similar to the perspective image scale [4]. The right side of (4) is sometimes termed the perspective coefficient. If we assume that $\delta E(x)$ is the original on the object plane and $\delta E'(x)$ is its central projection on the picture plane, then $\delta E'(x)/\delta E(x)$ can be treated as the image particular scale. In this representation, the projection parameters are $F(N)$, $\varphi(N)$, $2\pi Nx$, i.e., the CFC, PFC, and the sinusoid phase.

Thus, the transformation of (1) into (2) and the scale of this transformation, on which the image sharpness depends, really can be described in terms of the projective transformation.

Summarizing the above discussion, we can state that the common property of images is their geometric and energetic projectivity with respect to the originals.

Unified mathematical model of the image generation process. We mentioned previously that similarity is a form of isomorphism. Now we can refine this statement and show that the form is that of projectivity. Isomorphism permits representing one model by another model and examining the properties of an entire class of models on the example of any model of this class.

Let us consider an example with photographic and phototelevision images. Let A_0 be the model of an original which includes in itself the set of its elements a_1, a_2, \dots and operations $O_1(a_1, a_2, \dots)$, $O_2(a_1, a_2, \dots), \dots$.

/12

In this case we mean by operations, the breaking down of the original into geometric figures, identification of the spectral brightness, and textural ranges, determination of the mutual positioning and dimensions of the details of the original, and so on. It is obvious that the following transformation is valid for the photographic image, whose model we denote by A' : $a_1 \rightarrow b'_1, a_2 \rightarrow b'_2, \dots$; $O(a_1, a_2, \dots) \rightarrow O'_1(b'_1, b'_2, \dots)$; $O_2(a_1, a_2, \dots) \rightarrow O'_2(b'_1, b'_2, \dots)$, where $b'_1, b'_2, \dots, O'_1, O'_2, \dots$ are the elements of model A' . But for the phototelevision image A'' the transformation $a_1 \rightarrow b''_1, a_2 \rightarrow b''_2, \dots$; $O_1(a_1, a_2, \dots) \rightarrow O''_1(b''_1, b''_2, \dots)$, and so on (analogous notations), are also valid. Consequently, on the basis of the equivalence principle $A_0 \rightarrow A', A_0 \rightarrow A'', A' \rightarrow A'', A' \rightarrow A_0, A'' \rightarrow A_0, A'' \rightarrow A'$, i.e., the models A' and A'' are isomorphic, and one replaces the other.

Isomorphism also yields a more universal approach for generalizing the processes of image construction with the aid of various methods and equipment.

We denote by M_ϕ the model of the process for obtaining the photographic image. This model includes in itself the models A_0

and A' indicated above with their elements a, b' and the operations O, O' , and also the operations P_ϕ, P'_ϕ on the models A_0 and A' , which are their mutual projective and orthogonal transformations, necessary for the mapping $M_{\phi T}$. We denote by $M_{\phi T}$ the model of the process for obtaining the phototelevision image. It is obvious that its composition is analogous to that of the model M_ϕ , i.e., it includes in itself $A_0, A''; a, b''; O, O''$ and $P_{\phi T}, P'_{\phi T}$. It is logical to state that if A' and A'' , which are the final results of the processes of obtaining images by the photographic and phototelevision methods, are isomorphic, then the models $M_\phi, M_{\phi T}$, are also isomorphic and, consequently, there must exist the mapping $P_\phi \rightarrow P_{\phi T}, P'_\phi \rightarrow P'_{\phi T}$ and, conversely, $P_{\phi T} \rightarrow P_\phi, P'_{\phi T} \rightarrow P'_\phi$.

On the basis of this discussion, we conclude that the processes of obtaining images by the different methods can be described by a unified mathematical model.

We shall attempt to point out the general outlines of such a model.

We assume that the final image is the terminal objective form which does not change upon examination and is independent of subjective perception. We shall term this form the copy, and denote it by A . We represent the copy by the ensemble of conditional image elements, where each element is characterized by a position in the coordinate system belonging to the copy, and by the tone $A = (x, y, z, C, D)$, where x, y, z are the position coordinates, C and D are the color and density or brightness (tonal characteristics). For flat images, photographs, for example, the z coordinate can be neglected.

Generally speaking, the final image is its subjective form which arises in the human visual apparatus. It is a result of physiological processes which cannot yet be described sufficiently exactly mathematically. Therefore the terminal objective form A

/13

must, for the time being, be considered the final element of the mathematical model of the image generation process.

In addition to the form A , there also exists an incomplete objective form, also visualized, but varying in time. We term it A_t and describe it by the ensemble $A_t = (x, y, z, C, D, t)$, where the position and tone of each element are characterized by the time t as well. Such a form is, for example, the image on a kinescope or the optical image in a photographic camera. It is obvious that, in the general case, the ensemble A is some phase interval of the ensemble A_t , and the former is a function $A(A_t)$ of the latter.

The object of imaging can be represented by the ensemble $A_0 = (X, Y, Z, B_{\phi\lambda}, t)$, where X, Y, Z are the spatial coordinates of the original of an arbitrary image element in a coordinate system fixed in the object; $B_{\phi\lambda}$ is the energy radiated by the original of the element in the given direction ϕ , with spectral composition λ ; t is the current time.

The ensemble A_0 is the basic element of the image generation process model, which is transformed by a series of operations into the ensemble

$$A = A_0 P, \quad (5)$$

where $P = (P_1, P_2, \dots, P_n)$ is the ensemble of operations, which includes the operation transforming A_t into $A = A_t P_n$. A typical listing of the operations which make up the ensemble P is as follows.

Operations involving influence on the primary radiation of the medium in which it propagates. Filtering and redistribution of the energy in the primary radiation receiver, including accounting for receiver orientation relative to the system OXYZ. Transformation by the receiver sensitive element of the radiant energy into electrical or chemical energy. Amplification of the latter and its

transformation into the energy of coded signals corresponding to some information system. Signal transmission over the communication channels. Storage and retention of the information. Reproduction and visualization of the information and conversion of the latter into the form A.

It is clear that the actual composition of the operations in any particular image generation system may be different. Additional operations involving logical and geometric information processing may be carried out in parallel with the basic operations or in the interval between the latter. Such processing is an independent question, which we shall not examine.

Expression (5) is the symbolic form of the mathematical model of the image generation process. /14

The information contained in the image can be divided into information of the first kind (tonal relationships, representing the physical parameters of the original and the energetic essence of the images), and of the second kind (geometric structural relationships, reflecting the spatial distribution of the details of the original and the perspective essence of the images). Information of the first and second kinds cannot exist independently. Nevertheless, this distinction has developed historically and is convenient in practice in many cases. Two approaches to the expansion of (5) can be followed in accordance with this division.

In the first approach, we ignore completely the projective nature of the images, and examine only the energy transformation and dissipation process. An example here is the analysis of imaging systems by the CFC method. In the second approach, we ignore the energetic essence and examine only the perspective properties of the image. We use this approach, for example, in photogrammetry. The two approaches assume different forms of expansion of (5). We shall illustrate the possibilities of expansion of (5) by the example of the construction of the mathematical model describing the geometry

of terrain projection onto a photograph obtained under dynamic conditions, i.e., with movement of the camera. Such a model appears as follows:

$$x_\phi = x + \sigma x, \quad y_\phi = y + \sigma y; \quad (P_9)$$

$$x = x_s \cos(\omega_s t) - y_s \sin(\omega_s t), \quad y = x_s \sin(\omega_s t) + y_s \cos(\omega_s t); \quad (P_8)$$

$$x_s = \frac{f \operatorname{tg}(\omega_y f)}{1 - \frac{x_s}{f} \operatorname{tg}(\omega_y f)}, \quad y_s = \frac{y_s \sec(\omega_y f)}{1 - \frac{x_s}{f} \operatorname{tg}(\omega_y f)}; \quad (P_7)$$

$$x_s = \frac{x_s \sec(\omega_x f)}{1 - \frac{y_s}{f} \operatorname{tg}(\omega_x f)}, \quad y_s = \frac{f \operatorname{tg}(\omega_x f)}{1 - \frac{y_s}{f} \operatorname{tg}(\omega_x f)}; \quad (P_6)$$

$$x_3 = \frac{x_2 e^{\frac{W_H t}{H}} - f(e^{\frac{W_H t}{H}} - 1) K_2 \sin \alpha \sin \kappa}{e^{\frac{W_H t}{H}} - (e^{\frac{W_H t}{H}} - 1) K_2 \cos \alpha},$$

$$y_3 = \frac{y_2 e^{\frac{W_H t}{H}} + f(e^{\frac{W_H t}{H}} - 1) K_2 \sin \alpha \cos \kappa}{e^{\frac{W_H t}{H}} - (e^{\frac{W_H t}{H}} - 1) K_2 \cos \alpha}; \quad (P_5)$$

$$K_2 = \cos \alpha - \frac{-x_2 \sin \kappa + y_2 \cos \kappa}{f} \sin \alpha;$$

$$x_2 = \frac{x_1 + \frac{W}{H} t f (\cos \gamma \cos \kappa - \sin \gamma \sin \kappa \cos \alpha) K_1}{1 + \frac{W}{H} t K_1 \sin \gamma \sin \alpha}, \quad (P_4)$$

$$y_2 = \frac{y_1 + \frac{W}{H} t f (\cos \gamma \sin \kappa + \sin \gamma \cos \kappa \cos \alpha) K_1}{1 + \frac{W}{H} t K_1 \sin \gamma \sin \alpha};$$

$$K_1 = \cos \alpha - \frac{-x_1 \sin \kappa + y_1 \cos \kappa}{f} \sin \alpha;$$

$$x_1 = x_0 + x' \cos \kappa - y' \sin \kappa, \quad y_1 = y_0 + x' \sin \kappa + y' \cos \kappa; \quad (P_3)$$

$$x' = X' \frac{f}{H} K'^{-1}, \quad y' = Y' \frac{f}{H} K'^{-1} \cos \alpha; \quad (P_2)$$

$$K' = \sec \alpha + \frac{Y'}{H} \sin \alpha;$$

$$X' = l_1(X - X_0) + m_1(Y - Y_0) + n_1(Z - Z_0),$$

$$Y' = l_2(X - X_0) + m_2(Y - Y_0) + n_2(Z - Z_0). \quad (P_1)$$

In this model

$$(x_\phi, y_\phi) = A; (X, Y, Z, t) = A_0,$$

and the factors $C, D, B_{\phi, \lambda}$ are not considered.

The ensemble A_0 is reduced to the ensemble A by the sequential operations P_1, \dots, P_9 . The operations P_1, P_3, P_8, P_9 are orthogonal transformations, while P_2, P_4, P_5, P_6, P_7 are projective.

The operations are performed on the intermediate ensembles

$$A_1 = (X', Y'), A_2 = (x', y'), A_3 = (x_1, y_1), A_4 = (x_2, y_2, t),$$

$$A_5 = (x_3, y_3, t), A_6 = (x_4, y_4, t), A_7 = (x_5, y_5, t), A_8 = (x, y, t)$$

and in these operations we use the orientation elements $l_1, l_2, m_1, m_2, n_1, n_2, X_0, Y_0, Z_0$ of the auxiliary system $O'X'Y'$ relative to $OXYZ$; α, f, H of the oxy system relative to $O'X'Y'$; x_0, y_0, κ of the $o'x'y'$ system relative to oxy. In addition, we use the translational velocities W, W_H and the direction γ of displacement of the projection center relative to the system $OXYZ$; the angular velocities $\omega_x, \omega_y, \omega_z$ of rotation of the axes of the oxy projecting system relative to $OXYZ$; the overall corrections $\sigma_x \sigma_y$ for the geometric distortions caused by deviation of the real image from linear perspective. /16

The proposed model can serve as the basis for geometric models of images obtained by any other imaging systems.

In the form written above, it reflects the connection between the coordinates of the terrain points and picture points obtained by photographic, electronic television, and phototelevision methods. For these methods, σ_x and σ_y denote the sums of the corrections for atmospheric refraction, objective lens distortion, photographic material deformation, nonlinearity of the television channel scans, and so on.

For panoramic photographs, the operation (P_9) will have the form

$$\check{x}_\phi = x \cos \text{arctg}(y/f) + \sigma x; \quad \check{y}_\phi = f \text{arctg}(y/f) + \sigma y, \quad (P'_9)$$

where $\check{x}_\phi, \check{y}_\phi$ are the cylindrical coordinates of the image point on the panoramic photograph.

For single-line scanning television systems and IR radiometers, the model indicated above will reflect the connection between the picture and terrain coordinates within the limits of a single image line, if we set $\check{x}=x=0$, and $\check{y}=f \text{arctg } y/f$.

In all cases, $\alpha, f, H, x_0, y_0, z$ denote respectively, the perspective principal ray inclination relative to the vertical, the perspective principal distance (focal length of the objective), mapping altitude, coordinates of the origin and rotation angle of the $o'x'y'$ auxiliary system relative to the picture coordinate system. Depending on the posed problem, t denotes the exposure time, panning time, scanning time, interval between exposures, and so on.

The proposed model demonstrates the isomorphism of the images with respect to their geometric nature. A similar model can be constructed for the radiant energy transformation processes. However, it is advisable to develop a unified image generation model which will reflect the projective essence of the images as a whole, i.e., will combine both the perspective and energetic models.

It seems to us that the development of a unified model will be the primary problem of theoretical iconics. The unified model will become the unifying methodological basis of the various image generation methods and techniques, the core of practical iconics, determining the common approach in the development of specific imaging systems.

At the present time, various technical means for obtaining images are being developed independently of one another. It often

seems that the developments are carried out unilaterally. For example, some of the imaging systems used in space studies, while having high information content of the first kind (see above), yield images which are of little use for geometric interpretation. In these systems, no provision is made for even the very simple operations required for coordinate and space and time correlation of the image details. As a result, the information content of the second kind in such systems is very low. The unified model mentioned above should direct the imaging system developers towards ensuring high information content of both the first and second kinds.

The absence of a common methodological basis leads to a situation in which the images obtained by the individually developed imaging systems are difficult to correlate. The unified model makes it possible to develop common criteria for evaluating image quality.

It is well known that considerable attention is devoted to the problems of selecting image quality criteria with respect to the sharpness characteristic. Without belittling the importance of such studies, we should point out that the criteria for evaluating reproduction quality with respect to brightness relationships and geometric accuracy are being ignored. In space studies, in particular, photometric measurements of the planet images play a major role. Without a criterion for the quality of the brightness relationship representation, the results of photometric measurements may not be truly representative.

As a preliminary proposal, we can consider the image brightness and geometric accuracy criterion to be the deviation of the real pictures from projective correspondence, formalized by the unified mathematical model.

The idea that only terrain pictures obtained by so-called topographic cameras are suitable for precise geometric interpretation is widely accepted. These cameras have low photogrammetric distortion, have a focal plane shutter, and do not have image motion compensation. This idea is the result of using the particular imaging

process model developed for static conditions, when we can consider that the camera and the terrain are mutually stationary during the exposure time.

In space studies, imaging process dynamics become a major factor and consideration of the static model leads to considerable reduction of image information content. Specifically, in order to ensure high picture detail content, it is necessary to use long focal length cameras with image motion compensation. The objectives of such cameras have significant distortion. If we make use of the old concepts, the pictures obtained by such cameras are not suitable for precise geometric constructions. Moreover, the tendency to use topographical cameras for imaging in space studies leads to photography scale limitations, which reduces the information content of the first kind in the pictures and, in the final analysis, reduces the information content of the second kind as well. In the case of small imaging scales, the picture measurement errors, when referred to the surface of the planet, yield large errors in determining surface point coordinates. /18

The mathematical imaging model presented above already broadens considerably the application of the various images for precise geometric interpretation. However, the unified model yields still greater possibilities, since it will also reflect the processes which determine picture detail content, which influences significantly the accuracy of the geometric constructions.

The above-listed aspects of use of the unified image generation process model relate to the problems of iconics proper. They are associated with questions of accuracy, detail content, and comparability of images — to a considerable degree irrespective of image interpretation. This listing could be continued.

There are several aspects of unified model application as the methodological basis of image interpretation. We shall examine some of these aspects.

In spite of the great variety of image interpretation methods, they still can be combined into three fundamentally different groupings.

We include in the first group the interpretation forms based on heuristic principles which are not amenable to algorithmization. The second group includes the automatic pattern recognition methods. The basis of such methods are the logical image processing algorithms. The third group includes the methods using algorithms obtained from imaging models of one sort or another.

We shall examine the third group, since that it has a direct relationship to the theme of the present article.

The essence of the image interpretation methods forming the third group consists in seeking the unknown parameters of certain elements of the imaging model. Such elements may be an object, its radiation, the medium, the imaging system, and so on. On the basis of the imaging model, we formulate the equation or system of equations from the solution of which we determine the unknown parameters. The effectiveness of this interpretation depends on how completely the model describes the imaging process. We shall consider an example of topographical interpretation of lunar photographs obtained from spacecraft.

One of the tasks of topographical interpretation of photographs is to determine the coordinates of terrain points. The formulas of photogrammetry are usually used for this purpose. These formulas are the solution of the equations formulated from the imaging model describing the perspective correspondence of the image and the original. In these equations, the original parameters X , Y , Z are the unknowns. In our case, these coordinates are the selenocentric coordinates of the lunar surface points. /19

The pictures obtained from spacecraft permit effective use of the photogrammetric method for constructing a unified coordinate

system on the Moon and determining the absolute heights of the relief. However, the limitations imposed by the specific nature of space flight conditions do not permit interpretation by the photogrammetric method of small lunar relief elements from these pictures.

The photometric method is more effective for interpretation of small elements. This method is based on the imaging model which reflects the energetic correspondence of the image and the original — the lunar surface. However, these parameters are expressed by terrain slopes rather than by point coordinates. The photometric method makes it possible to determine precisely the slopes and heights of the relief elements, but it is not suitable for determining absolute heights.

It is obvious that both methods of topographical interpretation of lunar photographs taken from spacecraft have significant drawbacks, which are a consequence of the fact that partial imaging models are used in both methods: perspective in the first and energetic in the second. Therefore, a unified model of the imaging process which permits combining the photogrammetric and photometric methods and makes them more effective must be used as the basis of topographical interpretation of lunar photographs. This is also valid for the other forms of image interpretation by the third group mentioned above.

A unified model of the imaging process must form the methodological basis of the third group. It appears to us that the theoretical problem of iconology involves formulation from the unified model of equations with different unknowns, and the development of methods for solving these equations.

References

1. Ikonica (Iconics). Collection of articles. Nauka Press, Moscow, 1968.
2. Mikhaylov, V. Ya. Aerofotografiya i Obshchiye Osnovy Fotografii (Aerial Photography and the General Fundamentals of Photography), Geodezizdat, Moscow, 1959.

3. Apenko, M. I. and A. S. Dubovik. Prikladnaya Optika (Applied Optics). Nauka Press, Moscow, 1971.
4. Lobanov, A. N. Aerofototopografiya (Aerophototopography). Nedra Press, Moscow, 1971.

PROSPECTS FOR THE DEVELOPMENT OF PHOTOTELEVISION
METHODS IN SPACE STUDIES

A. S. Selivanov

In-space imaging of the surface of celestial bodies can be carried out by both television and photographic equipment.

/20

Television equipment of various types has the important property that when installed aboard a spacecraft it is capable of transmitting the image of the object being viewed directly during the time of imaging or, as we say, in real time. However, such operation is not possible in the great majority of cases because of the nature of information transmission over the spacecraft-ground communication line.

The inadequate energy handling capacity of the communications line usually forces reduction of the information transmission rate in comparison with the rate at which information is obtained by the television system. There are conditions when direct communication with the spacecraft is not provided at the moment of imaging. Then the need arises for storing the video information aboard the spacecraft for subsequent transmission at a definite time and at a definite rate. For this purpose, the television camera (TC) can be connected with a magnetic memory (M) of the magnetophone type. Such equipment is used on the Mariner automatic interplanetary stations [1] used to study Mars, and on many Soviet and American weather satellites. Image storage on photographic film is also possible, and was used on Luna 3 [2], Zond 3 [3], and Lunar Orbiter [4]. The

television technique is also used aboard these vehicles, but only for transmission of an image first obtained on photographic film. Therefore, such systems have been termed phototelevision systems (PTS).

The choice of a system of one type or the other is dictated by several considerations, the most important of which are the size and weight characteristics, other conditions being the same (power consumption, reliability, and so on).

Comparing the phototelevision and television-plus-magnetic memory systems, we note that the information handling process in the second system is more complicated, since image storage takes place in two stages, and this involves the use of two forms of memory (Figure 1). The first preliminary storage (for a comparatively short

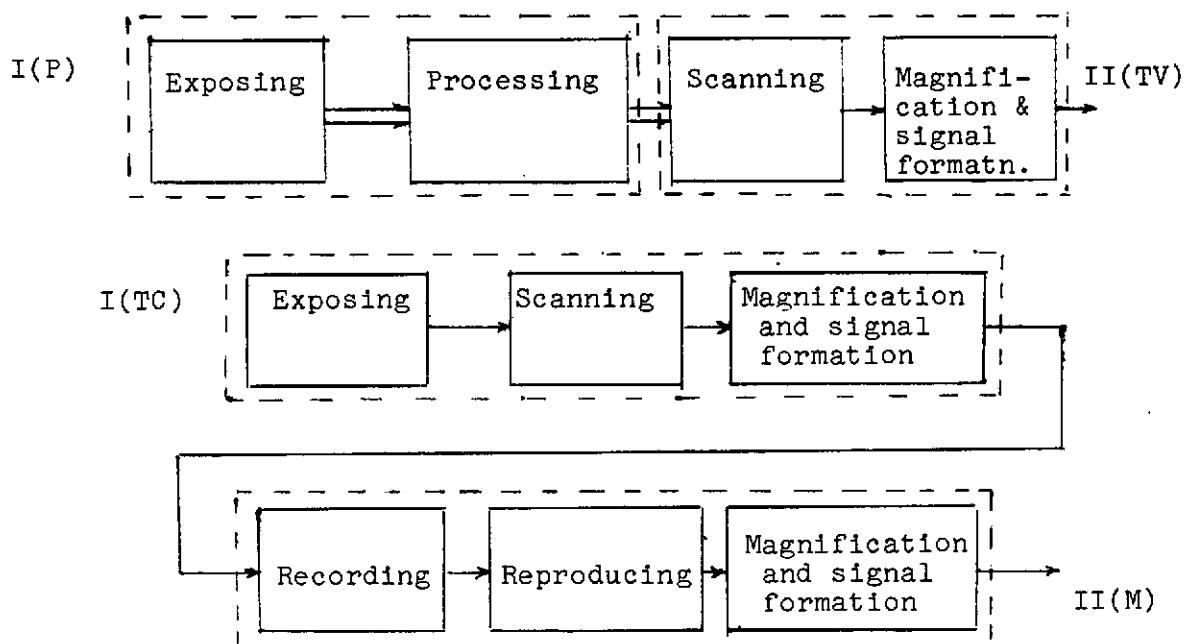


Figure 1. Block diagram of PTS and TC + M

time) takes place of exposing the target of the television transmitting tube, and then the video information is transferred to the mag-

/21

The internal structure of the phototelevision system can be roughly broken down into two functionally different blocks: the photographic (storage) part I(P), where exposure and processing of the carrier takes place, and the television (reproducing) part II(TV), where information readout takes place. The two parts have intimate structural coupling with another provided by the common information carrier — photographic film.

The more complex block diagram of the second system is also reflected in the structure, which consists of two blocks of different types which are coupled only electrically with one another. However, the fundamental difference between these systems lies in the characteristics of the information carriers used.

To date, photographic film remains an unsurpassed carrier with regard to information recording density, i.e., with regard to the number of image elements (or bits) recorded per unit surface area. As for magnetic film, while having linear recording density practically the same as that of photographic film (to several hundred lines/mm), it is inferior to the latter in regard to surface density, since to date magnetic recording is practically one-dimensional. Multitrack, and particularly transverse recording, which is used in ground-based video magnetic recorders, reflects the tendency toward two-dimensional recording. To date, only designs and prototypes of airborne video magnetic recorders with transverse recording exist. Because of their complexity, it has not been possible to make them sufficiently compact and lightweight.

/22

Comparison of photographic film with the television tube (on the basis of various characteristics) makes it possible in two cases to give preference to the television-magnetic equipment construction technique over the phototelevision method.

1. When it is necessary to record a relatively small volume of video information, for example, in the initial stage of planetary studies (Mariner). In this case, the required carrier (magnetic or photographic film) volume is not large and does not define the

design, which is acceptable for installation aboard a spacecraft in either version. Here, such factors as technical traditions, operating convenience, requirements of universality, utilization prospects, and so on, are decisive.

2. When repeated utilization of a relatively small carrier volume is required, for example, as is necessary in the weather satellite operating regime. In this case, the advantages of the television-magnetic method with respect to rapid recording and reproduction and recording economies are obvious.

Let us examine the first case in greater detail. The information volume limit, after which the advantages of the phototelevision equipment become obvious, is very arbitrary. Analysis shows that the current state of the art, this limit lies somewhere in the region of $10^7 - 10^{10}$ image elements. This limit will naturally increase with development of the technology. The existing situation is well illustrated by comparison of the parameters of the imaging equipment of the Mariner and Zond 3 flyby stations. Mariner studied Mars in 1965 and 1969, and Zond 3 photographed the back side of the Moon in 1965, although it was initially intended for a study of Mars as well [3]. Thus, the equipment had the same mission, but was implemented on a different technical basis. The equipment parameters are given in the table. We note such parameters as the equipment weight G , memory volume W , and the so-called γ -effectiveness ($\gamma = G/W$) of the design. We see that the parameters of the phototelevision equipment are better even for systems of this class.

Let us consider the effective resolution R , which is a most important parameter for all phototelevision devices. The resolution is determined by the selected image transmission scanning standard, from which we obtain by calculation the value of R presented in the table. The effective resolution has a limit determined by the objective-lens photographic-film system.

TABLE

SC	Eqpt. type	W, el	G, kg	$\gamma = W/g$ el/kg	R lines/mm	1/Rn, m/line
Zond-3, USSR, 1965	PTS	$3.4 \cdot 10^7$	6.5	$5.2 \cdot 10^6$	20	$5 \cdot 10^3$
Mariner 4, USA, 1965	TC, M	$8.4 \cdot 10^5$	9.2	$9.2 \cdot 10^4$	20	$2.4 \cdot 10^3$
Lunar Orbiter, USA, 1967	PTS	$1.3 \cdot 10^{11}$	68	$1.9 \cdot 10^9$	76	$8 \cdot 10^3$

Here it is important to emphasize that there are no serious technical limitations in the television part of the system to prevent full realization of the resolution of the photographic part. Therefore, the effective resolution choice is dictated primarily by the mission of the particular phototelevision system.

/23

If the system is designed to obtain a relatively small volume of basic information on the surface of the object (back side of the moon, Mars) and achievement of maximum surface resolution is not the most important objective, then it is advisable to design the system so that transmission of both large and small image details is not distorted by the photographic film grain structure. In other words, we should not approach the film resolution limit and utilize a lower "recording" density. The phototelevision system of the Zond 3 type was developed on the basis of these considerations. Here the effective resolution was 25 lines/mm (optical) with limiting resolution of about 40 lines/mm. The signal/noise ratio of the analyzer was no less than 20 (Figure 2).

Realization of the limiting resolution is advisable in the case when the primary purpose of the PTS is to detect on the surface of the object being studied very small relief details, particularly in connection with the need for imaging large areas. In this case, the television part and the communications channel should not

introduce marked distortions into the transmission of the information obtained on the photographic film; the limiting factor is the threshold of useful signal detection in the photographic noise.

This problem was resolved by the spacecraft of the Lunar Orbiter type, which were used to obtain selective mapping of the Moon with surface resolution $R_s^{-1} = 8$ m, and imaging of individual areas with resolution $R_s^{-1} = 1$ m. Here, the detection threshold was taken as $U_s/U_n = 1$, which was achieved with a resolution on the film of 76 lines/mm (see Figure 2).

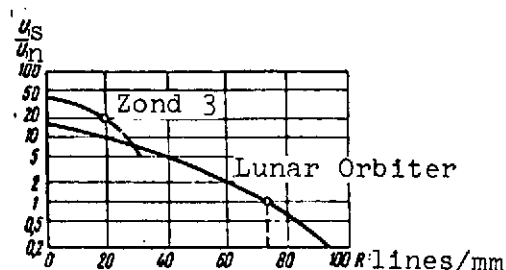


Figure 2. Resolution versus signal/noise ratio

The effective resolution is a very important information parameter of any imaging system, including the phototelevision system, and determines the potential capabilities of system use.

The television transmission method introduces distortions into the basic image obtained on the photographic film. /24

The geometric distortions introduced by the image transmission and reception devices are the most significant and technically difficult to overcome. While the distortions caused by objective lens distortion amount to tenths or hundredths of a percent, television transmission in certain cases may yield nonlinear geometric distortions of up to a few percent. This distortion magnitude makes analysis of the image very difficult, and sometimes prevents analysis entirely, for example, stereophogrammetric analysis. It is difficult to reduce the magnitude of the nonlinear geometric distortions to 1%. Therefore, the possibilities for improving the PTS characteristics lie in calibrating the equipment with the required degree of precision and increasing the operational stability of the scanning devices, even those which are quite nonlinear. This explains the extensive use in modern phototelevision systems of

optico-mechanical scanners, which have high stability of the characteristics in time and under the influence of various spaceflight factors.

Knowledge of the calibration data does not, in itself, yield the required accuracy. Therefore, considering the very extensive labor involved, it is necessary to plan for computer analysis of the images with account for the calibration data. Machine processing of images obtained from spacecraft is absolutely necessary for several reasons, and at the present time, definite success has been achieved in this promising direction.

A very noticeable negative feature of current PTS is dissection of the information transmitted by these systems. This is caused by the inadequate definition of the television transmitters. Here, we mean by definition the number of elements in the image scan line. As a rule, there are 600 - 1000 image elements in a single line of the transmitted image. At the same time, there are 10 - 18 thousand elements in the frame width of 70 mm aerial film, for example, depending on the film type. Therefore, in practice, the image on the film is dissected by one technique or other into several images which can be transmitted with lower definition. This is seen most clearly for the example of image transmission from the Lunar Orbiter spacecraft. /25 The photographs obtained from these satellites consist of individual strips with $600 \times 18,000$ element definition.

It is clear that the dissection process leads to information loss when joining the frames, reduces control accuracy, and gives rise to additional geometric and brightness distortions. However, in a well designed system, these deficiencies are not decisive and cannot serve as a serious argument against the use of PTS. These problems will be resolved in the future by the use of television scanners with superhigh definition (reports of such devices have already been published [5]):

The prospects for use of the phototelevision method in space studies are quite good. This method has absorbed the experience of

earth-based astronomy and aerial photography, and will be in the immediate future one of the basic techniques for studying the planets.

It should also be added that of all the onboard spacecraft subsystems, including telemetry, the television subsystem usually processes and transmits the largest volume of information. Therefore, the wide use of the phototelevision method depends directly on the development of equipment for long-range space communications.

References

1. Allen, I. Denton. A Mars Spacecraft Photographic System. JSMPTTE, Vol. 74, No. 6, 1965.
2. Bratslavets, P. F., I. A. Rosselevich, and L. I. Khromov. Television Apparatus for Scientific Studies of Space. Tekhnika kino i televideniya, No. 10, 1966.
3. Selivanov, A. S., G. M. Aleshin, and G. A. Golenko, et al. Phototelevision Systems for Space Studies. Tekhnika kino i televideniya, No. 7, 1969.
4. Kosovsky, L. G. and G. K. Broom. Photographic Equipment of Satellite Launched into Selenocentric Orbit. Doklady Akademii Nauk (DAN), Vol. 74, No. 9, 1965.
5. New Camera System for Geophysical Satellites. Aerospace Technology, Oct. 23, 1967.

FUTURE DEVELOPMENT OF IR THERMOVISION WEATHER
SATELLITE EQUIPMENT

A. V. Listratov

The self radiation of the surface being viewed is used for image synthesis in IR thermovision equipment. The installation of such equipment aboard weather satellites makes it possible to obtain cloud cover pictures of the Earth's surface in a complete orbit, regardless of the illumination conditions, and also provides quantitative information on the underlying surface temperature and cloud top height. Such equipment is used successfully aboard the Soviet satellites of the Meteor system, and experimentally on the American satellites of the Nimbus series [1]. /26

With regard to surface resolution, the present-day IR weather satellite equipment is inferior to the television equipment. This is due primarily to the comparatively low detectivity of the IR detectors used.

While IR equipment has several fundamental advantages in comparison with the conventional television equipment, the problem arises of determining the possibility for future development of weather satellite IR thermovision equipment. For this purpose, we need to examine the basic criteria for evaluating the quality of IR thermovision equipment. Analysis of the achievable values of its parameters and their interconnection makes it possible to evaluate the possibilities for development of equipment of this class.

Basic specific criteria for evaluating the quality of meteorological IR thermovision equipment. In the general case, the basic criteria for evaluating the quality of the conventional television image are applicable to the image obtained with the aid of IR equipment. Along with this, there are certain specific characteristics associated with the IR images obtained with the aid of narrow-angle

scanning radiometers (in the present article, we consider only thermovisors of this type). The primary characteristic is the advisability of expressing the threshold sensitivity in terms of the minimum detectable temperature differential ΔT_{\min} and the resolution in the form of the angular quantity θ , equal to the radiometer elementary scanning view angle.

Since IR detector reaction is proportional to the change of the thermal flux ϕ acting on it with change of the temperature of the surface in question from T to $T + \Delta T$ (in the following for the sake of brevity, we term $\Delta\phi$ the differential thermal flux), to determine the nature of the dependence of ΔT_{\min} on the temperature of the radiating surface it is necessary to know the analogous relation for the differential thermal flux.

Considering that for high quality thermovision equipment

$$\Delta T_{\min} (^{\circ}K) \ll T (^{\circ}K), \quad (1)$$

by differentiating the Planck radiation formula with respect to T , /27
we obtain

$$\Delta\Phi d\lambda = \frac{2\pi h^2 c^2 d\lambda}{k(e^{ch/\lambda kT} + e^{ch/\lambda kT} - 2)\lambda^2} \frac{\Delta T}{T^2}, \quad (2)$$

where $\Delta\Phi d\lambda$ is the specific spectral differential power of the radiation from unit surface area in the wavelength interval from λ to $\lambda + d\lambda$ with change of the radiating surface temperature from T to $T + |\Delta T|$. It is obvious that for determining $\Delta\Phi$ in any wavelength interval, $\lambda_1 - \lambda_2$ (2) must be integrated in this same interval. The results of integration in the range from 0 to ∞ can be expressed analytically [2]

$$\Delta\Phi = 4\sigma T^3 \Delta T. \quad (3)$$

Integration of (2) can be simplified by using the universal tabulated normalized function $\Delta\Phi(\lambda, T)$, similar to the analogous functions used for calculations using the Planck radiation formula.

Then

$$\Delta\Phi(T, \lambda_1 - \lambda_2) = 4\sigma T^3 \Delta T \omega(T, \lambda_1 - \lambda_2), \quad (4)$$

where $\omega(T, \lambda_1 - \lambda_2)$ is the so-called coefficient of differential thermal flux utilization, calculated with the aid of the universal tabulation function

$$\omega(T, \lambda_1 - \lambda_2) = \frac{\int_{\lambda_1}^{\lambda_2} \Delta\Phi(\lambda, T) d\lambda}{\int_0^{\infty} \Delta\Phi(\lambda, T) d\lambda}. \quad (5)$$

Using (4), we can write the expression connecting $\Delta T_{\min}(T)$ for any temperature T with $\Delta T_{\min}(T_0)$, measured (or calculated) for some one temperature T_0 of the radiating surface

$$\Delta T_{\min}(T) = \Delta T_{\min}(T_0) \frac{T_0^3 \omega(T_0, \lambda_1 + \lambda_2)}{T^3 \omega(T, \lambda_1 + \lambda_2)}. \quad (6)$$

The values of the function $N(T)$, which is the ratio $\Delta T_{\min}(T) / \Delta T_{\min}(T_0)$, for the spectral ranges $0 - \infty$ (continuous curve); $3.4 - 4.2$ (heavy dashed curve), $8 - 12$ (light dashed curve), and $10.5 - 12 \mu$ (dash-dot curve), calculated using (6) are shown in Figure 1.

Connection between the basic parameters of thermovision equipment and the parameters of its individual component parts. In order to find this relationship, we must first of all determine the criteria which characterize uniquely the capability of the IR detector to detect small differentials (changes) of the temperature of the surface being measured when operating in the given spectral band (for meteorological thermovision equipment, this band is one of the atmospheric transmission "windows").

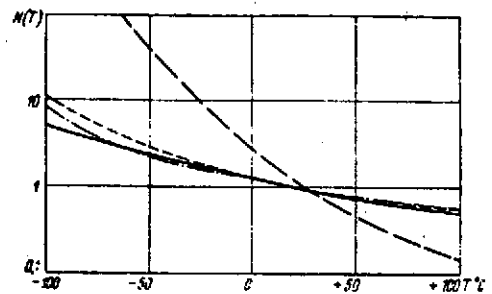


Figure 1. Threshold sensitivity versus radiating surface temperature

Analysis shows that such a criterion (we term it the IR detector detectivity for small temperature differentials and denote it by Q) can be the generalized IR detector parameter defined by the formula

$$Q = \frac{\sqrt{2} \sigma T^3 D^* (T_0, f, \Delta f) \omega [T, \phi(\lambda)]}{K_{ut} [T_0, \psi(\lambda)]} \frac{\text{Hz}^{1/2}}{\text{deg} \cdot \text{cm}} \quad (7)$$

where $D^* (T_0, f, \Delta f)$ is the IR detector detectivity (the conditions of D^* measurement are indicated in the parentheses); $\omega [T, \phi(\lambda)]$ is the flux difference utilization coefficient, determined from (5); $\phi(\lambda)$ is the product of the atmospheric spectral transmission function and the thermovision equipment spectral sensitivity; K_{ut} is the so-called radiant flux utilization coefficient; $\psi(\lambda)$ is the detector spectral sensitivity characteristic.

Physically, the IR detector detectivity Q for temperature differentials indicates the signal-noise ratio at the output of an effective IR detector having a dimension of 1 cm² with change of the measured surface temperature by 1° C with a passband of 1 Hz. By signal, we mean the effective value of the signal change at the IR detector output with change of the measured surface temperature.

Formula (7) yields the value of Q for the same conditions (modulation type, chopping frequency, frequency band) used in determining the value of D^* appearing in the formula. The corrections for other conditions, due to noise spectral density variation and detector inertia, can be easily introduced if these characteristics of the IR detector are known. We denote the value of Q determined in this fashion with account for use under actual conditions by Q*, and in the parentheses following this symbol, we indicate the radiating surface temperature T and the working spectral band $\lambda_1 - \lambda_2$ or the spectral characteristic for which the detectivity for temperature differentials has been determined. /29

The table presents the detectivity values of temperature differentials calculated using (7) for several types of IR detectors

TABLE #

Detector type	Spectral range λ , μ	Operating temp. T, $^{\circ}\text{K}$	D $\text{cm} \cdot \text{Hz}^{1/2} \cdot \text{W}^{-1}$	Q $\text{Hz} \cdot \text{deg}^{-1} \cdot \text{cm}^{-1}$
Thermistor bolometer	8-12	295	$1,95 \cdot 10^8$	4500
Thermistor bolometer	10,5-12	295	$1,95 \cdot 10^8$	1800
PbSe	3,4-4,2	195	$7,5 \cdot 10^8$	180
HgTe - CdTe	8-12	77	$3 \cdot 10^9$	$1,73 \cdot 10^5$
HgTe - CdTe	10,5-12	77	$3 \cdot 10^9$	$8,4 \cdot 10^4$
Ge:Hg	8-12	30	$1 \cdot 10^{10}$	$4,2 \cdot 10^5$
Ge:Hg	10,5-12	30	$1 \cdot 10^{10}$	$1,5 \cdot 10^5$

Note: The first two values of D^* were calculated for $f = 10$ Hz, and the remaining values — for $f = 900$ Hz.

*Commas represent decimal points.

when using them in the spectral band corresponding to the atmospheric transmission "windows". The calculation was made for radiating surface temperature equal to -50°C (223°K). The nature of the Q variation with change of the radiating surface temperature can be estimated in the first approximation from the curves of Figure 1.

In order to evaluate the equipment parameters achievable when using the most promising IR detector types, we shall examine the relationship between the threshold sensitivity ΔT_{\min} of the equipment as a whole and the angular resolution θ , IR detector detectivity Q , optical system parameters, and so on.

The flux difference $\Delta\Phi$ in the band $\phi(\lambda)$ with change of the measured surface temperature T by the small magnitude ΔT , perceived by the IR detector of a radiometer operating with respect to an extended source which is entirely inscribed in the elementary viewing angle, can be expressed (with account for the coefficient differential thermal flux utilization concept introduced above) by the formula

$$\Delta\Phi = \frac{\sigma T^3 \Delta T \omega [T, \phi(\lambda)] \theta^2 D^2 \eta}{2 \sqrt{2}}, \quad (8)$$

where D is the objective lens entrance aperture diameter, and η is the objective lens efficiency.

Equating ΔT to ΔT_{\min} , and replacing $\Delta\Phi$ by the IR detector threshold sensitivity, we obtain

$$\Delta T_{\min} = \frac{4K \sqrt{\Delta F} \sqrt{A_{\text{rec}}}}{\theta^2 Q^* (T, \lambda_1 - \lambda_2) D^2 \eta}, \quad (9)$$

where ΔF is the minimum required equipment passband in the video signal circuit, A_{rec} is the IR detector receiving surface area.

For the sake of exposition generality, we have also introduced into (9) the factor $K \geq 1$, accounting for amplifier noise, the required signal-noise ratio at the threshold differential, the non-sinusoidal nature of the modulation, and so on. In the following, we set $K = 1$.

It is convenient to use (9) when the specific dimension of the receiving area of the particular IR detector type is given, but recommendations on the selection of the optimum objective relative aperture "0" do not follow from (9) in explicit form. Replacing $\sqrt{A_{\text{rec}}}$ by the product θf (f is the objective focal length), we finally obtain the equation which is the basic thermovision apparatus equation

$$\Delta T_{\min} = \frac{4K \sqrt{\Delta F}}{\theta Q^* (T, \lambda_1 - \lambda_2) D \theta \eta}. \quad (10)$$

It follows from (9 - 10) that the concept of IR detector detectivity Q^* introduced above characterizes uniquely the equipment threshold sensitivity to small temperature differentials, and the best optical system, characterizing the potential properties of the thermovision equipment, is the optical system which provides a maximum of the product $D\theta\eta$. We also see that in order to ensure the maximum possible value of the relative aperture, required for improving the threshold sensitivity, the size of the detector receiving

area should be minimized to the degree that the technological capabilities make this possible without deterioration of the detectivity D^* . In the subsequent calculations, we took $A_{\text{rec.min}} = 0.01 \text{ mm}^2$.

$$(D/f)_{\text{max}} = 1 : 1.$$

The passband ΔF , appearing in (9 - 10), must be expressed in terms of parameters usually specified during design: angular resolution, satellite flight altitude, scanning band, permissible observation time, and so on. This implies that the solution of this question depends primarily on the orbital characteristics.

Three basic forms of satellite orbits from which weather observations can be made are under more or less detailed study at the present time [5, 6, and elsewhere]. These orbits include: near-Earth circular orbit with heights from several hundreds to thousands of kilometers, geosynchronous orbits, and lunar orbits. Let us examine each of these orbits.

IR equipment installed aboard satellites traveling in circular orbits near the Earth. In this case, the scan strip must be as large as possible; the strip width is determined by the flight altitude and the scanning sector. Because of the need for reducing distortions at large viewing angles, the scan sector is no greater than $\pm 40 - 50^\circ$. It is obvious that the observation time for a single imaging cycle for the equipment installed on such satellites can be taken equal to the period of revolution of the satellite around the Earth. The optimum system in this case is one which provides only line-by-line scanning of the terrain segment viewed (scanning along the orbit is accomplished as a result of displacement of the satellite itself).

Expressing the satellite velocity along the circular orbit using the known formulas of theoretical mechanics and assuming that in equipment of the television type the minimum required frequency band ΔF is equal to half the number of scan elements examined per second, we obtain

$$\Delta F = \frac{\gamma}{2\theta_0 g_0 T_0(H)}, \quad (11)$$

where

$$T_0(H) = H \frac{R+H}{R^2} \sqrt{\frac{R+H}{g_0}} \text{ [sec]}, \quad (12)$$

where γ is the entire scan sector (in radian measure); R is the radius of the Earth; H is the flight altitude; g_0 is the gravity force acceleration at the Earth's surface.

Substituting (11) into (9 - 10), solving these equations for θ , and expressing the linear resolution δ on the ground at the nadir point in terms of H and θ , we finally obtain

$$\delta = H \left[\frac{2\sqrt{2}}{\Delta T_{\min} Q^*(T, \lambda_1 - \lambda_2) D^* \eta \cdot 0} \sqrt{\frac{\gamma}{T_0(H)}} \right]^{1/2} \quad (13)$$

or, in the case when the detector receiving area size is given, this expression has the form

$$\delta = H \left[\frac{2\sqrt{2} \bar{A}_{\text{rec}}}{\Delta T_{\min} Q^*(T, \lambda_1 - \lambda_2) D^* \eta} \sqrt{\frac{\gamma}{T_0(H)}} \right]^{1/2}. \quad (13a)$$

Curves of maximum achievable resolution as a function of flight altitude, calculated using (13), are shown in Figure 2. In the calculations, we took $\Delta T_{\min} = \text{const} = 1^\circ \text{ C}$, with radiating surface temperature -50° C . The calculation was made for the three types of IR detectors indicated in the table (thermistor bolometer, Ge; Hg and AgTe - CdTe) for two spectral bands: $\lambda = 10.5 - 12 \mu$ (Figure 2a) and $\lambda = 8 - 12 \mu$ (Figure-2b). In the table and in the calculations, the values of D^* were taken from [3, 4].

With respect to scan strip size, the calculation was made for three conditions:

a) $\gamma = \text{const} = 80^\circ (\pm 40^\circ)$ — curves 1, 4, 7 (Figure 2);

b) for each of the flight altitudes, the scan strip was taken equal to the interorbital distance (along the equator) — curves 2, 5, 8;

c) the scan strip was taken constant, equal to 3000 km — curves 3, 6, 9.

In the calculations $D = 100$ mm (the value of the Nimbus satellite radiometer); $\eta = 0.5$; $0 = D/f = 1 : 1$ (or $A_{\text{rec.min}} = 0.01 \text{ mm}^2$).

The values of the optical system parameters taken here are to a considerable degree arbitrary, or in any case are not the limiting values. Therefore, on the basis of the calculations cited, we can conclude that when using high-quality and fast-response IR detectors during satellite flights in near-Earth orbits, the highest resolution required in practice for meteorological purposes can be provided.

/33

IR equipment installed on the moon and aboard geocentric satellites. The basic difference in the imaging conditions for equipment installed on such satellites in comparison with low-flying circum-Earth satellites is the fact that the satellite period of revolution around the Earth cannot be taken as the time of a single imaging cycle, and that the imaging itself with the aid of narrow-angle radiometers must be accomplished using scanning in two dimensions (for example, line and frame scanning).

It is desirable to obtain a symmetric picture of the studied terrain segment relative to the subsatellite point. Therefore, for the subject satellite class, the square or circular raster form, providing, respectively, parallel-line or spiral circular scanning, is best. Considering that the cloud cover field being examined has equiprobability of cloud appearance in any region, the best information qualities will be provided by trajectories with uniform scanning of the field (i.e., with provision for angular equidistance of the scanning lines or spirals without gaps and without overlaps) and with uniform angular scanning beam sweep velocity.

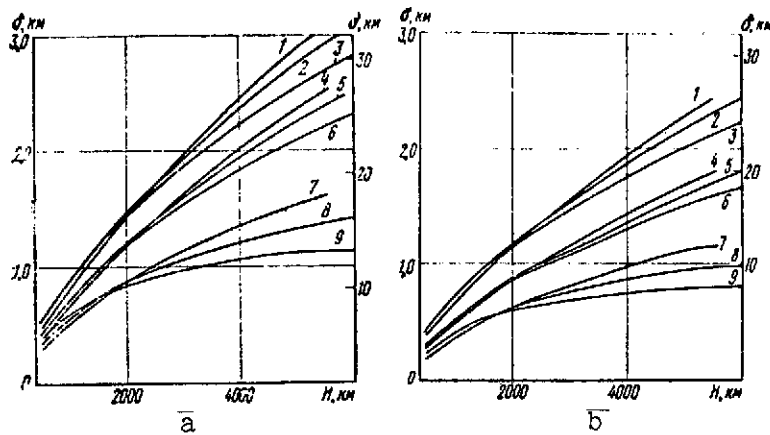


Figure 2. Resolution versus satellite flight altitude:

a — 1, 2, 3 — $Q^* (\Delta\lambda) = 8.4 \cdot 10^1$; 4, 5, 6 — $Q^* (\Delta\lambda) = 1.5 \cdot 10^5$; 7, 8, 9 — $Q_0^* (\Delta\lambda) = 1.8 \cdot 10^3 \text{ Hz}^{1/2} \text{ cm}^{-1} \text{ deg}^{-1}$; b — 1, 2, 3 — $Q^* (\Delta\lambda) = 1.73 \cdot 10^5$; 4, 5, 6 — $Q (\Delta\lambda) = 4.2 \cdot 10^5$; 7, 8, 9 — $Q_0^* = 4.5 \cdot 10^3$ (scales for curves 1 - 6 are on the left; scales for curves 7 - 9 are on the right)

We take the time of a single imaging cycle equal to τ and express the minimum required passband ΔF , appearing in (9 - 10), for the circular and square rasters in terms of angular scan sector size γ (diameter of circle or side of square) and angular resolution θ . As a result, we obtain

$$\Delta F_{\text{cir}} = \frac{\pi \gamma^2}{8 \tau \theta^2}, \quad \Delta F_{\text{sq}} = \frac{\gamma^2}{2 \tau \theta^2}. \quad (14)$$

Substituting (14) into (10), we obtain the following expressions for the resolution δ at the nadir on the surface:

$$\delta_{\text{cir}} = H \left[\frac{V \sqrt{2 \pi \gamma}}{\Delta T_{\text{min}} V \tau Q^* (T, \lambda_1 - \lambda_2) D \theta \eta} \right]^{1/2}, \quad (15)$$

$$\delta_{\text{sq}} = H \left[\frac{2 V \sqrt{2 \gamma}}{\Delta T_{\text{min}} V \tau Q^* (T, \lambda_1 - \lambda_2) D \theta \eta} \right]^{1/2}. \quad (16)$$

Considering that, with respect to maximum achievable resolution, the circular and square raster forms, other conditions being the same, differ by approximately 5%, all the further calculations will be made only for the circular raster form. /34

Analogously to the above analysis, in the case of a given (or technologically minimum achievable) IR detector size, we can obtain

$$\delta_{\text{cir}} = H \left[\frac{\sqrt{2\pi} \sqrt{A_{\text{rec}}} \gamma}{\Delta T_{\text{min}} \sqrt{\epsilon} Q^* (T, \lambda_1 - \lambda_2) D^2 \eta} \right]^{1/2}. \quad (17)$$

Curves of maximum achievable linear resolution as a function of the objective entrance aperture diameter, calculated using (15, 17), for IR equipment installed aboard geocentric satellites and on the moon, are shown in Figure 3a and 3b, respectively. The calculation was made for the spectral band from 10.5 to 12 μ for ΔT_{min} (-50°C) = /35
 1°C for the same three IR detectors used in the preceding section.

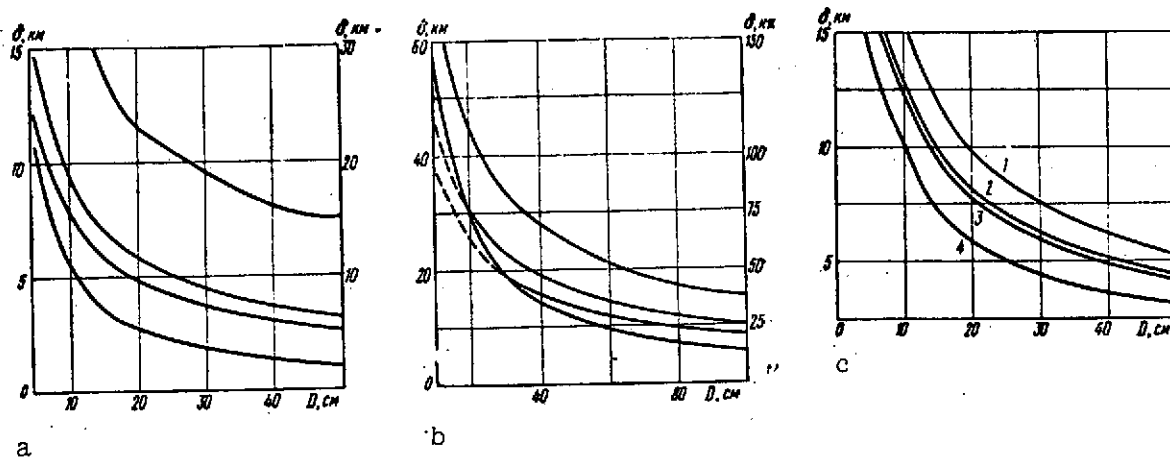


Figure 3. Resolution versus entrance aperture diameter for equipment installed aboard geocentric satellites and on the Moon

The time of a single imaging cycle was taken equal to three hours; the scan sector γ was equal to the maximum required value, i.e., 17.5° and 2° for equipment located, respectively, aboard geosynchronous satellites and on the Moon.

These same figures also show the maximum achievable resolution as limited by the optical system diffraction limit ($\lambda = 12 \mu$). We see from these curves that the limiting achievable angular resolution for the equipment of geosynchronous satellites is a quantity on the order of fractions of an angular minute. This orientation accuracy is not yet achievable in practice at the present time. Therefore, the variant with orientation of the geosynchronous satellite by rotation is of practical interest. In this case, the line scan can be obtained by satellite rotation and frame scan by scanning the radiometer in the plane perpendicular to the line scanning plane. The corresponding computational formulas can be obtained easily from (9 - 10) and (14), where in the expression for F_{sq} we must substitute $\gamma^2 = \gamma_x \gamma_y$, setting $\gamma_x = 2 \pi$.

Figure 3c shows δ as a function of objective entrance aperture diameter for satellite stabilization by rotation. The computation conditions are the same as in the preceding case.

As an illustration of resolution dependence on the information readout cycle time τ , curves are shown in Figure 4, calculated for the case of satellite stabilization by rotation for $D = 30$ cm. The curves in Figure 3c and 4 are for: 1 — Hg Te : Cd Te; 2 — Ge: Hg ($\Delta\lambda = 10.5 - 12 \mu$); 3 — Hg Te - Cd Te; 4 — Ge : Hg ($8 - 12 \mu$), and the curves in Figure 3a, b are analogous.

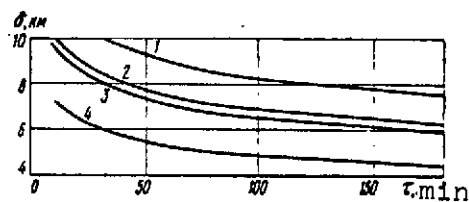


Figure 4. Resolution as function of information readout cycle time for equipment installed aboard geosynchronous satellites

We can conclude from these data that when thermovision equipment is installed aboard geosynchronous satellites, a resolution on the order of 5 - 10 km is quite feasible. For the case of thermovision equipment installation in a lunar observatory, the maximum resolution

when using cryogenic IR detectors can be brought to a value close to the diffraction limits.

References

1. Kondrat'yev, K. Ya. Meteorologicheskiye Sputniki (Weather Satellites), Gidrometeoizdat, Leningrad, 1963. /36
2. Locke, A. S. Guided Missiles (Russian translation). GIFML (State Publishing House of Physical and Mathematical Literature), Moscow, 1958.
3. Kruse, P. W., et al. Elements of Infrared Technology (Russian translation). Voenizdat, Moscow, 1964.
4. Shapiro, P. IR Detector Chart Outlines Materials and Characteristics, Electronics, No. 2, 1969.
5. Kondrat'yev, K. Ya, I. A. Semenov, T. P. Sidorchuk, et al. Lunar Meteorological Observatory for Observing the Earth. Collection: Kosmicheskiye Issledovaniye, Vol. 4, No. 3. Nauka Press, Moscow, 1966.
6. Kondrat'yev, K. Ya. Radiation Equipment of USA Weather Satellites. Meteorologiya i Gidrologiya, No. 12, 1968.

DETERMINING ICONOMETRIC PARAMETERS OF IMAGING DEVICES USING A WIDE-ANGLE COLLIMATOR

Ya. L. Ziman

Most imaging devices are interpreted as central projection systems, and for this reason their iconometric parameters are determined. The iconometric parameters include the elements specifying the spatial rectangular coordinate system of the imaging device and the elements characterizing the deviations of the image construction scheme from the central projection law.

In the flat-frame imaging devices, the origin of the coordinate system is aligned with the center of projection, while the coordinate system itself is realized by the coordinates $x_M, y_M, z_M = \text{const} = -f^*$ of definite picture points. The images of special coordinate marks, or the corners of the frame, if there are no special marks, are used as such points. The deviation of the image construction scheme from the central projection law is usually expressed by the so-called distortion corrections $\Delta x, \Delta y$ in the coordinates of the current picture points.

The problem of determining the iconometric parameters of the imaging device can be solved if the camera being calibrated is used to obtain the image of a group of reference points, the directions to which are known. In order to specify the imaging device coordinate system, it is sufficient in principle to obtain on the picture the images of three reference points which do not lie on a single straight line. Many more such points are required in order to determine the distortion corrections, and they must be distributed uniformly over the entire field of view of the camera being calibrated. /37

The system of reference directions can be obtained with the aid of a multiple collimator setup [1]. The number of collimators (reference directions) in these setups is limited, and it is difficult to obtain in practice on these setups pictures with the required number of reference points for determining the photogrammetric distortion. The problem of obtaining such pictures is resolved successfully by photographing the stars [2]. However, star images can be obtained only by cameras with large objective entrance pupils and light detectors of adequate sensitivity. A significant drawback of both of these techniques is the fact that they cannot be used for calibrating imaging systems when the latter are installed in a spacecraft. This requirement arises in many cases, specifically when it is necessary to determine the sought parameters with account for the distortions introduced by the porthole through which imaging is accomplished.

These drawbacks are eliminated when calibrating the imaging devices with the aid of a portable, wide-angle, large-aperture collimator. Figure 1 shows a schematic section of such a collimator in the plane passing through its optical axis. The marks 2, illuminated through the condenser 3 by the illuminator 4, are located in the focal surface PP of the wide-angle, large-aperture anastigmat.

The marks are crosses or dots engraved on plane-parallel glass plates. The number of marks and their distribution over the field are selected so that their images are exposed in definite segments of the picture obtained by the camera being calibrated. During alignment of the collimator, the marks must be displaced in the direction paral-

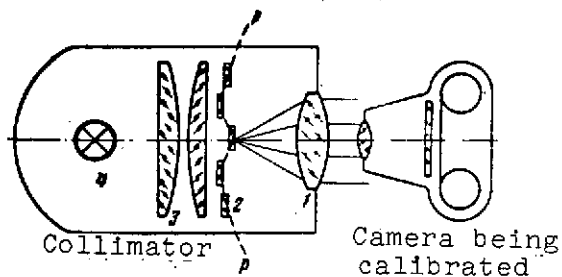


Figure 1. Optical schematic of collimator and camera being calibrated

lel to the optical axis and located so that the rays leaving each mark form parallel bundles after passing through the objective lens. /38
The marks can also be located in a single plane if the latter is close to the focal surface and the rays from each of them remain parallel at the collimator exit to within

$$\epsilon \leq \frac{m_{xy}}{3f}, \quad (1)$$

where m_{xy} is the mean square error of determination of the coordinates of the mark images on the pictures; f is the objective focal length of the camera being calibrated.

The directions of the rays leaving the collimator (their direction cosines l_M, m_M, n_M in the collimator coordinate system) must be known with this same accuracy for each mark.

The collimator is aligned (see Figure 1) opposite the imaging camera being calibrated, so that their optical axes are approximately

parallel and the principal points of the objectives are positioned as close as possible to one another. (In order to satisfy the latter condition, it is desirable that the collimator have an objective with front principal point located as far forward as possible.) With the camera being calibrated located in this position, pictures are taken with an image of the collimator marks, from which we then measure the coordinates x_i, y_i of these images.

Figure 2 shows two such pictures. The first picture was made by a photographic camera. The large central cross and the small crosses are the images of the coordinate marks of the photographic camera being calibrated; the medium size crosses are the images of the collimator marks. Figure 2b shows an enlarged phototelevision picture. Here, the collimator marks are the nodes of the square grid whose image covers the entire picture; the coordinate marks of the phototelevision camera are the crosses located along the margin of the frame.

/40

The calculation of the iconometric parameters from the measurements of the pictures obtained is made fundamentally just as in the case of star pictures. For each mark imaged on the picture, we formulate equations of the form

$$\begin{pmatrix} l_{m_i} \\ m_{m_i} \\ n_{m_i} \end{pmatrix} = A \begin{pmatrix} x_i/r_i \\ y_i/r_i \\ -f/r_i \end{pmatrix}, \quad \begin{aligned} x_i' &= x_i - x_0 + \Delta x_i, \\ y_i' &= y_i - y_0 + \Delta y_i, \\ r_i &= (x_i'^2 + y_i'^2 + f^2)^{1/2}. \end{aligned} \quad (2)$$

Here, A is an orthogonal matrix defining the mutual orientation of the coordinate systems of the collimator and the camera being calibrated (the elements of the matrix A are expressed in terms of three independent Euler angles ψ_1, ψ_2, ψ_3 ; x_0, y_0 are the sought coordinates of the picture principal point; $\Delta x_i, \Delta y_i$ are the distortion corrections to the measured coordinates of the collimator mark images).

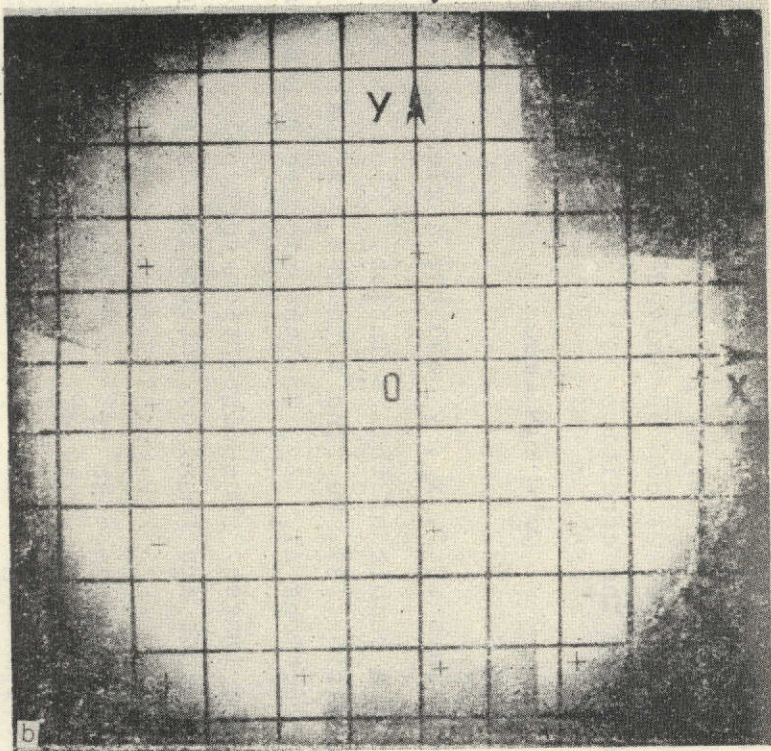
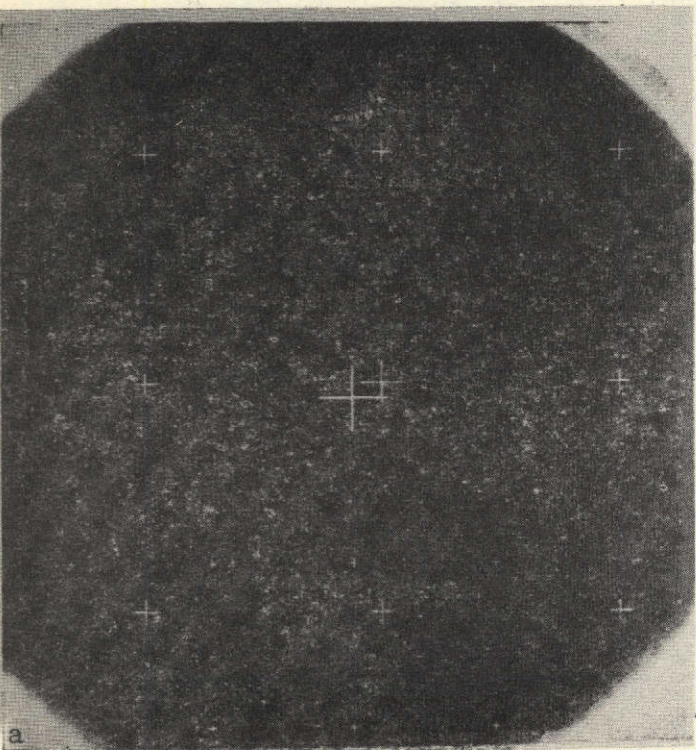


Figure 2. Pictures with image of collimator marks and
the camera being calibrated

The system (2) contains two independent equations for each reference point. When the number of points is more than three ($i > 3$), all the Equations (2) can be solved jointly by the least squares technique under the condition

$$[\Delta x^2] + [\Delta y^2] = \min. \quad (3)$$

The probable values of f , x_0 , y_0 and the angles ψ_1 , ψ_2 , ψ_3 will be obtained as a result of this solution. From the solution of (2), under the condition (3), we find both the residual errors and the distortion corrections Δx_1 , Δy_1 for the picture points where the collimator marks are imaged. The distortion corrections for all the remaining picture points are found by interpolation of these values.

If the collimator image does not cover the entire viewing field of the test camera, several additional pictures must be obtained with convergent positioning of the optical axes of the imaging camera and collimator so that the images of the collimator marks are shifted over the picture and cover the corresponding edge of the picture. As a minimum, two marks must be imaged in that picture region where the images of the collimator marks were obtained using the first (basic) setup.

The solution of the problem becomes more complicated in this case. All the pictures obtained are measured. For each picture, we formulate the system of equations (2) with its matrix A , but with common values of the unknowns f , x_0 , y_0 . Thus, we seek $3n + 3$ unknowns (n is the number of pictures obtained with different orientation of the collimator relative to the test camera). All the equations are solved jointly, which naturally leads to a more complicated computational scheme.

Experimental studies were made using this technique to calibrate photographic and phototelevision systems. The collimators used were equipped with objectives of the Telemar-17 ($f = 400$ mm), OF-233 ($f = 210$ mm), and Uran-27 ($f = 100$ mm) types; in these collimators, the marks were located in a single plane. Evaluation of the results of these experiments permits recommending the indicated collimators for calibrating television and phototelevision imaging systems, and also short-focus small-format photographic cameras.

References

1. Afremov, V. G. Description and Analysis of the TsNIIIGAik Photographic Bench. Transactions of the Central Scientific Research Institute of Geodesy, Aerophotosurveying, and Cartography, No. 165, 1965.
2. Ziman, Ya. L. Determining Photogrammetric Parameters of Photographic Cameras from Star Pictures. Astronomicheskii Zhurnal, Vol. 46, No. 3, 1969.

GEOMETRIC DISTORTIONS OF AUTOCOLLIMATION TYPE SCANNERS

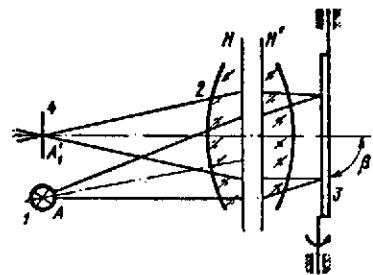
M. K. Narayeva

One criterion of image quality is its geometric similarity to the control test. The ability of television, phototelevision, phototelegraphic, and other systems to transmit geometrically similar images is characterized by the geometric distortion coefficient. The geometric distortions may be linear or nonlinear. The reason for the appearance of linear distortions is the inaccuracy of scanning mechanism element assembly. Therefore, the distortions caused by this factor can be minimized during adjustment operations or may be easily compensated during image reception. Nonlinear distortions arise because of nonuniformity of the horizontal scanning rate, and are defined by the nonlinearity coefficient

$$\eta = (v_{\max} - v_{\min})/v_{\max}, \quad (1)$$

where v_{\max} , v_{\min} are the maximum and minimum scanning rates.

The figure shows a schematic [1] of one of the autocollimation type scanners which have found practical application in phototelevision devices [2] designed for automatic sensing and subsequent transmission of planetary surface images. The image of the point radiation source 1, located in the focal plane of the objective 2, is projected by the latter together with the mirror 3 into the same plane, but because of tilt of the mirror 3 at the angle β to the optical axis the image is projected to a different point, point A'_1 , where the photographic film with the image fixed autocollimation mirror 3, driven by a cam mechanism, is used as the scanning element.



Schematic of autocollimation type scanner

Possible sources of the nonlinear distortions which arise in these devices are the scanning mechanism, objective distortion, and the nodding mirror.

Scanning mechanism. In the case of uniform angular displacement of the mirror, distortions arise caused by the tangential law of scanning element displacement. In general form, the nonlinear distortion coefficient η_{tg} in this case can be expressed as

$$\eta_{tg} = 1 - \cos^2 2\gamma, \quad (2)$$

where γ is the ray deflection angle.

Distortion is a field aberration which arises because of nonconstancy of the linear magnification in the image plane. In the subject devices, its presence may lead to nonconstancy of the horizontal scanning rate and, consequently, to geometric distortions.

If we denote by y'_0 the distance traveled by the ray in the Gaussian region during the time t with rotation of the mirror, then the corresponding distance outside this zone in the presence of distortion can be represented in the form

$$y'_n = y'_0(1 \pm \Delta), \quad (3)$$

where Δ is the relative distortion.

Then the scan rate at any point of a line is

$$v_n = v_0(1 \pm \Delta), \quad (4)$$

where v_0 is the scan rate at the center of the line.

Substituting (4) into (1), we can write the following expressions for the nonlinear distortion coefficients of scanners using objectives with negative and positive distortions

$$\eta_{neg} = \pm \Delta, \quad (5)$$

$$\eta_{pos} = \Delta/(1 + \Delta). \quad (6)$$

Thus, the nonlinear distortions may constitute a significant magnitude, particularly when working with objectives whose distortions are negative.

Nodding mirror. In view of the fact that the reflected ray trajectory depends on both the mirror operating conditions and mutual positioning of the reflecting surface and its axis of rotation [3, 4], the use of the nodding mirror in the scanner requires special analysis. In the subject devices, the scanning element trajectory corresponds to a quadratic parabola

$$X = (e^2/f) e^2 Y^2 \quad (7)$$

or for the devices used in the Zond 3 type phototelevision system [3],

$$X \cong (\beta/4.5f') Y^2, \quad (8)$$

where β is the inclination of the mirror reflecting surface to its axis of rotation; f' is the objective focal length, XOY is the coordinate system in the object focal plane with center at the principal focus and X axis parallel to the mirror axis of rotation.

Trajectory deviation always leads to nonlinear geometric distortions, whose magnitude is determined by

$$\eta = (3\gamma_{\max}^2)/(1 + 3\gamma_{\max}^2 - \beta^2), \quad (9)$$

where γ_{\max} is the maximum required ray deflection angle.

It is interesting to note that in the absence of mirror inclination to the axis of rotation, i.e., when $\beta = 0$, the trajectory degenerates into a straight line, and the corresponding nonlinear distortion coefficient is determined by (2).

Knowing the nonlinear distortions arising during operation of the scanner and the distortions η_{tg} which can occur in the absence of mirror inclination, we can determine the fraction η_β of the distortions introduced by inclination of the rotating mirror in the form of the difference $\eta_\beta = \eta - \eta_{tg}$.

After substituting (2) and (9) into this formula and making several transformations, the expression takes the form

$$\eta_a = - \frac{\gamma^2 [4(3\gamma^2 - \beta^2) + 1]}{1 + (3\gamma^2 - \beta^2)}.$$

In practice, $3\gamma^2 \gg \beta^2$ and, therefore, $\eta_a < 0$. Since $\eta_{tg} > 0$, we conclude that proper choice of the mirror tilt angle may lead to compensation of the nonlinear distortions caused by the tangential law of scanning element motion.

/44

References

1. Savvina, L. G., M. K. Narayeva, A. S. Selivanov, et al. Opticomechanical Scanner. Author's Certificate No. 221,027, Byull, Izobret., No. 375, 1969.
2. Selivanov, A. S., M. K. Narayeva, A. G. Shabanov, et al. Phototelevision Devices for Space Studies. Tekhnika kino i televideniya, No. 7, 1969.
3. Rusinov, M. M. Gabaritnyye raschety opticheskikh sistem (Dimensional Calculations of Optical Systems). Gosgeoltekhnizdat, Moscow, 1963.
4. Churbanov, I. A. General Case of Reflection from a Rotating Mirror. Optiko-mekhanicheskaya promyshlennost', No. 3, 1968.

GEOMETRIC DISTORTIONS OF OPTICOMECHANICAL PANORAMIC TELEVISION SYSTEMS

V. M. Govorov

One of the problems solvable by the space-borne television system, topographical surveying, makes high demands on image quality, particularly on the geometric distortions introduced by the television

camera. It is the geometric distortions which determine measurement accuracy and, consequently, the possibility of creating reliable planetary surface maps.

Comparative analysis of the different television systems capable of solving the posed problem shows that the requirements on quality of the transmitted images (stability of their geometric parameters) are best satisfied by television cameras with optico-mechanical scanning.

Let us explain the process of image construction by the optico-mechanical panoramic television camera. Viewing of surrounding space is accomplished by element-by-element scanning as a result of displacement of the optical image by the mirror 4 relative to the field stop 6, located in the focal plane of the objective 5 (Figure 1). The stop cuts off part of the light flux corresponding to the scan element, which falls on the light detector 1 where it is converted into an electrical signal. The diameter of the field stop determines the angular resolution of the system. The mirror 4 is rotated by the drive 3 containing the electric motor 2 and a complex kinematic chain consisting of worm drives to provide the specified scanning law.

In the design of panoramic television systems, the question arises of selecting the scanning ray sweep law. Most convenient, from the viewpoint of minimum geometric distortions, are scanners with line-by-line spiral and sphero-panoramic scanning, which are particular cases of linear three-dimensional scanning. On an oriented satellite, its motion may be used to obtain frame sweep of a single-line scanner.

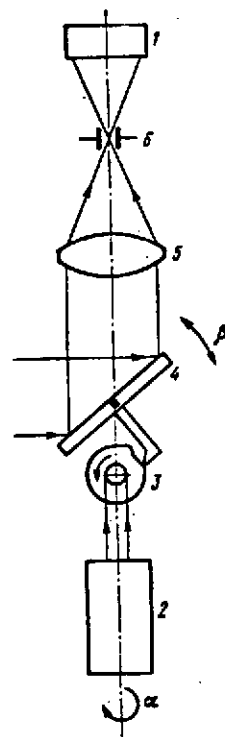


Figure 1. Optico-mechanical image construction scheme

In contrast with the conventional television and phototelegraphic systems, where image readout is accomplished from a flat (two-dimensional) original, tube photocathode or photograph, in the subject system direct scanning of the surrounding (three-dimensional) space is accomplished without intermediate recording. Therefore, the position of the scanning ray vector in the three coordinates is conveniently described by angular values.

The direction of the scanning ray vector depends on the scanning mirror position. If l^0, m^0, n^0 are the direction cosines of the scanning ray ahead of the mirror in the S_{xyz} coordinate system, then the direction cosines l, m, n of the scanning ray after the mirror are found from the expressions (Figure 2):

/46

$$\begin{aligned} l &= l^0 - 2l_n(l_n l^0 + m_n m^0 + n_n n^0), \\ m &= m^0 - 2m_n(l_n l^0 + m_n m^0 + n_n n^0), \\ n &= n^0 - 2n_n(l_n l^0 + m_n m^0 + n_n n^0), \end{aligned}$$

where l_n, m_n, n_n are the direction cosines of the normal to the mirror plane.

We express the direction cosines l, m, n , and l_n, m_n, n_n through the direction angles α and β

$$\begin{aligned} l &= \cos \alpha \cos \beta, \quad m = -\cos \alpha \sin \beta, \quad n = \sin \alpha; \\ l_n &= \cos \alpha_n \cos \beta_n, \quad m_n = -\cos \alpha_n \sin \beta_n, \quad n_n = \sin \alpha_n. \end{aligned}$$

The variation of the angles α and β or α_n and β_n is described by the differential equations reflecting the scanning law

$$d\alpha/dt = \omega_\alpha, \quad d\beta/dt = \omega_\beta; \quad d\alpha_n/dt = \omega_{\alpha_n}, \quad d\beta_n/dt = \omega_{\beta_n}.$$

Synthesis of optomechanical scanners involves constructing a mechanism which can reproduce the specified scanning law. If this mechanism were to reproduce the specified relationship with absolute

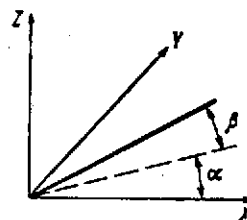


Figure 2. Determination of scanning ray directions

accuracy, the direction angles could be found from the expressions

$$\alpha = \int_0^t \omega_\alpha dt, \quad \beta = \int_0^t \omega_\beta dt.$$

Because of unavoidable errors in fabricating and assembling the individual elements, i.e., because of the so-called primary errors, the real mechanism reproduces the specified law only approximately. The accuracy of this approximation characterizes the quality of the mechanism.

Denoting the real rates of change of the angles α and β by $\tilde{\omega}_\alpha$ and $\tilde{\omega}_\beta$, we find the real direction angles $\tilde{\alpha}$ and $\tilde{\beta}$

$$\tilde{\alpha} = \int_0^t \tilde{\omega}_\alpha dt, \quad \tilde{\beta} = \int_0^t \tilde{\omega}_\beta dt.$$

The differences $\Delta\alpha = \alpha - \tilde{\alpha}$, $\Delta\beta = \beta - \tilde{\beta}$ between the ideal and real values of the scanning ray direction angles are termed the television system photogrammetric distortion components.

If image recording at the receiver is accomplished without error, the distribution of the distortion components in the system viewing /47
zone characterizes completely the geometric distortions.

Opticomechanical scanners consist of mechanical components and, therefore, have fundamentally high stability of their parameters. The scanning efficiency depends only on the opticomechanical element fabrication quality. The scanning element fabrication errors can always be taken into consideration when calibrating the television cameras, and, if we have the corresponding calibration data, we can minimize the errors in processing the images obtained.

We shall analyze a kinematic scanning scheme and find the expression for the systematic distortion components for the example of the opticomechanical television panoramic camera installed on the Luna 9 and Luna 13 automatic lunar stations.

Spatial scanning in this camera is accomplished with the aid of a flat mirror which performs two motions: oscillatory motion about the horizontal scanning axis, and rotational motion around the vertical panning axis. The oscillatory motion of the mirror around the scanning axis is accomplished with the aid of a cam whose profile ensures uniform rotation of the mirror during the horizontal scan period and fast return of the mirror to the initial position. The selected scanning law can be written as

$$\alpha = \omega_\alpha t, \beta = 2\omega_\beta t,$$

where ω_α and ω_β are the panning and scanning rates, i.e., the rates of mirror rotation around the panning and scanning axes.

The real scanning law differs from the selected law, and may be described by the relations

$$\alpha = \tilde{\alpha} + \Delta\alpha = \tilde{\omega}_\alpha t + \Delta\alpha, \beta = \tilde{\beta} + \Delta\beta = 2\tilde{\omega}_\beta t + \Delta\beta.$$

The distortion components $\Delta\alpha$ and $\Delta\beta$ in the panning cam gearing and scanning angles are caused by fabrication errors, and also by misalignment of the panning and scanning axes. Therefore, it is advisable to represent them as the sum of the particular components

$$\Delta\alpha = \Delta\alpha' + \Delta\alpha'', \Delta\beta = \Delta\beta' + \Delta\beta'' + \Delta\beta''',$$

where $\Delta\alpha'$ and $\Delta\beta'$ are the distortions caused by misalignment of the panning and scanning axes; $\Delta\alpha''$ and $\Delta\beta''$ are the distortions caused by the gearing fabrication error; $\Delta\beta'''$ is the scanning angle distortion caused by cam fabrication error.

Let us obtain the analytic expressions for these distortion components, which are necessary for their determination during calibration. We shall clarify the choice of the S_{xyz} coordinate system with origin at the rear principal point of the objective. We direct the S_z axis along the straight line connecting the rear objective principal point and the geometric center of the diaphragm. We take the positive direction of the S_z axis from the objective toward the

/48

scanning mirror. We take the abscissa axis S_x in the plane containing the S_z axis and the electrical contact on the instrument case, providing a signal corresponding to the initial image mark. We select the S_y axis so that the S_{xyz} coordinate system will be right-hand (Figure 3, 4).

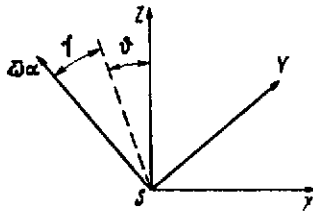


Figure 3. Determination of scanning ray direction

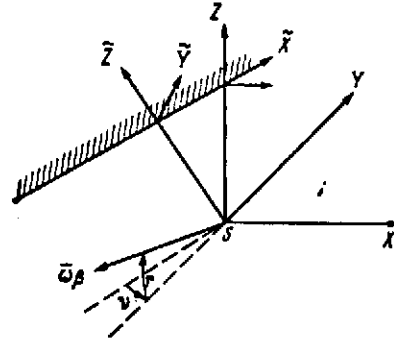


Figure 4. Determination of scanning ray direction

The direction cosines of the scanning ray ahead of the mirror in the selected coordinate system are $l^0=0, m^0=0, n^0=1$. The direction cosines l, m, n of the scanning ray after the mirror are $l=-2l_n n_n$, $m=-2m_n n_n$, $n=1-2n_n^2$.

Let ϕ and γ be the direction cosines of the panning axis in the S_{xyz} coordinate system, and τ and ν be the direction cosines of the scanning axis when $\alpha = 0$ and $\beta = 0$.

The selection of these angles is characterized by the relations

$$\begin{aligned} l_\alpha &= -\phi, & l_\beta &= \tau, \\ m_\alpha &= -\gamma, & m_\beta &= 1, \\ n_\alpha &= 1; & n_\beta &= \nu, \end{aligned}$$

where $l_\alpha, m_\alpha, n_\alpha$ and $l_\beta, m_\beta, n_\beta$ are the direction cosines of the panning and scanning axes.

The distortion components $\Delta\alpha'$ and $\Delta\beta'$ are expressed through the angles ϕ, γ and τ, ν as follows:

$$\begin{aligned}\Delta\alpha' &= -\theta \sin \tilde{\alpha} \operatorname{tg} \frac{90^\circ - \tilde{\beta}}{2} + \gamma (1 - \cos \tilde{\alpha}) \operatorname{tg} \frac{90^\circ - \tilde{\beta}}{2} - \\ &- \nu \sqrt{2} \left(1 - \cos \frac{\tilde{\beta}}{2}\right) \left(\cos \frac{\tilde{\beta}}{2} - \sin \frac{\tilde{\beta}}{2}\right) - \\ &- \tau \sqrt{2} \sin \frac{\tilde{\beta}}{2} \left(\cos \frac{\tilde{\beta}}{2} - \sin \frac{\tilde{\beta}}{2}\right), \\ \Delta\beta' &= -2\theta (1 - \cos \tilde{\alpha}) - 2\gamma \sin \tilde{\alpha}.\end{aligned}$$

/49

In order to determine the distortion components $\Delta\alpha''$ and $\Delta\beta''$, we express the panning and scanning rates through the scanning motor rate and transfer ratios of the individual kinematic pairs

$$\omega_\alpha = i_1 i_2 i_3 \omega_g = i \omega_g, \quad \omega_\beta = i_3 \omega_g,$$

where $i_1 = \omega_2/\omega_1$, $i_2 = \omega_3/\omega_2$, $i_3 = \omega_4/\omega_3$ are the ratios of the angular rates of the kinematic pair elements. Then,

$$\Delta\omega_\alpha = i \Delta\omega_g + \omega_g \frac{\partial i}{\partial \omega_1} \Delta\omega_1 + \omega_g \frac{\partial i}{\partial \omega_2} \Delta\omega_2 + \omega_g \frac{\partial i}{\partial \omega_3} \Delta\omega_3,$$

$$\Delta\omega_\beta = i_3 \Delta\omega_g + \omega_g \frac{\partial i_3}{\partial \omega_3} \Delta\omega_3.$$

Hence,

$$\begin{aligned}\Delta\alpha'' &= i \Delta\omega_g t + A_1 \sin \omega_\alpha t + B_1 \cos \omega_\alpha t + A_2 \sin \frac{1}{i_1 i_2} \omega_\alpha t + \\ &+ B_2 \cos \frac{1}{i_1 i_2} \omega_\alpha t + A_3 \sin \frac{1}{i_3} \omega_\alpha t + B_3 \cos \frac{1}{i_3} \omega_\alpha t. \\ \Delta\beta'' &= i_3 \Delta\omega_g t + C \sin \frac{1}{i_3} \omega_\beta t + D \cos \frac{1}{i_3} \omega_\beta t.\end{aligned}$$

Here, A_1 , B_1 , A_2 , B_2 , A_3 , B_3 , C , D are constant coefficients for a particular camera, characterizing the eccentricities of the gearing elements.

The errors caused by the cam result from noncoincidence of the cam rotation axis with the origin of the Archimedes spiral used to define the cam and the cam profile fabrication error.

The first factor leads to periodic variation of the scanning rate and, therefore, of the scanning angle. The variation of the

scanning angle because of cam profile fabrication errors can be approximated in general form by a power-law polynomial.

Then the error $\Delta\beta''$ is expressed as

$$\Delta\beta'' = a \sin \omega_\beta t + b \cos \omega_\beta t + d_0 + d_1\beta + d_2\beta^2 + d_3\beta^3 + d_4\beta^4 + \dots$$

The coefficients $a, b, d_0, d_1, d_2, \dots$ are constants, and are determined when calibrating the television camera.

/50

Thus, to determine the panning and scanning angles, we need to know the angular rates ω_α and ω_β , the angles $\theta, \gamma, \tau, \nu$, and the coefficients $A_1, B_1, A_2, B_2, A_3, B_3, C, D, a, b, d_0, d_1, d_2, d_3, d_4$.

Analysis of the kinematic scanning scheme made it possible to obtain an analytic relation for each element and evaluate the magnitude of the linear and nonlinear geometric distortions introduced by them.

Calibration involves comparing the angles to the reference marks measured by theodolite and calculated from the measured coordinates of the marks on the panoramic pictures. Analysis of the calibration results was carried out using a digital computer at the Institute of Space Studies of the Academy of Sciences of the USSR. The analysis results showed that the value of the angles $\theta, \gamma, \tau, \nu$ does not exceed $20'$; the accuracy of their determination is characterized by a mean square deviation of $\pm 2'$; change of the panning rate causes a maximum panning angle change of $\Delta\alpha'' = 12'$; the accuracy of determination of the correction $\Delta\alpha''$ is characterized by a mean square deviation of $\pm 4'$; the variation of the angle $\Delta\alpha''$ is described to within $\pm 4'$ by the sum of two sinusoids with period 2π and $2\pi/9$, with the amplitude of the latter reaching $6'$ in individual cameras; the maximum scanning angle does not exceed $12'$; the accuracy of determination of the correction $\Delta\beta''$ in the scanning angle is characterized by the mean square deviation $\pm 4'$; the scanning angle variation is characterized to within $\pm 4'$ by the sum of a sinusoid and a quadratic parabola.

These results indicate that these panoramic television cameras can be considered of instrumental accuracy and permit determining the direction to objects with an error practically equal to the resolution.

References

1. Pervyye Panoramyy Lunnoy Poverkhnosti (First Panoramas of the Lunar Surface). Nauka Press, Moscow, 1966.
2. Selivanov, A. S., V. M. Govorov, A. S. Titov, et al. Panoramic Television Camera for Automatic Lunar Stations. Tekhnika kino i televideniya, No. 1, 1968.

FILM PROCESSING IN SCIENTIFIC SPACECRAFT TELEVISION SYSTEMS

G. M. Aleshin

Photography and photochemical processing of the film in spacecraft phototelevision systems involve several aspects which require an approach to selection of the handling process which differs from that used under ground conditions, different processing technology and different construction of the instrument for carrying out the processing.

/51

The peculiarities of space photography include: action of penetrating radiation on the photographic film; weightlessness; unusual "climatic" conditions; requirement for minimum weight, size, and power consumption in obtaining the image; stability of the instrument when operating subject to vibrations and accelerations; complete automation of the handling processes; and high system operating reliability.

The spacecraft is continuously exposed to the action of penetrating radiation while crossing the radiation belts of the Earth and during the time of subsequent flight in interplanetary space. Passage of ionizing particles through the film emulsion layer, just like light, creates a latent image, and, depending on the radiation dose, leads to complete or partial exposure of the film [1].

The danger of radiation damage to photographic materials is a serious problem which makes questionable the possibility of using the photographic methods under conditions of long-duration space flights. The use of heavy metal shields as protection against radiation has led to considerable increase of vehicle weight, and there are no reliable methods which can be realized in practice for controlling the light sensitivity. As a result of several studies conducted in the Soviet Union, the problem of protecting photographic materials against the action of penetrating radiation has been successfully solved [2].

In contrast with condition on the ground, with complete or partial absence of the gravity force or equivalent inertial forces, a liquid will not take the form of a vessel into which it is poured. The liquid may take the shape of a formless mass floating inside the vessel or may distribute itself over the vessel walls, forming an internal cavity. If the vibrations preceded the transition to weightlessness, then in a partially filled vessel the liquid may be either in a fog state or in the form of a suspended mass of the foam type. Under weightlessness conditions, there are no forces aiding gas bubble discharge from the liquid, nor is there any tendency for the bubbles to coalesce. These effects make it difficult to ensure reliable contact between the processing solutions and the film emulsion layer and reliable solution flow in the hydraulic portion of the development system. Under weightless conditions, there is no convective transport of the chemical reaction products resulting from difference of the weight of the products formed. In contrast with ground conditions, under weightlessness heat propagation in liquids and gases takes place as a result of thermal conductivity, which is much less effective than convective heat transfer. This circumstance

/52

influences the system for solution thermostabilization and drying the photographic film after development. Careful removal of dust and lint in the film feed system is necessary to ensure cleanliness of the processed film, since after the vibrations preceding the transition to weightlessness, the dust and lint will be in the suspended state and may possibly deposit on the photographic film. The unusual nature of the climatic conditions lies in the fact that the atmosphere inside the vehicle consists of a mixture of inert gases. The processor must be capable of operating over a wide range of surrounding medium temperatures and pressures, and also with different humidities of this medium.

The requirement for reducing the weight, size, and power consumption leads to the necessity for using in the apparatus processes with a minimum number of processing operations and minimum solution consumption per unit area of the material being processed. A fast process is also desirable.

High reliability is the primary requirement determining process selection and the construction of the device for carrying out the process. This choice depends on the following factors: ensuring reliable contact of the processing solutions with the film emulsion layer in the given hydromechanical regime; storability of the processing solutions and photographic film during flight; achievement of the required temperature and time processing conditions; operational stability of the system for circulating the solutions and the drying gas; operating regime of the development device (cyclic or continuous), activation frequency, existence of interruptions in operation, and so on; simplicity in performing the technological operations when preparing the system for on-board operation and during ground tests.

In addition to the characteristics determined by space conditions, space photography processes and equipment must meet the requirements of the television system used to transmit the processed images to the Earth; the characteristics of the developed image must be compatible with the video signal generating channel; depending

on the mission being performed by the phototelevision system, there must be the possibility of altering the sensitometric characteristics of the film being processed; processing and drying of the photographic film should not have any influence on the microclimate in the very small closed volume of the phototelevision system. /53

The solution of the problems facing space photography requires the integrated solution of a large range of photochemical, physical, and system design problems.

Depending on the mission being performed by the phototelevision system, the handling process, composition and construction of the developing system may be quite varied. In the present paper, we shall examine the developing systems for spacecraft whose characteristic feature is that during flight they overfly the object under study only once, and the entire film supply is exposed and developed at one time. Therefore, the developing system needs to provide for only a single developing cycle.

Various processes were investigated in the course of the study from the viewpoint of the possibility of their use in the onboard equipment, Bimat process, single-stage process, double-frame development, and so on. It was found that none of the well-known processes satisfy completely the posed requirements.

The Bimat process, based on the use of developing-fixing webs, is simple and convenient but requires complex equipment for carrying out the process. It was used in the American Lunar Orbiter space photographic laboratory, and made it possible to obtain high-quality images of the lunar surface [3]. However, it has several drawbacks in spite of its favorable properties. First, the processing pastes have limited storability, particularly at high temperatures. Second, in the case of a long film being handled, the weight of the paste-web carrier becomes so great that it is better to have aboard a system for applying the solution to the film without using the web. The process is applicable for handling only special types of films and obtaining very definite film parameters during processing. This

does not satisfy the requirement of phototelevision system universality.

The use of the single-stage developing process was preferable for many reasons. However, study of the kinetics of the simultaneous developing and fixing process showed that its realization under weightless conditions requires complex processing equipment to avoid contamination of the developed images by the products of interaction of the solution with the film emulsion layer, particularly the silver. Moreover, it was found that the process requires rigid control of the conditions of emulsion layer wetting by the solution, and this control is difficult to achieve.

Exploratory studies, made to select the onboard developing system process and functional schematic, showed that the specified requirements are best met by developing the film in liquid or viscous concentrated solutions with the use of developing devices of the chamber type. /54

Film processing in these systems is accomplished by transporting the film through a series of chambers with the processing solutions. The primary advantage of systems of this type is that the developing device is combined with the vessel for the solutions, and reliable contact of the solutions with the film emulsion layer is provided with the aid of simple and inexpensive construction.

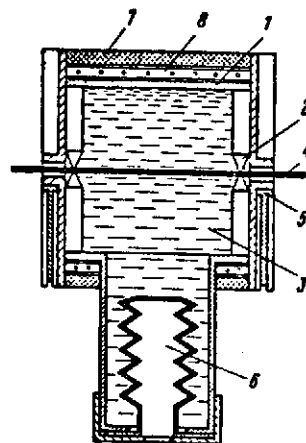
The developing unit of this type was constructed in the form of an assembly of identical modular chambers connected in series. Each chamber (see figure) has a cylindrical housing 1 made from chemically resistant titanium alloy, knife-edge rubber jaws 2 which seal the chamber with the solution 3 and limit movement of the solution from chamber to chamber during movement of the film 4, and the seals 5 which are controlled from a separate drive and seal the chamber prior to and after processing. The bellows 6 compensates for temperature changes of the solution volume and the solution carried away by the processed film, and also prevent excess pressure from

developing in the chamber with changes of the surrounding medium pressure. The chamber is enclosed in the thermal insulating jacket 7, and is equipped with the thermostatic system heating element 8.

Film travel through the solution volume and its axial position in the chamber create favorable conditions for reliable contact with the solution and facilitate thermostatic control of the solution. The chamber has only two slots for film passage, and sealing these slots does not offer any problem. Elastic rubber jaws were used for reliable sealing of the chamber during film travel and compensation bellows were provided in the chambers.

Studies to develop the drying and moisture absorption system made it possible to work out a simple drying scheme for chamber development without forced circulation of the dessicant gas. The system consists of a drying drum located near the surface of a cartridge containing a sorbent. The cartridge has radial discharge channels and a shell made from a material having the property of capillary absorption. Using this system, the drying thermal regime and the moisture absorption conditions ensure a glassy-hard emulsion layer.

A special process was developed to ensure obtaining the specified stable film parameters under weightless conditions after long-term (several months) storage under onboard conditions, without requiring rigid control of the processing temperature and time conditions. In this case, change of the solution formula for the different cases of phototelevision system application does not involve



Schematic of developing system chamber:

- 1 — chamber housing;
- 2 — knife-edge rubber jaws; 3 — solution;
- 4 — photographic film; 5 — chamber seals;
- 6 — compensation bellows; 7 — thermal insulating jacket; 8 — heating element

any need for matching the fixing and developing rates. Nor does the process require forced circulation of the solutions during processing.

The principles worked out for constructing the developing system and the photochemical film treatment process were applied in constructing small-scale automatic developing systems for the phototelevision systems of Mars 1, Zond 3, Luna 12, and so on, spacecraft [4].

The basic specifications of two developing systems versions are presented in the following table.

Parameter	Mars 1	Zond 3
Dry structural weight, g	4100	540
Solution weight, g	540	84
Sorbent weight, g	460	57
Processed film length, m	5.7	1.0
Film width, mm	70	25.4
Film length processed without change of characteristics, m	15	7.0
Processing speed range, mm/min	20-60	10-40
Average current in A at 14 V, less than	1.5	1.0

The Mars 1 developing system was intended for one-time processing of high-sensitivity perforated 70-mm film; the Zond 3 system was intended for unperforated 25.4-mm film.

Analysis of the telemetry information and studies of the photometric parameters of the images obtained from aboard the Zond 3 and Luna 12 spacecraft confirmed the validity of the principles which had been worked out for constructing the developing systems. In both cases, the systems functioned in complete accord with the design conditions and provided high-quality development of the exposed films. It should be particularly noted that the technique which we

/56

worked out for processing the information obtained from onboard made it possible to determine the sensitometric characteristics of the films developed onboard and construct the corresponding characteristic curves. These data formed the basis for proper reproduction of the images obtained from onboard and their subsequent photometric study [5, 6].

References

1. Antonov, S. M., K. S. Bogomolov, V. I. Uspenskiy, et al., Photographic Processes Used in the First Photography of the Back Side of the Moon. Collection: Iskusstvennyye sputniki zemli (Artificial Earth Satellites), No. 9. Nauka Press, Moscow, 1969.
2. Press Conference of the AN SSSR on the Flight of the Zond 3 Automatic Interplanetary Station. Pravda, August 23, 1965.
3. Kosofsky, L. I. and G. K. Broom. JSMPTE, Vol. 74, No. 9, 1965.
4. Selivanov, A. S., G. M. Sleshin, M. K. Narayeva, et al. Phototelevision Systems for Space Studies. Tekhnika kino i televideniya, No. 7, 1969.
5. Atlas obratnoy storony luny (Atlas of the Back Side of the Moon), edited by Yu. N. Lipskiy, Part 2. Nauka Press, Moscow, 1967.
6. Lebedinskiy, A. I., G. M. Aleshin, A. S. Selivanov, et al. UV Spectrum of the Moon in the 2800 - 3500 Å Region from Data Obtained from Zond 3 AIS. Space Research VII. North Holland Publ. Co., Amsterdam, 1967.

REDUCTION OF IMAGE BLURRING ON INDIVIDUAL
AERIAL PHOTOGRAPHS

Yu. I. Fivenskiy and Yu. L. Biryukov

Several publications [1 - 5] have appeared during the last three years in the Soviet and foreign literature devoted specifically to studying the theoretical and practical possibilities of obtaining sharp images from indistinct or blurred images, including those degraded by motion. This indicates the growing practical interest in "passive" methods of combatting the factors which cause loss of image sharpness. This intense interest in the "passive" methods is explained by both the impossibility of complete account for all the factors acting under real imaging conditions and the fact that in many cases the photographic systems used are far from perfect.

/57

The majority of the image restoration techniques described in the literature are based on the use of coherent optics methods. Another trend in the practical solution of the problem involves the use of digital techniques. Without negating the obvious advantages of the techniques which have been proposed, we should point out their essential deficiencies, which still prevent their broad application. They require complex special systems, availability of a coherent light source, and preparation of special spatial frequency filters.

These techniques for practical realization of image restoration conditions are not the only possible ones, at least not for the motion case. In 1965, we developed a technique [6, 7] for reducing image blurring photographically in application to the image motion case, which required the use of two pictures obtained simultaneously which include mutually complementary information about the object. The possibility of exact solution of the problem was proved. In the present article, we discuss a new technique for photographic reduction of blurring which was developed in 1967 and utilizes only a

single photograph. No special equipment which is not available at practically any photographic laboratory is required to carry out this technique.

When a single blurred photograph is available, the absence of any additional information prevents carrying out exact correction in the image frequency spectrum, specifically, frequencies corresponding to isolated zeros of the image motion transfer function which are lost in image motion cannot be restored. In this case, there remains the single possibility of operating with the amplitude and phase of the components present in the original image spectrum.

Let us examine an ideal photographing system whose operating quality is determined only by image motion. Assume the system is linear, and the photographic material has no grain. In the case of image motion, there are changes in the sharp-image spectrum $F(u, v)$

$$G(u, v) = F(u, v)H_a(u, v), \quad (1)$$

where $H_a(u, v)$ is the amplitude phase characteristic of the geometric shift of magnitude "a".

Since the stationary photographing system itself has a limited passband, we cannot hope for complete elimination of image blurring nor, for example, can we reduce blurring to a magnitude much less than the system linear resolution. Therefore, in the following, we shall examine the case of blurring reduction by some finite factor m . Then, if we multiply both sides of (1) by the function $K_m(u, v)$, such that

$$K_m(u, v) = H_{a/m}(u, v)H_a^{-1}(u, v),$$

where $H_{a/m}(u, v)$ is the transfer function of motion shift which is smaller by the factor m , we thereby perform the required correction of the original image spectrum

$$G(u, v)K_m(u, v) = F(u, v)H_{a/m}(u, v). \quad (2)$$

In general form, the problem of blurring reduction or sharp-image extraction (for $H_a/m = 1$) consists in finding a technique for practical realization of the transformation of the form (2).

It is well known that, in the case of inexact superposition of negative and positive images (for example, in the case of inefficient realization of the "sharp mask" technique), contouring of image details is observed. Mathematical examination of the phenomenon shows that in this case there are definite changes in the original image spectrum in the amplitude and phase of the components. We shall make use of this circumstance. We superpose the negative and positive of the original blurred picture with blurring so that the directions of blurring of identical image details coincide, and the origins are shifted relative to one another, in one direction or another, by a magnitude several times less than the shift. Considering the nature of this operation, for the case of a shift of magnitude "a", we write the result of the image subtraction performed in this case, in the form

$$H(p) = H_a(p) \left(1 - \bar{\gamma} e^{-p \frac{a}{m}} \right), \quad (3)$$

where m is the required shift reduction ratio; $\bar{\gamma}$ is the ratio of the negative and positive image contrasts.

We prepare from the negative and positive combined in this fashion, several copies on photographic material with transparent substrate. In so doing, we require that the relative image contrast, controllable by the developing conditions together with selection of the required photographic materials, decrease from copy to copy, in accordance with some definite law $\gamma_k = k_n(\lambda)$, where n is the total number of copies prepared or the number of elementary operations of the form (3) carried out; λ is the sequential number of the copy. Then we combine the images obtained while introducing sequential spatial delay between them (i.e., relative displacement of the images being combined) by a magnitude equal to the magnitude a of the original shift. To accomplish this, the copy-photos are superposed one on the other, while aligning the direction of blurring of

identical details and shifting the blurring origin in the order of reduction of the image contrast sequentially by the magnitude in the direction in which the original photograph developed to the lowest contrast coefficient $\bar{\gamma}$ was shifted.

The result of performing these operations can be represented by the expression

$$H(p) = H_a(p) \left(1 - \bar{\gamma} e^{-p \frac{a}{m}}\right) \sum_{\lambda=1}^n k_n(\lambda) e^{-p(\lambda-1)a}, \quad (4)$$

which is the realization of the image blurring reduction condition, written in general form.

We shall show this by a specific example. Assume the photographic system has a shutter with efficiency 100% and uniform image shift. In order to reduce the shift, we require that the image contrast on the copies decrease in the order of an arithmetic progression with last term equal to the progression difference, i.e.,

$$k_n(\lambda) = [n - (\lambda - 1)]/n \quad (\lambda = 1, 2, 3, \dots, n). \quad (5)$$

Making the corresponding transformations in (4), we find the amplitude-frequency characteristic of the resulting shift. It can be written as the product of two relative frequency functions

$$A(av) = A_{a/m}(av) Q(av), \quad (6)$$

where $A_{a/m}(av)$ is the amplitude-frequency characteristic of the shift, which is m times less than the original uniform shift

$$Q(av) = \frac{1}{m} \left\{ (1 + \bar{\gamma}) + \frac{\left[\sin \left(n + \frac{m-1}{m} \right) \pi av - \bar{\gamma} \sin \times \right] \times \left(n + \frac{m+1}{m} \right) \pi av \sin n \pi av}{n \sin \pi av \sin \pi \frac{av}{m}} \right\}. \quad (7)$$

Hence, we see that the proposed technique theoretically makes it possible to perform arbitrarily exact restoration of a blurred image. In point of fact, as the number of operations $n \rightarrow \infty$, the magnitude of the fraction in the braces of (7) approaches zero, and the factor

$Q(\omega)$ is independent of frequency. However, the practical realization of this condition involves well-known difficulties.

Nevertheless, even a comparatively small number of operations leads to a positive result. Figure 1 shows the resulting amplitude-frequency characteristics calculated for the case of reduction of the original shift by a factor of four ($m = 4$) for several choices of the parameters n and $\bar{\gamma}$ appearing in (7). Figure 1a shows for comparison the frequency characteristic of the original shift (solid curve), and the frequency character of the fourfold smaller shift (dashed).

We see from Figure 1b that the required phase changes in the basic frequency characteristic take place for even a single operation. Further increase of the number of operations leads only to redistribution of the amplitudes within the limits of the frequency band being restored as a result of increase of the number of cycles (Figure 1c), and reduction of their relative magnitude. For a number of operations $n = 10$ (Figure 1d), the frequency characteristic obtained is already a quite good approximation to the required characteristic curve.

We note that the number of peaks in each frequency band which is a multiple of the magnitude of the original shift

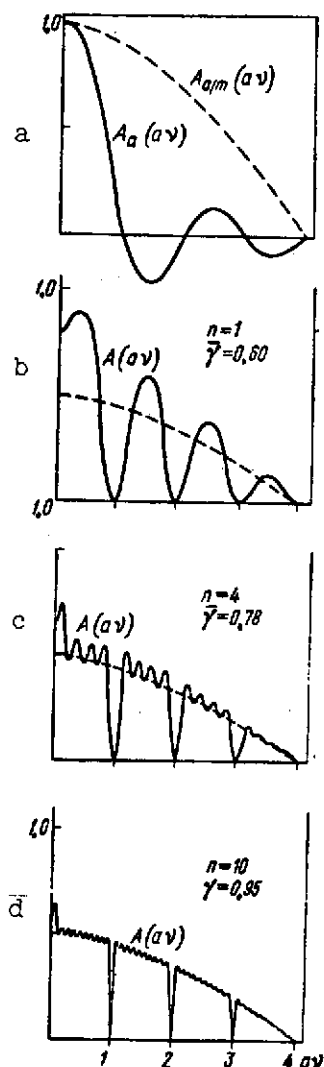


Figure 1. Influence of number n of operations performed on the form of the amplitude-frequency characteristic of the shift in the restored image

is equal to the number n of operations performed. Physically, this means that this same number of residual, periodically repeating (with period a) lower contrast images will be present on the restored image near each individual detail. The contrast of the residual images can be made less than the "noise" caused by photographic material graininess by increasing n . If there are a large number of details in the photograph, their residual images average out, are superposed on one another, and are lost in the photographic material "noise" at a smaller value of n . /61

If we set $\bar{\gamma}=1$ and $k_n(\lambda)=\text{const}$ in (4), we actually obtain the filter transfer characteristic examined in [3]

$$K(j\omega) = j\omega \frac{\sin 0.5n\omega a}{\sin 0.5\omega a}. \quad (8)$$

This filter works well under the assumptions made by the authors on behavior of the function being restored beyond the limits of the photograph; these assumptions are not usually satisfied in photography. Therefore, in the general case, the characteristics of the realizable filters can be obtained from (4) by selecting the values of the parameters appearing in this formula so as to have in practice quite good restoration results. Specifically, for the case of restoration of a photographic image obtained with uniform shift, comparison of (6, 7), shown in Figure 1, and (8), shows the significant advantage of the subject technique. For a given shift reduction coefficient m , the selection of the required values of the parameters n and $\bar{\gamma}$ can be made in accordance with the quality criterion adopted for the solution of the specific practical problem.

The problem solution becomes more complicated for a nonlinear system, which photography is, in the general case. The primary difficulty is that the techniques for adding and subtracting photographic image opacities are not yet known. Therefore, we must replace these operations by the operations of multiplication and division, i.e., addition and subtraction of the optical densities. It can be shown that in this realization of the proposed technique, the difference ΔD of the densities of two neighboring points of the restored image, the distance between which is considerably less than

the magnitude of the original shift, is obtained as follows:

$$\Delta D \approx 1.7372 \gamma \gamma_k \frac{\alpha_m(x)}{m} \left[1 \pm \frac{1}{\sqrt{n}} \frac{\bar{\alpha}_m}{\alpha_m(x)} \right], \quad (9)$$

where $\bar{\alpha}_m$ is the average contrast of the image obtained with shift m times less than the original shift.

It follows from (9) that the restored photograph transmits the contrast between details located close together in accordance with the way in which this contrast is transmitted by a photograph with shift less by a factor of m , i.e., better than the original blurred photograph. This same formula shows that relatively high-contrast details are restored better than low-contrast details, which are masked to a greater degree by the residual images. To reduce the factor in the square brackets, we need only to increase the number n of operations. However, experience shows that the total number of operations required for achieving the same result is somewhat smaller than in the case of addition and subtraction of the photographic image opacities. Figure 2 shows one version of blurred photographic image restoration for a minimum number of operations performed ($n = 1$, $\gamma = 0.75$, $m = 4$).

/62

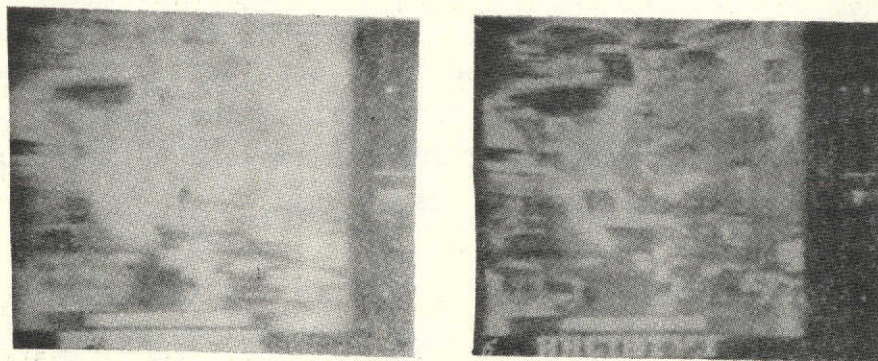


Figure 2. Example of blurred image restoration:

a — original photograph; b — result of image restoration

REPRODUCIBILITY OF THE
ORIGINAL PAGE IS POOR

We have examined above a somewhat idealized photographic system. It was assumed that the photographic material has no grain, the shutter efficiency is 100%, and the image shift exceeds considerably the system resolution.

The use of a single original photograph, in contrast with the technique of blurring reduction using two photographs, leads to considerable increase of the restored image graininess. This is associated with the larger number of photographs participating in the operations of addition and subtraction of image optical densities. It is clear that the number of photographic copies prepared cannot be increased without limit. Actually, in spite of the fact that we see from the above formulas that contrast transmission improves with increase of the number n of operations, at the same time an increasing number of low-contrast details are masked by noise because of increasing graininess. A similar process takes place with increase of the shift reduction coefficient m . Therefore, we can recommend obtaining several restored images for different values of the parameters m and n , and examining them together with the original photograph. Some details will be transmitted better on certain photographs, while others will be transmitted better on other photographs.

The general theory of the technique examined above holds good with reduction of the blurring on the image obtained by a photographic system with shutter efficiency less than unity. The only difference /63 lies in the fact that restoration of such an image usually requires performance of a larger number n of operations.

In conclusion, we note that the technique theory presented makes it possible in principle to realize this technique using the methods of television technology as well as those of photography. This can lead to increased speed in handling blurred photographs. For example, if we take the route of developing an analog computer based on the "scanning beam" television system or some similar system, the problem of blurring reduction can be solved in a few seconds using relatively small equipment.

References

1. Harris, J. L. Image Evaluation and Restoration. J. O. S. A., No. 5, 1966.
2. Stroke, G. W. and R. G. Zech. A Posteriori Image-Correcting Deconvolution by Holographic Fourier-Transform Division. Phys. Letters, 25A, 1967.
3. Slepian, D. Restoration of Photographs Blurred by Image Motion. Bell Syst. Techn. J., No. 10, 1967.
4. Khalfin, L. A. Resolution of Optical Instruments. Optika i spektroskopiya, Vol. 6, No. 1, 1969.
5. Stroke, G. W. Image Deblurring and Aperture Synthesis Using A Posteriori Processing by Fourier-Transform Holography. Optika Acta, No. 4, 1969.
6. Biryukov, Yu. L., Yu. I. Fivenskiy, Yu. M. Chesnokov. Use of Photographic Masking to Reduce the Influence of Shift on Photographic Image Sharpness. ZhNIPFIK (Journal of Applied Scientific Photography and Cinematography), No. 6, 1968.
7. Biryukov, Yu. L. and Yu. I. Fivenskiy. Photographic Reduction of Image Blurring. Collection: Kachestvo aerofotoizobrazheniya (Aerial Photography Image Quality). Nauka Press, Leningrad, 1969.

APPLICABILITY OF THE DIFFUSION APPROXIMATION

Yu. L. Biryukov, L. G. Titarchuk, and
Yu. M. Chesnokov

Several methods using an approximate form of the scattering indicatrix have been proposed for simplifying the calculation of radiation transport in planetary atmospheres. Specifically, the use in place of the exact indicatrix $X(\gamma)$ of the approximate value

$$\bar{X}(\gamma) = 1 + x_1 \cos \gamma, \quad (1)$$

where x_1 is the first coefficient of the expansion of the indicatrix $X(\gamma)$ in Legendre polynomials, leads to the diffusion approximation of [1].

In several cases, calculations using the indicatrix $\bar{X}(\gamma)$ yield /64
considerable discrepancy with the results of exact calculating using the indicatrix $X(\gamma)$.

Heyney and Greenstein [2] suggested using an indicatrix of the form

$$\bar{X}(\gamma) = \frac{1 - (x_1/3)^2}{[1 + (x_1/3)^2 - 2 \cdot x_1/3 \cdot \cos \gamma]^{1/2}},$$

however, it yields unsatisfactory agreement with the exact calculations made by Hansen [3].

The indicatrix proposed by Kagiwada and Kalaba [4] gives still poorer agreement with the exact calculations.

In the present paper, we discuss the possibility of using the indicatrix (1), and suggest still another approximate indicatrix form whose use in practice has shown good agreement with the experimental data.

The scattering indicatrix is the probability distribution density of the angle of light quantum deviation from a straight line after a scattering event.

Knowing the scattering indicatrix, we can find $X_2(\gamma)$, the probability distribution density of the angle of light quantum deviation from the initial straight line after the second encounter, as the distribution density of the sum of two independent random quantities. We can find similarly the probability distribution density of the angle of light quantum deviation from the initial straight line after the n^{th} scattering event. For the sake of brevity, we shall call this probability distribution density the n^{th} scattering indicatrix.

We note that the angular distribution of the radiation leaving a layer is determined to a considerable degree by the indicatrices of the last scatterings, taking place immediately prior to the quantum leaving the layer.

The order number of such scattering may be different for different quanta. Its average value increases monotonically with increase of the layer optical thickness τ .

Let us find the expansion of the n^{th} scattering indicatrix into a series in Legendre polynomials. The radiation direction at a given point will be characterized by the angles θ , ϕ (θ is the angle between the radiation direction and the solar ray incidence direction; ϕ is the azimuth in the corresponding horizontal plane).

On the basis of the theorem on spherical functions

$$F_{ij} = \int P_i(\gamma') P_j(\gamma) \frac{d\omega}{4\pi} = \begin{cases} 0, & \text{if } i \neq j, \\ \frac{P_i(\gamma)}{2i+1}, & \text{if } i = j, \end{cases} \quad (2)$$

where $\cos \gamma' = \cos \theta'$, $\cos \gamma'' = \cos \theta \cos \theta' + \sin \theta' \sin \theta \cos(\varphi - \varphi')$ and the integration is performed over all solid angles. /65

Using (2), it is not difficult to write the form of the n^{th} scattering indicatrix

$$X_n(\gamma) = 1 + \sum_{k=1}^{\infty} x_k \left(\frac{x_k}{2k+1} \right)^{n-1} P_k(\gamma) \quad (n \geq 1), \quad (3)$$

where x_k are the coefficients in the Legendre polynomials for the initial indicatrix $X(\gamma)$.

We see from this expression that if we use in the calculations in place of the exact form of the indicatrix, its approximation in the form

$$\bar{X}(\gamma) = 1 + x_1 \cos \gamma,$$

then the error in determining the probability distribution density of the light quantum deviation from the initial line is

$$\Delta X_n(\gamma) = X_n(\gamma) - \bar{X}_n(\gamma) = \sum_{k=2}^{\infty} x_k \left(\frac{x_k}{2k+1} \right)^{n-1} P_k(\gamma).$$

$\Delta X_n(\gamma)$ reaches its maximum value for $\gamma = 0$, since for this value of γ , all the Legendre polynomials $P_k(\gamma)$ have the same sign and take the maximum value, equal to 1.

By virtue of continuity of the function $\Delta X_n(\gamma)$ (it is larger than zero), in some neighborhood of the point $\gamma = 0$. For other values of γ , $\Delta X_n(\gamma)$ is close to zero because of the difference in the signs of $P_k(\gamma)$, and is basically negative since its volume is negative.

For sufficiently large n ,

$$|\Delta X_n(\gamma)| \ll |\bar{X}_n(\gamma)|.$$

As a rule, for the spherical particle indicatrix,

$$\frac{x_{k-1}}{2k-1} > \frac{x_k}{2k+1}. \quad (4)$$

As a result of this, the stronger statement that

$$\frac{|\Delta X_n(\gamma)|}{x_1 (x_1/3)^{n-1}} \ll 1$$

is valid for sufficiently large n .

In fact, as a consequence of (4)

/66

$$\frac{|\Delta X_n(\gamma)|}{x_1 (x_1/3)^{n-1}} < \frac{(x_2/5)^{n-1} \sum_{k=2}^{\infty} x_k P_k(0)}{(x_1/3)^{n-1} x_1} = \frac{X(0) - 1 - x_1}{x_1} \frac{(x_2/5)^{n-1}}{(x_1/3)^{n-1}},$$

and since $\frac{x_1}{3} > \frac{x_2}{5}$ according to (4), then

$$\lim_{n \rightarrow \infty} \frac{X(0) - 1 - x_1}{x_1} \left(\frac{x_2/5}{x_1/3} \right)^n = \lim_{n \rightarrow \infty} \frac{|\Delta X_n(\gamma)|}{x_1 (x_1/3)^{n-1}} = 0. \quad (5)$$

For more exact account for the form of the scattering indicatrix, we consider the fact that $X(\gamma)$ has a quite sharp peak in the vicinity of $\gamma = 0$. Consequently, it is natural to replace $X(\gamma)$ by the indicatrix $\tilde{X}(\gamma)$ represented with the aid of the δ -function

$$\tilde{X}(\gamma) = v(1 + \tilde{x}_1 \cos \gamma) + (1-v)\delta(\gamma) \quad (v < 1). \quad (6)$$

In order to find a method for calculating radiation propagation when using the indicatrix (6), we note that during each scattering taking place in accordance with $\tilde{X}(\gamma)$, the light quantum with probability v is scattered in accordance with the indicatrix $1 + \tilde{x}_1 \cos \gamma$ and with probability $(1 - v)$ continues on without altering its direction, i.e., we can consider that scattering takes place only with the indicatrix $1 + \tilde{x}_1 \cos \gamma$, but takes place on the average $1/v$ times less often than would be the case for conventional scattering with this same indicatrix.

This leads correspondingly to reduction of the attenuation coefficient α and, therefore, of τ by a factor of $1/v$.

Thus, in order to calculate radiation transport in accordance with the indicatrix $\tilde{X}(\gamma)$, we need to make calculations in the approximation of [5] for the indicatrix $1 + \tilde{x}_1 \cos \gamma$ with the optical thickness τv .

In order to select the parameters v and \tilde{x}_1 , we find the form of the n^{th} scattering indicatrix $\tilde{X}_n(\gamma)$

$$\tilde{X}_n(\gamma) = \int \tilde{X}(\gamma') \tilde{X}_{n-1}(\gamma'') \frac{d\omega}{4\pi}. \quad (7)$$

Applying (7) sequentially to $\tilde{X}(\gamma), \tilde{X}_2(\gamma), \dots, \tilde{X}_{n-1}(\gamma)$, we obtain the form of the n^{th} scattering indicatrix $\tilde{X}_n(\gamma)$

$$\tilde{X}_n(\gamma) = (1 - (1-v)^n) + 3 \left[\left(\frac{v x_1}{3} + 1 - v \right)^n - (1-v)^n \right] \cos \gamma + (1-v)^n \delta(\gamma).$$

In order for the indicatrix $\tilde{X}(\gamma)$ to be used for quite large n , it is necessary that

$$\tilde{X}_n(\gamma) - \bar{X}_n(\gamma) = O(x_1/3)^n \quad (8)$$

and

$$1 - v = u < x_1/3.$$

It follows from (3), (5), (8), that

$$\frac{x_1}{3} = u + (1-u) \frac{\tilde{x}_1}{3}$$

or

$$\tilde{x}_1 = \frac{x_1 - 3u}{1-u}.$$

In order to calculate the distribution of the radiation leaving the atmosphere of a planet, we select u such that, in the vicinity of $\Theta = \pi$, the indicatrix $\tilde{X}_n(\gamma)$ reflects quite exactly the aft peak of the indicatrix $X_n(\gamma)$.

For this it is necessary to require that

$$X_n(\pi, \varphi) - \tilde{X}_n(\pi, \varphi) = O(x_2/5)^n. \quad (9)$$

In fact, $X_n(\pi, \varphi)$ is a sign-altering series with monotonically decreasing coefficients. Consequently,

$$5(x_2/5)^n - 7(x_2/7)^n < X_n(\pi, \varphi) < 5(x_2/5)^n$$

and even for $n > 5$, we can consider with adequate accuracy that

$$X_n(\pi, \varphi) = 5(x_2/5)^n.$$

Therefore, in order that (9) be satisfied, we need to set

$$u^n (8(\pi) - 1 - 3 \cos \pi) = 5(x_2/5)^n \quad (10)$$

or

$$u = (5/2)^{1/n} \cdot x_2/5 \approx x_2/5. \quad (11)$$

Satisfaction of (10) ensures sufficiently exact correspondence of $X_n(\gamma)$ and $\tilde{X}(\gamma)$ not only at the point π but also in some vicinity of this point, since by virtue of the arguments presented above,

$$X_n(\gamma) = \tilde{X}_n(\gamma) = 3 \cdot \frac{5}{2} (x_2/5)^n \cos \gamma (1 + \cos \gamma) + 0(x_2/5)^n.$$

Thus, in order to calculate radiation transport in a dense atmosphere in the presence of strata with markedly elongated indicatrices, we can use the theory presented in [5]. To do this, we must replace in the corresponding expressions x_1 by $\frac{x_1 - 3u}{x_1 - u}$, τ by $\tau(1 - u)$, where u is found from (11)

/68

Specifically, for the two-layer spherical atmosphere (cloud, gas) model discussed in [5] and [6], we can obtain analytic expressions for the radiation leaving the planetary atmosphere $I_1(0, \xi, \eta, \mu)$, the radiation arriving from above and below at the interface of the cloud and gas layers $I_1(\tau_{cl}, \xi, \eta, \mu), I_1(\tau_{cl}, \xi, \eta, \mu)$, and also that arriving at the planetary surface $I_1(\tau_{cl} + \tau_{go}, \xi, \eta, \mu)$. There, τ is the optical depth in the atmosphere; τ_{cl}, τ_{go} are the optical thicknesses of the cloud and gas layers, respectively; ξ is the cosine of the angle at a given point between the direction to the sun and the direction of the radius vector; η is the cosine of the angle between the radiation direction and the direction of the radius vector; μ is the cosine of the azimuth in the corresponding horizontal plane.

We integrate the transport equation

$$\frac{dI}{dT} = -I + B$$

as follows:

$$I = Ce^{-T} + e^{-T} \int_0^T e^{T'} B dT'.$$

We use the expression for B from [1]

$$B = J + x_{1,i} \eta H + x_{1,i} \sqrt{1 - \eta^2} G \mu + \frac{S}{4} X_i(\tau_1) \quad (i = 1, 2),$$

where

$$J = \int I d\omega / 4\pi; \quad H = \left[\frac{\partial J}{\partial \tau} - (S/4) x_{1,i} \xi e^{-\tau_0} \right] [1/(3 - x_{1,i})];$$

$$G = \left(-\frac{1}{\alpha R} \frac{\partial J}{\partial \psi} + \frac{S}{4} X_{1,i} \sqrt{1 - \xi^2} e^{-\tau_0} \right) \frac{1}{3 - \tilde{x}_{1,i}};$$

$x_{1,1} = \tilde{x}_1$ and $x_{1,2} = 0$, R is the radius of the planet, T_0 is the optical distance along the sun's ray to the given point in the atmosphere; T is the optical distance along the scattered ray; α is the bulk attenuation coefficient

/69

$$\cos \tau_1 = -\eta \xi + \sqrt{1 - \eta^2} \sqrt{1 - \xi^2} \mu.$$

We obtain the following expressions from [5]:

$$\begin{aligned} I_{\uparrow}(0, \xi, \eta, \mu) &= \frac{S \tilde{x}_1}{4 W_0} C_1 (C_2 \eta + 1) \left[\frac{\xi}{1 - (\tilde{x}_1/3)} + \right. \\ &+ \left. \frac{\mu \sqrt{1 - \xi^2} \sqrt{1 - \eta^2}}{\alpha R [(3/\tilde{x}_1) - 1]} \right] - \frac{1}{(3/\tilde{x}_1) - 1} J(0, \xi) + \frac{3S}{4} \frac{1}{-W_0 [1 - (x_1/3)]} \cdot \\ &\cdot [F_1(\xi, \eta) + F_2(\xi, \eta)] + \frac{S}{4} \frac{\xi}{\xi + \eta} \left[X(\tau_1) + \frac{\tilde{x}_1^2}{3 - \tilde{x}_1} (-\eta, \xi) \right] + \\ &+ \frac{1}{(3/\tilde{x}_1) - 1} \frac{3S/4}{\alpha R (-W_0)} [L_1(\xi, \eta) + L_2(\xi, \eta)] \frac{\sqrt{(1 - \xi^2)(1 - \eta^2)}}{\xi^2 \mu} + \\ &+ e^{-\tau_0} e^{1/\eta} J(\tau_{c1}, \xi) \left[\frac{1}{(3/\tilde{x}_1) - 1} + C_{2,1} \eta + 1 \right], \\ I_{\downarrow}(\tau_{c1}, \xi, \eta, \mu) &= J(\tau_{c1}, \xi) \left[(C_2 \eta + 1) + \frac{e^{\tau_{c1} g_0 \eta}}{1 + \frac{3}{2} \frac{1 - A}{1 + A} \tau_{c1} g_0} \right], \\ I_{\downarrow}(\tau_{c1}, \xi, \eta, \mu) &= \frac{S \tilde{x}_1}{4 W_0} C_1 \left(\frac{1}{1 + \frac{3 - \tilde{x}_1}{2} \frac{1 - A_g}{1 + A_g} \tau_{c1}} + C_1 \eta \right) \times \\ &\times \left(\frac{\xi}{1 - \frac{\tilde{x}_1}{3}} + \frac{\mu \sqrt{1 - \xi^2} \sqrt{1 - \eta^2}}{\alpha R [(3/\tilde{x}_1) - 1]} \right) - \frac{1}{1 - 3/\tilde{x}_1} J(\tau_{c1}, \xi) + \\ &+ \frac{3}{4} \frac{S}{-W_0} \times F_2(\xi, \eta) + \frac{1}{(3/\tilde{x}_1) - 1} \frac{3S/4}{\alpha R (-W_0)} L_2(\xi, \eta) \times \end{aligned}$$

$$x = \frac{\sqrt{1-\eta^2} \sqrt{1-\xi^2}}{\xi^2} \mu + \frac{1}{1-3/x_1} J(0, \xi) I^{\tau_{cl}}_{\eta};$$

$$I_1(\tau_{cl} + \tau_{go}, \xi, \eta, \mu) = \left[\frac{1}{1 + \frac{3}{2} \frac{1-A}{1+A} \tau_{go}} + \right.$$

$$\left. + C_{2,1} \eta - e^{\frac{\tau_{go}}{\eta}} (1 + C_{2,1} \eta) \right] J(\tau_{cl}, \xi) + e^{\frac{\tau_{go}}{\eta}} I(\tau_{cl}, \xi, \eta, \mu).$$

Here,

170

$$F_1(\xi, \eta) = \frac{\xi \eta}{\xi + \eta} \left(C_1 + \frac{\xi \eta}{\xi + \eta} \right) \left(1 + \frac{C_2 \eta (\eta + 2\xi)}{\xi + \eta} \right) + C_2 \frac{\xi^2 \eta^2}{(\xi + \eta)^2};$$

$$F_2(\xi, \eta) = \frac{\xi^2}{\xi + \eta} \left(C_1 + \frac{\xi \eta}{\xi + \eta} \right) \left(1 + \frac{C_2 \xi (\xi + 2\eta)}{\xi + \eta} \right) + C_2 \frac{\xi^4 \eta^2}{(\xi + \eta)^2};$$

$$L_1(\xi, \eta) = \frac{\xi^2 \eta^2}{(\xi + \eta)^2} \left(C_1 + \frac{2\xi \eta}{\xi + \eta} \right) \left(1 + \frac{C_2 (\eta + 3\xi) \eta}{\xi + \eta} \right);$$

$$L_2(\xi, \eta) = \frac{\xi^3}{\xi + \eta} \left(C_1 + \frac{\xi \eta}{\xi + \eta} \right) \left[\frac{2\eta + \xi}{\xi + \eta} + 2\xi \left(1 + \frac{\eta (\xi + 2\eta)}{(\xi + \eta)^2} \right) C_2 \right] +$$

$$+ \frac{\xi^4 \eta^2}{(\xi + \eta)^2} \left(1 + \frac{C_2 \xi (\xi + 3\eta)}{\xi + \eta} \right);$$

$$F_3(\xi, \eta) = \xi (C_1 + \xi) (1 + C_2 (\tau_{cl} + \eta));$$

$$L_3(\xi, \eta) = \xi^2 (C_1 + 2\xi) (1 + C_2 (\tau_{cl} + \eta));$$

$$C_1 = \frac{2}{3 - \tilde{x}_1}; \quad C_2 = \frac{A_g - 1}{A_g + 1} \frac{\frac{3 - \tilde{x}_1}{2}}{1 + \frac{3 - \tilde{x}_1}{2} \frac{1 - A_r}{1 + A_r} \tau_{cl}};$$

$$W_0 = -\frac{1}{1 - C_1 C_2}; \quad A_g = 1 - \frac{1}{\frac{1}{1 - A} + \frac{3}{4} \tau_{go}};$$

$$J(0, \xi) = \frac{\xi C_1 S}{4W_0} (\tilde{x}_1 - 3(C_2 \xi + 1));$$

$$J(\tau_{cl}, \xi) = \frac{S(C_2 \tau_{cl} + 1) \xi}{4W_0} [\tilde{x}_1 C_1 - 3(C_1 + \xi)];$$

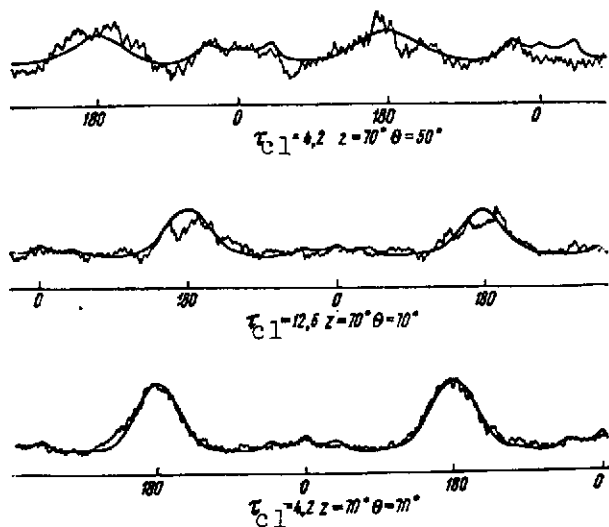
$$C_{2,1} = \frac{A - 1}{A + 1} \frac{\frac{3}{2}}{1 + \frac{3}{2} \frac{1 - A}{1 + A} \tau_{go}};$$

and A is the surface albedo.

A comparison was made of the brightness angular distribution at the upper edge of stratus clouds, calculated using the above technique with the distribution measured in [7]. The measurements were

made from an airplane flying above the clouds. During the measurements, the brightness meter optical axis was deflected from the vertical by one of the fixed angles θ , and was rotated through 360° about the vertical axis. /70

The measurement results were recorded on an oscillograph. Three such oscillograms (wavy curves) are shown in the figure. The smoother curves in this figure were obtained by calculation. The cloud optical thicknesses τ_{cl} , equal to 4.2 and 12.6, were calculated on the basis of the cloud thicknesses measured during flight and the average water content for stratus clouds. The scattering indicatrix corresponding to an average droplet radius of five microns was taken from [8]. The optical thickness of the atmospheric layer below the clouds was taken as 0.2.



Angular distribution of brightness at upper edge of stratus clouds with sun angle $z = \arccos \xi = 70^\circ$, and $\tau_{cl} = 4.2$ and 12.6

References

1. Sobolev, V. V., I. N. Minin. Scattering of Light in a Spherical Atmosphere. Collection: *Iskusstvennyye sputniki zemli* (Artificial Earth Satellites), No. 14. Nauka Press, Moscow, 1962.
2. Heyney, L. G., and L. J. Greenstein. Diffuse Radiation in the Galaxy. *Astrophys. J.*, 94, 1941.
3. Hansen, G. E. Exact and Approximate Solutions for Multiple Scattering by Cloudy and Hazy Planetary Atmosphere. *J. Atmos. Sci.*, Vol. 26, No. 3, 1969.

4. Kagiwada, H. and R. Kalaba. Multiple Anisotropic Scattering in Slabs with Axially Symmetric Fields. RAND Corp., Mem. RM-5245-PR. Santa Monica, 1967.
5. Titarchuk, L. G. Scattering of Light in a Spherical Multilayer Atmosphere. In present collection.
6. Biryukov, Yu. L., A. S. Panfilov, and L. G. Titarchuk. Estimates of the Optical Characteristics of the Venus Atmosphere in Application to the Problem of Photographing Its Clouds and Surface. In present Collection. /72
7. Kozlov, V. P. and Ye. O. Fedorova. Spatial Distribution of the Brightness of Lower Clouds. Izv. AN SSSR, Seriya Geofiz., No. 7, 1962.
8. Chesnokov, Yu. M. Aktinometriya i Optika Atmosfery (Actinometry and Optics of the Atmosphere). Nauka Press, Moscow, 1964.

SCATTERING OF LIGHT IN A SPHERICAL MULTILAYER ATMOSPHERE

L. G. Titarchuk

In the present paper, as in [1 - 5], we examine the problem of radiation diffusion in the atmosphere of a planet illuminated by solar rays. The basic equations of the problem were obtained in [1] and the solution was found in [2, 4] for the case when the absorption coefficient in the atmosphere is constant. In [3], the assumption was introduced of exponential variation of absorptivity with altitude, and a first approximation solution was proposed for this case.

In Section 1 of the present article, we present the problem solution for the nonuniform atmosphere case under the same assumptions used in [3]. An analysis and evaluation of this solution are also presented, which make it possible to obtain an approximate

solution convenient for numerical realization and an estimate of the accuracy of this approximation.

In Section 2, we examine the problem of light scattering in a uniform atmosphere with account for the true absorption. As in Section 1, the solution of this problem is analyzed and, as a result, we find a comparatively simple expression for calculating the average intensities in the range from 0 to 89° sun zenith angle. An estimate of the error of this approximation is made.

The multilayer spherical atmosphere model is examined in Section 3 on the basis of the results of the preceding sections. Each i th layer for the n -layer model ($i = 1, \dots, n$) is represented by four parameters, namely, $\Delta\tau_i = \tau_{0,i} - \tau_{0,i-1}$, where $\tau_{0,i-1}$, $\tau_{0,i}$ are the optical depths of the upper and lower edges of the layer, respectively, the scattering indicatrix $X_i(\gamma)$, the probability λ_i of quantum survival in an elementary scattering event (particle albedo), and absorptivity variation with altitude $\alpha(h)$ (exponential for $\lambda_i = 1$, or constant for any $\lambda_i \neq 1$). The latter actually does not limit the possibilities of applying this model in practice, since the exponential law case corresponds to a purely gaseous layer with constant temperature, and the case $\alpha = \text{const}$ with any $\lambda_i \neq 1$ is realized with continuous cloud cover.

/73

The final results are formulas for calculating the average intensities through the entire depth of the atmosphere for sun zenith angles from 0 to 90° .

1. Light Propagation in Spherical Nonuniform Atmosphere

Basic equations. We shall assume that the atmosphere is illuminated by parallel solar rays, creating illumination of an area perpendicular to the rays equal to πS . The distance of any point in the atmosphere from the center of the planet is denoted by r , and the angle between the radius vector and the direction to the sun is

denoted by ψ . Let $J(r, \psi)$ be the average intensity of the diffuse radiation at a point with the coordinates r and ψ . Hereafter, we shall use, in place of r , another variable — the optical thickness τ , equal to

$$\tau = \int_r^{r_H} \alpha(r') dr' \quad (R \leq r \leq r_H),$$

where r_H is the distance from the center of the planet to the upper edge of the atmosphere, and R is the radius of the planet.

We suppose that the absorptivity $\alpha(r)$ decreases exponentially with height, i.e.,

$$\alpha(r) = \alpha(R) e^{-(r-R)/H_*},$$

where H_* is the height of the uniform atmosphere. Then

$$\tau = H_* (\alpha(r) - \alpha(r_H)).$$

The optical thickness of the atmosphere is

$$\tau_0 = H_* (\alpha(R) - \alpha(r_H)).$$

We make the change of variables

$$\tau = \alpha(r) H_* = \tau + \alpha(r_H) H_* = \tau + \tau_H.$$

An approximate equation of the following form was obtained in [3] for the average intensities in the pure scattering case:

$$\tau^2 \frac{\partial^2 J}{\partial \tau^2} + \frac{H_*^2}{R^2} \frac{\partial^2 J}{\partial \psi^2} = -\tau^2 f(\tau, \psi) \quad (1.1)$$

with the boundary conditions at the upper edge of the atmosphere [2], 74
where $\tau = \tau_H$,

$$\frac{\partial J}{\partial \tau} - \frac{3-x_1}{2} J = \frac{S}{4} x_1 \cos \psi \quad (1.2)$$

and for a planet, where $\tau = \tau_0 + \tau_H = \tau_0$,

$$\frac{\partial J}{\partial \tau} + \frac{3-x_1}{2} \frac{1-A}{1+A} J = \frac{S}{2} e^{-T(\tau, \psi)} \cos \psi \left(\frac{x_1}{2} + \frac{(3-x_1)A}{1+A} \right). \quad (1.3)$$

Here,

$$J = \frac{3S}{4} e^{-T(\tau, \psi)}; \quad (1.1')$$

x_1 is the first coefficient in the expansion of the scattering index $x(\gamma)$ in Legendre polynomials; T is the optical distance from the sun to the given spot in the atmosphere. A is the albedo of the planetary surface.

Analytic solution of the problem (1.2; 1.2; 1.3). We seek $J(\tau, \psi)$ in series form

$$J(\tau, \psi) = \sum_{n=0}^{\infty} D_n(\tau) \cos n\psi. \quad (1.4)$$

We divide the right and left sides of (1.1) by τ^2 , and after this we expand the right sides of (1.1), (1.2), (1.3) into a Fourier cosine series. As a result of these expansions and the representation of (1.4), we obtain the following boundary value problem for determining the coefficients:

$$D_n''(\tau) - \frac{1}{\tau^2} \frac{n^2 H^2}{R^2} D_n(\tau) = -f_n(\tau), \quad (1.5)$$

$$D_n'(\tau) + \frac{3-x_1}{2} \frac{1-A}{1+A} D_n(\tau) \Big|_{\tau=\tau_0} = \varphi_{2,n}(\tau_0), \quad (1.6)$$

$$D_n'(\tau) - \frac{3-x_1}{2} D_n(\tau) \Big|_{\tau=\tau_H} = \varphi_{1,n}(\tau_H), \quad (1.7)$$

where

$$f_0(\tau) = \frac{3}{4} S \frac{1}{\pi} \int_0^\pi e^{-T(\tau, \psi)} d\psi,$$

$$f_{n>0}(\tau) = \frac{3}{4} S \frac{2}{\pi} \int_0^\pi e^{-T(\tau, \psi)} \cos n\psi d\psi, \quad (1.8) \quad \underline{75}$$

$$\varphi_{1,1} = \frac{S}{4} x_1 \text{ and for } n \neq 1 \varphi_{1,n} = 0, \quad (1.9)$$

$$\begin{aligned}\Phi_{2,0}(\tau_0) &= \frac{1}{\pi} \int_0^\pi \Phi_2(\tau_0, \psi) d\psi, \\ \Phi_{2,n}(\tau_0) &= \frac{2}{\pi} \int_0^\pi \Phi_2(\tau_0) \cos n\psi d\psi.\end{aligned}\quad (1.10)$$

The Green's function [6] for such a problem is represented in the form

$$G_n(t, \tau) = \begin{cases} \frac{1}{W_n} \left(C_{1,n} t^{-b_n + \frac{1}{2}} + t^{b_n + \frac{1}{2}} \right) \left(C_{2,n} \tau^{b_n + \frac{1}{2}} + \tau^{-b_n + \frac{1}{2}} \right) & \text{for } t \leq \tau, \\ \frac{1}{W_n} \left(C_{1,n} t^{b_n + \frac{1}{2}} + t^{-b_n + \frac{1}{2}} \right) \left(C_{2,n} \tau^{-b_n + \frac{1}{2}} + \tau^{b_n + \frac{1}{2}} \right) & \text{for } t \geq \tau, \end{cases} \quad (1.11)$$

where $b_n^2 = \frac{1}{4} + \frac{n^2 H^2}{R^2}$,

$$\begin{aligned}C_{1,n} &= \frac{\tau_n^{2b_n} [(3-x_1) \tau_n - (2b_n + 1)]}{[-2b_n + 1 - (3-x_1) \tau_n]}, \\ C_{2,n} &= \frac{\left[2b_n - 1 + (3-x_1) \frac{A-1}{A+1} \tau_0 \right]}{\tau_0^{2b_n} \left[2b_n + 1 + (3-x_1) \frac{1-A}{1+A} \tau_0 \right]},\end{aligned} \quad (1.12)$$

$$W_n = -2b_n [1 - C_{1,n} C_{2,n}]. \quad (1.13)$$

Then we write the solution of the problem (1.1 - 1.3), which we call the A problem, in the form

$$J(\tau, \psi) = \sum_{n=0}^{\infty} (G_n(\tau_n, \tau) \Phi_{1,n} - \int_{\tau_n}^{\tau_0} G_n(t, \tau) f_n(t) dt - G_n(\tau_0, \tau) \Phi_{2,n}) \cos n\psi. \quad (1.14)$$

To ensure that the Series (1.14) is the solution of the A problem, it is necessary to prove the convergence of this series, and after this invoke the theorem of uniqueness of the solution for the type A problem [7].

We shall prove that the Series (1.14) converges by examining the Green's function $G_n(t, \tau)$ and showing its uniform boundedness [7] with respect to n . Let $t \leq \tau$, then

$$\begin{aligned}
G_n(t, \tau) = & - \frac{(C_{1,n} t^{-b_n+1/2} + t^{b_n+1/2}) (C_{2,n} \tau^{b_n+1/2} + \tau^{-b_n+1/2})}{2b_n [1 - C_{1,n} C_{2,n}]} = \\
& \frac{(t\tau)^{1/2} \left(\frac{\tau_n}{\tau_0}\right)^{b_n} \left(\frac{\tau_n}{t}\right)^{b_n} \left(\frac{\tau}{\tau_0}\right)^{b_n} \left(-1 - \frac{4b_n}{(-2b_n+1) - (3-x_1)\tau_n}\right) \times}{\times \left(-1 + \frac{4b_n}{\left[2b_n+1+(3-x_1)\frac{1-A}{1+A}\tau_0\right]}\right)} \times \\
= & - \frac{2b_n [1 - C_{1,n} C_{2,n}]}{2b_n [1 - C_{1,n} C_{2,n}]} - \\
& - \frac{(t\tau)^{1/2} \left(\frac{\tau_n}{\tau}\right)^{b_n} \left(\frac{\tau_n}{t}\right)^{b_n} \left(-1 - \frac{4b_n}{(-2b_n+1) - (3-x_1)\tau_n}\right)}{2b_n [1 - C_{1,n} C_{2,n}]} + \\
& + \frac{(t\tau)^{1/2} \left(\frac{t}{\tau}\right)^{b_n} \left(\frac{\tau}{\tau_0}\right)^{b_n} \left(-1 + \frac{4b_n}{\left[2b_n+1+(3-x_1)\frac{1-A}{1+A}\tau_0\right]}\right) + (t\tau)^{1/2} \left(\frac{t}{\tau}\right)^{b_n}}{2b_n [1 - C_{1,n} C_{2,n}]} .
\end{aligned}$$

We see from this expression that all the terms in the numerator are bounded by a single constant which is independent of n and depends only on τ_0 , while the denominator W_n is of order $O(n)$, consequently we can state that $|G_n(t, \tau)| < C(\tau_0)$ for $t \leq \tau$. In the same way, we can show the uniform boundedness of $G_n(t, \tau)$ with respect to n for $t > \tau$, i.e.,

$$|G_n(t, \tau)| \leq C(\tau_0). \quad (1.15)$$

Now let us assume that the functions $f(\tau, \psi)$ and $\varphi_2(\tau, \psi)$ have continuous derivatives of any order; then, as is well known [8], the following inequalities hold:

$$|f_n(\tau)| \leq \frac{a_{1,k}(\tau)}{n^{k+1}}, \quad (1.16)$$

$$|\varphi_{2,n}(\tau)| \leq \frac{a_{2,k}(\tau)}{n^{k+1}}, \quad (1.17)$$

where k is the number of the derivative with respect to ψ , respectively, of f and φ_2 , and $a_{1,k}(\tau)$ and $a_{2,k}(\tau)$ are continuous functions of τ and depend on the behavior of the derivative of k^{th} order for $f(\tau, \psi)$ and $\varphi_2(\tau, \psi)$ with respect to ψ . Since $\{\cos n\psi\}$ is uniformly

177

C. 2

bounded with respect to n , convergence of the Series (1.14) follows from the Inequalities (1.15), (1.16), (1.17).

Expansion of the A Problem in a Small Parameter

Case a

Let

$$\frac{2H_*^2}{(3-x_1)R^2} \leq \tau_n \leq \frac{1}{2(3-x_1)}. \quad (1.18)$$

Then for

$$n \leq n_0 = \left[\frac{R}{H_*} \sqrt{\frac{\tau_n(3-x_1)}{2}} \right]. \quad (1.19)$$

$$\begin{aligned} C_{1,n} \tau^{-b_{n+1}/2} + \tau^{b_{n+1}/2} &= \tau^{b_n-1/2} \left[\left(\frac{\tau_n}{\tau} \right)^{2b_n-1} \frac{\frac{2}{3-x_1} - \tau_n + \frac{2b_n-1}{3-x_1}}{1 - \frac{2b_n}{(3-x_1)\tau_n}} + \tau \right] = \\ &= \frac{2}{3-x_1} - \tau_n + \tau + \xi_{1,n}(\tau) \left(\frac{2}{3-x_1} - \tau_n + \tau \right) + \xi_{2,n}(\tau) \xi_{3,n}(\tau) + \\ &+ \xi_{3,n}(\tau) \xi_{4,n}(\tau) + \left(\frac{2}{3-x_1} - \tau_n \right) \xi_{2,n}(\tau) \xi_{4,n}(\tau) + \xi_{2,n}(\tau) \xi_{3,n}(\tau) \xi_{4,n}(\tau) + \\ &+ \left(\frac{2}{3-x_1} - \tau \right) (\xi_{2,n}(\tau) + \xi_{4,n}(\tau)) + \xi_{3,n}(\tau), \end{aligned} \quad (1.20)$$

where

$$\begin{aligned} \xi_{1,n}(\tau) &= \tau_n^{b_n-1/2} - 1, & \xi_{2,n}(\tau) &= (\tau_n/\tau)^{2b_n-1} - 1, \\ \xi_{3,n}(\tau) &= \frac{2b_n-1}{3-x_1}, & \xi_{4,n}(\tau) &= \frac{1}{1 + (2b_n-1)/((3-x_1)\tau_n)} - 1. \end{aligned}$$

From the form of the residual term of the Taylor series in the Lagrange form [8], we have the following estimates for $\xi_{1,n}$, $\xi_{2,n}$, $\xi_{3,n}$, $\xi_{4,n}$:

$$|\xi_{1,n}(\tau)| \leq \frac{n^2 H_*^2}{R^2} |\ln \tau_n|, \quad (1.21)$$

$$|\xi_{2,n}(\tau)| \leq \frac{2n^2 H_*^2}{R^2} \left| \ln \frac{\tau_n}{\tau} \right|, \quad (1.22)$$

$$|\xi_{3,n}(\tau)| \leq \frac{2n^2 H_*^2}{R^2} \frac{1}{3-x_1}, \quad (1.23)$$

$$|\xi_{1,n}(\tau)| \leq \frac{2\pi^2 H_*^2}{R^2} \frac{1}{(3-x_1)\tau_n} \quad (1.24) \quad /78$$

$$\text{if, } \tau_n > \frac{1}{2(3-x_1)}, \text{ then } n_0 = [0.5 R/H_*]. \quad (1.25)$$

Case b

Let

$$0 \leq \tau_n \leq \frac{2H_*}{R^2(3-x_1)} \quad (1.26)$$

and $n > 0$. Then

$$|C_{1,n}| = \left| \tau_n^{2b_n} \frac{\frac{2}{3-x_1} - \tau_n + \frac{2b_n-1}{3-x_1}}{\frac{2b_n-1}{3-x_1} + \tau_n} \right| \leq \tau_n (2 - (3-x_1)\tau_n) \frac{R^2}{2\pi^2 H_*^2} \quad (1.27)$$

Specifically, for $\tau_n = 0$ $C_{1,n} = 0$. $C_{1,n}\tau^{-b_{n+1/2}} + \tau^{b_{n+1/2}}$ has the following expansion:

$$C_{1,n}\tau^{-b_{n+1/2}} + \tau^{b_{n+1/2}} = \tau + \tau \xi_{1,n}(\tau). \quad (1.28)$$

We turn to the function $C_{2,n}\tau^{b_{n+1/2}} + \tau^{-b_{n+1/2}}$. Let

$$0 \leq n \leq [0.5 R/H_*]. \quad (1.29)$$

Then,

$$\begin{aligned} C_{2,n}\tau^{b_{n+1/2}} + \tau^{-b_{n+1/2}} &= \left[1 + \frac{(3-x_1) \frac{A-1}{A+1} \tau}{2 + (3-x_1) \frac{1-A}{1+A} \tau_0} \right] + \\ &+ \eta_{2,n}(\tau) \left[1 + \frac{(3-x_1) \frac{A-1}{A+1} \tau}{2 + (3-x_1) \frac{1-A}{1+A} \tau_0} \right] + \\ &+ \frac{(3-x_1) \frac{A-1}{A+1} \tau}{2 + (3-x_1) \frac{1-A}{1+A} \tau_0} [\eta_{2,n}(\tau) + \eta_{4,n}(\tau)] + \eta_{3,n}(\tau) + \eta_{2,n}(\tau) \eta_{4,n}(\tau) + \\ &+ \eta_{3,n}(\tau) \eta_{4,n}(\tau) + \frac{(3-x_1) \frac{A-1}{A+1} \tau}{2 + (3-x_1) \frac{1-A}{1+A} \tau_0} \eta_{2,n}(\tau) \eta_{4,n}(\tau) + \\ &+ \eta_{2,n}(\tau) \eta_{3,n}(\tau) \eta_{4,n}(\tau), \end{aligned} \quad (1.30)$$

where

$$\eta_{1,n}(\tau) = \tau^{-b_{n+1/2}} - 1, \quad \eta_{2,n}(\tau) = (\tau/\tau_0)^{2b_n-1} - 1,$$

$$\eta_{3,n}(\tau) = \frac{\tau}{\tau_0} \frac{2b_n-1}{2+(3-x_1)\frac{1-A}{1+A}\tau_0}, \quad \eta_{4,n}(\tau) = \left[\frac{2b_n-1}{2+(3-x_1)\frac{1-A}{1+A}\tau_0+1} \right]^{-1}.$$

Just as above, using the residual term in the Lagrange form for the Taylor formula, we obtain the following estimates for $\eta_{1,n}(\tau)$, $\eta_{2,n}(\tau)$, $\eta_{3,n}(\tau)$, $\eta_{4,n}(\tau)$:

$$\tau > 1 \quad |\eta_{1,n}(\tau)| \leq \frac{n^2 H^2}{R^2} |\ln \tau_0|, \quad (1.31)$$

for

$$\tau \leq 1 \quad |\eta_{1,n}(\tau)| \leq \frac{n^2 H^2}{R^2} \tau^{-n^2 H^2 / R^2} |\ln \tau_0|, \quad (1.32)$$

$$|\eta_{2,n}(\tau)| \leq \frac{2n^2 H^2}{R^2} \left| \ln \frac{\tau}{\tau_0} \right|, \quad (1.33)$$

$$|\eta_{3,n}(\tau)| \leq \frac{2n^2 H^2}{R^2} \frac{\tau}{\tau_0} \left| 1 - \left[2 + (3-x_1) \frac{1-A}{1+A} \tau_0 \right] \right|, \quad (1.34)$$

$$|\eta_{4,n}(\tau)| \leq \frac{2n^2 H^2}{R^2} \left| 1 - \left[2 + (3-x_1) \frac{1-A}{1+A} \tau_0 \right] \right|. \quad (1.35)$$

Expansion of the Green's function. Let τ_H obey one of the Inequalities (1.18) or (1.26); then for $0 < n \leq n_0$, where n_0 corresponds to its own inequality, we obtain

$$G_n(t, \tau) = G_0(t, \tau) + D_n \left(t, \tau \frac{H^2}{R^2}, C_{1,0}, C_{2,0} \right), \quad (1.36)$$

where

$$D_n = \frac{(C_{1,0}+1)\Gamma_{1,n}(\tau)}{W_0} + \frac{(C_{2,0}\tau+1)\Gamma_{2,n}(t)}{W_0} + \frac{\Gamma_{2,n}(t)\Gamma_{1,n}(\tau)}{W_0} +$$

$$+ \Gamma_{3,n}G_0(t, \tau) + \frac{\Gamma_{3,n}((C_{1,0}+1)\Gamma_{1,n}(\tau) + (C_{2,0}\tau+1)\Gamma_{2,n}(t))}{W_0} + \frac{\Gamma_{3,n}\Gamma_{2,n}(t)\Gamma_{1,n}(\tau)}{W_0}, \quad (1.37)$$

$$\Gamma_{1,n}(\tau) = (C_{2,n}\tau^{b_{n+1/2}} + \tau^{-b_{n+1/2}}) - (C_{2,0}\tau + 1) \quad (1.38)$$

$$\Gamma_{2,n}(\tau) = (C_{1,n}\tau^{-b_{n+1/2}} + \tau^{b_{n+1/2}}) - (C_{1,0} + \tau), \quad (1.39) \quad \underline{80}$$

$$\Gamma_{3,n} = W_0/W_n - 1 = \gamma_n + \mu_n + \gamma_n \mu_n; \quad (1.40)$$

here $\gamma_n = 1/2b_n - 1$,

$$\mu_n = \{1 - [C_{2,0}(\xi_{3,n} + C_{1,0}\xi_{4,n} + \xi_{3,n}\xi_{4,n}) + C_{1,0}(\eta_{3,n} + C_{2,0}\eta_{4,n} + \eta_{3,n}\eta_{4,n})] W_0^{-1}\}^{-1}.$$

Evaluating $|\gamma_n|$, $|\mu_n|$, as above, we obtain

$$|\gamma_n| \leq 2n^2 H^2 / R^2, \quad (1.41)$$

$$|\mu_n| \leq \frac{|\eta_{3,n} + C_{2,0}\eta_{4,n} + \eta_{3,n}\eta_{4,n}| |\xi_{3,n} + C_{1,0}\xi_{4,n} + \xi_{3,n}\xi_{4,n} + C_{1,0}|}{W_0} +$$

$$+ \frac{|\xi_{3,n} + C_{1,0}\xi_{4,n} + \xi_{3,n}\xi_{4,n}| |C_{2,0}|}{W_0}. \quad (1.42)$$

As a result of the estimates made above (1.2. - 1.24); (case a); (1.31) - (1.35); (1.41); (1.42), we can obtain the estimate of $D_n(t, \tau)$,

$\left| \int_{\tau_n}^{\tau} D_n f_n(\tau) d\tau \right|$ and write the solution of problem A in the form

$$J(\tau, \psi) = J_0(\tau, \psi) + R(\tau, \psi), \quad (1.43)$$

where

$$J_0(\tau, \psi) = G_0(\tau_n, \tau) \varphi_1 - \int_{\tau_n}^{\tau} G_0(t, \tau) f(t, \psi) dt - G_0(\tau_0, \tau) \varphi_2(\tau_0, \psi) \quad (1.44)$$

is the solution of the ordinary nonhomogeneous differential equation

$$\partial^2 J_0 / \partial \tau^2 = -f \quad (1.45)$$

with the boundary conditions (1.2) and (1.3), and

$$\begin{aligned} R(\tau, \psi) = & \sum_{n=n_0}^{\infty} \left\{ \int_{\tau_n}^{\tau} [G_0(t, \tau) - G_n(t, \tau)] f_n(t) dt + [G_0(\tau_0, \tau) - \right. \\ & \left. - G_n(\tau_0, \tau)] \varphi_{2,n} \right\} \cos n\psi + \sum_{n=1}^{n=n_0} \left[D_n(\tau_n, \tau) \varphi_{1,n} - \right. \\ & \left. - \int_{\tau_n}^{\tau} D_n(t, \tau) f_n(t) dt - D_n(\tau_0, \tau) \varphi_{2,n} \right] \cos n\psi. \end{aligned}$$

Case b. In this case, $0 \leq \tau_H \leq 2H^2/R^2$, we consider the solution of problem A only for $\tau_H=0$; for other values of τ_H , corresponding to this case, we obtain the same representation plus $O(\tau_H)$.

Let $0 < n \leq n_0 = \frac{1}{2} \frac{R}{H_*}$; then according to (1.36), we have the following representation of the Green's function

$$G_n(t, \tau) = \frac{1}{W_n} (C_{1,n} t^{-b_{n+1/2}} + t^{b_{n+1/2}}) (C_{2,n} \tau^{b_{n+1/2}} + \tau^{-b_{n+1/2}}) = \\ = -\tau (C_{2,0} \tau + 1) + D_n(t, \tau, H^2/R^2, C_{1,0}, \xi_{1,n}, C_{2,0}) \Big|_{\substack{C_{1,0}=0 \\ \xi_{1,n}=0}}, \quad (1.47)$$

where $D_n \Big|_{\substack{C_{1,0}=0 \\ \xi_{1,n}=0}}$ is defined by the Equality (1.37) for values $C_{1,0}=0$, $\xi_{1,n}=0$.

Now we can write the solution of problem A

$$J(\tau, \psi) = J_0(\tau, \psi) + R(\tau, \psi) \Big|_{\substack{C_{1,0}=0 \\ \xi_{1,n}=0 \\ \tau_H=0}} = J_0(\tau, \psi) + j(\tau) + R_0(\tau, \psi), \quad (1.48)$$

where

$$J_0(\tau, \psi) = \int_0^{\tau_0} G_0(t, \tau) \Big|_{C_{1,0}=0} f(\tau, \psi) d\tau - G_0(\tau_0, \tau) \Big|_{C_{1,0}=0} \varphi_2(\tau_0, \tau)$$

is the solution of the following boundary value problem

$$\frac{\partial^2 J_0}{\partial \tau^2} = -f, \quad (1.49)$$

$$J_0 \Big|_{\tau=0} = 0, \quad (1.50)$$

$$\frac{\partial J_0}{\partial \tau} + \frac{3-x_1}{2} \frac{1-A}{1+A} J_0 \Big|_{\tau=\tau_0} = \varphi_2(\tau_0, \psi), \quad (1.51)$$

$$j(\tau) = \int_0^{\tau_0} [G_0(t, \tau) - G_0(t, \tau) \Big|_{C_{1,0}=0}] f_0(t) dt - [G_0(\tau_0, \tau) - \\ - G_0(\tau_0, \tau) \Big|_{C_{1,0}=0}] \varphi_{2,0}(\tau_0), \quad (1.52)$$

The estimate of $|R(\tau, \psi)|$ is possible if we have an estimate of $|f_n(\tau)|$. According to the Equality (1.8), $f_n(\tau)$ is represented in the form

$$f_n(\tau) = \frac{3}{4} S \frac{2}{\pi} \int_0^{\pi} e^{-\tau(\tau, \psi)} \cos n\psi d\psi \text{ for } n > 0. \quad (1.53)$$

We see from this equality that the representation $T(\tau, \psi)$ is necessary for estimating the function $f_n(\tau)$. As is known [3], $T(\tau, \psi)$ is represented as

$$T(\tau, \psi) = a(\tau) \int_{r \cos \psi}^{\infty} e^{-\frac{1}{H_n} (\sqrt{r^2 \sin^2 \psi + Z^2 - 1})} dZ. \quad (1.54)$$

It was also shown in [3] that $T(\tau, \psi)$ can be calculated with high accuracy from the formula

$$T(\tau, \psi) = \tau b(\psi), \quad (1.55)$$

where for

$$\left(0 \leq \psi \leq \frac{\pi}{2}\right) \quad b(\psi) = g(a) \sec \psi, \quad (1.56)$$

$$a = \frac{R}{H_n} (1 - \sin \psi), \quad g(a) = 2 \sqrt{a} e^a \int_{\sqrt{a}}^{\infty} e^{-t^2} dt, \quad (1.57)$$

for

$$\pi > \psi > \frac{\pi}{2} \quad b(\psi) = 2e^a b\left(\frac{\pi}{2}\right) - b(\pi - \psi).$$

It is well known that the coefficients $f_n(\tau)$ of the Fourier series for $f(\tau, \psi)$ obey the inequality [8]

$$|f_n(\tau)| \leq \frac{2V_k(\tau)}{\pi} \frac{1}{n^{k+1}}, \quad (1.58)$$

where V_k is the entire change of the k^{th} derivative of $f(\tau, \psi)$ with respect to ψ in the interval $[0, \pi]$. The residual of this Fourier series is defined by the inequality

$$|\hat{R}_n(\tau)| \leq \frac{V_k(\tau)}{n^k}. \quad (1.59)$$

Examining V_k , we can show that

$$V_k \leq a_0 |f_{\psi}^{(k)}(\tau, \psi_0)|, \quad (1.60)$$

where

$$|f_{\psi}^{(k)}(\tau, \psi_0)| = \max_{[0, \pi]} |f_{\psi}^{(k)}(\tau, \psi)|.$$

$|f_n(\tau)|$ is estimated with the aid of $V_2(\tau)$. In order to obtain the estimate of $V_2(\tau)$, it is necessary to study the behavior of $f_{\psi}^{(2)}(\tau, \psi)$, which is represented in the form

$$f_{\psi}^{(2)}(\tau, \psi) = \frac{3}{4} S \tau \left(\tau \left(\frac{\partial b(\psi)}{\partial \psi} \right)^2 - \frac{\partial^2 b(\psi)}{\partial \psi^2} \right) e^{-\tau b(\psi)}. \quad (1.61) \quad /83$$

Analysis of the behavior of the function $\frac{\partial^2 f}{\partial \psi^2}(\tau, \psi)$ shows that

$$\int_0^{\tau_0} V_2(\tau) d\tau \leq a_0 \int_0^{\tau_0} |f_{\psi}^{(2)}(\tau, \psi_0)| d\tau \leq \frac{3S}{4} \frac{2R}{H_* b\left(\frac{\pi}{2}\right)}. \quad (1.62)$$

Let us turn directly to the estimate of $|R(\tau, \psi)|$. We estimate the first sum in the Equality (1.46)

$$\begin{aligned} |R_1| &\leq \left| \sum_{n=n_0}^{\infty} \int_{\tau_n}^{\tau_0} (G_0(t, \tau) - G_n(t, \tau)) f_n(t) dt \cos n\psi \right| \leq \\ &\leq \sum_{n=n_0}^{\infty} \int_{\tau_n}^{\tau_0} |G_0(t, \tau) - G_n(t, \tau)| |f_n(t)| dt. \end{aligned} \quad (1.63)$$

We note that $G_n(t, \tau)$, as a function of n , does not change sign up to

$$n_1 = \frac{r}{2H_*} \sqrt{\left(1 + (3 - x_1) \frac{1 - A}{1 + A} \tau_0\right)^2 - 1}$$

and that $|G_0(t, \tau)| > |G_n(t, \tau)|$ for fixed t, τ for all n . Consequently, the Inequality (1.63) may be continued

$$\begin{aligned} &\sum_{n=n_0}^{\infty} \int_{\tau_n}^{\tau_0} |G_0(t, \tau) - G_n(t, \tau)| |f_n(t)| dt \leq \\ &\leq \sum_{n=n_0}^{\infty} \int_{\tau_n}^{\tau_0} |G_0(t, \tau)| |f_n(t)| dt + \sum_{n=n_1}^{\infty} \int_{\tau_n}^{\tau_0} |G_0(t, \tau)| \cdot |f_n(t)| dt = L_2. \end{aligned} \quad (1.64)$$

Denoting

$$F_1(\tau, \tau_2) = \int_{\tau_1}^{\tau_2} |f_{\psi}^{(2)}(\tau, \psi)| d\tau,$$

$$F_2(\tau_1, \tau_2) = \int_{\tau_1}^{\tau_2} \tau |f_{\psi}^{(2)}(\tau, \psi)| d\tau,$$

$$L_1 \leq \frac{2(1/n_0^2 + 1/n_1^2)}{W_0} [(C_{2,0}\tau + 1)(C_{1,0}F_1(\tau_n, \tau) + F_2(\tau_n\tau)) + (C_{1,0} + \tau)(C_{2,0}F_2(\tau, \tau_0) + F_1(\tau, \tau_0))]. \quad (1.65)$$

We obtain a similar inequality for the second term of the first sum of the Equality (1.46)

$$I_2 = \left| \sum_{n=n_0}^{\infty} (G_0(\tau_0, \tau) - G_n(\tau_0, \tau)) \varphi_{2,n}(\tau_0, \tau) \cos n\psi \right| \leq a_1 |G_0(\tau_0, \tau)| |\varphi_{2,\psi}^{(2)}(\tau_0, \psi)| \left(\frac{1}{n_0^2} + \frac{1}{n_1^2} \right), \quad (1.66)$$

where $a_1 = 2$.

Further examination of the Inequalities (1.65) and (1.66) shows that the relative error $a_1 = \frac{L_1 + L_2}{|J_0|}$ of the first sum of Equality (1.46) is evaluated by the inequality

$$d_1 \leq 2q \sqrt{\frac{2}{\pi} \frac{H_*}{R} \frac{H_*}{R}} b(\psi), \quad (1.67)$$

if $\frac{(3-x_1)(1-A)}{(1+A)\tau_0} \gg \frac{1}{8}$, and by the inequality

$$d_1 \leq 4q \sqrt{\frac{2}{\pi} \frac{H_*}{R} \frac{H_*}{R}} b(\psi), \quad (1.68)$$

in the remaining cases

$$q = \begin{cases} \text{for (1.18)} & \frac{2}{(3-x_1)\alpha_n H_*} \\ \text{for (1.26)} & 4. \end{cases}$$

Let us turn to $|R_2|$.

$$|R_2| = \left| \sum_{n=1}^{n_0} (D_n(\tau_n, \tau) \varphi_{1,n} - \int_{\tau_n}^{\tau_0} D_n(t, \tau) f_n(t) dt - D_n(\tau_0, \tau) \varphi_{2,n}) \cos n\psi \right|. \quad (1.69)$$

Using the Inequalities (1.58) and (1.60), and also the Representation /85 (1.37) for D_n , we can obtain the estimate of $d_2 = \left| \frac{R_2}{J_0} \right|$ in the form

$$d_2 \leq 3 \frac{H_2}{R} (\ln n_0) \left(M + \frac{2}{(3-x_1) \alpha_H H_*} + 2 \right) \frac{b(\psi)}{b\left(\frac{\pi}{2}\right)}, \quad (1.70)$$

where $M = \max\{|\ln \tau_0|, |\ln \tau_H|\}$ for the Conditions (1.18), (1.19) (case a)

and for (1.26) (Case b) we obtain the estimate for $d_2 = \left| \frac{R_2}{J_0} \right|$ of the form

$$d_2 \leq 3 \frac{H_2}{R} (\ln n_0) (|\ln \tau_0| + 2) \frac{b(\psi)}{b\left(\frac{\pi}{2}\right)}, \quad (1.71)$$

where

$$b\left(\frac{\pi}{2}\right) = \sqrt{\frac{\pi}{2} \frac{R}{H_*}}.$$

Numerical results and conclusions. Setting $T = \tau b(\psi)$, we can reduce (1.44) to a form convenient for calculations

$$\begin{aligned} J_0^{\Delta}(\tau, \psi) = \frac{S}{W_0} \left\{ C_{1,0} (C_{2,0}^{\Delta} \tau + 1) \frac{x_1}{4} \cos \psi - \frac{3}{4} [(C_{2,0}^{\Delta} \tau + 1) (C_{1,0} S_0(0, \tau) + \right. \\ \left. + S_1(0, \tau)) + (C_{1,0} + \tau) (C_{2,0} S_1(\tau, \tau_0) + S_0(\tau, \tau_0))] - (C_{2,0}^{\Delta} \tau_0 + \right. \\ \left. + 1) (C_{1,0} + \tau) \varphi_2(\tau_0, \psi) \right\}, \end{aligned} \quad (1.72)$$

where

$$S_i(\tau_1, \tau_2) = \frac{\tau_1^i e^{-\tau_1 b(\psi)} - \tau_2^i e^{-\tau_2 b(\psi)}}{b(\psi)} + \frac{i}{b(\psi)} S_{i-1}(\tau_1, \tau_2),$$

and $W_0, C_{1,0}, C_{2,0}, \varphi_2(\tau_0, \psi)$ are defined, respectively, by (1.13), (1.12), (1.17).

Since there is no diffuse radiation downward at the upper edge of the atmosphere, the radiation leaving the atmosphere is

$$J_2(0, \psi) = 2J_0(0, \psi). \quad (1.73)$$

The calculation using (1.73) and the estimate of the accuracy for $80^\circ \leq \psi \leq 90^\circ$ are shown in the table. The calculations were made for $A=0; x_1=0; \tau_0=10; \tau_H=1; H_*/R=10^3$. We see from the table that the error $d = d_1 + d_2$ does not exceed 6% under the conditions selected:

ψ , deg	$I_2 (\psi) \cdot 10^3$ S	$d \cdot 10^2$
80	178.2	1.3
82	153.6	1.7
84	119.8	2.0
86	95.2	2.2
88	64.9	3.5
90	40.0	6.0

The Formulas (1.44) and (1.48) obtained above for the average intensity and the Estimates (1.67 - 1.71) make it possible to refine the theory presented in [1 - 3], and at the same time it is easier to carry out the numerical realization of this theory than in [5]. The Estimates (1.67 - 1.71) also make it possible to compare the results for (τ, ψ) from (1.14) with the results of [3] in a wide range of initial values, and conclude that there is quite good agreement between the results obtained and the approximate solution of the problem in [3] under the conditions which follow from the estimates (1.67 - 1.71).

The results of this study make it possible to evaluate the error introduced by dropping the term $\frac{H^2}{R_1} \frac{\partial^2 J}{\partial \psi^2}$ in (1.6) without resorting to numerical solutions.

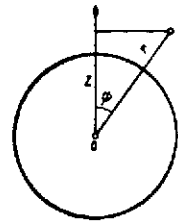
2. Scattering of Light in a Spherical Uniform Atmosphere with Account for the True Absorption

In the present section, we propose a problem solution method using the Green's function under the same assumptions used in [4]. But the use of this solution, just as the use of the solution of [4], to describe the scattering of light in a cloudy atmosphere requires suitable transformation of the parameters τ_0, x_1 .

Problem formulation. Let R be the radius of the planet, R_1 the radius of the outer edge of the atmosphere. The location of a

point in the atmosphere is characterized by the spherical coordinates r and ψ with Z axis directed from the center of the planet toward the sun (see figure).

We consider that the planet is illuminated by solar rays creating illumination of an area equal to πS perpendicular to the rays. As was shown earlier [1], in the case when the coefficient of absorption (attenuation) $\alpha = \text{const}$, the quantity J , which is the average intensity of diffuse radiation at a given point of the atmosphere, is defined by the equation



Coordinate system

/87

$$\frac{\partial^2 J}{\partial r^2} + \frac{1}{R^2} \frac{\partial^2 J}{\partial \psi^2} = \alpha^2 (k^2 J - f), \quad (2.1)$$

where

$$k^2 = (3 - \lambda x_1)(1 - \lambda), \quad (2.2)$$

$$f = \frac{\lambda S}{4} [3 + (1 - \lambda)x_1] e^{-\tau}, \quad (2.3)$$

$$T = \alpha (\sqrt{R_1^2 - r^2 \sin^2 \psi} - r \cos \psi). \quad (2.4)$$

It is obvious that the Expression (2.3) for the quantity f is valid only for the part of the atmosphere illuminated by the Sun. For the unilluminated part of the atmosphere, we must consider $f = 0$. Introducing the new independent variable

$$\tau = \alpha(R_1 - r), \quad (2.5)$$

we represent (2.1) in the form

$$\frac{\partial^2 J}{\partial \tau^2} + \frac{1}{R^2 \alpha^2} \frac{\partial^2 J}{\partial \psi^2} = k^2 J - f. \quad (2.6)$$

The boundary conditions must be added to (2.6). As was shown in [2], at the outer edge of the atmosphere we have (for $\tau = 0$)

$$\frac{\partial J}{\partial \tau} - \frac{3 - \lambda x_1}{2} J = \frac{\lambda S}{4} x_1 \cos \psi, \quad (2.7)$$

and at the inner edge (for $r = R$, or $\tau = \tau_0$)

$$\frac{\partial J}{\partial \tau} + \frac{3 - \lambda x_1}{2} J = \frac{S}{4} \cos \psi \left[\lambda x_1 + \frac{2A}{1+A} (3 - \lambda x_1) \right] e^{-T(\tau, \psi)}. \quad (2.8)$$

We note that for $\psi > \pi/2$, the second term in the right side of (2.8) vanishes, since in this case $T(\tau_0, \psi) = \infty$. Thus, problem B consists of solving (2.6) with the boundary conditions (2.7) and (2.8).

Solution of problem B. We seek $J(\tau, \psi)$ in series form

$$J = \sum_{n=0}^{\infty} D_n(\tau) \cos n\psi. \quad (2.9)$$

We expand the right sides of (2.6), (2.7), (2.8) into a Fourier cosine series. As a result of these expansions and the Representation (2.9), we obtain the following boundary value problem for determining the coefficients $D_n(\tau)$:

$$D_n''(\tau) - \left(k^2 + \frac{n^2}{\alpha^2 R^2} \right) D_n(\tau) = -f_n(\tau), \quad (2.10)$$

$$D_n'(\tau) - \frac{3 - \lambda x_1}{2} D_n(\tau) \Big|_{\tau=0} = \varphi_{1,n}, \quad (2.11)$$

$$D_n'(\tau) + \frac{3 - \lambda x_1}{2} \frac{1-A}{1+A} D_n(\tau) \Big|_{\tau=\tau_0} = \varphi_{2,n}, \quad (2.12)$$

where $f_n, \varphi_{1,n}, \varphi_{2,n}$ are the Fourier coefficients, respectively, of f and the right sides of (2.7) and (2.8). The Green's function for this problem has the form

$$G_n(t, \tau) = \begin{cases} \frac{1}{W_n} \left(a_{1,n} \exp(-\beta_n t) + \frac{\text{sh } \beta_n t}{\beta_n} \right) \times \\ \times \left(a_{2,n} \frac{\text{sh } \beta_n \tau}{\beta_n} + \exp(-\beta_n \tau) \right) \text{ for } t \leq \tau, \\ \frac{1}{W_n} \left(a_{2,n} \frac{\text{sh } \beta_n t}{\beta_n} + \exp(-\beta_n t) \right) \times \\ \times \left(a_{1,n} \exp(-\beta_n \tau) + \frac{\text{sh } \beta_n \tau}{\beta_n} \right) \text{ for } t \geq \tau, \end{cases} \quad (2.13)$$

where

$$\beta_n = \sqrt{k^2 + \frac{n^2}{\alpha^2 R^2}}, \quad (2.14)$$

$$\left. \begin{aligned} a_{1,n} &= \frac{1}{\frac{3-\lambda x_1}{2} + \beta_n}, \\ a_{2,n} &= \frac{\beta_n + \frac{3-\lambda x_1}{2} \frac{A-1}{A+1}}{\exp(\beta_n \tau_0) \left(\operatorname{ch} \beta_n \tau_0 + \frac{3-\lambda x_1}{2} \frac{1-A}{1+A} \frac{\operatorname{sh} \beta_n \tau_0}{\beta_n} \right)}, \\ W_n &= -[1 - a_{1,n} a_{2,n}]. \end{aligned} \right\} \quad (2.15)$$

(2.15)

(2.16)

Then we write the solution of problem B in series form

$$J(\tau, \psi) = \sum_{n=0}^{\infty} (G_n(0, \tau) \varphi_{1,n} - \int_0^{\tau_0} G_n(t, \tau) f_n(t) dt - G_n(\tau_0, \tau) \varphi_{2,n}) \cos n\psi. \quad (2.17)$$

The convergence of the Series (2.17) is shown just as in Section 1, which, after invoking the theorem on uniqueness of the solution of problem B [7], permits us to conclude that the Series (2.17) is the unique solution of problem B. /89

Expansion of the problem B solution in the small parameter $1/R$.

Expansion of the functions

$$\left(a_{1,n} \exp(-\beta_n t) + \frac{\operatorname{sh} \beta_n t}{\beta_n} \right), \left(a_{2,n} \frac{\operatorname{sh} \beta_n t}{\beta_n} + \exp(-\beta_n t) \right).$$

We shall examine initially the first function. Let

$$\frac{1}{a^2 R^2} \leq k^2, \quad (2.18)$$

then for $n \leq n_0 = [a R k]$,

$$\begin{aligned} a_{1,n} \exp(-\beta_n t) + \frac{\operatorname{sh} \beta_n t}{\beta_n} &= \left(\frac{\exp(-kt)}{\frac{3-\lambda x_1}{2} + k} + \frac{\operatorname{sh} kt}{k} \right) + \\ &+ (\xi_{1,n}(t) + \xi_{2,n}(t)) \frac{\exp(-kt)}{\frac{3-\lambda x_1}{2} + k} + \frac{\operatorname{sh} kt}{k} (\xi_{3,n}(t) + \xi_{4,n}(t)) + \\ &+ \xi_{1,n}(t) \xi_{2,n} \frac{\exp(-kt)}{\frac{3-\lambda x_1}{2} + k} + \frac{\operatorname{sh} kt}{k} \xi_{3,n}(t) \xi_{4,n}. \end{aligned} \quad (2.18^a)$$

From the residual term of the Taylor formula in Lagrange form [8], we have the following estimates for $\{\xi_{in}\}$:

$$|\xi_{1,n}(t)| \leq \frac{1}{2} \frac{n^2 t}{\alpha^2 R^2 k}, \quad (2.19)$$

$$|\xi_{2,n}| \leq \frac{\frac{1}{2} \frac{n^2}{\alpha^2 R^2 k}}{\frac{3 - \lambda_{x_1}}{2} + k}. \quad (2.20)$$

$$|\xi_{3,n}(t)| \leq \frac{1}{2} \frac{e^{\frac{sh t}{k}}}{sh k t} \frac{n^2 t}{\alpha^2 R^2 k}, \quad (2.21)$$

$$|\xi_{4,n}| \leq \frac{1}{2} \frac{n^2}{\alpha^2 R^2 k^2}. \quad (2.22)$$

If $0 \leq k^2 < \frac{1}{\alpha^2 R^2}$, then

/90

$$n \leq n_0 = \left[\alpha R (\ln 2) \frac{1}{\tau_0} \right] - 1. \quad (2.23)$$

Introducing the notation $\xi_{3,n} = \frac{sh \beta_n t}{\beta_n t} - 1$, we obtain

$$\begin{aligned} a_{1,n} \exp(-\beta_n t) + \frac{sh \beta_n t}{\beta_n} &= \frac{2}{3 - \lambda_{x_1}} + t + \\ &+ (\xi_{1,n}(t) + \xi_{2,n}) \frac{2}{3 - \lambda_{x_1}} + \xi_{3,n}(t) + \frac{2}{3 - \lambda_{x_1}} \xi_{1,n}(t) \xi_{2,n}. \end{aligned} \quad (2.23^a)$$

In this case, the following estimates for $\xi_{1,n}$ are valid:

$$|\xi_{1,n}(t)| \leq \frac{nt}{\alpha R}, \quad (2.24)$$

$$|\xi_{2,n}| \leq \frac{2n}{\alpha R (3 - \lambda_{x_1})}, \quad (2.25)$$

$$|\xi_{3,n}(t)| \leq \frac{nt}{\alpha R}. \quad (2.26)$$

For the corresponding n , the expansion of the second function in the small parameter has the form

$$\begin{aligned} a_{2,n} \frac{sh \beta_n t}{\beta_n} + \exp(-\beta_n t) &= \frac{\left(k + \frac{3 - \lambda_{x_1} A - 1}{2} \frac{sh k t}{A + 1} \right) \frac{sh k t}{k}}{\exp(k \tau_0) \left(ch k \tau_0 + \frac{3 - \lambda_{x_1} 1 - A}{2} \frac{sh k \tau_0}{1 + A} \frac{sh k \tau_0}{k} \right)} \times \\ &\times (1 + \eta_{1,n}(\tau_0) + \xi_{3,n}(t) + \xi_{4,n} + \eta_{1,n}(\tau_0) (\xi_{3,n}(t) + \xi_{4,n}) + \\ &+ \eta_{1,n}(\tau_0) \xi_{3,n}(t) \xi_{4,n} + \xi_{3,n}(t) \xi_{4,n}) + \exp(-k t) (1 + \xi_{1,n}(t)), \end{aligned} \quad (2.27)$$

where

$$\eta_{1,n}(\tau_0) = \frac{a_{2,n}}{a_{2,0}} - 1$$

and

$$\begin{aligned}
 |\eta_{1,n}(\tau_0)| \leq & \frac{\frac{1}{2} \frac{n^2}{\alpha^2 R^2 k}}{\frac{3-\lambda_{x_1}}{2} \frac{1-A}{1+A}} + |\xi_{1,n}(\tau_0)| + \left(\frac{\frac{\text{sh } k\tau_0 \cdot e^{\frac{k\tau_0}{2}} \frac{n^2 \tau_0}{2 \alpha^2 R^2 k}}{\text{ch } k\tau_0 + \frac{3-\lambda_{x_1}}{2} \frac{1-A}{1+A} \frac{\text{sh } k\tau_0}{k}} + \right. \\
 & \left. + \frac{\frac{3-\lambda_{x_1}}{2} \frac{1-A}{1+A} \frac{\text{sh } k\tau_0}{k} (\xi_{3,n}(\tau_0) + \xi_{4,n} + \xi_{5,n}(\tau_0) \xi_{4,n})}{\text{ch } k\tau_0 \frac{3-\lambda_{x_1}}{2} \frac{1-A}{1+A} \frac{\text{sh } k\tau_0}{k}} \right) \times \\
 & \times \left(\frac{\frac{1}{2} \frac{n^2}{\alpha^2 R^2 k}}{\frac{3-\lambda_{x_1}}{2} \frac{1-A}{1+A}} |\xi_{1,n}(\tau_0)| + |\xi_{1,n}(\tau_0)| + \frac{\frac{1}{2} \frac{n^2}{\alpha^2 R^2 k}}{\frac{3-\lambda_{x_1}}{2} \frac{1-A}{1+A}} + 1 \right) + \\
 & + \frac{\frac{1}{2} \frac{n^2}{\alpha^2 R^2 k}}{\frac{3-\lambda_{x_1}}{2} \frac{1-A}{1+A}} |\xi_{1,n}(\tau_0)|.
 \end{aligned} \tag{2.28}$$

If $0 \leq k^2 < \frac{1}{\alpha^2 R^2}$, then for $n \leq n_0 = \left[\alpha R (\ln 2) \frac{1}{\tau_0} \right] + 1$

$$\begin{aligned}
 a_{1,n} \frac{\text{sh } \beta_n t}{\beta_n} + \exp(-\beta_n t) = & \left(\frac{\frac{3-\lambda_{x_1}}{2} \frac{A-1}{A+1} \cdot t}{1 + \frac{3-\lambda_{x_1}}{1-A} \frac{1-A}{1+A} \tau_0} + 1 \right) \times \\
 & \times (1 + \eta_{1,n}(\tau_0) + \xi_{3,n}(t) + \eta_{1,n}(\tau_0) (\xi_{3,n}(t)) + 1 + \xi_{1,n}(t)).
 \end{aligned} \tag{2.29}$$

In this case

$$\begin{aligned}
 |\eta_{1,n}(\tau_0)| \leq & \frac{\frac{n}{\alpha R}}{\frac{3-\lambda_{x_1}}{2} \frac{1-A}{1+A}} + |\xi_{1,n}(\tau_0)| + \frac{\frac{n}{\alpha R} + \frac{3-\lambda_{x_1}}{2} \frac{1-A}{1+A} \tau_0 (1 + \xi_{3,n}(\tau_0))}{1 + \frac{3-\lambda_{x_1}}{2} \frac{1-A}{1+A} \tau_0} \times \\
 & \times \left(\frac{\frac{n}{\alpha R}}{\frac{3-\lambda_{x_1}}{2} \frac{1-A}{1+A}} |\xi_{1,n}(\tau_0)| + |\xi_{1,n}(\tau_0)| + \right. \\
 & \left. + \frac{\frac{n}{\alpha R}}{\frac{3-\lambda_{x_1}}{2} \frac{1-A}{1+A}} + 1 \right) + \frac{\frac{n}{\alpha R} |\xi_{1,n}(\tau_0)|}{\frac{3-\lambda_{x_1}}{2} \frac{1-A}{1+A}}.
 \end{aligned} \tag{2.30}$$

Expansion of the Green's function.

Let k obey one of the Inequalities (2.18) or (2.23), then for the corresponding n , the following is valid for $t \leq \tau$:

$$\begin{aligned}
G_n(t, \tau) &= \frac{1}{W_n} \left(a_{1,n} \exp(-\beta_n t) + \frac{\text{sh } \beta_n t}{\beta_n} \right) \left(a_{2,n} \frac{\text{sh } \beta_n \tau}{\beta_n} + \exp(-\beta_n \tau) \right) = \\
&= \frac{1}{W_0} \left(a_{1,0} \exp(-kt) + \frac{\text{sh } kt}{k} \right) \times \left(a_{2,0} \frac{\text{sh } k\tau}{k} + \exp(-k\tau) \right) + \\
&+ D_n \left(t, \tau, \frac{1}{\alpha R}, a_{1,0}, a_{2,0} \right), \quad (2.31)
\end{aligned}$$

where

$$\begin{aligned}
D_n \left(t, \tau, \frac{1}{\alpha R}, a_{1,0}, a_{2,0} \right) &= - \frac{\left(a_{1,0} \exp(-kt) + \frac{\text{sh } kt}{k} \right) \Gamma_{1,n}(\tau)}{W_0} + \\
&+ \frac{\left(a_{2,0} \frac{\text{sh } k\tau}{k} + \exp(-k\tau) \right) \Gamma_{2,n}(t)}{W_0} + \frac{\Gamma_{1,n}(\tau) \Gamma_{2,n}(t)}{W_0} + \Gamma_{3,n} G_0(t, \tau) + \\
&+ \frac{\Gamma_{1,n}(\tau) \cdot \Gamma_{2,n} \left(a_{1,0} \exp(-kt) + \frac{\text{sh } kt}{k} \right)}{W_0} + \frac{\Gamma_{2,n}(t) \Gamma_{3,n} \left(\frac{\text{sh } k\tau}{k} + \exp(-k\tau) \right)}{W_0} + \\
&+ \frac{\Gamma_{3,n} \Gamma_{1,n}(\tau) \Gamma_{2,n}(t)}{W_0}, \quad (2.32)
\end{aligned}$$

$$\Gamma_{1,n}(\tau) = \left(a_{2,n} \frac{\text{sh } \beta_n \tau}{\beta_n} + \exp(-\beta_n \tau) \right) - \left(a_{2,0} \frac{\text{sh } k\tau}{k} + \exp(-k\tau) \right), \quad (2.33)$$

$$\Gamma_{2,n}(t) = \left(a_{1,n} \exp(-\beta_n t) + \frac{\text{sh } \beta_n t}{\beta_n} \right) - \left(a_{1,0} \exp(-kt) + \frac{\text{sh } kt}{k} \right), \quad (2.34)$$

$$\Gamma_{3,n} = \frac{W_0}{W_n} - 1. \quad (2.35)$$

Here, $\Gamma_{2,n}$ and $\Gamma_{1,n}$ are found with the aid of (2.18), (2.23) and (2.27), (2.29), and $\Gamma_{3,n}$ is evaluated by means of the inequality

$$|\Gamma_{3,n}| \leq \frac{|a_{1,0} a_{2,0}| (|\xi_{2,n}| + |\eta_{1,n}| + |\xi_{2,n}| |\eta_{1,n}|)}{|W_0|}. \quad (2.36)$$

When $k=0$, $G_0(t, \tau)|_{k=0} = \lim_{k \rightarrow 0} [G_0(t, \tau)|_{k \neq 0}]$.

As a result of the Expansions (2.31 - 2.35) presented above, we can write the solution of problem B in the form

$$J(\tau, \psi) = J_0(\tau, \psi) + R(\tau, \psi), \quad (2.37)$$

where

$$J_0(\tau, \psi) = G_0(0, \tau) \varphi_1 - \int_0^\tau G_0(t, \tau) f(t, \psi) dt - G_0(\tau_0 \tau) \varphi_2(\tau_0, \psi) \quad (2.38)$$

is the solution of the ordinary differential equation

$$\frac{\partial^2 J}{\partial \tau^2} = k^2 J - f \quad (2.39)$$

with the boundary conditions (2.7), (2.8), and

$$\begin{aligned} R(\tau, \psi) = & \sum_{n=n_0}^{\infty} \left\{ \int_0^{\tau_0} [G_0(t, \tau) - G_n(t, \tau)] f_n(t) dt + [G_0(\tau_0, \tau) - \right. \\ & \left. - G_n(\tau_0, \tau)] \varphi_{1,n} \right\} \cos n\psi + \sum_{n=1}^{n=n_0} \left[D_n(0, \tau) \varphi_{1,n} - \int_0^{\tau_0} D_n(t, \tau) f_n(t) dt - \right. \\ & \left. - D_n(\tau_0, \tau) \varphi_{1,n} \right] \cos n\psi. \end{aligned} \quad (2.40)$$

If k obeys the Inequality (2.23), then in the Equality (2.38),

$$G_0(t, \tau) = G(t, \tau) |_{h=0}.$$

Let us turn to the estimate of $|R(\tau, \psi)|$.

Estimate of $|R(\tau, \psi)|$. As is well known [7], the Fourier cosine coefficient $f_n(t)$ for $n > 0$ for $f(t, \psi)$ are represented in the form

$$f_n(t) = \frac{2}{\pi} \int_0^{\pi} f(t, \psi) \cos n\psi d\psi.$$

Using (2.3), we obtain

$$f_n(t) = \frac{2}{\pi} \frac{\lambda S}{4} [3 + (1 - \lambda) \cdot x_1] \int_0^{\pi} e^{-\tau} \cos n\psi d\psi. \quad (2.41)$$

In order to evaluate $R(\tau, \psi)$, it is necessary to evaluate

$$|f_n|_1 = \int_0^{\tau_0} |f_n(t)| dt. \quad (2.42)$$

It is well known [7] that the Fourier coefficients $f_n(t)$ for $f(t, \psi)$ obey the following inequality:

$$|f_n(t)| \leq \frac{2V_k(t)}{\pi} \frac{1}{n^{k+1}}, \quad (2.43)$$

where V_k is the entire change of the k^{th} derivative with respect to ψ in the interval $[0, \pi]$. /94

The residue of the Fourier series is defined by the inequality

$$|R_n(t)| \leq \frac{V_k(t)}{n_k}. \quad (2.44)$$

Examining V_k , we can show

$$V_k(t) \leq a_0 |f_\psi^{(k)}(t, \psi_0(t))|, \quad (2.45)$$

where

$$|f_\psi^{(k)}(t, \psi_0(t))| = \max_{[0, \pi]} |f_\psi^{(k)}(t, \psi)|. \quad (2.46)$$

Hence follows the inequality for $|f_n|_1$

$$|f_n|_1 \leq \frac{2}{\pi} \frac{a_0}{n^{k+1}} \int_0^{\tau_k} |f_\psi^{(k)}(\tau, \psi_0(\tau))| d\tau. \quad (2.47)$$

Analysis of the behavior of $\frac{\partial^k f}{\partial \psi^k}(\tau, \psi)$ and $\frac{\partial f}{\partial \psi}(\tau, \psi)$ shows that

$$\int_0^{\tau_k} |f_\psi^{(0)}(\tau, \psi_0(\tau))| d\tau \leq \frac{1}{4} |\ln(2R\alpha)|, \quad (2.48)$$

$$\int_0^{\tau_k} |f_\psi^{(2)}(\tau, \psi_0(\tau))| d\tau \leq \frac{\alpha R}{8}, \quad (2.49)$$

and $a_0 = 2$.

Evaluating the first and second sums in the Equality (2.40) with the aid of the Inequalities (2.18), (2.23), (2.27), (2.29), (2.36), we obtain the estimate for the relative error

$$d = \frac{|R(\tau, \psi)|}{|J_0(\tau, \psi)|}. \quad (2.50)$$

In the case when

$$k = \sqrt{(3 - \lambda x_1)(1 - \lambda)} > \frac{1}{\alpha R} \text{ and } \ln \alpha R k > 4$$

$$d \leq \frac{2H_*}{\pi R} \frac{\ln \alpha R k}{4kS(\psi)}, \quad (2.51)$$

where $H_* = R_1 - R$ and

/95

$$S(\psi) = \alpha \int_0^{H_*} e^{-T(h, \psi)} dh \cong \begin{cases} \cos \psi & 0 \leq \psi \leq \arccos \frac{H_*}{R}, \\ \frac{1}{\alpha R} & \psi = \frac{\pi}{2}, \\ \alpha \int_0^{H_*} e^{-[2\alpha(R+h)\cos(\pi-\psi)+T(h, \pi-\psi)]} dh & \psi > \frac{\pi}{2}, \end{cases} \quad (2.52)$$

and in the case when $0 \leq k \leq \frac{1}{\alpha R}$ and $\ln \left((\ln 2) \frac{\alpha R}{H_*} \right) > 4$,

$$d \leq \frac{2H_*}{\pi R} \frac{\ln \left[\frac{2\alpha R^2}{H_*} \ln 2 \right]}{2S(\psi)}. \quad (2.53)$$

The Formulas (2.17) and (2.37) obtained above for the average intensity, and the Estimates (2.51), (2.53) permit refining the theory presented in [1.2], and at the same time permit simplifying its numerical realization. For example, setting $k=0.1$; $\alpha=1$; $R=6000$ km; $H_*=10$ km, we obtain from the Inequality (2.53) for $0^\circ \leq \psi \leq 89^\circ$, the relative error

$$d \leq \frac{1}{90 \cos \psi}. \quad (2.54)$$

Assuming that k satisfied the Inequality (2.23), we find from the Inequality (2.53) that for $0^\circ \leq \psi \leq 89^\circ$,

$$d \leq \frac{1}{120 \cos \psi}. \quad (2.55)$$

It follows from the Inequalities (2.54 - 2.55) that in the interval $0^\circ \leq \psi \leq 89^\circ$, the solution of the problem (2.17) can be replaced with good accuracy by an expression (2.38) of simpler form, which can be transformed as follows:

$$\begin{aligned} J(\tau, \psi) = & \frac{S}{W_0} \left\{ a_{1,0} \left[a_{2,0} \frac{\text{sh } k\tau}{k} + \exp(-k\tau) \right] \frac{\lambda x_1}{4} \cos \psi - \frac{\lambda S}{4} \times \right. \\ & \times [3 + (1-\lambda)x_1] \left[\left(a_{2,0} \frac{\text{sh } k\tau}{k} + \exp(-k\tau) \right) (a_{1,0} S_0(0, \tau) + S_1(0, \tau)) + \right. \\ & + \left(a_{1,0} \exp(-k\tau) + \frac{\text{sh } k\tau}{k} \right) (a_{2,0} S_1(\tau, \tau_0) + S_0(\tau, \tau_0)) \left. \right] - \\ & \left. - \left(a_{2,0} \frac{\text{sh } k\tau_0}{k} + \exp(-k\tau_0) \right) \left(a_{1,0} \exp(-k\tau) + \frac{\text{sh } k\tau}{k} \right) \varphi_2(\tau_0, \psi) \right\}, \end{aligned}$$

$$S_0(\tau_1, \tau_2) = \int_{\tau_1}^{\tau_2} e^{-k\tau} e^{-\tau \sec \psi} d\tau = (e^{-\tau_1(k+\sec \psi)} - e^{-\tau_2(k+\sec \psi)}) / (k + \sec \psi);$$

$$S_1(\tau_1, \tau_2) = \int_{\tau_1}^{\tau_2} \frac{\operatorname{sh} k\tau}{k} e^{-\tau \sec \psi} d\tau = [(e^{-\tau_1(\sec \psi - k)} - e^{-\tau_2(\sec \psi - k)}) \times \\ \times (\sec \psi - k)^{-1} - (e^{-\tau_1(\sec \psi + k)} - e^{-\tau_2(\sec \psi + k)}) (\sec \psi + k)^{-1}] \cdot 2k;$$

for $k = 0$, $J_0(\tau, \psi)$ is obtained from (2.38) by passage to the limit, which leads to replacement of $\frac{\operatorname{sh} k\tau}{k}$ by τ , $\exp(-k\tau)$ by 1, $\operatorname{ch} k\tau$ by 1, and $S_1(\tau_1, \tau_2)$ by

$$S_1(\tau_1, \tau_2) = \frac{\tau_1 e^{-\tau_1 \sec \psi} - \tau_2 e^{-\tau_2 \sec \psi}}{\sec \psi} + \frac{i}{\sec \psi} S_{1-1}(\tau_1, \tau_2).$$

In the range $80^\circ \leq \psi \leq 89^\circ$, the error of $J_0(\tau, \psi)$ increases correspondingly from 10 to 100%.

3. Spherical Multilayer Atmospheric Model

In the preceding sections, we obtained the approximate formulas for the average intensity in the cases of nonhomogeneous atmosphere with exponential variation of the attenuation coefficient and homogeneous atmosphere with account for the true absorption. Now let us examine the model of a spherical multilayer atmosphere.

As noted previously, in this model each i^{th} layer is represented by the parameters $\tau_{0,i}$, $X_i(\gamma)$, $\alpha_i(h)$, λ .

It is well known [1] that to find $J(r, \theta, \psi, \varphi)$, it is sufficient to determine the average intensity $J(\tau, \psi)$ and its derivatives $J_\tau(\tau, \psi)$ and $J_\psi(\tau, \psi)$. Therefore, the problem reduces to finding the equations defining $J(\tau, \psi)$ and solving these equations.

It is interesting to examine two possible models, in one of which there is a thin gaseous layer above, and we can consider forward scattering to be single only, neglecting scattering of higher orders; in the second model, a gaseous or cloud layer of sensible optical

thickness begins above. Mathematically, the two cases can be described as follows:

$$2(3-x_1) \frac{1-A_1}{1+A_1} \tau_{01} \leq 1, \quad (3.1)$$

$$2(3-x_1) \frac{1-A_1}{1+A_1} \tau_{01} \geq 1. \quad (3.2)$$

Assume the Inequality (3.1) is satisfied, then as noted previously we consider single forward scattering

/97

$$I_F(\tau, \psi, \theta, \varphi) = \begin{cases} \text{for } \psi \neq \theta \frac{S}{4} \frac{e^{-\tau b(\psi)} - e^{-\tau b(\theta)}}{b(\theta) - b(\psi)} X(\gamma) b(\theta), \\ \text{for } \psi = \theta \frac{S}{4} T e^{-\tau} X(\gamma) + \pi S \cos \psi e^{-\tau}, \end{cases} \quad (3.3)$$

where γ is the angle between the direction of the (solar) radiation incident on the given volume and the direction of the radiation scattered by this volume.

We denote

$$I_1(\tau, \psi) = \frac{1}{2\pi} \int_0^{2\pi} d\varphi \int_{\frac{\pi}{2}}^{\pi} I_F(\tau, \psi, \theta, \varphi) \sin \theta d\theta, \quad (3.4)$$

$$A(\tau_{01}, \psi) = \frac{E_b(\tau_{01}, \psi)}{E_{1,F}(\tau_{01}, \psi)}, \quad (3.5)$$

where $E_{1,F}$ is the forward light flux, opposite the direction of the radius vector to the point (τ_{01}, ψ) , referred to the elementary area, $E_{1,b}$ is the backward light flux (along the direction of the radius vector).

Using the well-known Eddington relation, we can rewrite (3.5), on the one hand, in the form

$$A(\tau_{01}, \psi) = \frac{I_2(\tau_{01}, \psi)}{I_1(\tau_{01}, \psi) + S e^{-\tau_{01} b(\psi)} \cos \psi}, \quad (3.6)$$

where I_2 is the averaged intensity of the backward scattered radiation; on the other hand

$$A(\tau_{01}, \psi) = \frac{E_b(\tau_{01}, \psi)}{E_{1,F}(\tau_{01}, \psi)} = \frac{E_{1,F}(\tau_{01}, \psi) - E_n(\tau_{01}, \psi)}{E_{1,F}(\tau_{01}, \psi)}. \quad (3.7)$$

Here, $E_n(\tau_{0,1}, \psi)$ is the light flux absorbed by the subsequent layers, calculated from the formula

$$E_n(\tau_{0,1}, \psi) = (1 - A(\tau_{0,1}, \psi)) E_{\bar{F}}(\tau_{0,2}, \psi) + E_{ta}(\tau_{0,2}, \psi), \quad (3.8)$$

$E_{ta}(\tau_{0,2}, \psi)$ is the light flux absorbed within the second layer in the presence of the true absorption ($\lambda \neq 1$),

$$E_{ta}(\tau_{0,2}, \psi) = E_F(\tau_{0,2}, \psi)_\lambda - E_{\bar{F}}(\tau_{0,2}, \psi)_\lambda. \quad (3.9) \quad /98$$

$E_F(\tau_{0,2}, \psi)$ is expressed in terms of $J(\tau_{0,2}, \psi)$ as follows:

$$\begin{aligned} E_F(\tau_{0,2}, \psi)_\lambda &= \pi (I_1(\tau_{0,2}, \psi)_\lambda + S e^{-\tau_{0,2} b(\psi)} \cos \psi) = \\ &= \pi \frac{2J(\tau_{0,2}, \psi)_\lambda + S e^{-\tau_{0,2} b(\psi)} \cos \psi}{1 + A(\tau_{0,2}, \psi)}. \end{aligned} \quad (3.10)$$

Then

$$E_{ta}(\tau_{0,2}, \psi) = \frac{2\pi (J(\tau_{0,2}, \psi)_\lambda - J(\tau_{0,1}, \psi)_\lambda)}{1 + A(\tau_{0,2}, \psi)} \text{ for } \lambda = 1 \quad E_{ta}(\tau_{0,2}, \psi) = 0. \quad (3.11)$$

By virtue of (3.8), (3.10), (3.11), the Expression (3.7) takes the form

$$\begin{aligned} A(\tau_{0,i}, \psi) &= 1 - \frac{(1 + A(\tau_{0,i}, \psi)) [(2J(\tau_{0,i+1}, \psi) + S e^{-\tau_{0,i+1} b(\psi)} \cos \psi) \times \\ &\times (1 - A(\tau_{0,i}, \psi)) + 2(J(\tau_{0,i+1}, \psi)_1 - J(\tau_{0,i+1}, \psi)_\lambda)]}{(2J(\tau_{0,i}, \psi) + S e^{-\tau_{0,i} b(\psi)} \cos \psi) (1 + A(\tau_{0,i}, \psi))} \times \\ &\times (i = 1, \dots, n-1, A_n = A_{\text{sur}}). \end{aligned} \quad (3.12)$$

Here, $J(\tau_{0,i+1}, \psi)$ is defined in terms of $J(\tau_{0,i}, \psi)$ and the boundary conditions for $\tau = \tau_{0,i+1}$, i.e., in terms of the solution of the boundary value problem for the Equations (1.1) or (2.1). Thus, for $i = 1$

$$\begin{aligned} J(\tau, \psi)|_{\tau=\tau_{0,1}} &= J(\tau_{0,1}, \psi) = \frac{1}{2} (I_1(\tau_{0,1}, \psi) + I_2(\tau_{0,1}, \psi)) = \\ &= \frac{1}{2} [I_1(\tau_{0,1}, \psi) (1 + A(\tau_{0,1}, \psi)) + A(\tau_{0,1}, \psi) S e^{-\tau_{0,1} b(\psi)} \cos \psi] \end{aligned} \quad (3.13)$$

and

$$\begin{aligned} \frac{\partial J}{\partial \tau} + \frac{3-\lambda x_{1,2}}{2} \frac{1-A(\tau, \psi)}{1+A(\tau, \psi)} J \Big|_{\tau=\tau_{0,2}} &= \\ &= e^{-\tau(\tau_{0,2}, \psi)} \cos \psi \left(\frac{x_{1,2}}{4} + \frac{A(\tau_{0,2}, \psi)}{1+A(\tau_{0,2}, \psi)} \frac{3-\lambda x_{1,2}}{2} \right) = \varphi_2(\tau_{0,2}, \psi). \end{aligned} \quad (3.14)$$

Solving in place of (1.1) the Equation (1.45), or in place of (2.1) the Equation (2.39) with the same boundary conditions, we obtain the expression for $J(\tau_{0,i+1}, \psi)$ in terms of $J(\tau_{0,i}, \psi)$ in the form

$$J(\tau_{0,i+1}, \psi) = K_1(\tau_{0,i+1}) \left(J(\tau_{0,i}, \psi) - \int_0^{\tau_{0,i+1}-\tau_{0,i}} K_2(\tau) f(\tau) d\tau - K_2(\tau_{0,i+1}) \varphi_2(\tau_{0,i+1}, \psi) \right), \quad (3.15)$$

$$K_1(\tau_{0,i+1}) = \begin{cases} \frac{(1 + \operatorname{th}[k(\tau_{0,i+1} - \tau_{0,i})]) \exp[-k(\tau_{0,i+1} - \tau_{0,i})]}{1 + \frac{(3 - \lambda x_1)(1 - A(\tau_{0,i+1}, \psi)) \operatorname{sh}[k(\tau_{0,i+1} - \tau_{0,i})]}{2 \operatorname{ch}[k(\tau_{0,i+1} - \tau_{0,i})] (1 + A(\tau_{0,i+1}, \psi)) k}} & \text{for } \lambda \neq 1, \\ \frac{1}{1 + \frac{3 - x_1}{2} \frac{1 - A(\tau_{0,i+1}, \psi)}{1 + A(\tau_{0,i+1}, \psi)} (\tau_{0,i+1} - \tau_{0,i})} & \text{for } \lambda = 1. \end{cases} \quad (3.16) \quad /99$$

$$K_2(\tau_{0,i+1}) = \begin{cases} \frac{\operatorname{sh} k \tau_{0,i+1}}{k} & \text{for } \lambda \neq 1 \\ \tau_{0,i+1} & \text{for } \lambda = 1. \end{cases} \quad (3.17)$$

The corrections for the resulting approximation can be obtained using the estimation method presented in Sections 1 and 2.

The solution of (3.12) using (3.15) yields the expression for $A(\tau_{0,1}, \psi)$,

$$A(\tau_{0,1}, \psi) = \frac{1 - \frac{Q_1 \left(I_1(\tau_{0,1}) + 2 \int_0^{\tau_{0,2}-\tau_{0,1}} K_2(\tau) f(\tau) d\tau + 2K_2(\tau_{0,2}) \varphi_2(\tau_{0,2}, \psi) \right)}{Q_2}}{\frac{Se^{-\tau_{0,2}\psi} \cos \psi + I_1(\tau_{0,1}) (K_1(\tau_{0,2})_1 - K_1(\tau_{0,2})_\lambda) + \int_0^{\tau_{0,2}-\tau_{0,1}} (K_2(\tau)_1 - K_2(\tau)_\lambda) f(\tau) d\tau + (K_2(\tau_{0,2}) - K_2(\tau_{0,2})_\lambda) \varphi}{Q_2}} \quad (3.18)$$

where $Q_1 = K_1(\tau_{0,2}) \frac{1 - A(\tau_{0,2}, \psi)}{1 + A(\tau_{0,2}, \psi)}$, $Q_2 = I_1(\tau_{0,1}) + Se^{-\tau_{0,1}\psi} \cos \psi$, $Q_3 = 1 + Q_1 + K_1(\tau_{0,2})_1 - K_1(\tau_{0,2})_\lambda$.

Thus, we can calculate

$$J(\tau_{0,1}, \psi) = \frac{1}{2} [I_1(\tau_{0,1}, \psi) + A(\tau_{0,1}, \psi) (I_1(\tau_{0,1}, \psi) + S e^{-\tau_{0,1} K(\psi)} \cos \psi)]. \quad (3.19)$$

Making the change of variables $l = \tau_{0,1} - \tau$, we solve the following boundary value problem for $J(\tau_1, \psi)$ in the upper layer:

/100

$$\frac{\partial^2 J}{\partial l^2} = -f(l, \psi), \quad (3.20)$$

$$\frac{\partial J}{\partial l} + \frac{3 - x_1}{2} J \Big|_{l=\tau_{0,1}} = \frac{x_1 S}{4} \cos \psi, \quad (3.21)$$

$$J(l, \psi) \Big|_{l=0} = J(\tau_{0,1}, \psi). \quad (3.22)$$

The solution of this problem has the form

$$\begin{aligned} J(l, \psi) = & (C_{2,0} l + 1) J(0, \psi) + (C_{2,0} l + 1) \frac{3S}{4} \int_0^l t e^{-\tau(t, \psi)} dt + \\ & + \frac{3S}{4} l \int_0^{\tau_{0,1}} (C_{2,0} t + 1) e^{-\tau(t, \psi)} dt - \frac{S x_1}{L} \cos \psi l (C_{2,0} \tau_{0,1} + 1), \end{aligned} \quad (3.23)$$

where $C_{2,0} = -\frac{1.5}{1 + 1.5\tau_{0,1}}$ and the average intensity $I_2(\tau_{0,1}, \psi)$ of the outgoing radiation is

$$I_2(\tau_{0,1}, \psi) = \frac{2J(0, \psi)}{1 + \frac{3}{2}\tau_{0,1}} - \frac{\frac{3}{2}S}{1 + \frac{3}{2}\tau_{0,1}} \frac{1 - (1 + \tau_{0,1} \delta(\psi)) e^{-\tau_{0,1} K(\psi)}}{\delta^2(\psi)}. \quad (3.24)$$

Introducing the new unknown

$$y_l = [1 - A(\tau_{0,l}, \psi)] / [1 + A(\tau_{0,l}, \psi)], \quad (3.25)$$

we solve (3.12) for y_1

$$\begin{cases} y_l = \frac{a_l(y_{l+1}) + c_l(y_{l+1}) (M_l(y_{l-1}) + P_l y_l) + C_l(y_{l+1}) (1 + m_l y_l)}{M_l(y_{l-1}) + P_l y_l + d_l (1 + m_l y_l)} \\ y_n = y_{\text{sur}} \quad (l = 2, \dots, n-1), \end{cases} \quad (3.26)$$

where

$$\begin{aligned} M_l(y_{l-1}) = & \frac{1 + i h k(\tau_{0,l} - \tau_{0,l-1})}{e^{k(\tau_{0,l} - \tau_{0,l-1})}} \times \\ & \times \left(J(\tau_{0,l-1}, \psi) - \int_0^{\tau_{0,l} - \tau_{0,l-1}} K_2(\tau) f(\tau) d\tau + \frac{3S}{4} K_2(\tau_{0,l}) e \cos \psi^{-\tau_{0,l} K(\psi)} \right), \end{aligned} \quad (3.27) \quad /101$$

$$J(\tau_{0,i-1}) = \frac{M_{i-1}(y_{i-2}) + P_{i-1}y_{i-1}}{1 + m_{i-1}y_{i-1}} \quad (i = 3, \dots, n-1) \quad (3.28)$$

and $J(\tau_{0,i}, \psi)$ is defined by (3.19).

$$a_i(y_{i+1}) = y_{i+1} \frac{1 + \operatorname{th} k(\tau_{0,i+1} - \tau_{0,i})}{e^{k(\tau_{0,i+1} - \tau_{0,i})} \left(1 + \frac{3 - \lambda x_1}{2} y_{i+1} \frac{\operatorname{th} k(\tau_{0,i+1} - \tau_{0,i})}{k} \right)}, \quad (3.29)$$

$$c_i(y_{i+1}) = K_1(\tau_{0,i+1})_i - K_1(\tau_{0,i+1})_\lambda = \frac{1}{1 + \frac{3 - x_1}{2} y_{i+1} (\tau_{0,i+1} - \tau_{0,i})} - \frac{1 + \operatorname{th} k(\tau_{0,i+1} - \tau_{0,i})}{e^{k(\tau_{0,i+1} - \tau_{0,i})} \left(1 + \frac{3 - \lambda x_1}{2} y_{i+1} \frac{\operatorname{th} k(\tau_{0,i+1} - \tau_{0,i})}{k} \right)}, \quad (3.30)$$

$$d_i = \frac{S}{2} e^{-\tau_{0,i+1} \psi(\psi)} \cos \psi \quad (3.31)$$

$$P_i = -K_2(\tau_{0,i}) \frac{1 + \operatorname{th} k(\tau_{0,i} - \tau_{0,i-1})}{e^{k(\tau_{0,i} - \tau_{0,i-1})}} \frac{S e^{-\tau_{0,i} \psi(\psi)} (3 - \lambda x_1) \cos \psi}{4}, \quad (3.32)$$

$$m_i = \begin{cases} \lambda \neq 1 & \frac{3 - \lambda x_1}{2} \frac{\operatorname{th} k(\tau_{0,i} - \tau_{0,i-1})}{k} \\ \lambda = 1 & \frac{3 - x_1}{2} (\tau_{0,i} - \tau_{0,i-1}) \end{cases} \quad (3.33)$$

$$c_i(y_{i+1}) = \left[- \int_0^{\tau_{0,i+1} - \tau_{0,i}} K_2(\tau) f(\tau) d\tau + K_2(\tau_{0,i+1}) \varphi_2(\tau_{0,i+1}, \psi) \right] \times \\ \times a_i(y_{i+1}) + \frac{S}{2} e^{-\tau_{0,i+1} \psi(\psi)} \cos \psi +$$

$$+ \int_0^{\tau_{0,i+1} - \tau_{0,i}} \left(K_2(\tau)_i \cdot \frac{1}{1 + \frac{3 - x_1}{2} y_{i+1} (\tau_{0,i+1} - \tau_{0,i})} - K_2(\tau)_\lambda \times \right. \\ \times \frac{1 + \operatorname{th} k(\tau_{0,i+1} - \tau_{0,i})}{\exp[k(\tau_{0,i+1} - \tau_{0,i})] \left(1 + \frac{3 - \lambda x_1}{2} y_{i+1} \frac{\operatorname{th} k(\tau_{0,i+1} - \tau_{0,i})}{k} \right)} \Big) \times \\ \times f(\tau) d\tau + \left(K_2(\tau_{0,i+1})_\lambda \frac{1}{1 + \frac{3 - x_1}{2} y_{i+1} (\tau_{0,i+1} - \tau_{0,i})} - \right. \\ \left. - K_2(\tau_{0,i+1})_\lambda \frac{1 + \operatorname{th} k(\tau_{0,i+1} - \tau_{0,i})}{e^{k(\tau_{0,i+1} - \tau_{0,i})} \left(1 + \frac{3 - \lambda x_1}{2} y_{i+1} \frac{\operatorname{th} k(\tau_{0,i+1} - \tau_{0,i})}{k} \right)} \right) \times \\ \times \varphi_2(\tau_{0,i+1}, \psi). \quad (3.34)$$

/102

REPRODUCIBILITY OF THE
ORIGINAL PAGE IS POOR

In the general case, it is quite difficult to solve (3.26) purely analytically; however, for $n = 3$ the system becomes essentially a second-degree equation whose solution, when discarding the extraneous root, is represented in the form

$$y_2 = - \frac{M_2 + d_2 - (a_2 + l_2) P_2 - c_2 m_2 + \sqrt{(M_2 + d_2 - (a_2 + l_2) P_2 - c_2 m_2)^2 + 4(d_2 m_2 + P_2)((a_2 + l_2) M_2 + C_2)}}{2(d_2 m_2 + P_2)} \quad (3.35)$$

In the case when

$$M_2 + d_2 - (a_2 + l_2) P_2 - c_2 m_2 \gg 4(d_2 m_2 + P_2)((a_2 + l_2) M_2 + C_2), \quad (3.36)$$

which is possible for $\tau_{0.2} \gg 0.8$, we can use the formula

$$y_2 = \frac{(a_2 + l_2) M_2 + C_2}{M_2 + d_2 - (a_2 + l_2) P_2 - c_2 m_2}. \quad (3.37)$$

For $\tau_{0.2} \gg 3$, this formula yields

$$y_2 = a_2 (y_{\text{sur}}) + l_2 (y_{\text{sur}}) \quad (3.38)$$

Thus, substituting y_2 into (3.25), we obtain the value of $A_2(\tau_{0.2}, \psi)$. The System (3.25) is also easily solved when $n > 3$ and $\tau_{0.2} \gg 3$. In this case, the System (3.25) can be replaced with a high degree of accuracy by a recurrent system of the type

$$y_i = a_i(y_{i+1}) + l_i(y_{i+1}), \quad (3.39)$$

$$y_n = y_{\text{sur}} \quad i = 2, \dots, n-1,$$

whose solution is obtained by sequential substitution of $y_n = y_{\text{sur}}$ into the equation for $y_{n-1}, y_{n-2}, y_{n-3}$ and up to $i = 2$. Substituting y_1 into (3.25), we obtain the value for $A(\tau_{0.2})$.

Now let (3.2) be satisfied; then we can no longer restrict ourselves to only single forward scattering. Therefore, in order to find $I(\tau, \psi)$ in the upper layer, it is necessary to solve the boundary value problem (1.1), (1.2), (1.3) or (2.6), (2.7), (2.8). In this case, the determination of $A(\tau_{0.2}, \psi)$ is accomplished in the same way, using the System (3.26) and the Formula (3.25) with the sole difference that the system includes the equation for $i = 1$, and the

following expressions for M_1 , P_1 , m_1 are valid*:

$$P_1 = \begin{cases} \frac{(3-x_1) Se^{-\tau_{0,1} \delta(\psi)} \cos \psi (a_{1,0} + \tau_{0,1})}{4} & \text{for } \lambda = 1, \\ \frac{(3-\lambda x_1) Se^{-\tau_{0,1} \delta(\psi)} \cos \psi \left(a_{1,0} e^{-k\tau_{0,1}} + \frac{\text{sh } k\tau_{0,1}}{k} \right)}{4} \frac{1 + \text{th } k\tau_{0,1}}{e^{-k\tau_{0,1}}} & \text{for } \lambda \neq 1; \end{cases} \quad (3.40)$$

$$m_1 = \begin{cases} \frac{3-x_1}{2} \tau_{0,1} + 1 & \text{for } \lambda = 1, \\ \frac{3-\lambda x_1}{2} \left(\frac{\text{th } k\tau_{0,1}}{k} + \frac{e^{-k\tau_{0,1}}}{\left(\frac{3-\lambda x_1}{2} + k \right) \text{ch } k\tau_{0,1}} \right) & \text{for } \lambda \neq 1. \end{cases} \quad (3.41)$$

$$M_1 = \frac{1 + \text{th } k\tau_{0,1}}{e^{k\tau_{0,1}}} \left[\left(a_{1,0} e^{-k\tau_{0,1}} - \frac{\text{sh } k\tau_{0,1}}{k} \right) \frac{x_1 S}{4} \cos \psi + \right. \\ \left. + \int_0^{\tau_{0,1}} \left(a_{1,0} e^{-k\tau} + \frac{\text{sh } k\tau}{k} \right) f(\tau) d\tau - \left(a_{1,0} e^{-k\tau_{0,1}} + \frac{\text{sh } k\tau_{0,1}}{k} \right) \times \right. \\ \left. \times \left(\frac{Se^{-\tau_{0,1} \delta(\psi)} \lambda x_1}{4} \cos \psi + \frac{Se^{-\tau_{0,1} \delta(\psi)} (3-\lambda x_1) \cos \psi}{4} \right) \right] \times \\ \times \frac{1}{\left(\frac{3-\lambda x_1}{2} + k \right) \text{ch } k\tau_{0,1} e^{k\tau_{0,1}} - 1}. \quad (3.42)$$

After finding all the $A(\tau_{0i}, \psi)$, we can calculate $J(\tau, \psi)$ beginning with the first layer through the entire depth of the atmosphere. For the first layer in the case of Inequality (3.1), $J(\tau, \psi)$ is calculated using (3.23), and in the case of Inequality (3.2) — using (1.72), (2.38). For the succeeding layers, we solve problems of the type (3.13), (3.14), for (1.45) or (2.39) we obtain the solution in the form (3.15). To evaluate the error of the resulting values of $J(\tau, \psi)$ we determine the corrections with the aid of the Inequalities

* Actually, to obtain the solution of (3.26) analytically, condition $\tau_{0,3} \gg 3$ is satisfied and condition $\tau_{0,2} \gg$ when (3.2) is satisfied. For this case, the System (3.26) with $n = 2$ (two-layer model) becomes a quadratic equation, and its solution is described in a form analogous to (3.35).

(1.68), (1.70), (2.51), (2.53). Then using the formulas presented in [1], with the aid of J , J_ψ , J_τ , we calculate the angular and spatial intensity distributions $I(\theta, \varphi, \psi, r)$.

Conclusion

Let us examine the three-layer spherical atmospheric model when the upper layer is a quite thin gaseous shell with ($\tau_{01} \leq 0.03$), the second layer consists of dense cloud formations $\Delta\tau_{cl} = \tau_{02} - \tau_{01} \geq 6$, $\lambda_2 = 1$, the third layer consists of a gas with $\lambda_3 = 1$ and optical thickness of the layer $\tau_{03} - \tau_{02} > 1$.

It follows from (3.18) that the light flux E_{out} leaving the planetary atmosphere along the direction of the radius vector is found from the formula

$$E_{out} = \pi S \cos \psi \left[1 - \frac{1}{2} (1 - A_{sph}) \left(1 + \frac{3}{2} \cos \psi \right) \right]. \quad (3.43)$$

The albedo A_g of the gaseous sublayer is found from the formula, which follows from (3.38),

$$A_g = A_s = 1 - \frac{1}{\frac{3}{4} \Delta\tau_r + \frac{1}{1 - A_{sur}}}. \quad (3.44)$$

The formula for the cloud layer optical thickness, derived with the aid of (3.10), (3.15), (3.18), has the form

$$\Delta\tau_{cl} = \frac{4}{3 - A_{cl}} \left[\frac{1}{1 - A_{sp}} - \frac{1}{1 - A_r} \right], \quad (3.45)$$

where A_{sp} is the spherical albedo, and is found from the results of planetary observations.

The light flux beneath the clouds is calculated using the following formula, also derived with the aid of (3.10), (3.15), (3.18),

$$E_{\text{bel cl}} = \frac{1}{2} \pi S \cos \psi \left(1 + \frac{3}{2} \cos \psi \right) \frac{1 - A_{\text{sp}}}{1 - A_g}. \quad (3.46)$$

It follows from (3.10) that the average intensity $J_{\text{bel cl}}$ below the clouds is

$$J_{\text{bel cl}} = \frac{1}{\pi} \frac{1 + A_r}{2} E_{\text{bel cl}}(\psi). \quad (3.47)$$

Hence, using (3.15) and (3.10), we obtain the planetary surface illumination level $E_{\text{to pl sur}}$

$$E_{\text{to pl sur}}(\psi) = \frac{(1 + A_g) E_{\text{bel cl}}(\psi) \frac{1}{1 + \frac{3 - x_{\text{tr}}}{2} \frac{1 - A_{\text{sur}}}{1 + A_{\text{sur}} \Delta \tau_g}}}{1 + A_n} \quad (3.48)$$

and the light flux from the planet in the direction of the radius vector

$$E_{\text{fr pl sur}}(\psi) = A_{\text{sur}} E_{\text{to sur}}(\psi). \quad (3.49)$$

The possibility of using this model in the visible part of the spectrum for the Venus atmosphere is justified in [9]. A calculation is also made of the optical thickness $\Delta \tau_g = \tau_{03} - \tau_{02}$ of the gaseous sublayer for various wavelengths. In this connection, it is interesting to calculate on the basis of planetary observations the light flux leaving the Venus atmosphere by radiation $E_{\text{out}}(\psi)$ as a function of the Sun angle ψ , the light flux $E_{\text{bel cl}}(\psi)$ beneath the clouds in the direction opposite the radius vector, the illumination level $E_{\text{to pl sur}}$ at the surface of the planet, the light flux $E_{\text{fr pl sur}}(\psi)$ from the planet, and the optical thickness $\Delta \tau_{\text{cl}}$ of the cloud formations.

References

1. Sobolev, V. V. and I. N. Minin. Scattering of Light in a Spherical Atmosphere. Collection: *Iskusstvennyye sputniki zemli* (Artificial Earth Satellites), No. 15. Izdatel'stvo AN SSSR, 1962.
2. Sobolev, V. V. and I. N. Minin. Scattering of Light in a Spherical Atmosphere. Collection: *Kosmicheskiye issledovaniya*, Vol. 1, No. 2. Nauka Press, Moscow, 1969.
3. Sobolev, V. V. and I. N. Minin. Scattering of Light in a Spherical Atmosphere. Collection: *Kosmicheskiye issledovaniya*, Vol. 2, No. 4. Nauka Press, Moscow, 1964.
4. Smoktiy, O. I. Determining the Brightness of a Uniform Spherical Symmetric Planetary Atmosphere. *Izvestiya AN SSSR, Fizika atmosfery i okeana*, Vol. 3, No. 3, 1967.
5. Smoktiy, O. I. Determining the Brightness of a Nonuniform Spherical Symmetric Planetary Atmosphere. *Izv. AN SSSR, Fizika atmosfery i okeana*, Vol. 3, No. 4, 1967.
6. Sobolev, S. L. *Uravneniya matematicheskoy fiziki* (Equations of Mathematical Physics). Nauka Press, Moscow, 1966.
7. Petrovskiy, I. G. *Lektsii po uravneniyam s chastnymi proizvodnymi* (Partial Differential Equations). Gostekhizdat, 1963.
8. Fikhtengol'ts, G. M. *Kurs differentsial'nogo i integral'nogo ischisleniya* (Differential and Integral Calculus), Vol. 3. Nauka Press, Moscow, 1969.
9. Biryukov, Yu. L., A. S. Panfilov, and L. G. Titarchuk. Estimates of the Optical Characteristics of the Venus Atmosphere with Application to the Problem of Photographing its Clouds and Surface. In present collection.

ESTIMATES OF THE VENUS ATMOSPHERE OPTICAL CHARACTERISTICS
WITH APPLICATION TO THE PROBLEM OF PHOTOGRAPHING
ITS CLOUDS AND SURFACE

Yu. L. Biryukov, A. S. Fanfilov, and
L. G. Titarchuk

Estimate of cloud layer albedo and cloud cover optical thick- /106
ness. We shall use the dependence of the pressure P , temperature T , and density ρ on the height h from [1, 2], and also the dependence of the Venusian spherical albedo A_{sph} on wavelength λ (curve 1 in Figure 1) obtained by Irvine from Earth observations [3].

We calculate the spherical albedo wavelength dependence $A_{\text{sph}}(\lambda)$ under the assumption of absence of any aerosol component. For this, we use the expression for the light flux leaving the atmosphere $E_{\text{out}}(\psi)$ [4]:

$$E_{\text{out}}(\psi) = \pi S_{\lambda} \cos \psi \left(1 - \frac{3}{2} k_1 \cos \psi \right) / (1 + k_1), \quad (1)$$

where

$$k_1 = \frac{1}{(1+A)/(1-A) + 3/4 \Delta \tau_{g,\lambda}^0};$$

ψ is the Sun's zenith distance; A is the albedo of the planet surface; $\Delta \tau_{g,\lambda}^0$ is the total optical thickness of the atmosphere for Rayleigh molecular scattering; πS_{λ} is the spectral solar constant for the planet. The corollary of (1) is the formula for $A_{\text{sph}}(\lambda)$

$$A_{\text{sph}}(\lambda) = 1 - \left(\frac{1}{(1-A)} + \frac{3}{4} \Delta \tau_{g,\lambda}^0 \right) - 1. \quad (2)$$

Let us determine the basic data necessary for calculating $A_{\text{sph}}(\lambda)$. At the present time, no data are available on the Venus surface albedo in the visible and IR parts of the spectrum;

Therefore, for the analysis we shall use the known data on the albedo of terrestrial and lunar rocks. Following [5], [6], we take $A_{\max} = 0.4$; $A_{\min} = 0.02$; $\bar{A} = 0.2$.

By definition,

$$\Delta\tau_{g,\lambda}^0 = \int_0^H \sigma_\lambda(h) dh, \quad (3)$$

where h is the height; H is the height of the upper edge of the $\sigma_\lambda(h)$ is the Rayleigh scattering coefficient; $\Delta\tau_{g,\lambda}^0$ is expressed in terms of the scale height H_*

/107

$$\Delta\tau_{g,\lambda}^0 = \sigma_\lambda H_*, \quad (4)$$

where

$$\sigma_\lambda = 32\pi^3(n-1)^2/(3N'\lambda^4),$$

where n is the coefficient of refraction of the medium; N' is the number of scattering particles per unit volume, equal to $N' = (N\rho)/\mu$; $N = 6.023 \cdot 10^{23}$ is the Avogadro number; ρ is the density of the gas; μ is the molecular weight of the gas.

The refractivity n of the medium as a function of T and P is

$$n = 1 + \beta \frac{P}{T}. \quad (5)$$

For the Venusian atmosphere the constant $\beta = 0.13$ deg/atm.

The scale height is found from the formula $H_* = (kT)/\mu g$, where $k = 1.38 \cdot 10^{-16}$ erg/deg is the Boltzmann constant; g is the gravity force acceleration. As a result, we obtain the following expression for $\Delta\tau_{g,\lambda}^0$

$$\Delta\tau_{g,\lambda}^0 = \frac{32\pi^3(\beta P)^2 k}{3N\rho\lambda^4 g T}. \quad (6)$$

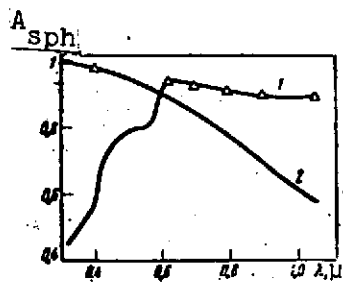


Figure 1. Spherical albedo A_{sph} of Venus vs. wavelength

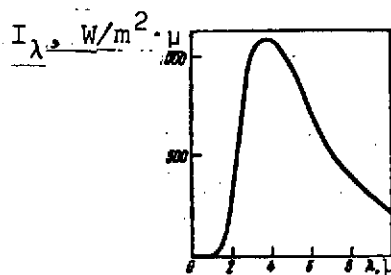


Figure 2. Self-radiation of planet surface vs. wavelength

In calculating $\Delta\tau_{g,\lambda}^0$, we assumed that the Venusian atmosphere consists entirely of carbon dioxide, and the atmospheric parameters were taken from [2].

Taking the surface albedo $\bar{A} = 0.2$ and using (6), we obtain from (2) the values of $\bar{A}_{sph}(\lambda)$. The results of $\Delta\tau_{g,\lambda}^0$ and $\bar{A}_{sph}(\lambda)$ calculations are shown, respectively, in Table 1 and as curve 2 in Figure 1. We see from the figure that significant absorption is possible in the wavelength region shorter than 0.6 microns.

/108

TABLE 1. SPHERICAL ALBEDO AND RAYLEIGH OPTICAL THICKNESS*

λ, μ	$\Delta\tau_{g\lambda}^0$	\bar{A}_{sph}	A_{sph}	λ, μ	$\Delta\tau_{g\lambda}^0$	\bar{A}_{sph}	A_{sph}
0,300	212,0	0,994	0,994	0,700	7,06	0,85	0,923
0,400	67,0	0,980	0,932	0,800	4,15	0,770	0,903
0,500	27,4	0,954	0,965	0,900	2,59	0,686	0,895
0,628	11,2	0,895	0,938	1,06	1,4	0,560	0,886

* Commas represent decimal points.

Observations of Venus from the Earth indicate the existence of dark details in the upper layers of its atmosphere which are noted only when using light filters which do not pass radiation longer

than 0.6 microns. This is additional indirect confirmation of the existence of absorption in the shortwave region.

In the wavelength region longer than 0.6 microns, the observed spherical albedo is higher than the pure gaseous value. If we assume the scattering of light in the wavelength region longer than 0.6 microns to be conservative, then we can evaluate the albedo of the cloud layer which leads to excess of the observed spherical albedo above the purely gaseous value. On the basis of [4], we have the following expression for calculating the cloud layer albedo:

$$A_{cl} = 1 - \left(\frac{1}{1 - A_{sph}} - \frac{3}{4} \Delta\tau_{g,\lambda}^0 - \frac{1}{1 - A} \right)^{-1} \quad (7)$$

The calculation of A_{cl} using (7) with underlying albedo surface $A = 0 - 0.4$ shows that the former is practically constant over the entire wavelength range from 0.62 to 1.06 microns, and equal to 0.87 - 0.88. This value is the lower estimate of the cloud layer albedo, since we assumed no noticeable absorption. Assuming that the constancy of the cloud layer albedo as a function of wavelength is determined by the large size of the particles constituting the cloud, on the basis of [4] we can calculate the cloud layer optical thickness $\Delta\tau_{cl}$. These calculations lead to a value on the order of 60. On the other hand, assuming A_{cl} constant and equal to 0.87 and $A = 0.2$, we can calculate the spherical albedo for different wavelengths

$$A_{sp,\lambda} = 1 - \left[\frac{3}{4} \Delta\tau_{g,\lambda}^0 + \frac{1}{1 - A_{cl}} + \frac{A}{1 - A} \right]^{-1}$$

The calculation data, shown by the triangles in Figure 1, for $\lambda > 0.6 \mu$ agree well with the experimental values (curve 1). The cloud optical thickness value $\Delta\tau_{cl} \approx 60$ also agrees well with the estimates presented in [8] for the model with minimum H_2O concentration.

/109

Estimate of planetary surface self-radiation influence. We shall calculate the self-radiation of the planet surface in the wavelength region examined above in order to determine the longwave limit of the imaging spectral band. The absolute energy distribution obtained from the formula $I_\lambda = \epsilon_\lambda B_\lambda (T_n)$, where I_λ is the monochromatic intensity; ϵ_λ is the radiation coefficient; $B_\lambda (T_n)$ is the radiation intensity of a blackbody with temperature T_n .

Assuming the Venus surface to be a blackbody, i.e., $\epsilon_\lambda = 1$, and writing $B_\lambda (T_n)$ in accordance with the Planck law, we obtain

$$I_\lambda = (C_1 \lambda^{-5}) / (e^{C_2 / \lambda T_n} - 1), \quad (8)$$

where $C_1 = 1.18 \cdot 10^8 \text{ W} \cdot \text{ster}^{-1} \cdot \text{m}^{-2} \cdot \mu^4$; $C_2 = 14,350 \mu \cdot \text{deg}$; $T_n = 768^\circ \text{ K}$. The results of the planet surface self-radiation calculation using (8) are shown in Figure 2. The maximum monochromatic intensity corresponds to the wavelength λ_{\max} , which is determined from the Wien displacement law $\lambda_{\max} T_n = 2880 \mu \cdot \text{deg}$; hence, $\lambda_{\max} = 3.75 \mu$.

Thus, if we select the longwave limit of the imaging spectral range equal to one micron, the planet surface background self-radiation will be practically eliminated. We have noted above that the experimental data indicate the possibility of significant radiation absorption in the Venus atmosphere for $\lambda < 0.6 \mu$. Therefore, in the following calculations, we consider the spectral region $0.6 - 1 \mu$.

Estimate of light flux distribution as function of atmospheric height. Since the values obtained for the wavelength dependence of cloud layer albedo and optical thickness are quite realistic, there is no basis to assume significant absorption in the subject range, at least not in the upper layers of the atmosphere. In order to obtain in the absence of absorption the lower estimate of the illumination below some level above the planet surface, it is necessary

to assume that the main mass of the aerosol component is located above this level. For the specific calculations, we took as an example the level corresponding to a pressure of 0.56 atm, located at a height of 57 km above the surface of the planet [2].

The formula for the light flux incident from the upper hemisphere on an elementary area perpendicular to the radius vector at a given point (ψ , h) has the form

/110

$$E_{in}(h, \psi) = \frac{1}{2} \pi S_{\lambda} \cos \psi \left(1 + \frac{3}{2} \cos \psi \right) \frac{1 - A_{sph, \lambda}}{1 - A_{g, \lambda}(h)}, \quad (9)$$

and the expression for $A_{g, \lambda}(h)$ is found as follows:

$$A_{g, \lambda}(h) = 1 - \left[\frac{1}{1 - A} + \frac{3}{4} \Delta \tau_{g, \lambda}(h) \right]^{-1}, \quad (10)$$

where $\Delta \tau_{g, \lambda}(h)$ is the optical thickness of the layer of height measured from the surface of the planet. The values of $A_{sph, \lambda}$ are taken from the data of Irvine (curve 1 in Figure 1).

The calculations of illumination distribution as a function of height were made for four sun positions $\psi = 0^\circ, 30^\circ, 60^\circ, 89^\circ$ for $\lambda = 0.6 \mu; 0.7 \mu; 0.8 \mu; 0.9 \mu$ (Figure 3a - d). The integral brightness below the clouds ($h = 57$ km, $P = 0.56$ atm) in the wavelength range from 0.6 to 1.06 μ for $\psi = 0$ is on the order of 400 W/m².

These results depend on the accuracy of the determination of A_{sph} and $A_{g, \lambda}$. Change of the surface pressure by 15 - 20% has relatively little influence on the determination of $\Delta \tau_{cl}$ and the illumination below the clouds. However, increase of $A_{sph, \lambda}$ by 3% leads to doubling of $\Delta \tau_{cl}$ and, therefore, to two-fold reduction of the illumination below the clouds.

Upper estimate of the observed contrasts. Since the Venus cloud formations may have breaks, it is interesting from the viewpoint of photographic possibilities to estimate the contrasts which occur in this case. In order to obtain an upper estimate of such contrasts, we must also assume that the major portion of the aerosol component is in the upper parts of the atmosphere. However, if the clouds are stratified to a significant degree, the observed contrasts may be significantly lower.

Since for a gaseous layer the scattering indicatrix is nearly spherical, we can consider the edge of the gaseous layer to be an orthotropic surface. For simplicity, we take the edge of the cloud layer to be orthotropic. Then the contrasts, when viewing clouds from above, can be calculated from the formula [4]

$$K(\psi) = \left[\frac{1}{\frac{2}{1-A} + \frac{3}{2} A_{\text{g},\lambda}^0} - \frac{1}{2} (1 - A_{\text{sph},\lambda}) \right] / \left[\frac{1}{1 + \frac{3}{2} \cos \psi} - \frac{1}{2} (1 - A_{\text{sph},\lambda}) \right]. \quad (11)$$

TABLE 2. CONTRASTS WHEN VIEWING CLOUDS FROM ABOVE *

λ, μ	ψ°				
	0°	30°	60°	80°	89°
0,626	0,061	0,054	0,042	0,030	0,024
0,700	0,104	0,032	0,070	0,050	0,040
0,800	0,200	0,182	0,133	0,094	0,076
0,900	0,294	0,269	0,197	0,137	0,110

*Commas represent decimal points.

We see from Table 2 that the contrasts $K(\psi)$ above the clouds decrease with increase of ψ .

/111

The contrasts determined using (11) are an average of the contrasts observed for zenith angles ψ . The contrasts K will actually depend on ψ . Specifically, near the reflecting indicatrix peaks they will be higher than the contrasts shown in Table 2.

Estimates of surface optical parameters. The brightness characteristics of the surface in the selected spectral band ($0.6 - 1 \mu$) are determined by surface illumination and reflectivity. Since nothing is known of the Venus surface albedo wavelength dependence, we shall assume the reflected radiation spectrum to be analogous to the incoming radiation spectrum. The surface reflectivity is characterized by the brightness coefficient $\bar{r} = r_0 f(i, \epsilon, \phi)$, where r_0 is a constant which determines the absolute value of the reflectivity; $f(i, \epsilon, \phi)$ is a function defining the relative reflectivity change as a function of the angles of incidence, i reflection ϵ , and the difference ϕ of the azimuths of the incident and reflected rays.

Because of the large optical thickness of the Venus atmosphere, the illumination of its surface is accomplished entirely by scattered radiation. The radiation intensity at large optical depths is independent of azimuth, but is a function of the zenith distance θ [9];

$$I(\Delta\tau_{cl} + \Delta\tau_{g,\lambda}^0, \theta, \psi) = S\bar{\sigma}(\theta, \psi)\cos\psi. \quad (12)$$

The sky brightness coefficient $\bar{\sigma}(\theta, \psi)$ is written as

$$\bar{\sigma}(\theta, \psi) = \frac{\left(1 + \frac{3}{2}\cos\psi\right) \left[(1-A)\left(1 + \frac{3}{2}\cos\theta\right) + 2A\right]}{4 + (3 - \bar{X}_1)(\Delta\tau_{g,\lambda}^0 + \Delta\tau_{cl})(1-A)} \quad (13)$$

where \bar{X}_1 is the scattering indicatrix parameter averaged over the entire thickness of the atmosphere. Therefore, the surface brightness is independent of azimuth. For an orthotropic surface, the brightness coefficient \bar{r} is written in terms of the plane albedo A [5] $\bar{r} = r_0 = A/\pi$, and the surface brightness is defined in terms of its illumination $B = \bar{r}E = (A/\pi)E$. Since no data are available on absorption in the Venus atmosphere, we shall determine the upper illumination limit. In the pure scattering case, the surface illumination is determined by (9) for $A_{g,\lambda}$ equal to the surface albedo.

Figure 4a shows the dependence of the monochromatic surface

/113

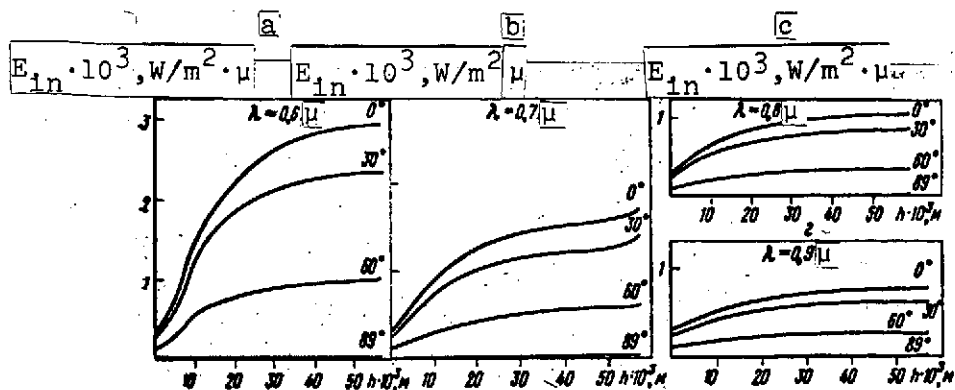


Figure 3. Illumination as function of altitude

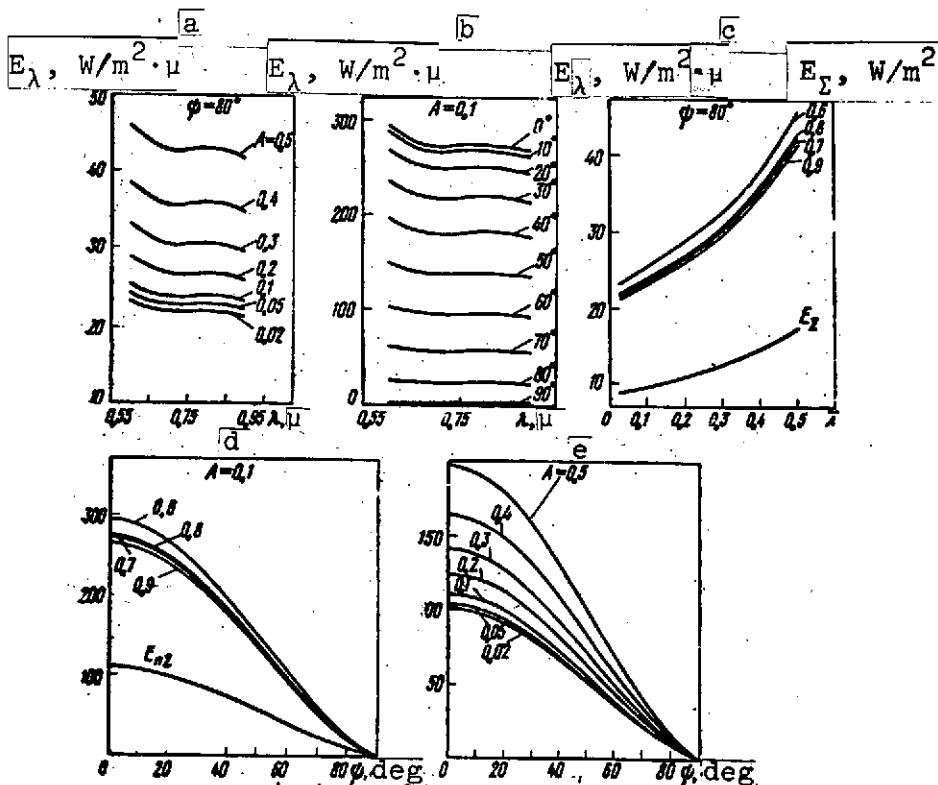


Figure 4. Monochromatic and integral illumination of planet surface

illumination E_λ as a function of wavelength for different values of the surface albedo A and the sun zenith distance $\psi = 80^\circ$. Figure 4b shows the analogous relation for various values of sun zenith distance ψ and the surface albedo $A = 0.1$. Figure 4c shows the

monochromatic illumination E_λ for various wavelengths and the integral illumination E_Σ versus the surface albedo A for the sun zenith distance $\psi = 80^\circ$. Figure 4d shows the same quantities as functions of sun zenith distance ψ for the surface albedo $A = 0.1$. Figure 4e shows the integral surface illumination ($E_{n\Sigma}$, W/m² for various surface albedo values.

Usually, in the case of directional illumination, the presence of surface irregularities leads to the appearance of shadows and, therefore, contrasts. Since direct solar radiation does not reach the surface of Venus and it is illuminated by scattered radiation, there are no shadows on its surface. However, contrasts may still exist because of surface irregularities. The reason for this is the fact that surfaces with different slopes are illuminated by radiation fluxes enclosed in different solid angles and arriving from different parts of the sky, which affects the spatial distribution of the brightness of these surfaces. Let us consider the case when the elementary areas are orthotropic. Then the expression for the contrast can be written as follows:

$$K = \frac{B_{\max} - B_{\min}}{B_{\max}} = \frac{E_{\max} - E_{\min}}{E_{\max}}.$$

Let us find the illumination of the elementary areas A, B, C (Figure 5a) in the immediate vicinity of their intersection. The illumination in the elementary area is written as

$$E = \int I \cos \vartheta d\omega,$$

where I is the radiation intensity and ω is the solid angle. In a polar coordinate system with Z-axis directed along the normal to the elementary surface, the solid angle element is equal to $d\omega = \sin \vartheta d\vartheta d\varphi$.

/114

Then the illumination of the horizontal elementary area

$$E = \int_0^{2\pi} d\varphi \int_0^{\frac{\pi}{2}} I \cos \vartheta \sin \vartheta d\vartheta. \quad (14)$$

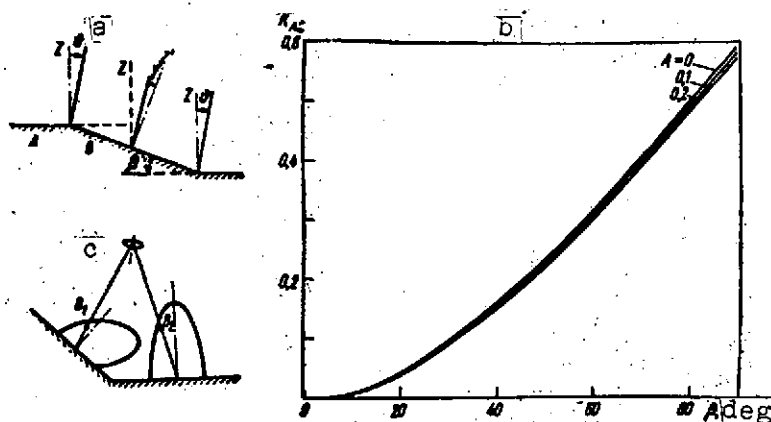


Figure 5. Contrast between areas A and B vs. area slope:

a — schematic for calculating surface contrasts;
b — contrast between areas vs. β ; c — influence of reflection indicatrix on the contrasts

The radiation intensity at the surface is defined by (12). In the expression (13), for $\bar{\sigma}(\theta, \psi)$ we introduce the following notations:

$$a = \frac{1 + \frac{1}{2} \cos \psi}{4 + (3 - \bar{R}_1)(1 - A)(\Delta \tau_{C1}^0 + \Delta \tau_{g, \lambda}^0)}, \quad b = 1 + A, \quad c = \frac{1}{2}(1 - A). \quad (15)$$

Then, $\bar{\sigma}(\theta, \psi) = a(b + c \cos \psi)$. Using (12), (14 - 15), we obtain the illumination of the elementary A (Figure 5a)

$$E_A = \int_0^{2\pi} d\varphi \int_0^{\frac{\pi}{2}} S \cos \psi a (b + c \cos \psi) \cos \theta \sin \theta d\theta = 2\pi S \cos \psi a. \quad (16)$$

The expressions for the illuminations of the elementary areas C and D can be obtained similarly. Neglecting mutual exposure between these elementary areas, we have

$$E_c = \pi S \cos \psi a \left[\frac{1}{2} b (1 + \cos \beta) + \frac{2}{3\pi} c (\pi - \beta + \sin \beta \cos \beta) \right], \quad (17)$$

$$E_d = \pi S \cos \psi a \left\{ \frac{1}{2} b (1 + \cos \beta) + \frac{2}{3\pi} c [\sin \beta + (\pi - \beta) \cos \beta] \right\}.$$

Using (15 - 17), we obtain the expression for the contrast between areas A and B as a function of the slope β of area B

$$K_{AB} = \frac{E_A - E_B}{E_{sA}} = 1 - \frac{1}{4}(1 + A)(1 + \cos \beta) - \\ - \frac{1}{2\pi}(1 - A)[\sin \beta + (\pi - \beta) \cos \beta].$$

This relation is shown graphically for the surface albedos $A = 0$; 0.1; 0.2 in Figure 5b. A similar relation can be obtained for the contrast between areas B and C.

In the case of nonorthotropic elementary areas, the surface reflection indicatrix will also influence the spatial distribution of the surface brightness. This is illustrated graphically in Figure 5c, which shows the brightness distribution of two specular surfaces: horizontal and inclined.

Estimate of contrast decrease with altitude. The maximum surface imaging altitude will be determined by the acceptable decrease of surface contrast with increasing height above the surface. Therefore, we need to obtain the dependence of the contrast decrease on altitude for various wavelengths. The contrast at the height h can be expressed in terms of the surface brightness B_s , the brightness B_{sc} of the scattered radiation in the gas layer between the surface and the imaging camera, and the optical thickness $\Delta\tau$ of this layer as follows:

$$K_h = \frac{B_{s \max} e^{-\Delta\tau} - B_{s \min} e^{-\Delta\tau}}{B_{s \max} e^{-\Delta\tau} + B_{sc}}.$$

Then the contrast decrease at height h , in comparison with the contrast K_0 at the surface is written as

$$\frac{K_h}{K_0} = \left[\frac{B_{sc} e^{-\Delta\tau}}{B_{s \max}} \right]^{-1}.$$

Accounting for the surface brightness $B_{sc} = B_g - B_s e^{-\Delta\tau}$, B_g is the brightness of the gas layer, we obtain the expression for the contrast decrease with altitude in terms of the surface E_s and gas layer E_g illumination and the corresponding albedos — maximum A_{max} and average \bar{A} of the surface and average \bar{A}_g of the gas

/116

$$K_0/K_h = 1 + \frac{e^{\Delta\tau} \bar{A}_g E_g - \bar{A} E_s}{A_{max} E_s}.$$

Using Relations (9) and (10) and considering that in the present case $E_{in}(h, \psi) = E_g$ and $\Delta\tau_{g,\lambda}(h) = \Delta\tau$, after transformations, we obtain the contrast decrease as a function of gas layer optical thickness $\Delta\tau$ for given surface albedos

$$\frac{K_h}{K_0} = \left\{ 1 - \frac{\bar{A}}{A_{max}} + \left[\frac{\bar{A}}{A_{max}} + \frac{3(1-\bar{A})}{4A_{max}} \Delta\tau \right] e^{\Delta\tau} \right\}^{-1}. \quad (18)$$

The plot of $K_h/K_0 = f(\Delta\tau)$ is shown in Figure 6a (we used $\bar{A} = 0.1$; $A_{max} = 0.2$).

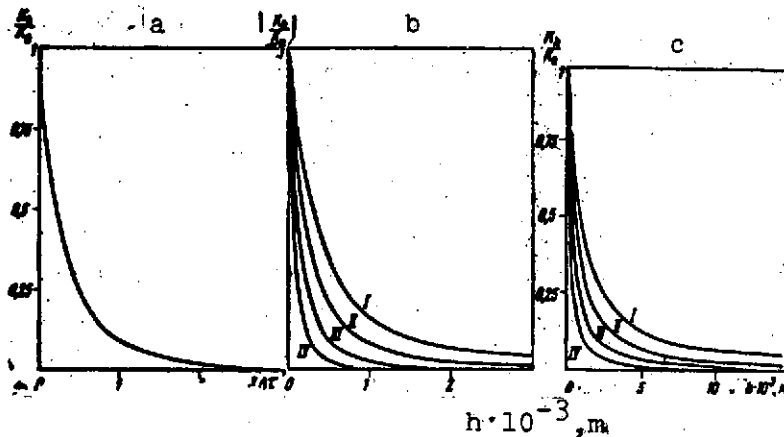


Figure 6. Contrast decrease as function of:
a — change of optical height $\Delta\tau$ above planet surface; b — geometric height above surface for small areas; c — same for large areas

In order to relate the contrast decrease with the height change, we need to know the connection between height and the corresponding gas optical thickness.

In the polytropic atmosphere case,

$$\tau_0 - \Delta\tau/\tau_0 = [(T_0 - \gamma h)/T_0]^{1/\gamma R}.$$

We can determine the contrast decrease with height for various wavelengths from the functions $K_N/K_0 = f(\Delta\tau)$ and $\Delta\tau = f(h)$. This relation is shown graphically in Figure 6b, where curve I corresponds to $\lambda = 0.9 \mu$, II — $\lambda = 0.8 \mu$; III — $\lambda = 0.7 \mu$; IV — $\lambda = 0.6 \mu$.

According to [4], the contrasts between large areas which arise as a result of difference of the albedos A_1 and A_2 of these areas, vary with altitude following the formula

/117

$$K_N/K_0 = \left\{ \left[1 + \frac{3}{4} \frac{1-A_1}{A_1} \Delta\tau_g(h) \right] \left[1 + \frac{3}{4} (1-A_2) \Delta\tau_g(h) \right] \right\}^{-1}. \quad (19)$$

If $0.1 \leq A_2 \leq A_1 \leq 0.3$, then with an adequate degree of accuracy,

A_1 and A_2 in (19) can be replaced by $\bar{A} = \frac{A_1 + A_2}{2}$. The Relation (19) is shown graphically for $\bar{A} = 0.1$ and 0.2 in Figure 6c (curves I - IV correspond to the same wavelengths as in Figure 6b).

The contrast decrease with height near the planet surface will take place faster when the atmosphere is dusty. Calculations using (18 - 19) yield maximum values of the optical image contrast in the objective lens focal plane.

References

1. Avduyevskiy, V. S., N. F. Borodin, V. V. Kuznetsov, et al. Temperature, Pressure, and Density of the Venus Atmosphere from Measurements of the Venus 4 Automatic Interplanetary Station, DAN SSSR, 179, No. 2. 1968.

2. Avduyevskiy, V. S., M. Ya. Marov, and M. K. Rozhdestvenskiy. Results of Measurements Aboard the Venus 5 and Venus 6 Automatic Interplanetary Stations and a Model of the Venus Atmosphere. Collection: Kosmicheskiye issledovaniya (Space Studies), Vol. 8, No. 6. Nauka Press, Moscow, 1970.
3. Irvine, W. M. Monochromatic Phase Curves and Albedos for Venus. J. Atmos. Sci., Vol. 25, No. 4, 1968.
4. Titarchuk, L. G. Scattering of Light in a Spherical Multilayer Atmosphere. In the present collection.
5. Sharonov, V. V. Priroda planet (Nature of the Planets). FIGML, (State Publishing House of Physical and Mathematical Literature), Moscow, 1958.
6. Mikhaylov, V. Ya. Aerofotografiya i obshchiye osnovy fotografii (Aerial Photography and General Fundamentals of Photography). Geodezizdat, Moscow, 1959.
7. Biryukov, Yu. A., L. G. Titarchuk, and Yu. M. Chesnokov. Applicability of the Diffusion Approximation. In the present collection.
8. Ginzburg, A. S. and Ye. M. Feygel'son. Some Optical Properties of the Venus Atmosphere and the Radiation Equilibrium Regime. Collection: Kosmicheskiye issledovaniya (Space Studies), Vol. 7, No. 2. Nauka Press, Moscow, 1969.
9. Sobolev, V. V. Perenos luchistoy energii v atmosferakh zvezd i planet (Radiant Energy Transport in Star and Planet Atmospheres). GITTL (State Publishing House of Theoretical and Technical Literature), Moscow, 1956.

DETERMINING SPACECRAFT AND AIRPLANE ANGULAR
ORIENTATION FROM STAR PHOTOGRAPHS

K. I. Elbakyan

The problem of exact spacecraft angular orientation determination arises in estimating the accuracy characteristics of spacecraft orientation systems and airplane navigation equipment components. Moreover, the determination of space photograph external orientation elements is necessary in solving several problems of space geodesy.

/118

The advantages of determining spacecraft angular orientation from star photographs include the documental nature and objectivity of the photographic image and also the high accuracy of construction of the reference system based on the stars.

Use of the method presupposes installation aboard the vehicle of a specialized photographic camera adapted for photographing the stellar sky.

From the mathematical viewpoint, the essence of the method amounts to the following:

- 1) certain directions in space are identified and their direction cosines are determined in a specified coordinate system;
- 2) the direction cosines of these same directions are determined relative to a coordinate system fixed with the vehicle;
- 3) the sought angular orientation of the vehicle is calculated using the coupling equations between the specified and vehicle-fixed coordinate systems.

In principle, vehicle angular orientation can be determined relative to any given reference system. If the reference system is

the $OX_1X_2X_3$ equatorial system, the sought orientation is termed absolute. We denote the vehicle-fixed coordinate system by $OY_1Y_2Y_3$. Identifying in space n directions to heavenly bodies, we represent their direction cosines in the equatorial system by the following matrix

$$X = \begin{pmatrix} x_{11} & x_{12} & \dots & x_{1n} \\ x_{21} & x_{22} & \dots & x_{2n} \\ x_{31} & x_{32} & \dots & x_{3n} \end{pmatrix}, \quad (1)$$

where x_{1n} , x_{2n} , x_{3n} are the direction cosines of the unit direction toward the star.

We represent the direction cosines of these same directions relative to the system fixed with the vehicle in the form

$$Y = \begin{pmatrix} y_{11} & y_{12} & \dots & y_{1n} \\ y_{21} & y_{22} & \dots & y_{2n} \\ y_{31} & y_{32} & \dots & y_{3n} \end{pmatrix}. \quad (2)$$

Then, using the relations for the connection between the direction cosines in two rectangular coordinate systems, we write

/119

$$X = AY, \quad (3)$$

where A is a matrix defining the rotation of one coordinate system relative to the other. Since this rotation is unknown, the problem reduces to finding the matrix A .

Considering the Relation (3) as the equation for finding the matrix A , we note that its elements must satisfy exactly the equations of orthogonality

$$A'A = E, \det A = +1. \quad (4)$$

An attempt to seek the solution without satisfying (4) leads to nonorthogonality of the transformation and, therefore, to an incorrect solution. Therefore, (3) and (4) must be solved jointly.

It is interesting to note the conditions for existence of the problem solution. We suppose that the solution exists, and use (3) and (4) to find

$$X'X = Y'A'AY = Y'Y. \quad (5)$$

In clarifying the sense of this condition, we note that it corresponds to the geometric interpretation of an orthogonal transformation which maintains angles between vectors and also maintains the orientation of each selected vector triad. The resulting necessary conditions for solution existence are, at the same time, sufficient.

The presence of errors in the initial data, i.e., in the measured coordinate in either system, leads to a situation in which the probability of absolutely exact satisfaction of the Conditions (5) is negligibly small, and, consequently, the system (3), (4) is contradictory. Therefore, a new problem arises of how to determine the values of the unknown elements of the matrix A so that, in some sense, all the equations of the System (3), (4) will be satisfied with the smallest error. Here, it is important to note that the Equalities (4), expressing orthogonality of the matrix A, must be satisfied absolutely exactly, while the Equations (3) must be satisfied optimally.

Depending on the optimality criterion adopted, the problem can be solved by various methods: Chebyshev equalization, least squares, and so on.

In the present case, it is better to use the least squares method; then the equalization problem is formulated as follows:

find that matrix A for which the Condition (4) is satisfied exactly and the sum of the squares of all the deviations (v_{j1}) takes the smallest possible value

$$s^2 = \sum_{i=1}^n \sum_{j=1}^m \sigma_{ji}^2 = \min. \quad (6)$$

Omitting several transformations, we write the expression for ϵ^2 in the following form:

$$\epsilon^2 = 2n - \sum_{k=1}^n a_{ks} m_{ks},$$

where m_{ks} are elements of the matrix $M = XY'$.

To solve the posed equalization problem by the least squares method, we use the Lagrange multiplier method and form the auxiliary function Φ by adding to the expression for ϵ^2 , terms containing the undetermined multipliers μ :

$$\begin{aligned} \Phi = & \epsilon^2 + \mu_1(a_{11}^2 + a_{21}^2 + a_{31}^2) + \mu_2(a_{12}^2 + a_{22}^2 + a_{32}^2) + \\ & + \mu_3(a_{13}^2 + a_{23}^2 + a_{33}^2) + \mu_4(a_{11}a_{12} + a_{21}a_{22} + a_{31}a_{32}) + \\ & + \mu_5(a_{11}a_{13} + a_{21}a_{23} + a_{31}a_{33}) + \mu_6(a_{12}a_{13} + a_{22}a_{23} + a_{32}a_{33}). \end{aligned} \quad (7)$$

Differentiating the function Φ , we write the necessary conditions for the existence of $\min \epsilon^2$ in the form

$$\frac{\partial \Phi}{\partial a_{ks}} = A\mu - M, \quad (8)$$

where μ is a symmetric matrix formed from the Lagrange multipliers

$$\mu = \mu' = \begin{pmatrix} \mu_1 & \mu_4 & \mu_5 \\ \mu_4 & \mu_2 & \mu_6 \\ \mu_5 & \mu_6 & \mu_3 \end{pmatrix}. \quad (9)$$

Then the system of equations for solving the problem is written in final form as

$$\begin{array}{lll} A\mu = M & (a); & \det A = +1 \quad (c); \\ A'A = E & (b); & \mu' = \mu \quad (d). \end{array} \quad (10)$$

Since (10) can have several solutions in its general form, and among these there may be solutions providing not only $\min \epsilon^2$, but also $\max \epsilon^2$, it is advisable to determine the sufficient conditions /121

for solution of the problem. We note that the matrixes A and μ are the unknowns when solving (10).

Since the sufficient condition for the minimum of a function of several variables is positive definiteness of its second differential taken at a stationary point with respect to the independent variable, we shall obtain the expression for this differential. The first differential has the form

$$d\left(\frac{s^2}{2}\right) = -\text{Sp} (M dA'). \quad (11)$$

Since the elements of the matrix dA' are connected by the conditions, i.e., they are not independent, we write the connection between them and the independent increments using the following relations

$$dA' = d\Omega A'.$$

where

$$d\Omega = \begin{pmatrix} 0 & -d\omega_2 & +d\omega_1 \\ d\omega_2 & 0 & -d\omega_1 \\ d\omega_1 & d\omega_1 & 0 \end{pmatrix} = (d\omega_{ik}).$$

Then the value of the second differential of the function is written as

$$d^2\left(\frac{s^2}{2}\right) = -\text{Sp} (A \mu d\Omega d\Omega A') = W = \sum_{k,l=1}^3 \mu_{kl} d\omega_k d\omega_l.$$

After performing several transformation, we write in the final form

$$W = (\tilde{\mu}_1 + \tilde{\mu}_2)(d\tilde{\omega}_1)^2 + (\tilde{\mu}_1 + \tilde{\mu}_2)(d\tilde{\omega}_2)^2 + (\tilde{\mu}_1 + \tilde{\mu}_2)(d\tilde{\omega}_3)^2, \quad (12)$$

where $\tilde{\mu}_1, \tilde{\mu}_2, \tilde{\mu}_3$ are the eigenvalues of the matrix μ .

*Translator's note: Sp is incorrectly printed in the foreign text as S_p .

Analyzing (12), we note that for the existence of $\min \epsilon^2$, it is sufficient that the eigenvalues of the matrix μ satisfy the inequalities

$$(\tilde{\mu}_2 + \tilde{\mu}_3) > 0, \quad (\tilde{\mu}_1 + \tilde{\mu}_2) > 0, \quad (\tilde{\mu}_1 + \tilde{\mu}_3) > 0. \quad (13)$$

The value of ϵ^2 obtained in this case is

$$\epsilon_{\min}^2 = n - SpMA' = 2(n - (\tilde{\mu}_1 + \tilde{\mu}_2 + \tilde{\mu}_3)) \quad (14)$$

Generally speaking, the Conditions (13) can be satisfied for several solutions of the system of equations (1) and, therefore, the value of ϵ^2 will have several local minima. In accordance with the Relation (14), we select that for which

$$\mu_1 + \mu_2 + \mu_3 = \max \quad (15)$$

Converting to the solution of the system consisting of (10a), (10b), (10d), we write

$$\begin{aligned} \mu' &= \mu'A' = \mu A', \\ M'M &= \mu A' A \mu = \mu^2. \end{aligned} \quad (16)$$

Since $\det M'M \neq 0$, i.e., we consider the basic case when the rank of the matrix is equal to three, the matrix $M'M$ is symmetric with positive spectrum. The following expansion is valid for this matrix [1]:

$$M'M = U' \begin{pmatrix} \lambda_1 & 0 & 0 \\ 0 & \lambda_2 & 0 \\ 0 & 0 & \lambda_3 \end{pmatrix} U, \quad (17)$$

where $\lambda_1, \lambda_2, \lambda_3$ are the eigenvalues of the matrix $M'M$; U is an orthogonal matrix.

In accordance with (16) and (17), we write the matrix μ in the form

$$\mu = U' \begin{pmatrix} \pm \sqrt{\lambda_1} & 0 & 0 \\ 0 & \pm \sqrt{\lambda_2} & 0 \\ 0 & 0 & \pm \sqrt{\lambda_3} \end{pmatrix} U. \quad (18)$$

The Condition (15) will be satisfied when the eigenvalues of the matrix μ are positive. With account for this, in accordance with (1) and (18), we obtain the final expression for the sought matrix A

$$A = M\mu^{-1} = MU' \begin{pmatrix} \frac{1}{\sqrt{\lambda_1}} & 0 & 0 \\ 0 & \frac{1}{\sqrt{\lambda_2}} & 0 \\ 0 & 0 & \frac{1}{\sqrt{\lambda_3}} \end{pmatrix} U.$$

This technique leads to a computational scheme for determining the elements of the matrix A, consisting of the following operations:

1) calculation of the matrixes X and Y (1) and (2) and the product $M = XY'$;

2) calculation of the matrix $M'M$;

/12/

3) solution for the matrix $M'M$ of the complete eigenvalue problem* [2];

4) calculation of the matrix A.

An obvious advantage of the method is that we obtain an exact solution of the equalization problem and reduce the solution process to performing quite well known and well developed computational algorithms of linear algebra. The uniqueness of the solution obtained

* In place of the solution of the complete eigenvalue problem for the matrix $M'M$, we can use the method of determining the principal values for the matrix M. The latter leads to some simplification of the computational scheme.

follows unambiguously from the theorem on the polar expansion of a nonsingular matrix [1].

References

1. Gantmakher, F. R. Teoriya matrits (Matrix Theory). Nauka Press, Moscow, 1966.
2. Voyevodin, V. V. Chislennyye metody algebry (Numerical Methods of Algebra). Nauka Press, Moscow, 1966.

GEOGRAPHIC CORRELATION OF TELEVISION PICTURES OBTAINED FROM WEATHER SATELLITES

A. V. Bushuyev

The geographical control of satellite pictures, using the terminology of aerial photography, can be treated as the problem of analysis of a single picture with the objective of obtaining a ground contour map. /123

There are several methods for solving this problem: graphical transformation of the pictures with the aid of perspective grids; optico-mechanical transformation; analytic solution of the spatial photogrammetric resection to determine the external orientation elements, and calculation of the coordinates of the points being determined.

According to our studies, graphical correlation using orbital data provides an accuracy of $\pm 20 - 30$ km; using ground reference points whose coordinates are known, the accuracy is ± 6 km. In the second case, the accuracy is quite acceptable for the solution of

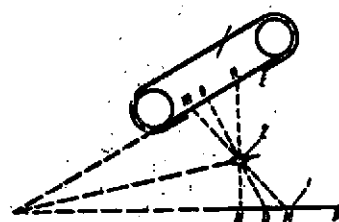
many practical problems in observing both clouds and sea ice. However, along with advantages such as simplicity and speed, the graphical correlation method has significant disadvantages: individual pictures rather than the overall photographic model are reduced and analyzed, analysis of the pictures using careful geographical correlation requires considerable time, and errors in the twofold "eyeball" conversion have a significant influence on the accuracy.

/12/

The need for developing simple photogrammetric instruments for real-time analysis of television pictures is obvious.

A method for optico-mechanical transformation of the television pictures of the "Meteor" system has been developed at the Arctic Institute, and a prototype of the scanner and the projector for the assembled pictures has been fabricated in the experimental shops of the institute.

The scanner, whose schematic is shown in the figure, provides the possibility for transforming negatives directly and positive prints ("reflection" transformation).



Schematic of scanner:

1 — negative being transformed; 2 — objective; 3 — cassette

A diapositive of the expanded double picture, having the form of two trapezoids aligned with shift of the short sides, is obtained on standard 35-mm movie film installed in the scanner cassette.

The resulting diapositive is projected with the aid of a special projector fabricated from a "multiplex" projector onto a planar base (chart of the corresponding projection). The best alignment of the fiducial points of the picture and map is obtained by altering the scale and tilt. After this, the boundaries and edges are transferred to the map or photographic paper is exposed for subsequent composition of the photographic map.

The studies conducted showed the possibility and capability of the method of composing photographic maps from transformed television pictures. It should be noted that the process of mounting the large number of pictures is time-consuming when performing the operations using the technique described above.

Optico-mechanical transformation solves the problem of geographical correlation for operational purposes. However, this technique does not compensate for electronic distortion, and accounts for Earth sphericity only approximately. However, for certain purposes (studying ice drift), the maximum possible accuracy is required. Therefore, the analytic geographical correlation methods using digital computers should be considered promising.

References

1. Bushuyev, A. V. Technique for Analysis and Geographical Control of Satellite Television Pictures for Mapping Sea Ice. Collection: Tezisy dokladov Pervoy konferentsii po morskomu ledovedeniyu (Reports of First Conference on Marine Glaciology), mimeograph, AN SSSR, Moscow, 1968.
2. Kondrat'yev, K. Ya. Meteorologicheskiye sputniki (Weather Satellites). Gidrometeoizdat, Leningrad, 1963.
3. Kondrat'yev, K. Ya., Ye. P. Borisenkov, and A. A. Morozkin. Prakticheskoye ispol'zovaniye dannykh meteorologicheskikh sputnikov (Practical Use of Weather Satellite Data). Gidrometeoizdat, Leningrad, 1966.

GEOGRAPHICAL CORRELATION OF TV AND IR IMAGES
OBTAINED FROM WEATHER SATELLITES

Ya. L. Ziman, B. V. Nepoklonov, and
B. N. Rodionov

The requirements on the accuracy of geographical correlation of TV and IR cloud cover images are determined by the objective of the analysis of the weather information contained in these images. In the operational analysis case, the correlation accuracy need not be high. Errors of several tens of kilometers in determining the location of the cloud formation contours are considered acceptable in this case. Such correlation must be provided in real image reception time. Scientific studies require accurate correlation of the cloud formation contours. The errors in determining their position should be commensurate with the imaging system resolution.

In the present article, we discuss the geometric aspects of developing methods and equipment for geographical correlation of television and infrared images of cloud cover taken from the Meteor satellites.

I.

Regardless of the technique used for obtaining and recording the images and the required geographical correlation precision, the geometric basis is the same and is described by the fundamental equations of iconometry — the equations connecting the coordinates of ground-points and their images and the equations of the selected cartographic projections. Several coordinate systems are employed to describe these equations.

/12

In the OXYZ geocentric coordinate system, the origin is located at the center of the Earth, the OZ axis is directed along the Earth's rotation axis, and the OX axis lies in the plane of the Greenwich

meridian. In the SX"Y"Z" orbital frame, the origin is at the projection center of the imaging device, the SZ" axis is directed along the satellite geocentric radius-vector, and the SX" abscissa axis lies in the orbital plane in the direction of flight. The body system Sx'y'z' has its origin at the imaging device projection center. The system axes coincide with the spacecraft structural axes. In the oriented position of the satellite, the body system coincides with the orbital system to within the errors of orientation system operation.

In the Sxyz imaging device coordinate system, the origin lies at the imaging device projection center. For the TV cameras, we align the Sz axis along the direction of the optical axis, the abscissa Sx and ordinate Sy axes are defined by coordinate marks provided on the vidicon faceplate. For the scanning radiometer, we direct the Sx abscissa axis along the objective optical axis and the Sz axis in the plane containing the normal to the scanning mirror at the initial instant of time t_0 .

We express the rotations when converting from one coordinate system to another by the following formulas

$$\begin{aligned}\bar{r}_s &= C\bar{r}_1, \quad C = C(L_s, \Phi_s, A_s); \\ \bar{r}_s &= T\bar{r}_2, \quad T = T(\psi, \theta, \gamma); \\ \bar{r}_s &= B\bar{r}_3, \quad B = B(\alpha, \omega, \gamma),\end{aligned}\tag{1}$$

where $\bar{r}_1^0, \bar{r}_2^0, \bar{r}_3^0, \bar{r}_4^0$ are the unit vectors of the same directions in the coordinate systems which we have selected; Φ_s, L_s, A_s are the geocentric latitude, longitude, and azimuth of the satellite SX" axis; ψ, θ, γ are the satellite yaw, pitch, and roll angles; α, ω, γ are the imaging device installation angles in the reference coordinate system.

II.

We find the geocentric coordinates $\bar{R}(\overline{xyz})$ of the cloud formation points from the measured coordinates $\bar{r}_s(\overline{xyz})$ of their images by

joint solution of the fundamental equations, (2) connecting the ground points and their images

/127

$$\frac{\bar{R} - \bar{R}_s}{|\bar{R} - \bar{R}_s|} = Q^T \bar{r}_s, \quad (2)$$

$$\bar{R} = R (\cos \Phi \cos L \bar{i}_1 + \cos \Phi \sin L \bar{j}_1 + \sin \Phi \bar{k}_1), \quad (3)$$

where $\bar{R}_s (X_s Y_s Z_s)$ is the satellite geocentric radius-vector; Q^T is the transpose of the matrix

$$Q = BTC; \quad (4)$$

Φ, L are the geocentric coordinates of the current point; $\bar{i}_1, \bar{j}_1, \bar{k}_1$ are the unit vectors of the geocentric coordinate system. We express the vector \bar{r}_s of the image point in terms of the direction cosines l, m, n of the corresponding projecting (scanning) ray

$$\bar{r}_s = l \bar{i}_s + m \bar{j}_s + n \bar{k}_s. \quad (5)$$

The geocentric radius-vector of the photographed point is

$$R = \frac{a_\oplus}{\sqrt{1 + e_\oplus^2 \sin^2 \Phi}} + h. \quad (6)$$

Here, a_\oplus, e_\oplus are the semimajor axis and the second eccentricity of the terrestrial ellipsoid; h is the height of the point being defined above the reference ellipsoid.

The initial values necessary for the problem solution are the satellite coordinates and the angles φ, θ, γ .

The satellite coordinates are defined by the osculating elements of its orbit at the moment the image of the desired point is obtained.

The satellite orbital parameters are determined from analysis of trajectory measurements. The angles φ, θ, γ are measured by the vehicle orientation system sensors and are telemetered to the Earth.

The algorithm for determining cloud formation point coordinates is the same for images obtained by both framing television systems

and scanning radiometers. The only difference lies in determining the direction of the projecting and scanning rays.

When analyzing the TV picture point coordinate measurements, the direction cosines of the projecting rays are determined just as in the analysis of aerial photographs [1, 2].

The direction cosines of the scanning rays are defined by the formulas

$$\begin{aligned} l &= -\mu(1 - \cos \beta), \\ m &= \sin \beta - \phi(1 - \cos \beta) - \mu \sin 2\beta, \\ n &= -\cos \beta - \mu \sin^2 \beta, \end{aligned} \quad (7)$$

where β is the scan angle; μ, ϕ are the direction angles of the scanning mirror rotation axis (scanning axis) in the radiometer Sxyz coordinate system. The scan angle β is found from the measured image ordinate

/128

$$\beta = \omega_p \left(\frac{y}{V_z} - t_0 \right), \quad (8)$$

where ω_p is the scan velocity; V_z is the ground-based photorecorder line scan velocity.

The scan velocity ω_p , time t_0 , angles μ and ν are the iconometric parameters of the radiometer.

The stereographic and Mercator projections are used in composing synoptic charts. In order to determine the coordinates of the sought point in these projections, it is necessary to convert under the condition of conformal representation of the ellipsoid on the sphere from the rectangular geocentric coordinates to the geographic latitudes ϕ and longitudes λ . To within ϵ_0^4 , these coordinates are equal to

$$\varphi = \arctg \frac{z}{\sqrt{x^2 + y^2}}, \quad \lambda = \arctg Y/X. \quad (9)$$

Using the projection equations, we find in the projection the rectangular coordinates x_k and y_k of the point being determined. For example, for the stereographic projection, we obtain

$$x_k = -2MR_{\oplus} \frac{\cos \varphi \cos \lambda}{1 + \sin \lambda}, \quad y_k = 2MR_{\oplus} \frac{\cos \varphi \sin \lambda}{1 + \sin \lambda}, \quad (10)$$

where M is the scale factor; R_{\oplus} is the radius of the terrestrial sphere.

Realization of the described exact algorithm for transforming the image into a cartographic projection is possible only by analytic methods. Here, the use of digital computers permits complete automation of geographic correlation of TV and IR images. However, the time spent on entering, transforming, and outputting a single TV picture is large, and amounts to more than an hour with a computer operating speed of 10^6 operations per second. This limits the use of digital computers for real-time geographical correlation of the cloud cover images obtained.

III.

The exact formulas for transforming images into the cartographic projection can be approximated theoretically with any accuracy by power-law polynomials of the form

$$\begin{aligned} x_k &= a_{00} + a_{10}x + a_{01}y + a_{11}xy + a_{20}x^2 + a_{02}y^2 + a_{21}x^2y + a_{12}xy^2 + \dots \\ y_k &= b_{00} + b_{10}x + b_{01}y + b_{11}xy + b_{20}x^2 + b_{02}y^2 + b_{21}x^2y + b_{12}xy^2 + \dots \end{aligned} \quad (11) \quad /11$$

Coordinate transformations of this sort can be modeled on specialized analog electronic computers. In such computers, we can control the electron beam tube sweeps, transforming the TV raster in accordance with the Relations (11). If this transformed raster is modulated by the video signal of the original image, we obtain the transformed image on the tube screen.

The idea of such electronic transformation was realized in the cartographic transformer of M. P. Bordyukov. However, in this transformer, control of the scanning units is accomplished manually. Moreover, it did not permit applying to the image the geographical coordinate grid on the basis of which the transformation is monitored.

Therefore, a specialized electronic transformation and correlation system was developed and constructed for geographical correlation of the TV cloud images obtained from the Meteor satellites [3].

In this system, picture transformation is performed into a special cartographic projection, which provides the possibility of constructing continuous orbital montages from the pictures. The studies made permitted us to find such a projection, defined by the equations

$$\begin{aligned}x_k &= M \left[(R + H) \Phi + H \frac{(1 - \cos L) \cos \Phi \sin \Phi}{\frac{H}{R} + (1 - \cos L) \cos^2 \Phi} \right], \\y_k &= -MH \frac{\cos \Phi \sin L}{\frac{H}{R} - (1 - \cos L) \cos^2 \Phi},\end{aligned}\quad (12)$$

where H is the projection constant (flight altitude); M is the scale factor.

Transformation of the TV pictures into this projection is accomplished using the formulas

$$\begin{aligned}x_k &= -MH \frac{x' \cos(A_s - \psi) + y' \sin(A_s - \psi)}{x'}, \\y_k &= -MH \frac{-x' \sin(A_s - \psi) + y' \cos(A_s - \psi)}{x'},\end{aligned}\quad (13)$$

where

$$\begin{pmatrix} x' \\ y' \\ z' \end{pmatrix} = T^T B^T \begin{pmatrix} x \\ y \\ -f \end{pmatrix}; \quad (14)$$

f is the imaging camera focal length, reduced to the scale of the image recorded on the ground. The systematic error of these formulas amounts to 6 km for a strip width of 1000 km.

Experimental operation of the electronic transformation and correlation system for real-time analysis of TV pictures confirmed the advisability of using for geographical correlation, specialized analog computers to perform the geographical correlation in real time.

IV.

Along with this technique of electronic analog transformation of the TV images, we developed techniques for graphoanalytic geographical correlation of the images. Such techniques use for geographical correlation of the images auxiliary transformation grids which permit the entire transformation or its individual subprocesses to be performed graphically by linear interpolation.

It is advisable that transformation of the images into any cartographic projection be performed using grids representing the image of the parallels and meridians in the projection of these images. For the framing TV pictures, the projection of the geographic coordinate grid on the picture is defined by the Equations (2).

In constructing such a grid for images obtained by scanning radiometers, we need to determine the time t_{sc} of scanning ray passage through the Earth's surface points which are the intersections of the meridians and parallels. This time can be found from the solution of the equation of the scalar product of the geocentric radius-vector \bar{R}_C of the grid node and the unit vector \bar{I}_2 of the orbital coordinate system abscissa axis under the condition that this product equal zero.

$$\bar{R}_C \bar{I}_2 = 0. \quad (15)$$

The calculation can be performed by successive approximations. We first find the time t_{sc} without account for the yaw, pitch and roll angles. Then the satellite orientation angles are selected on the basis of the time found and the spatial orientation of the unit

vector \bar{i}_2 is refined. After solving (15), we again refine the time of scanning ray passage through the specified geographic grid node and, after two or three approximations, this time is found with the required accuracy. This time defines the corresponding panorama line, and then we use the scan angle and Formula (8) to calculate the ordinate on the panorama of the corresponding geographic grid node.

/131

The grids can be constructed in this fashion only after performing the photography and obtaining data on spacecraft orientation.

Transformation grids were constructed for operational geographic correlation which permit scaling the resulting images and transforming them into the selected projection without account for the spacecraft yaw, pitch, and roll angles. This grid formed squares with 2-cm sides on the resulting map.

The calculation of such grids for the TV pictures was made using (2), in which the projection center coordinates were taken equal to $X_S = 0$, $Y_S = 0$, $Z_{sc} = h$, and the elements of the matrix Q were calculated using the TV camera mounting angles α , ω , κ .

In calculating the grids for the panoramas, the abscissas of the grid nodes were determined by using the minute marks on the satellite velocity; for calculating their ordinates — we used (8). In this case, the panoramas were artificially framed.

Geographical correlation of the images was accomplished simultaneously with their analysis on special light tables by redrawing cloud cover contours onto a blank with the geographic coordinate grid printed on a transparent base. The blank was superposed on the grid with respect to the satellite coordinates, and was oriented to the azimuth A of the sx abscissa axis with account for the yaw angle.

Account for the pitch and roll angles was accomplished by displacing the center of the grid superposed on the picture by the magnitudes

$$\Delta x = -f\theta, \quad \Delta y = -f\gamma. \quad (16)$$

The systematic error of this geographical correlation process for the edge of the picture, when the picture covers a strip 500 km wide on the ground, does not exceed 12 km.

* * *

The techniques described were used in analysis of TV and IR images obtained from the Soviet weather satellites. The results of this study made it possible to draw the following conclusions.

When performing the geographical correlation analytically on digital computers, the problem is solved most exactly but considerable time is expended, particularly on image input into and output from the computer. For real-time analytic handling, it is necessary to develop specialized systems for video information introduction into the computer directly from the receivers, as the information arrives from the spacecraft, and specialized output devices which permit obtaining at the exit weather maps of the photographed formations with the results of their nephanalysis. /132

Most effective is the method of geographical correlation on specialized electronic analog computers. In standardizing the on-board weather satellite imaging equipment, it is advisable to outfit the ground stations for image reception with instruments of this type which process the video information in real time and generate photographic maps of the photographed routes.

When a large number of weather analysts are available, the graphico-analytic method satisfies the requirements of real-time processing and can be recommended in the absence of specialized analog electronic computers.

References

1. Urmayev, N. A. Elementy fotogrammetriy (Elements of Photogrammetry). Geodezizdat, Moscow, 1941.
2. Lobanov, A. N. Vozdushnaya stereofotogrammetricheskaya s'yemka (Aerial Stereophotogrammetric Surveying). V. V. Kuibyshev Air Force Engineering Academy, 1957.
3. Dubenskiy, V. P., B. L. Nemkovskiy, and B. N. Rodionov. System for Electronic Transformation and Geographic Correlation of Satellite Television Information. In present collection.

SYSTEM FOR ELECTRONIC TRANSFORMATION AND GEOGRAPHIC
CORRELATION OF SATELLITE TELEVISION INFORMATION

V. P. Dubenskiy, B. L. Nemkovskiy,
B. N. Rodionov

System purpose and characteristics. One of the basic stages in processing the television information coming from weather satellites is the geographical correlation of this information and preparation of cloud cover photographic maps. The use for these purposes of manual methods with application of pre-calculated grids cannot provide the operational speed and required economics of these operations, since this requires a large staff of highly qualified personnel.

The authors have developed for the Meteor space weather system an electronic transformation and correlation (ETC) system which provides transformation and scaling of the original picture with account for satellite flight altitude and inclinations of the optical axes of the transmitting devices, with simultaneous superposing of the geographical coordinate grid on the transformed picture.

/133

The weather satellites used in the Meteor system are injected into a circular near-polar orbit with altitude on the order of 600 km. In order to ensure the required width of coverage on the ground (1000 km), two TV cameras are installed aboard the satellite, and their optical axes are tilted at an angle on the order of 20° to the satellite vertical axis. The shutter of the second camera triggers 10 seconds after that of the first camera. The image stores on the vidicon photosensitive layer is read out and stored with the aid of an onboard tape recorder. Code signals containing information on the number of each pair of frames are also included in the video signal. Accelerated transmission of the stored information is accomplished as the satellite flies over the ground station. This information is also stored on magnetic tape at the ground station. In addition to TV and other forms of weather information, data on spacecraft angular orientation at the moments of exposure of each pair of frames arrive at the ground station over the telemetry channel.

The ETC system was used to process the image signals coming from the Kosmos 122, 144, 156, and other satellites, and showed good results.

The processing was organized as follows. Prior to beginning the communications session, tables of the predicted coordinates of the subsatellite point and the flight altitude corresponding to the times of exposure of each pair of frames were generated by the ETC. Upon termination of the communication session, the angular orientation parameters arriving over the telemetry channel were generated. The magnetic film stored in the ground-based video magnetic tape recorder was reproduced on the tape recorder forming part of the ETC. The geographic coordinates of the subsatellite point and the satellite angular orientation parameters (pitch, roll, and yaw angles) were introduced for each frame pair from the ETC control panel. The frames obtained by the two transmitting cameras were reproduced on the photorecorder CRT screen. This provided for pairwise mounting of the frames and their recording on 19-cm photographic film. Transformation and scaling of the image were accomplished by

giving the proper shape to the line and frame scan signals applied to the photorecorder cathode ray tube deflection system. This operation was performed by a special unit — an analog converter. The geographic coordinate grid signal was combined with the recorded signal for geographic correlation of the images. This coordinate grid signal was formed with the aid of a scanning beam system which read out the grid image from a transparent glass template.

The geographic grid used for the correlation was made using a special zonal projection with identification of the meridians; the longitude was indicated in the legend printed on the margins of the image, together with several other data (frame number, geographical correlation parameters, satellite angular orientation, and so on).

Block diagram of ETC system. The ETC equipment is a closed-circuit television system whose scans are controlled by a special analog computer (scan converter). It consists of the following basic units and devices (Figure 1).

The video magnetic tape recorder is 1; 2 is the sync generator; 3 is the analog scan converter; 4 is the scan amplifier; 5 is the video amplifier; 6 is the geographic grid input unit; 7 is the photorecorder.

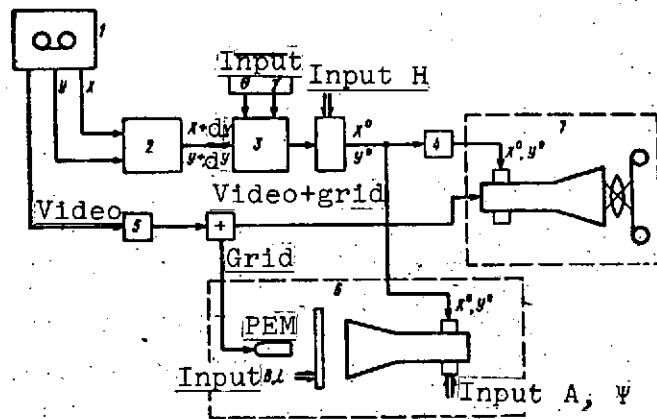


Figure 1. Simplified block diagram of ETC system

The video magnetic tape recorder in the ETC system operates in the start-stop mode. A single frame pair is handled in each cycle. Since the instant of exposure of the second frame (half-frame) of the pair is rigidly fixed relative to the first frame, the geographic correlation and angular orientation parameters are introduced

simultaneously into both half-frames, and the image of the second half-frame is shifted relative to the first by a magnitude determined by the satellite flight altitude and yaw angle at the instant of exposure.

Upon video magnetic tape recorder activation, the photorecorder camera shutter opens. The frame and line sync pulses coming from the video magnetic tape recorder trigger the ETC sync generator. The latter generates the linear X and Y scan signals, and the nonlinear components dX and dY , which are fed to the analog scan converter. /135

The converter forms scan signals of the required shape, in accordance with the magnitudes of the roll and pitch angles. Then the signals pass through a regulator, which alters their scale in accordance with the flight altitude, are amplified, and are fed to the photorecorder cathode ray tube deflection system.

After amplification, these same transformed scan signals are fed to the geographic grid input unit. The latter includes a scanning beam tube, photoelectronic multiplier (PEM), and glass template which is set by a mechanical system in a position corresponding to the coordinates of the subsatellite point. The corresponding grid segment is read out with the aid of the PEM, and the resulting signal is combined with the received video signal.

Upon termination of the cycle, the video magnetic tape recorder stops, the photorecorder shutter closes, and the exposed segment film is advanced. Then new values of the angular orientation and geographic coordinates are introduced, after which the cycle repeats.

A set of reference grids, corresponding to different flight altitudes and different satellite tilt angles, were prepared in order to align the system. These grids were made to the same scale as the image. Alignment was accomplished by placing the grids on the photorecorder camera pressure glass, and selecting the amplitudes of the transformed signal components, so as to ensure.

coincidence of the lines of the grid reproduced on the cathode ray tube screen and the reference grids. This alignment was later repeated several times in order to verify the stability of the system. Experience showed that realignment is not required for operation of the ETC system in the course of 6 - 7 hours, nor when activating the system after an interruption of several days.

Characteristics of the ETC system. One of the most specific circuit features of the ETC system is the analog scan signal converter. The distortions caused by Earth's surface curvature were not considered in developing the ETC system, since the flight altitude was on the order of 600 - 700 km, and a special zonal projection was used for correlation. In this case, the primary role is played by the perspective distortions associated with tilt of the transmitting camera optical axes relative to the local vertical, and those due to the installation angle and variability of the satellite geometric axis position in space.

The following considerations formed the basis for development of the scan converter.

It is well known that in order to obtain the connection between the coordinates of the transformed and nontransformed photographs, it is necessary to use the matrixes of transformed photograph coordinate axes rotations through the three Euler angles. In the present case, we use the yaw ψ , pitch θ , and roll γ' angles, information on which came from onboard the satellite. The angle γ consists of two parts: the installation angle γ_0 and the roll angle proper γ . Generation of the yaw angle in the ETC system is accomplished mechanically by rotation of the deflection system mounted on the neck of the scanning beam tube. The image of the geographic grid is thus rotated through the required angle. The analog converter generates only the pitch θ and roll $\gamma' = \gamma_0 + \gamma$ angles.

The connection between the transformed and nontransformed picture coordinates is expressed by the following well-known formulas:

$$X^0 = -h \frac{a_{11}x + a_{12}y - a_{13}h}{a_{21}x + a_{22}y - a_{23}h}, \quad Y^0 = -h \frac{a_{31}x + a_{32}y - a_{33}h}{a_{21}x + a_{22}y - a_{23}h}, \quad (1)$$

where h is the flight altitude and focal length, referred to unit scale of the transformed image.

The coefficients a_{ij} are found from the matrixes:

$$\begin{aligned} \begin{bmatrix} X^0 \\ Y^0 \\ Z^0 \end{bmatrix} &= \begin{bmatrix} \cos \theta & 0 & \sin \theta \\ 0 & 1 & 0 \\ -\sin \theta & 0 & \cos \theta \end{bmatrix} \begin{bmatrix} x_1 \\ y_1 \\ z_1 \end{bmatrix}, \\ \begin{bmatrix} x_1 \\ y_1 \\ z_1 \end{bmatrix} &= \begin{bmatrix} 1 & 0 & 0 \\ 0 & \cos \gamma' & -\sin \gamma' \\ 0 & \sin \gamma' & \cos \gamma' \end{bmatrix} \begin{bmatrix} x \\ y \\ z \end{bmatrix}. \end{aligned} \quad (2)$$

hence, substituting these coefficients into (1), we obtain

$$\begin{aligned} X^0 &= h \frac{x \cos \theta + y \sin \theta \sin \gamma' - h \sin \theta \cos \gamma'}{h \cos \theta \cos \gamma' + x \sin \theta - y \cos \theta \sin \gamma'}, \\ Y^0 &= h \frac{y \cos \gamma' + h \sin \gamma'}{h \cos \theta \cos \gamma' + x \sin \theta - y \cos \theta \sin \gamma'}. \end{aligned} \quad (3)$$

If we consider the quantities θ and γ' sufficiently small, after expanding (3) into a Taylor series and some regrouping of terms, we obtain

$$\begin{aligned} X^0 &= -h\theta + \left(x - x^2 \frac{\theta}{h}\right) + \left(x - x^2 \frac{\theta}{h}\right) \left(y + y^2 \frac{\gamma'}{h}\right) \frac{\gamma'}{h}, \\ Y^0 &= h\gamma' + \left(y + y^2 \frac{\gamma'}{h}\right) - \left(y + y^2 \frac{\gamma'}{h}\right) \left(x - x^2 \frac{\theta}{h}\right) \frac{\theta}{h}. \end{aligned} \quad (4)$$

These formulas describe converter operation quite well for small tilt angles; in this case, the accuracy is about 0.5%.

/137

However, the existence of the installation angles γ_0 does not permit considering the quantity γ' small; considering that the roll angle γ is small (does not exceed 5°), we can assume that the angles γ and γ_0 are independent of one another and can be generated separately. In final form, the formulas describing the operation of the ETC system converter are:

$$\begin{aligned}
X^0 &= Cx_0 + (x + k_0 x^2) + (x + k_0 x^2)(y + k_1 y^2 + k_1 y^2)(k_1 + k_1), \\
Y^0 &= Cy_0 + Cy_1 + (y + k_1 y^2 + k_1 y^2) + \\
&+ (y + k_1 y^2 + k_1 y^2)(x + k_0 x^2) k_0,
\end{aligned}
\tag{5}$$

where Cx_0 , Cy_1 , Cy_0 are raster shifts through the angles θ , γ , γ_0 , respectively; k_0 , k_1 , k_0^* are weighting coefficients which indicate in what proportion the corresponding scan signal components are introduced.

We see from (4) and (5) that the complete X and Y scan output signals contain: constant components, nonlinear components (quadratic parabolas), and components which are the product of the sum of linear and nonlinear components of one signal by the same sum of the other signal. These components are determined by the magnitudes of the tilt angles. As indicated above, the selection of the component levels to ensure generation of the installation angle γ_0 is accomplished with the aid of reference grids. As a result of this, the corresponding weighting coefficients were proportional to functions of the angle. Generation of the variable tilt angles θ and γ was accomplished with the aid of a relay register. Using the reference grids, we selected signal component levels corresponding to the limiting tilt angle values, and in the interval between these values the weighting coefficients were varied linearly, i.e., in proportion to the magnitudes of the angles themselves.

/138

A block diagram of the converter is shown in Figure 2. The maximum transformation error is determined by the fact that the scan output signals do not contain components proportional to the cube of the input signal. In developing the ETC system, it was considered that these components could be ignored, since this would require equipment complication which was not justified by the accuracy obtained. Moreover, the absence of these components is partly compensated by the distortions inherent in the photorecorder cathode ray tube used, and this was taken into consideration during calibration.

*Translator's Note: Incorrectly cited as k_1 in foreign text.

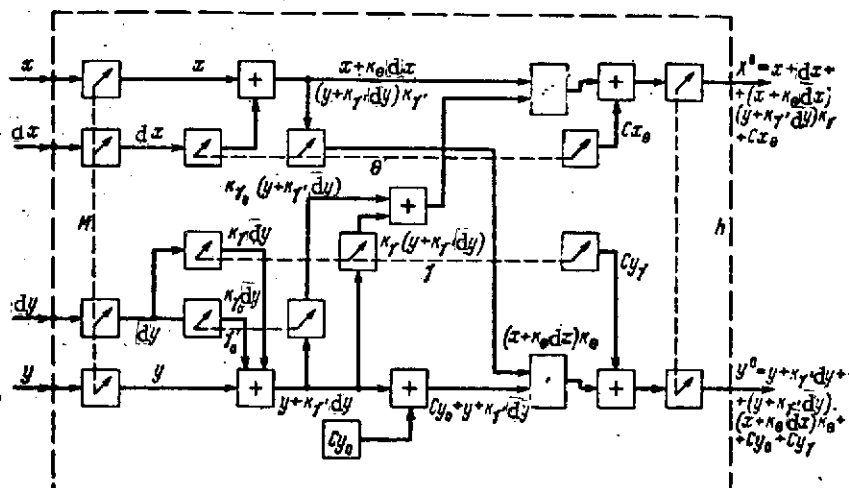


Figure 2. Simplified block diagram of ETC system converter

Parameters of the ETC system and possible improvement techniques.

Structurally, the ETC system is made in two standard four-section cabinets, between which there is located a nonstandard cabinet with the mechanical devices and control panel arranged thereon. The photorecorder is portable, and is connected with the remainder of the system by a cable. This recorder includes a cathode ray tube with deflection and focusing systems and other auxiliary devices, and a photocamera with film advance device and a unit to imprint the legend. The arrangement of the ETC system units is shown in Figure 3. /139

As a result of experience in developing and operating the ETC system, it should be noted that a feature of the analog systems is the possibility of ensuring quite high information processing speed (up to 10 frames/sec or more), although with limited accuracy. Therefore, such systems can be used for information processing in real time. From the economic viewpoint, the use of analog systems for processing the information from weather satellites is more favorable than the use of digital computers, which must have very high operating speeds to provide immediate processing (for real time operation, the speed must be on the order of 10^7 op/sec). Experience in processing the images from weather satellites of the Meteor

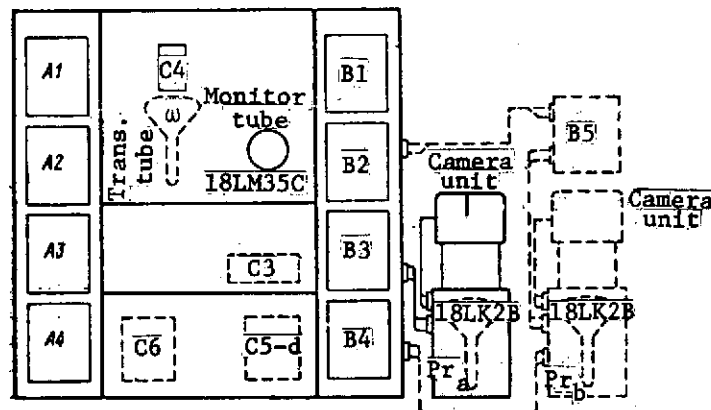


Figure 3. Location of ETC system units:

A1 — sync generator; A2 — auxiliary circuit unit; A3 — quantizer; A4 — power supply; B1 — transmitting and monitor tube scan amplifiers; B2 — photorecorder scan amplifier and shift mixers; B3 — converter; B4 — power supply; B5 — photo-recorder scan amplifier and power supply; C1 — control panel; C3 — cycle programmer; C4 — PEM; C5-d — 15-kV rectifier; C6 — 27-V rectifier

system shows that even with manual information input, the processing of all the frames obtained during a single communications period requires no more than 20 - 30 minutes (without considering the subsequent photochemical processing, whose duration is the same for all cases).

The ETC system made is possible to obtain high-quality images with satisfactory halftone transmission and the required correlation accuracy. Using the uncontrolled montage method, it is possible to obtain quite quickly a photomap of the cloud cover segment photographed during a single orbit.

It appears to us that the possible ways to improve processing quality and, first of all, speed, should be sought in automation of devices similar to the ETC system. Here, the basic question is automation of the correlation operation, consisting in superposing the geographic coordinate grid on the distortion-free image. As for

automation of the transformation operation, this problem was essentially solved in the ETC system.

In conclusion, we should note that such important problems as improving correlation accuracy and increasing the resolution can be solved basically by creating onboard devices with suitable parameters: here the analog transformation and correlation systems do not impose any significant limitations.

References

1. Uspekhi SSSR v issledovanii kosmicheskogo prostranstva (USSR Successes in Studying Space). Nauka Press, Moscow, 1968. /140
2. Bratslavets, P. F., I. A. Rosselevich, and L. I. Khromov. Kosmicheskoye Televideniye (Space Television). Svyaz' Press, Moscow, 1967.
3. Vetlov, I. P. The Meteor Space System. Aviatsiya i kosmonavtika, Nos. 9, 10, 1967.
4. Bordyukov, M. P. Electronic Cartographic Converter. Trudy MIIGAik (Transactions of the Moscow Institute of Engineers of Geodesy, Aerial Surveying, and Cartography), No. 31, 1959.
5. Urmayev, N. A. Elementy fotogrammetrii (Elements of Photogrammetry). Geodezizdat, Moscow, 1941.
6. Kondrat'yev, K. Ya., Ye. P. Borisenkov, and A. A. Morozkin. Prakticheskoye ispol'zovaniye dannykh meteorologicheskikh sputnikov (Practical Use of Weather Satellite Data). Gidrometeoizdat, Leningrad, 1966.

GEOGRAPHICAL CORRELATION OF EARTH CLOUD COVER PICTURES
OBTAINED FROM UNORIENTED SATELLITES

V. I. Solov'yev

The geographical correlation of pictures received from Earth satellites, i.e., the determination of the geographic coordinates ϕ_1 and λ_1 of the image point with the coordinates x_1 and y_1 , can be accomplished using the Formulas (1) - (5)*

$$\phi_1 = \arctg \left\{ \frac{Z_{T1}}{\sqrt{X_{T1}^2 + Y_{T1}^2}} \right\}, \quad (1)$$

$$\lambda_1 = \arctg \left\{ \frac{Y_{T1}}{X_{T1}} \right\}, \quad (2)$$

$$\begin{bmatrix} X_{T1} \\ Y_{T1} \\ Z_{T1} \end{bmatrix} = k_1 \begin{bmatrix} a_{11}a_{12}a_{13} \\ a_{21}a_{22}a_{23} \\ a_{31}a_{32}a_{33} \end{bmatrix} \cdot \begin{bmatrix} b_{11}b_{12}b_{13} \\ b_{21}b_{22}b_{23} \\ b_{31}b_{32}b_{33} \end{bmatrix} \cdot \begin{bmatrix} c_{11}c_{12}c_{13} \\ c_{21}c_{22}c_{23} \\ c_{31}c_{32}c_{33} \end{bmatrix} \cdot \begin{bmatrix} x_1 \\ y_1 \\ f \end{bmatrix} + \begin{bmatrix} X_S \\ Y_S \\ Z_S \end{bmatrix}; \quad (3)$$

$$k_1 = - \frac{[H + R(1 - \cos \sigma)]}{x_1 b_{31} + y_1 b_{32} + f b_{33}}, \quad \sigma = \arcsin \left[\frac{H + R}{R} \sin \theta \right] - \theta, \quad (4)$$

$$\lg \theta = \frac{\sqrt{(xb_{11} + yb_{12} + fb_{13})^2 + (xb_{21} + yb_{22} + fb_{23})^2}}{xb_{31} + yb_{32} + fb_{33}}, \quad (5)$$

where X_S, Y_S, Z_S are the satellite geocentric coordinates at the instant of exposure; x_1, y_1 are the image point coordinates; a, b, c /141 are the elements of the orthogonal transformation matrices; k_1 is the scale factor, H is the satellite altitude, and f is the focal length of the imaging camera.

The matrix elements c are defined by the imaging camera installation angles relative to the satellite structural axes. The matrix elements b are defined in terms of the three satellite angular orientation parameters: pitch θ , roll γ , and yaw ψ . The values of the coefficients a are determined from the known values of the geographic coordinates ϕ_N and λ_N of the subsatellite point and the azimuth A_V of the satellite absolute velocity vector at this point.

*In deriving the formulas the earth was taken to be a sphere of radius R .

Characteristic of Earth's cloud cover imaging from nonmeteorological satellites is the absence of data on the angular orientation of the imaging camera relative to the local vertical at the instant of photographing.

In order to determine the angular orientation elements ϑ , γ , and ψ (with the objective of subsequent use of these values to calculate the matrix elements b and realize the aforementioned analytic geographical correlation method), it is proposed that we use the images of geographic features present on the pictures, which may be the outlines of continental coastlines, courses of large rivers and canals, and so on.

The coordinate systems and notations used in the following analysis are shown in Figure 1, where $OX_{\Gamma}Y_{\Gamma}Z_{\Gamma}$ is a rectangular geocentric coordinate system whose origin coincides with the center of the sphere of radius R ; the OZ_{Γ} axis is directed toward the North Pole, and the OX_{Γ} axis lies in the plane of the zero meridian.

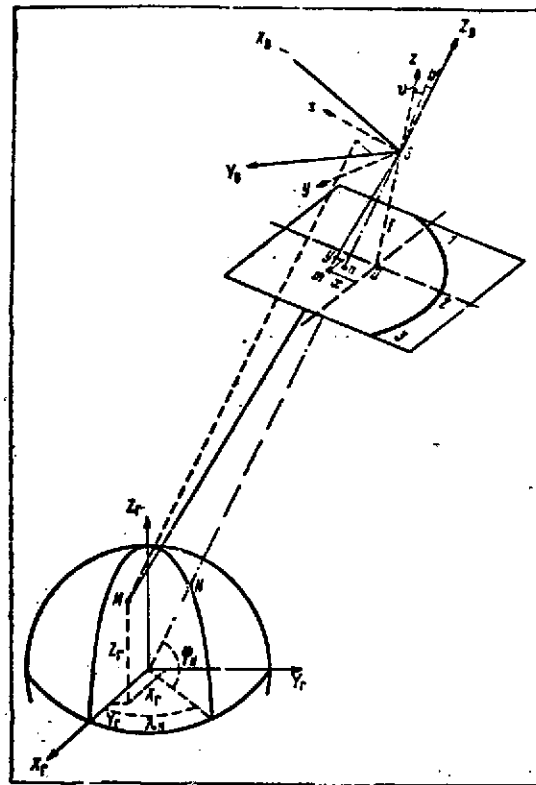


Figure 1. Rectangular coordinate systems

In the general case, the imaging camera coordinate system S_{xyz} coincides with the satellite structural axes system.

$SX_B Y_B Z_B$ is an auxiliary rectangular coordinate system whose SZ_B axis is directed along the local vertical, and SX_B axis coincides

with the direction of the satellite absolute velocity vector. M is a point of the Earth's surface with known geographic coordinates ϕ_M and λ_M (X_{FM} , Y_{FM} , Z_{FM} are its coordinates in the rectangular geocentric system, and x_m , y_m are the coordinates of the identified point in the image plane).

In the subject problem, the known parameters are the satellite coordinates at the instant of photographing, and the coordinates of the geographic features on the ground and on the picture. Determination of the angular orientation elements is accomplished by means of transformation formulas utilizing series expansion of trigonometric functions of small angles. The problem is solved by successive approximations.

A minimum of two geographical features must be identified on the picture for the solution of the problem by the proposed method.

Specifying the initial values of the picture angular orientation elements ϑ , γ , ψ , the following formulas are used to calculate the rectangular coordinates of the identified points in the auxiliary coordinate system: /142

$$\begin{aligned} Z_B &= -[H + R(1 - \cos \sigma)], \\ X_B &= Z_B \frac{x'}{z'} = Z_B \frac{xb_{11} + yb_{12} + fb_{13}}{xb_{21} + yb_{22} + fb_{23}}, \\ Y_B &= Z_B \frac{y'}{z'} = Z_B \frac{xb_{21} + yb_{22} + fb_{23}}{xb_{31} + yb_{32} + fb_{33}}. \end{aligned} \quad (6)$$

The transformation formulas (6) mean that the inclined picture plane is referred to the horizontal plane $Sx'y'$ coinciding with the plane SX_BY_B , and the new calculated image point coordinates (x', y', z') are reduced to a scale equal to X_B/z' . /143

These same rectangular coordinates of the identified points in the auxiliary coordinate system can be obtained if their geographic

coordinates and the geographic coordinates of the subsatellite point at the same instant of photographing are known

$$\begin{aligned} X_3 &= (X_{\Gamma M} - X_{\Gamma S})a_{11} + (Y_{\Gamma M} - Y_{\Gamma S})a_{21} + (Z_{\Gamma M} - Z_{\Gamma S})a_{31}, \\ Y_3 &= (X_{\Gamma M} - X_{\Gamma S})a_{12} + (Y_{\Gamma M} - Y_{\Gamma S})a_{22} + (Z_{\Gamma M} - Z_{\Gamma S})a_{32}, \\ Z_3 &= (X_{\Gamma M} - X_{\Gamma S})a_{13} + (Y_{\Gamma M} - Y_{\Gamma S})a_{23} + (Z_{\Gamma M} - Z_{\Gamma S})a_{33}. \end{aligned} \quad (7)$$

If the angular orientation elements θ, γ, ψ are known exactly, then X_B, Y_B, Z_B , found using (6), coincide with the values X_3, Y_3, Z_3 of the same points found using (7). In the case when the angles θ, γ, ψ are known with some error, which occurs in the subject case, then the differences $\Delta X = X_3 - X_B$, $\Delta Y = Y_3 - Y_B$, and $\Delta Z = Z_3 - Z_B$ will be nonzero. This means that the $Sx'y'$ plane to which the picture is reduced does not coincide with the horizontal plane SX_BY_B . The angles $\Delta\theta', \Delta\gamma'$ and $\Delta\psi$ characterizing the rotation of the unit vectors of the system, associated with the plane $Sx'y'$ relative to the unit vectors of the system $SX_BY_BZ_B$, are called the residual tilt angles. In order to establish the connection between these angles and the errors $\Delta X, \Delta Y$, we write the re-transformation formulas. Since upon re-transformation, the values of X_B' and Y_B' should equal the values of X_3 and Y_3 found using (7), the right sides of the transformation formulas may be equated, respectively, to the values of X_3 and Y_3 . With account for smallness of the angles $\Delta\theta', \Delta\gamma', \Delta\psi'$, the re-transformation formulas reduce to the form

$$\begin{aligned} X_3 &= -\frac{Z'_B}{f} x' \cos \Delta\psi - \frac{Z'_B}{f} y' \sin \Delta\psi + Z'_B (\Delta\gamma' \sin \Delta\psi + \Delta\theta' \cos \Delta\psi), \\ Y_3 &= -\frac{Z'_B}{f} x' \sin \Delta\psi + \frac{Z'_B}{f} y' \cos \Delta\psi + Z'_B (\Delta\theta' \sin \Delta\psi - \Delta\gamma' \cos \Delta\psi). \end{aligned} \quad (8)$$

We substitute into these expressions the coordinates of the two identified points, and subtract from the equations of the first point the corresponding equations of the second. Setting $(Z_{B_1}) \cong (Z_{B_2})$, we obtain

$$\begin{aligned}\Delta X_3 &= -\frac{Z'_B}{l} \Delta x' \cos \Delta \psi + \frac{Z'_B}{l} \Delta y' \sin \Delta \psi, \\ \Delta Y_3 &= -\frac{Z'_B}{l} \Delta x' \sin \Delta \psi + \frac{Z'_B}{l} \Delta y' \cos \Delta \psi,\end{aligned}\quad (9)$$

where

$$\begin{aligned}\Delta X_3 &= (X_3)_1 - (X_3)_2, \quad \Delta x' = x'_1 - x'_2, \\ \Delta Y_3 &= (Y_3)_1 - (Y_3)_2, \quad \Delta y' = y'_1 - y'_2.\end{aligned}$$

From (9), we can find $\Delta \psi$:

$$\Delta \psi = \arcsin \left\{ \frac{A}{B} \right\}, \quad (10)$$

where

$$A = \Delta X_3 \Delta y' - \Delta Y_3 \Delta x', \quad B = \frac{Z'_B}{l} [(\Delta x')^2 + (\Delta y')^2].$$

After finding the angle $\Delta \psi$, we can find the quantities $\Delta \theta'$ and $\Delta \gamma'$:

$$\begin{aligned}\Delta \theta' &= \frac{(X_3 \cos \Delta \psi + Y_3 \sin \Delta \psi) - X_B}{Z_B}, \\ \Delta \gamma' &= \frac{(X_3 \sin \Delta \psi - Y_3 \cos \Delta \psi) - Y_B}{Z_B},\end{aligned}\quad (11)$$

where the values of X_B , Y_B , Z_B are calculated using (6).

The quantities $\Delta \theta'$ and $\Delta \gamma'$ are the residual pitch and roll angles relative to the intermediate axes Sx' and Sy' , obtained as a result of the first transformation using (6). The angles θ and δ , which require refinement, are measured relative to the Sx and Sy axes; therefore, the magnitudes of the corrections obtained should also be referred to these axes. Since the angle between the Sxy and $Sx'y'$ frames is equal to the angle ψ , it is known that transformation of the residual angles $\Delta \theta'$ and $\Delta \gamma'$ into the quantities $\Delta \theta$ and $\Delta \gamma$ can be accomplished using the coordinate system rotation formulas

$$\Delta \theta = \Delta \theta' \cos \psi - \Delta \gamma' \sin \psi, \quad \Delta \gamma = \Delta \theta' \sin \psi + \Delta \gamma' \cos \psi. \quad (12)$$

Substituting (11) into (12), we finally obtain

$$\begin{aligned}\Delta\theta &\simeq \frac{[X_3 \cos(\psi + \Delta\psi) + Y_3 \sin(\psi + \Delta\psi)] - [X_B \cos\psi + Y_B \sin\psi]}{Z_B}, \\ \Delta\gamma &\simeq \frac{[X_3 \sin(\psi + \Delta\psi) - Y_3 \cos(\psi + \Delta\psi)] - [X_B \sin\psi - Y_B \cos\psi]}{Z_B}.\end{aligned}\quad (13)$$

The sought orientation angles are obtained as the sum of the values obtained in several successive approximation

$$\theta = \Sigma \Delta\theta_i, \quad \gamma = \Sigma \Delta\gamma_i, \quad \psi = \Sigma \Delta\psi_i.$$

Characteristic of Earth's surface imaging from high-orbit satellites is the fact that on most of the pictures we see the image of the horizon line, which can also be used for determining the imaging camera angular orientation elements relative to the local vertical and for refining the photographic altitude. The idea of the proposed technique is that, if the optical axis of the imaging camera coincides with the local vertical, the horizon line will be a circle whose center coincides with the picture principal point. Therefore, we can estimate the magnitudes of the pitch and roll angles from the distance between the center of curvature of the horizon line and the picture principal point. /145

The problem of determining the pitch and roll angles for a picture having an image of the horizon line is solved by successive approximations.

The horizon line is taken as a circle whose center coordinates a and b are obtained from the solutions of the system of equations [14]:

$$\begin{aligned}(x_1 - x_2)a + (y_1 - y_2)b &= \frac{(x_1^2 + y_1^2) - (x_2^2 + y_2^2)}{2}, \\ (x_1 - x_3)a + (y_1 - y_3)b &= \frac{(x_1^2 + y_1^2) - (x_3^2 + y_3^2)}{2}.\end{aligned}\quad (14)$$

where x_i, y_i ($i=1, 2, 3$) are the coordinates of three arbitrary points of the horizon line image.

The value of the pitch θ and roll γ angles are calculated from the found values of the circle center coordinates:

$$\gamma' = -\operatorname{arctg} \frac{b}{f}, \quad \theta' = \operatorname{arctg} \frac{a \cos \gamma'}{f}, \quad (15)$$

where f is the focal length of the imaging camera.

The found approximate orientation angles are used to calculate the transformed image point coordinates

$$\begin{aligned} x_i' &= -f \frac{x_i \cos \theta' + y_i \sin \gamma' \sin \theta' - f \sin \theta' \cos \gamma'}{-x_i \sin \theta' + y_i \cos \theta' \sin \gamma' - f \cos \theta' \cos \gamma'}, \\ y_i' &= -f \frac{y_i \cos \gamma' + f \sin \gamma'}{-x_i \sin \theta' + y_i \cos \theta' \sin \gamma' - f \cos \theta' \cos \gamma'}. \end{aligned} \quad (16)$$

After this, the calculation process is repeated, beginning with determination of new values of the horizon line center of curvature coordinates. The solution is considered terminated when the horizon line center of curvature coordinates obtained as a result of the last approximation are equal to zero. /146

Using the coordinates of the horizon line image points obtained in the last approximation, we can calculate the photographing altitude

$$H = \left[R - R \sin \left(\operatorname{arctg} \frac{r}{f} \right) \right] / \sin \left(\operatorname{arctg} \frac{r}{f} \right), \quad (17)$$

where $r = \sqrt{x_i'^2 + y_i'^2}$ is the radius of curvature of the horizon line in the last approximation.

The proposed methods were realized at the Hydrometcenter of the USSR on a Minsk-22 computer, and were used to process the Earth cloud cover pictures obtained from the communications satellite



Figure 2. Picture of the Earth obtained from the Zond-5 automatic interplanetary station with grid of meridians and parallels

Molniya 1 and the automatic stations Zond 5 and Zond 7. Experience in using these methods showed that the accuracy of orientation angular element determination is on the order of 1° .

Figure 2 shows a picture obtained from the Zond 5 station. The grid of meridians and parallels for this picture was obtained using the formulas presented above.

References

1. Solov'yev, V. I. and I. S. Solov'yeva. Determination of the External Orientation Angular Elements of Pictures from Weather Satellites. Trudy Gidromettsentra SSSR, No. 11, 1967.
2. Solov'yev, V. I. and I. S. Solov'yeva. Cartography of Cloud Cover Pictures Obtained from the Molniya 1 Satellites. Trudy Gidromettsentra SSSR, No. 30, 1968.

GEOLOGICAL AND GEOPHYSICAL STUDIES FROM SPACE AND
PROSPECTS FOR THEIR DEVELOPMENT

G. B. Gonin, A. I. Vinogradova,
B. V. Shilin, N. A. Yakovlev

Photographic and television images of the Earth's surface, obtained from spacecraft in the visible part of the spectrum, are widely used for geological interpretation. We shall analyze the possibilities of using images obtained by devices which detect the reflected and self-radiation of the Earth's surface and atmosphere in other parts of the spectrum.

Table 1 lists the imaging systems used for geological purposes and the associated spacecraft. Space imaging can be considered a new technique for geological and geophysical study of our planet. /147

It is advisable here to use space imaging to solve, first of all, those problems in which qualitatively new data can be obtained. At the same time, all the data obtained from spacecraft must be used together with the data of surface and aerological studies.

The images in the visible portion of the spectrum obtained from space make it possible to analyze the characteristics of the geological structure of the imaged area, and measure this structure. These measurements make it possible to obtain the quantitative characteristics of the various structural elements, carry out cartography and correlation of the data obtained by nonphotographic sensors.

The arbitrary classification of the images obtained from spacecraft, shown in Table 2, has been proposed.

Soviet and foreign experience in geological interpretation of photographs obtained from low orbital altitudes shows that they can be used to solve the following problems: /148

TABLE 1. REFLECTED AND SELF-RADIATION OF EARTH'S SURFACE
ELEMENTS RECORDED ABOARD SPACECRAFT

Spectral region	Band	Atmospheric absorption	Recording	SC
Visible	0.4-1.0 μ	Weak	Photographic Television Spectro-graphic	Soyuz, Gemini, Zond, Apollo Meteor, ESSA, Nimbus ATS, MSC, Soyuz
Infrared	1.0-20.0 μ	Windows 1.8-5.3 μ 7.0-14.0 μ	Scanning radiometers	Meteor, Nimbus
Radio-thermal*	0.8-1.35 cm	Strong (depends on atmos. moisture)	Radiometers	Kosmos 243
	3.4-8.5 cm	Very weak	—	—
Magnetic field**	—	None	Magnetometers	Kosmos 43

*Sensitivity 1 - 5° C depending on underlying surface temperature.

**Sensitivity to $\pm 0.5 \gamma$.

TABLE 2. TYPICAL DATA ON PHOTOGRAPHIC IMAGES OF THE EARTH
OBTAINED FROM SPACE

Orbital altitudes	SC	Image scales	Surface resolution	Surface coverage
Low (200 - 300 km)	Soyuz, Gemini, Apollo	1:2·10 ⁶ - 1:8·10 ⁶	20 - 200 m	10 ³ km
Middle (1000 - 2000 km)	Weather AES	1:6·10 ⁶ - 1:10·10 ⁷	1 - 3 km	~1000 km
High (30,000 - 90,000 km)	ATS Technology AES, Zond, Apollo	1:5·10 ⁷ - 1:2·10 ⁸	6 - 15 km	Entire Earth's disk

1. Revision, refinement, and correlation of geological maps of scale 1 : 200,000 and smaller; a specific objective would be use of such photographs in updating various geological maps.

2. Preparation of preliminary photogeological maps of scale 1 : 200,000 for regions in which accelerated geological surveys are planned.

3. Revision, refinement, and preparation of small-scale tectonic, geomorphological, and other maps.

4. Identification, analysis, and refinement of the formation of folded structures of size on the order of tens of kilometers and more, discontinuous fracture zones tens and hundreds of kilometers in extent, and also the spatial interrelationships of these structures.

5. Study of areas which are promising in regard to ore deposits, oil, and gas exploration

6. Study of large igneous rock massifs, identification of the annular structures of magmatic complexes and fracture systems.

7. Studying the nature and intensity of the contemporary physical and geological processes whose action shows up in large regions, measured in thousands of square kilometers (denudation and accumulation processes).

This listing will be broadened and refined continuously as we accumulate space imaging data and experience in their geological interpretation; a characteristic feature will be the resolution of primarily regional and global problems.

Experience in geological interpretation of television pictures obtained from intermediate altitudes indicates the advisability of their use as an additional source of information on the geological structure of vast regions.

/149

The possibilities of geological interpretation of photographs obtained from high altitudes can be evaluated on the basis of analysis of the photographs of Africa obtained from the Zond 5 spacecraft. Preliminary analysis led to the conclusion that there was promise in using the data from these pictures to refine the content of various sorts of synoptic geological maps in solving global geological problems, and verifying geological hypotheses. In the analysis process, it was found to be valuable to compare photographs of a particular region obtained from different altitudes, and differing markedly in scale. A previously unknown global fault running east-northeast, which can be traced nearly across the entire continent, was tentatively identified on a photograph from the Zond 5 spacecraft in the north of Africa. Data confirming its existence were obtained in studying larger scale pictures from Gemini 4 and perspective aerial photographs of areas located along the path of the fault.

The television pictures obtained from technology satellites are equivalent, in regard to field of view, to the photographs from the Zond 5 spacecraft, but are somewhat inferior in resolution. Geological problems of global nature can also be solved using these pictures.

The information in the visible part of the spectrum, obtained with the aid of spectrographs, occupies a special position. The spectrograph was first used for measuring the optical characteristics of landscape features on the Soyuz 6 and Soyuz 7 manned spacecraft. In this case, the additional information on the optical characteristics of the landscape features will play the same role as in aerial spectrophotometry using airplanes.

The radiativity and thermal regime of individual geological formations can be determined with the aid of IR and microwave systems. Table 1 lists only the scanning radiometers operating in the IR band. The IR systems intended for obtaining averaged values of the radiation and the thermal regime over areas of hundreds of thousands of square kilometers are not of interest for geological purposes.

The scanning radiometers provide spatial resolution on the order of a few degrees, with sensitivity to temperature differentials from ± 1 to $\pm 10^\circ$. With these parameters, the IR images can be used to study only very large geological structures and vast regions. However, installation aboard spacecraft in the next few years of IR scanning systems with resolution of about 0.1 mrad and ground sensitivity of no less than 2° C is quite realistic. With the aid of such systems, the temporal variations of the temperature contrasts of the landscape features, as shown by periodic surveys, provide important additional geological information, primarily on soil moisture content, geological formations, land subdivision systems with moisture content increase, regions of active geothermal activity, and so on. /150

The use of microwave systems in studying the Earth's surface is in the stage of satellite and airplane experiments. The practically total transparency of the atmosphere and cloud cover for the centimeter band and the satisfactory transparency for the millimeter band favor the application of these systems. Measurement of the Earth's thermal radiation was first accomplished from the Kosmos 243 satellite in 1968. The use of this band for studying the oceans is most promising. The study of the thermal radiation of the land for geological purposes lies further in the future because of the low spatial resolution of the systems.

The effectiveness of Earth's magnetic field measurements from spacecraft is not clear. According to the calculated data, the decay of the magnetic field intensity of very large geological formations to the normal geoid field takes place at altitudes not exceeding one hundred kilometers. Joint analysis of magnetic measurements from spacecraft and airplanes makes it possible to verify the validity of the theoretical magnetic field calculations for large anomalies with complex field, and also the depth of occurrence of certain geological features (effusive synclinal layers, effusive platform mantles, and so on). Of interest in this regard are the studies made of the residual geomagnetic fields (less than 100 gamma), obtained as the difference of the values measured aboard the Kosmos 49

satellite and calculated analytically. The differences obtained were compared with the anomalous magnetic field at the Earth's surface, with account for the peculiarities of the geological structure and thermal flux distribution.

The use of other receivers and systems installed aboard spacecraft for geological and geophysical purposes remains in the future, and in many cases is very problematical. Studies of the geochemical (gas content in the atmosphere), luminescent, and certain other images from space, make it possible to conclude that these images are not effective for geological purposes.

The systems operating in the microwave band include sidelooking radars and scatterometers, used for quantitative differentiation of the subsurface layer with the aid of reflected radiowaves. Such systems are being prepared for tests aboard spacecraft. Their use in geology is of definite interest.

/151

The need should be noted for improvement of the characteristics of the photographic systems, which are one of the basic technological techniques in geology. This improvement is coming in two directions. First, the photographic systems will be expanded in order to obtain images of different scales. Second, photographic surveys in narrow spectral zones, with the aid of narrow-band light filters and recording on photographic film, are beginning to be developed. Proposals have been made for installation of photoelectronic systems for obtaining images in the 20 - 40 nm band. One such system is a camera which permits obtaining images with given ratio of the spectral brightness coefficients. The use of such a camera makes it possible to identify and map specific geological features which have been identified by their optical characteristics. For this purpose, we must study the optical characteristics of geological features or their indicators during observation from space.

The resolution of the television systems operating in the visible band needs to be improved to the level of the conventional photographic systems.

This listing of presently used and future systems for obtaining geological information indicates the necessity even today to conduct studies on selection the most effective detector types. The experimental studies in this field must be conducted using special test ranges.

On the basis of the interests of geological and geophysical investigations, the basic criteria for test range selection are the following: representative of the basic geological conditions of the USSR in regard to the theoretical and practical problems of modern geology; display of geological features on the Earth's surface under conditions of various landscapes with different intensity of economic development, including shallow-water shelf regions; good geological-geophysical and geographical information, availability of geodesic reference when studying the metric properties of images obtained by the different systems; favorable conditions for the organization of aerial and ground studies with minimum expenditures of funds and time.

When performing integrated regional space imaging studies, we can obtain a direct image of large elements of the geological structure and operations can be planned with specific goals in mind. In solving the posed problems, we must be certain the test ranges are representative of the basic geological and economic conditions of the territory of the USSR. The following regions meet these selection criteria and experimental investigation objectives: the Baltic shield, the region of traprock and kimberlite distribution on the Siberian platform, the Crimea-Caucasus region and adjacent water areas of the Black, Azov, and Caspian Seas; the Southern and Central Urals, including the iron-ore belt of the Turgaisk fold; the Kuril-Kamchatka region; the Baikal region; Pamir-Tyan'-Shan, the Dneper-Donets region — Donbass; Central Kazakhstan; southwestern Turkmenia and the adjacent water area of the Caspian Sea; and Western Siberia.

The eleven regions listed encompass diverse landscape conditions for both land areas and seacoasts.

Ground studies and surveys from definite altitudes using different energy sensors should be made on each of the listed test ranges on the basis of the specific geological and geographic conditions.

The objectives and content of the studies for each of the test ranges require special discussion. The area of each of the test ranges should be determined on the basis of the dimensions of the geological features. On the average, for pictures on a scale of 1 : 2,000,000 - 1 : 3,000,000, the area of a single test range will be on the order of 300,000 km².

Along with the resolution of the interpretation problems, one of the central research questions is the development of photogrammetric methods in application to images from space. Specifically, one of the urgent problems is the creation of photomaps or refined photodiagrams with scales on the order of 1 : 1,000,000 - 1 : 3,000,000. The creation of such photomaps and photodiagrams is of great interest for geology and other branches of the national economy.

The questions of geological interpretation and photogrammetry must be developed in application to images obtained by both framing and scanning systems.

Such are the prospects for the growth of geological and geophysical studies from space. These techniques will be refined and implemented as space technology develops, and experience is accumulated.

EXPERIENCE IN INTEGRATED GEOLOGICAL AND GEOGRAPHICAL
INTERPRETATION OF SPACE PHOTOGRAPHS OBTAINED
IN THE USSR

B. V. Vinogradov, A. A. Grigor'yev

The successes in the individual areas of development of space methods of geographical study are varied; we shall discuss only the recording techniques which provide the most information — the photographic and television (TV) systems. /153

We shall discuss two examples of regional interpretation of a picture taken aboard the Zond 7 automatic interplanetary station and a TV image from the Kosmos satellite.

Two dust and sand streams flowing above the Arabian Peninsula were recorded on the ultra-small-scale color photograph (Figure 1). The beginning of one vortex-like flow above the eastern part of the Mediterranean water area and Asia Minor is clearly seen in the photograph. From this region, it travels as a wide band of width up to 300 km in the southeast direction above Northern Arabia, Iraq, and Southwestern Iran. A high degree of correspondence between the extent of the flow and the large relief forms (Figure 2) is noted. The flow travels above the low-lying northern part of the Arabian Peninsula and the plains of Central and Southern Arabia. This direction of motion of the dust and sand flow is determined by the direction of the winds and the location of the large relief forms. The flow continues for a distance of 2000 km along the natural corridor formed by this relief.

Another dust and sand flow seen in the photograph begins in the South of the Libyan Desert, crosses the Red Sea (see Figure 1), then crosses the Rub-al-Khali Desert in the northeast direction, and continues on across the Persian Gulf. It is particularly



Figure 1. Ultra-small-scale color photographic image of northeast Africa, Arabia, and Asia Minor (fragment of global photograph of the Eurasian and northeastern African continents) obtained on August 8, 1969 from the Zond 7 automatic interplanetary station (scale $\approx 1 : 30,000,000$)

noticeable above the Red Sea and the Strait of Ormuz in the form of a whitish shroud masking the water surface.

It is important that the zone of movement of these flows correspond to regions covered by large sandy massifs — the Great Nefud Desert, the Dehna Desert, and the largest of all, the Rub-al-Khali. Various types of aeolian relief are common in these deserts in the

zone where these flows travel; however, the dominant form is the ridge-type relief of the seifs — huge longitudinal dunes.

Comparison of the occurrence of the dust and sand flows and the longitudinal dunes demonstrates a high degree of correspondence between the orientation of the seifs and the vortex-like flows over the entire path of their travel (Figure 2). The seifs of the Great Nefud Desert (in the Ed-Dahna region), oriented from northwest to southeast, are replaced by seifs whose directions change gradually near the junction with the Rub-al-Khali Desert, and in the Rub-al-Khali Desert the longitudinal dunes are now oriented in the NNW-SSE direction and then in the NE-SW direction. The last "bursts" of aeolian activity along the path of the air flow are noted in the Ramlat-es-Sabtain Desert. In the larger-scale space photographs, we see clearly how the seifs literally run into the mountain chains bounding the desert on the south and southwest.

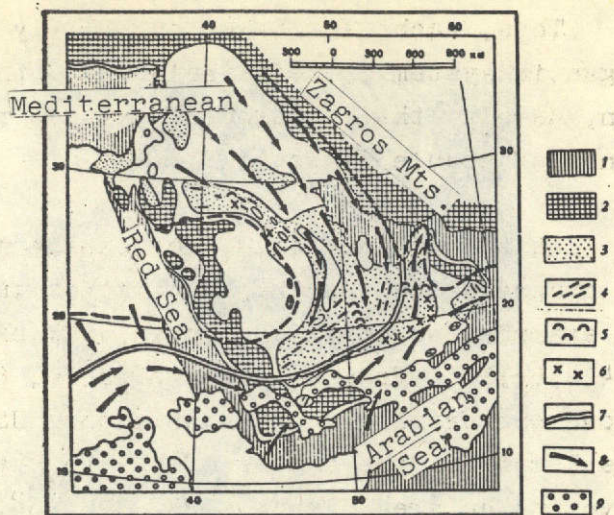


Figure 2. Diagram-chart of interconnection between the dust and sand flows interpreted from a space photograph (Figure 1) and the occurrence of highlands, aeolian relief forms, and wind-blown sands (prepared by B. V. Vinogradov, A. A. Grigor'ev, and V. P. Lipatov):

- 1 — water areas; 2 — highlands (mountains and plateaus) with absolute heights above 1.8 km; 3 — regions of wind-blown sands; 4 — regions of dominant development of longitudinal dunes (their orientation is shown); 5 — regions of dominant development of barchans; 6 — regions of dominant development of hilly sands; 7 — zone of intertropical convergence; 8 — regions of development of dust and sand flows, interpreted from a space photograph obtained from the Zond 7 automatic interplanetary station; 9 — cloud cover

/154

Thus, each self taken separately is a portion of a single gigantic system of selfs related by the common nature of their origin, namely: the functioning in this region of constantly acting winds of stable directions.

At the present time, most space images arrive at the Earth over TV channels from weather satellites in medium altitude orbits. As /155
an example, we shall interpret a TV picture obtained by the Kosmos 144 satellite from a height of about 600 km. The TV image (Figure 3) shows the territory of southwestern USA and northwestern Mexico (in the limits of the states of California, Lower California, and Sonora) covering an area of about 230,000 km². The scale of the original TV picture was about 1 : 7,100,000. The picture was taken in clear weather. The landscapes of subtropical semideserts and early spring deserts are recorded on the TV picture.

1. The landscape of the alluvial delta plane of the Colorado river (Figure 4) is well identified from its triangular blade-like shape, the branchings of the Colorado River, and the relatively darker image tone, contrasting with the image of the adjacent territories. The two parts of the delta formed by sand-clay alluvial deposits are clearly differentiated — the upper and lower deltas.

The upper, older, and relatively higher part of the delta plain, covered by brush and tree vegetation and partly by agricultural farms, is characterized by low albedo values and is imaged by a nonuniform dark-gray tone.

The lower, younger, and relatively lower-lying part of the delta is marked by more sparse vegetative cover, through which the ground surface "radiates" over a considerably larger area, is characterized by high albedo values and is imaged by a somewhat brighter non-uniform gray tone.

The nonuniformity of the delta image structure is due to the heterogeneity of the landscape pattern. The darkest image tone is characteristic of the Colorado River channels.

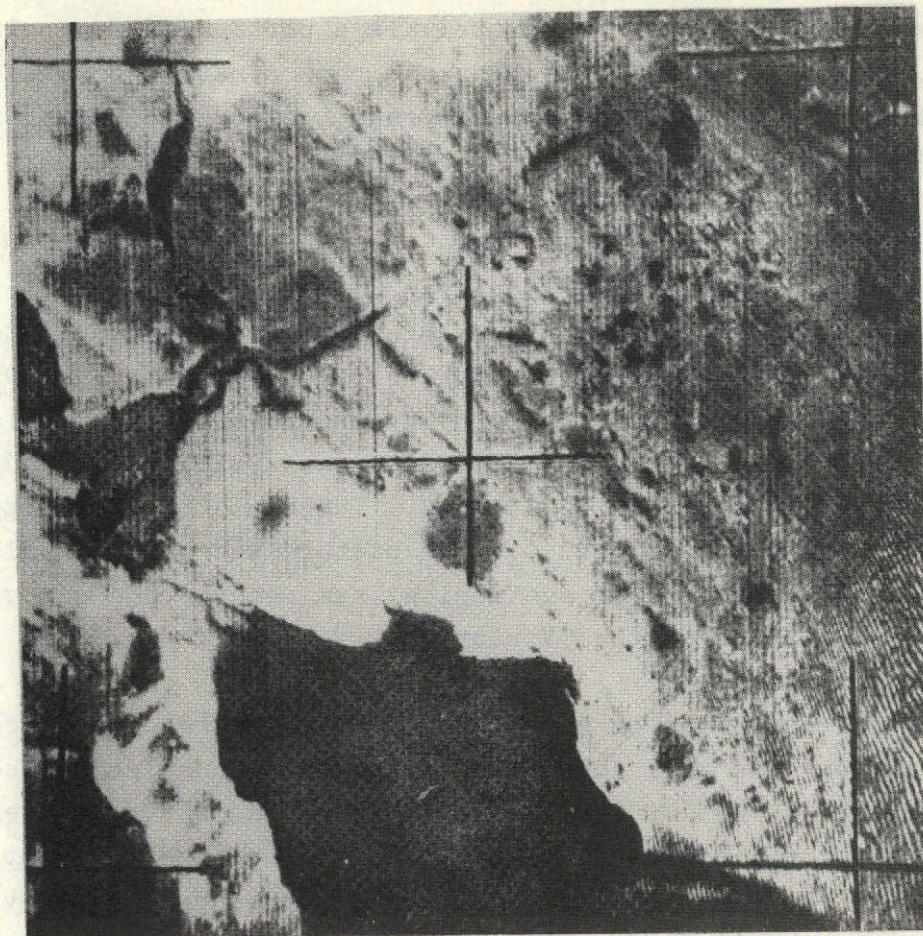


Figure 3. Fragment of TV picture of southwestern USA and northwestern Mexico, obtained on March 23, 1967 from the Kosmos 144 satellite at an altitude of about 600 km (blown up from a negative of scale about 1 : 7,000,000)

The image of the channels contrasts markedly with the image of the adjacent delta segments.

Just as clearly differentiated are the natural complexes of flat plains, which have developed in the limits of the lower delta and are made up of surfaces with salt deposits (primarily halites). These are gigantic salt flats, among which Lago Salinas stands out. They are practically devoid of vegetative cover, are characterized by

high albedo, and are imaged by a brighter tone in comparison with all the other landscape elements.

2. The ancient lacustrine Mesa Orientale plain is formed by alluvial-lacustrine sand-clays with gravelly and sandy deposits with sparse creosol desert vegetation. The considerably simpler in structure, in comparison with the delta, landscape of the ancient lacustrine plain is identified on the TV picture from the homogeneous gray tone of the image; the image brightness in this case is due primarily to the soils, which are scarcely masked by any vegetation at all.

3. The Pinacate lava plateau with rugged relief is formed by a large number of volcanos, lava flows, and lava beds formed by young Pliocene-Quaternary formations. The plateau landscape is characterized by small

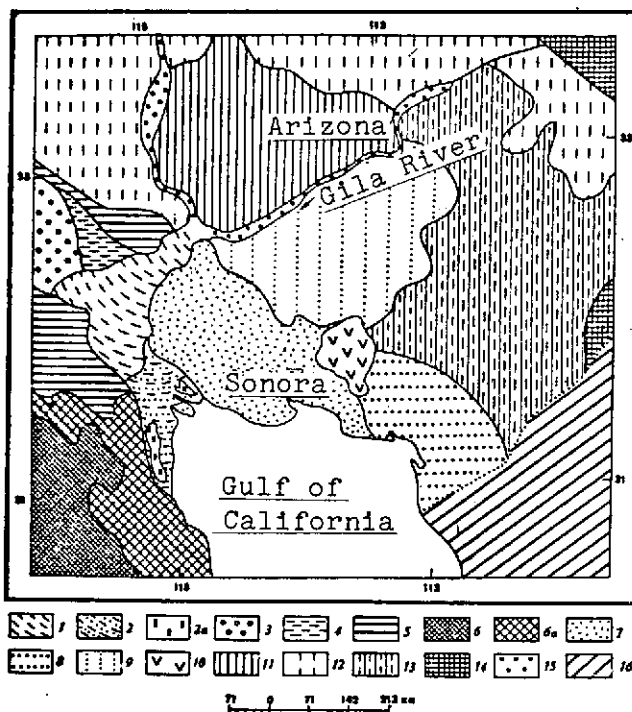


Figure 4. Landscape interpretation of TV image (Figure 3)

1 — landscapes of low-lying alluvial-lacustrine plains of large intermontane depression: 1 — upper-delta plains with wooded scrub vegetation and agricultural farms; 2 — lower delta plains with salt flats and marshes; 3 — salt flat plains; 4 — relatively low-lying alluvial-lacustrine plains, primarily with agricultural lands; 5 — lacustrine plains with creosol desert vegetation; 6 — alluvial-lacustrine and alluvial-marine plains with creosol desert vegetation; 7 — low and intermediate mountain landscapes, formed primarily by intrusive rocks with chaparral and pine-juniper forests; 8 — sloping piedmont plains in combination with foothill "insular" ridges; 9 — landscapes of sand-clay accumulative plains with creosol desert vegetation in combination with isolated ridges formed primarily by intrusive and volcanic rocks with sparse-pine-juniper forests; 10 — low-lying plains with numerous aeolian forms and individual "insular" ridges; 11 — low-lying plains with aeolian forms and infrequent (cont'd)

/157

albedo values due to the dark coloring of the volcanic rocks which make up the plateau, which is only weakly masked by sparse vegetation and is identified in the picture by the very dark tone, the only darker tone being that of the water area of the Gulf of Mexico. The volcanic plateau stands out clearly in the form of an irregular circular spot on the lighter background of the surrounding plain. The small scale of the TV picture limits interpretation of the image of most of the volcanos and lava flows; nevertheless, we can differentiate on the picture the larger volcanic forms, which are identified by the relatively darker tone and the circular, in the form of freckles, image.

4. The landscape of the flat accumulative plain with extensive development of aeolian forms and sparse creosol scrub desert vegetation shows up in the Gran Desierto. Within the limits of the Gran Desierto, the plainlike nature of the terrain is infrequently disrupted by "insular" ridges, but far more often we find here aeolian forms and, on the whole, the landscape has a high degree of structure uniformity. As a result of the bright coloring of the Quaternary deposits making up the plain and the sparseness of the vegetative cover, the landscape is characterized by quite homogeneous, relatively high albedo, and is represented on the TV picture by a quite homogeneous light gray tone. One of the "insular" ridges, formed by darker colored intrusive rocks, can be clearly identified in the central and eastern parts of the desert on the light background — its image stretching from the NW to the SE as a dark streak.

In conclusion, we can say that experience in interpreting the TV image of a comparatively thoroughly studied region of the Earth

(Figure caption cont'd)

"insular" ridges; 9 — plains in combination with narrow, subparallel "insular" ridges; 10 — very rugged volcanic plateau; 11 — plains in combination with "insular" ridges with extensive development of elements; 12 — plains in combination with nonoriented, primarily large "insular" ridges; 13 — plains in combination with numerous "insular" ridges of differing orientation; 14 — intermontaine landscapes formed by volcanic and intrusive rocks, with pine and pine-juniper forests in combination with bolsons; 15 — river valley landscapes; 16 — break in image reception

indicates the advisability of using such images for geological and geographic studies of those regions of the earth for which original space photographs do not exist.

References

1. Bugayev, V. A. Analysis of the State of the Atmosphere Above the Earth from an Altitude of $90 \cdot 10^6$ m from a Picture Obtained by the Zond 5 Space Station. *Meteorologiya i gidrologiya*, No. 7, 1969. /158
2. Vinogradov, B. V. Space Photography for Geographic Study of the Earth. *Izvestiya VGO* (News of the All-Union Geographic Society), 98, No. 2, 1966.
3. Vinogradov, B. V. Combined Interpretation of Images of the Earth's Surface Obtained from Nimbus 1. *Izvestiya VGO*, 101, No. 3, 1969.
4. Vinogradov, B. V. Geographic Zonation of the African Sector of the Earth from Global Photography from the Zond 5 Spacecraft. *DAN SSSR*, 191, No. 6, 1970.
5. Vinogradov, B. V. Global Photography of the Earth. *Zemlya i Vselennaya*, No. 1, 1970.
6. Vinogradov, B. V., and A. A. Grigor'yev. Possibilities of Geological Interpretation of Space Photographs of the Earth. *Izvestiya AN SSSR, seriya geol.*, No. 1, 1970.
7. Vinogradov, B. V., and K. Ya. Kondrat'yev. Study of Natural Resources with the Aid of Artificial Earth Satellites. *Vestnik AN SSSR*, No. 12, 1969.
8. Vinogradov, B. V., K. Ya. Kondrat'yev, and D. V. Stepanenko. Possibilities for Interpretation of the Earth from Space Observed in Various Parts of the Spectrum. Collection: *Kosmicheskiye Issledovaniya* (Space Studies), Vol. 4, No. 6. Nauka Press, Moscow, 1968.
9. Gonin, G. B. Aerial Photographic Survey from High Altitudes and Photography from Space for Solving Geological Problems. Collection: *Prikladnaya Fotogrammetriya* (Applied Photogrammetry). Nauka Press, Leningrad, 1969.
10. Sonechkin, D. M. Classification of Types of TV Images of Cloud Cover and the Earth's Surface Obtained from Satellites of the Meteor Experimental System. *Meteorologiya i gidrologiya*, No. 9, 1968.

11. Bashilova, I. I. Possibility of using TV Pictures Obtained From Weather Satellites for Studying the Geological Structure of the Earth. In present collection.

USE OF TV PICTURES OBTAINED FROM WEATHER SATELLITES TO
STUDY THE GEOLOGICAL STRUCTURE OF THE EARTH

I. I. Bashilova

The television pictures which serve as the primary material for the present paper were obtained from Earth satellites of the Meteor system, and are intended for meteorological studies. All the television pictures were received at the Gidrometcenter (Hydrometeorology Center) of the USSR. The picture format was 66 x 66 mm, the scale was 1 : 6,200,000 - 1 : 7,500,000. The theoretical resolution of the television pictures is 1.25 km; in practice, the human analyst's eye can distinguish objects on the picture no smaller than 1 mm, i.e., 7 km on the ground. The pictures may have significant distortions and numerous interferences associated with image transmission; all this makes their interpretation difficult.

A region encompassing part of Central Asia, the eastern part of /159 Iran, and the western regions of Afghanistan and Pakistan was selected for detailed interpretation. Tectonically, this area is part of the Turansk platform and the adjacent alpine folding region to the south. The approximate area of the region is 2,500,000 km².

A montage of television pictures of varying quality was put together for the described region.

The television picture interpretation technique does not differ significantly from interpretation of conventional aerial photographs.

Interpretation of the features identified during analysis was accomplished by comparing these features with physical, geographic, geological, and tectonic maps. It was found that some of the identified objects correspond to natural objects of geographic or geological content, the other (smaller) part consists of television imaging defects and acts as noise in analysis. It was found that all the large geographic objects shown in a physical map of scale 1 : 5,000,000 could be identified and recognized on the television pictures.

Analysis and interpretation of geological objects are more complex processes than interpretation of geographic objects. However, the very first experiment in the study showed that the differences in tonality on the television pictures can be explained by the difference in the composition of the geological formations making up the particular portion of the region.

The light phototone with several comparative gradations from white to light gray and the dark phototone from gray to dark gray are easily noticed on the television pictures. The lighter phototone corresponds to loose Quaternary deposits, while the dark phototone corresponds to bedrock.

The Quaternary deposits can be separated from the older formations quite reliably on the basis of the television pictures of the studied region. The fine phototone shades make it possible to separate the Quaternary deposits with respect to the genetic types shown on maps of corresponding scale.

The first attempt to interpret and analyze bedrock of different ages led to the conclusion that so far we can identify the bedrock from television pictures only very arbitrarily, the boundaries between the interpreted lithological and stratigraphic rock complexes are not visible in many places and, therefore, the contours remain unclosed.

The most interesting and valuable information extracted in analyzing the television pictures relates to the tectonic structure of the region, and the television-photographic image pattern rather than phototone plays the primary role in interpreting regional tectonics. In analyzing regional tectonics by comparing the interpretation diagram with the Tectonic Map of Eurasia to scale 1 : 5,000,000, /160 it was found that segments having the same image pattern belong to a common structural region, while segments having different image pattern belong to different structural regions.

The Turanskaya platform, as a whole, is characterized by a uniform gray phototone without any pattern, with individual dark spotty and striped segments. This television-photographic [telephoto] image pattern corresponds to individual uplifts — regions of Hercynian folding in the eastern part of the Turanskaya platform.

The alpine folded belt is identified on the television pictures by the very marked nonuniform spotty, at times clearly banded, pattern of the telephoto image.

All the large and small depressions of the alpine folded belt are characterized by a light phototone without pattern, and are easily interpreted.

The areas of alpine geosynclinal folded complex have a very specific telephoto image pattern, characterized by narrow and sinuous dark strips, corresponding to ridges.

Another structural unit, foundation projections, has a different telephoto image pattern. This can be noted even on pictures of poor quality. There are two areas with foundation projections in the region described. In spite of the fact that these segments are not equal in area, we can note similarity in their images on the television pictures: isometricity dominates in their form and they are like pieces of flat blocks. A small area in the Kopet-Dag ridge region looks like a "foreign body" among the fine sinuous strips of the geosynclinal folded complex pattern.

An area in the west of the region between the Lut depression and the Namakzar depression has a telephoto image pattern which is characteristic and markedly different from those described above. This pattern can be termed mosaic. Less sharp than for the geosynclinal complex areas, this pattern without dark stripes bands (ridges) makes it possible to assume that this region has possibly experienced subsidence, and is similar to the downfold regions.

The region between the Arabian Sea and the Haran depression has a more or less uniform, finely banded pattern with clearly visible white stripes of sublatitudinal direction (depressions made by the Quaternary deposits). The pattern of the telephoto image of this region is similar to that of the geosynclinal folded complex regions but differs from the latter in details. It is probable that the region between the Arabian Sea and the Haran depression is a geosynclinal folded complex region, formed by rocks of a different structural stage than those described above. Thus, this region is also described on the Tectonic Map of Eurasia. An area with mosaic-banded telephoto image pattern is found in the southwestern part of the region. /161

The mosaic-banded telephoto image pattern is intermediate between the geosynclinal folded complex region pattern and that of the downfolding region. It is possible that this structural region can be treated as intermediate between the two indicated types.

The area of the Predkopetdag frontal downfold is emphasized on the television pictures by a white, uneven, cloud-like strip, owing to the proluvial Quaternary deposits. A similar strip is observed along the coastline of the Arabian Sea. In other words, these regions have a similar telephoto image pattern on the television pictures, which provides a basis for posing the question of whether the Arabian Sea coast area is a frontal downfold.

Discontinuous fractures are easily and quite completely identified on the television pictures. Faults show up differently, but do

not differ essentially from their conventional appearance on aerial photographs.

Thus, when comparing the regional tectonic pattern formulated by interpreting the television pictures with the Tectonic Map of Eurasia (map scale is coarser than the television picture scale), all the large regional structural forms were identified and had a quite definite telephoto image; some structural features which are not on the mentioned map were also identified, and this information altered somewhat the ideas on the tectonic structure of the described region. These differences in tectonic pattern from the Tectonic Map of Eurasia reduce to the following.

The Namakzar Depression in the central part of the region is separated by a folded area and faults from the Southern Afghan depression. On the Tectonic Map of Eurasia, these areas show up as a single extensive depression.

The Southern Afghan depression is surrounded by faults, and is possibly a graben. These faults are not shown on the Tectonic Map.

Faults of very long length with meridional and submeridional directions which are not shown on the Tectonic Map were detected.

The Mekranskaya depression, which is shown in the Tectonic Map of Eurasia, can, on the basis of its interpretive characteristics, be considered an edge downfold.

In the southern half of the region, we can identify six large areas (not counting the foundation projection) which can be interpreted as separate and individual structural zones. On the Tectonic Map of Eurasia in this part of the region, we see two structural stages and a single substage of the geosynclinal folded complex.

/162

Thus, the first experimental study showed that television pictures of the Earth from space can be used for geological and structural analysis.

GLOBAL SMALL-SCALE LUNAR CARTOGRAPHY

Yu. N. Lipskiy, Yu. P. Pskovskiy, Zh. F. Rodionova,
V. V. Shevchenko, V. I. Chikmachev,
L. I. Volchkova

Creation of a map of the entire lunar surface first became possible after photographing of the back side by the Soviet automatic interplanetary stations (AIS) Luna 3, in 1959, and Zond 3, in 1965. On the basis of the Luna 3 pictures, Shternberg State Astronomical Institute [GAISH], together with TsNIIGAik (Central Scientific Research Institute for Geodesy, Aerial Photography, and Cartography) prepared the first Map of the Back Side of the Moon in 1960.

The axes of the Luna 3 photographic cameras at the moment of exposure nearly coincided with the direction of the solar rays, which created lighting conditions similar to full moon conditions. The lack of shadows, typical of full moon conditions, made recognition of the lunar formations and their characteristics difficult. Various methods, including the method of photometric sections, were used to improve the recognitional properties of the photographs. As a result, it was possible to identify about 400 formations. Similar operations were carried out to analyze the Luna 3 pictures, both at Pulkovo and later at the University of Arizona. The difference in the number of identified formations is due to the different methods used. Nearly 90% of all the formations shown on the map prepared by Shternberg State Astronomical Institute and TsNIIGAik were confirmed by later photographs of these areas.

The eastern sector of the back side of the moon was photographed by the Zond 3 spacecraft. A large portion of the pictures were obtained with oblique illumination of the surface by the solar rays. The resolution of these pictures is nearly the same as that of the photographs obtained by modern telescopes at ground-based observatories.

The pictures of the Luna 3 and Zond 3 AIS were correlated in the selenographic coordinate system. The series of Luna 3 pictures covered 25% of the eastern edge zone, while the initial pictures of the Zond 3 series covered 50% of the visible hemisphere. The reference points used were points from the summary catalog of spatial coordinates of reference point, prepared at the Main Astronomical Observatory of the Academy of Sciences of the Ukraine SSR. On the basis of this information, GAISH and the Topographic and Geodesic Service of the USSR prepared in 1966 the first geodesic Complete Lunar Map and a complete Lunar Globe, reflecting 95% of its surface. Since the Luna 3 and Zond 3 pictures did not have adequate overlap with one another, and the extension of the selenographic network was made separately from the west and from the east, there was an unavoidable shift in the grids, maximum at the 180th meridian.

In 1966 - 1967, the American Lunar Orbiter spacecrafts repeated the photography of the back side of the Moon with higher resolution. The question arose of a second edition of the Complete Lunar Map and Lunar Globe.

The primary information for compiling this map were the photographs of the visible hemisphere obtained by Earth-based observatories, the Luna 3 and Zond 3 pictures, and a small number of Lunar Orbiter pictures. The surface of the visible side is reflected quite completely in photographic atlases of the Moon. The best of these is still the Kuiper Photographic Atlas [1] and the Rectified Atlas [2]. However, we should bear in mind that all parts of the lunar disk are not covered by equivalent data. On pictures obtained by Earth-based telescopes, we can differentiate in the center of the disk details larger than 700 m, while at the edge this quantity reaches 5 km. Moreover, at the edges of the disk, the image is highly distorted because of perspective.

However, the photographs of the lunar surface from space are obtained from different distances, with different obliquity, different aspects, and different lighting conditions. These factors

alone created problems in preparing the material for drawing the maps. Moreover, the appearance of the lunar landscape changes markedly as a function of the lighting. However, on the map, the relief must be represented for some specially selected lighting conditions.

As a rule, the lunar surface pictures obtained by spacecraft are perspectives. In preparing these materials for composition operations, we must exclude both the distortions caused by deviation of the photocamera axis from the vertical to the surface and the distortions resulting from curvature of the surface. Usually, they are eliminated by phototransformation and projection onto a sphere. The Complete Lunar Map to scale 1 : 5,000,000 was constructed in an arbitrary cylindrical projection up to the 60th parallel, maintaining the scales at the parallels $\pm 30^\circ$. The regions near the poles are presented in an azimuthal projection, again to a scale of 1 : 5,000,000, in contrast with the first edition, where the polar caps were presented to a scale of 1 : 10,000,000. The catalog of 500 reference points of the Main Astronomical Observatory of the Academy of Sciences of the Ukraine SSR was used as the system of reference points. The correlation of the pictures of the back side in the unified selenographic coordinate system was accomplished by projection onto a sphere, the method developed in the Division of Lunar and Planetary Physics of GAISH. The result was refinement of the selenographic coordinate system on the back hemisphere.

The idea of rectification on the basis of orienting points involves comparison of the photographic image projected onto a spherical screen (Figure 1) with the images of certain contours or points of the given surface segment, plotted on the spherical screen to a given scale from the known coordinates of these features. Thus, the projector with specially prepared slide inserted is positioned at that point in relation to the surface of the spherical screen which the spacecraft imaging camera had at the instant of exposure, relative to the lunar surface. This technique was used to correlate the Zond 3 pictures covering the area from -60 to 170° in longitude, and from $+40$ to -50° in latitude. The mean square error on the photographic map does not exceed $\pm 30'$ in latitude and longitude [4].

/165

We see from comparison of the newly correlated grid with the first edition of the Complete Lunar Map that there was, on the latter, a constantly accumulating shift of the grid. The possibility of error accumulation when shifting from picture to picture, and the appearance of a general shift of the entire grid was noted in the Atlas of the Back Side, Part 2.

In addition to the strip of pictures from Zond 3, several pictures from the Lunar Orbiter spacecraft, comprising two other strips, were correlated (Figure 2). However, the correlation accuracy in these regions is about $\pm 2^\circ$, since the available Lunar Orbiter pictures did not have adequate overlap. The correlation is also refined in the new editions of the American maps. The deviations are of a random nature. However, in the eastern sector region, the

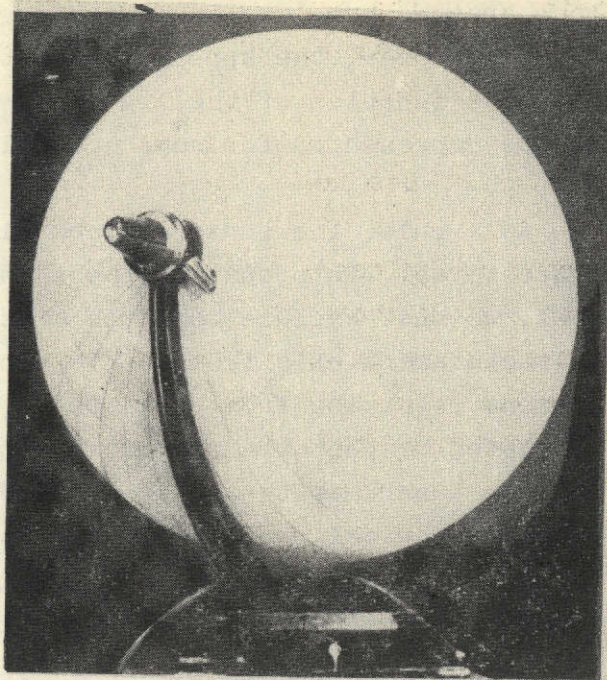


Figure 1. Spherical screen

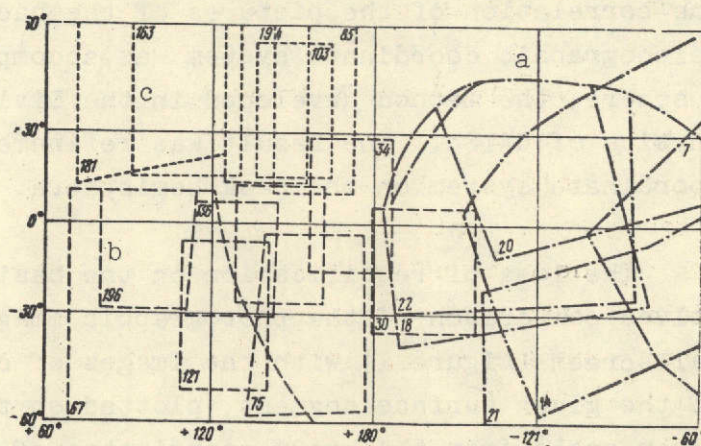


Figure 2. Correlation of pictures of the back side of the Moon:

a — strip 1 (pictures from Zond 3, accuracy $\pm 0.5^\circ$); b — strip 2; c — strip 3 (pictures from Lunar Orbiter (accuracy $\pm 2^\circ$))

position of the meridian and parallel grid on the American maps is approaching nearer and nearer that given in the Complete Lunar Map, second edition.

One of the techniques for independent selenographic correlation of the pictures of the back side was that of determining the selenographic coordinates of the observation point from the position of the Earth's disk above the lunar horizon [5]. The initial data used is primarily the information contained in the image itself. This technique was used to tie the Lunar Orbiter spacecraft pictures to the limb region of the western sector of the back side and the Zond 6 pictures to the eastern limb region. In the first case, the coordinates of the photographing point were determined to within $\Delta\beta \pm 25'$ and $\Delta\lambda \pm 15'$. The calculated accuracy of selenographic coordinate grid plotting was $\Delta\beta \pm 15'$ and $\Delta\lambda \pm 10'$. Shift of the grid relative to the picture because of the error in determining the azimuth of the Earth occurs only in latitude in the limits of $\pm 10'$. However, the calculated grid coincides with a region close to the limb, where the influence of perspective distortions and relief is particularly strong, which may lead in many cases to more significant errors.

/166

The vertical grid control of the eastern sector of the back side of the Moon is characterized by computational errors of the sub-vehicle point: $\Delta\lambda \pm 30'$ and $\Delta\beta \pm 15'$. The corresponding errors of selenographic grid location were $\Delta\lambda \pm 0^\circ, 7$ and $\Delta\beta \pm 0^\circ, 1$. Comparison of the data of control by the astronomical technique and by projection onto a sphere showed that the discrepancies between them are random and are evaluated by mean object position errors of $\Delta\lambda \pm 0^\circ, 6$ and $\Delta\beta \pm 0^\circ, 7$.

The primary content of the Complete Lunar Map is the surface relief and its tonal characteristics. In preparing the map, particular attention was devoted to the variety of lunar relief forms. Formations of the crater type occupy a large part of the lunar surface. The maria, which have dark coloring in contrast with the light continents, amount to about 16% of the entire lunar surface. The large

mountain massifs are most frequently the boundaries of maria of regular form (Figure 3).

The lunar craters are formations which are varied in size and structure. They differ, first of all, in such characteristics as the wall condition, presence of a central peak, characteristics of the floor, and so on. However, among this variety, we can identify certain general patterns relating to lunar crater structure. For example, the crater depth is small in comparison with the diameter, the crater floor lies below the surrounding surface, the height of the outer wall is less than the crater depth, the curvature of the inner slope is greater than that of the outer slope.

Troughs, cracks, and domes are encountered in the maria. Moreover, for the same scale, some portions of the maria appear darker and others lighter than the surrounding surface. All these characteristics of the lunar relief were shown by the "washout" technique, i.e., by a halftone pattern. However, if we display the lunar relief for some one lighting condition, then many of its characteristics will not be depicted. The shadows of relief details are clearly seen under oblique lighting, but the ray systems which are visible at full moon are hard to distinguish, and the gentle maria walls can be identified only with a low sun position (Figure 4). A certain arbitrariness in lighting selection was used in order to increase the information content of the map. The average angle of solar ray incidence was taken as 60° with washout of the large relief forms. However, the ray systems, low maria walls, and other similar formations were shown in greater detail than is possible for this solar ray incidence angle. In other words, each detail of the lunar relief was depicted under lighting conditions which are optimum for the particular detail. Moreover, the contrast between the maria and continents is specially emphasized on the map. Individual mockups were prepared in order to identify the maria boundaries. /167

The color spectrum of the map was selected not only with account for the natural coloring of the lunar surface, but also with the objective of achieving maximum expressiveness.

REPRODUCIBILITY OF THE
ORIGINAL PAGE IS POOR

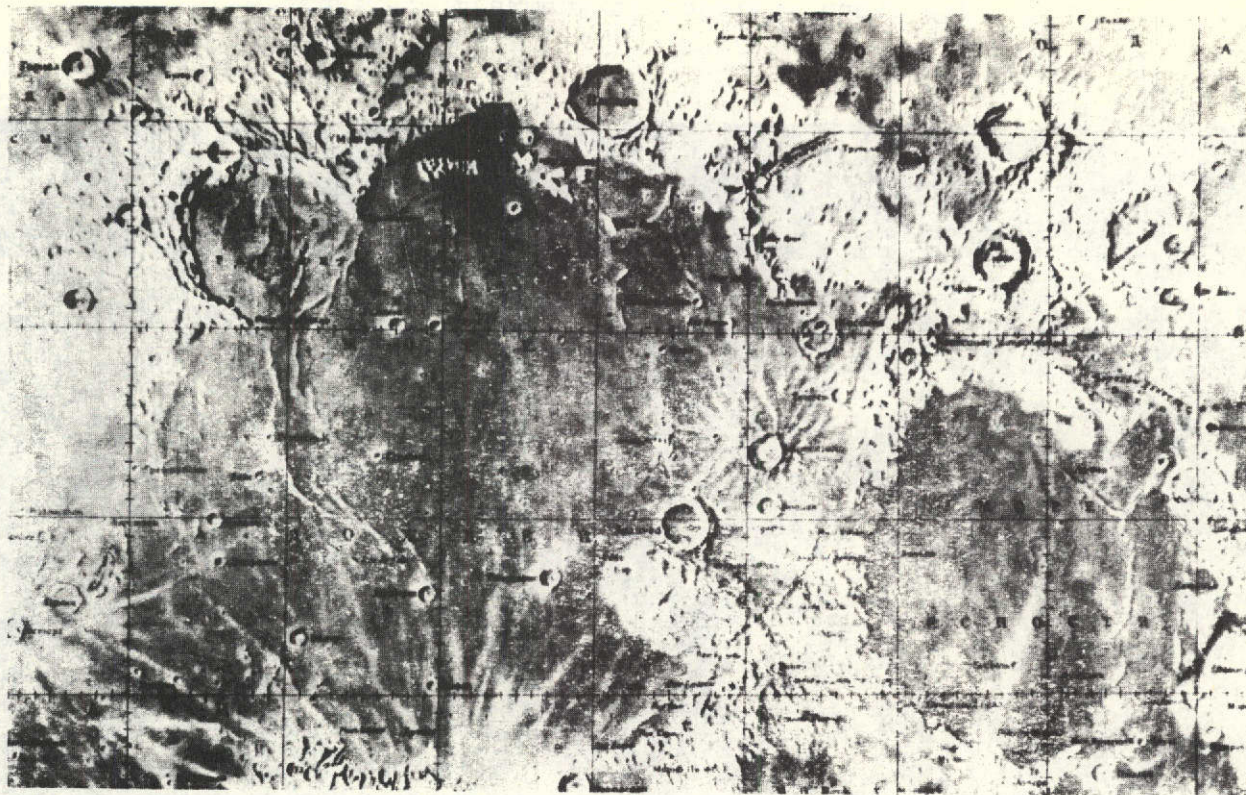


Figure 3. Fragment of Complete Lunar Map

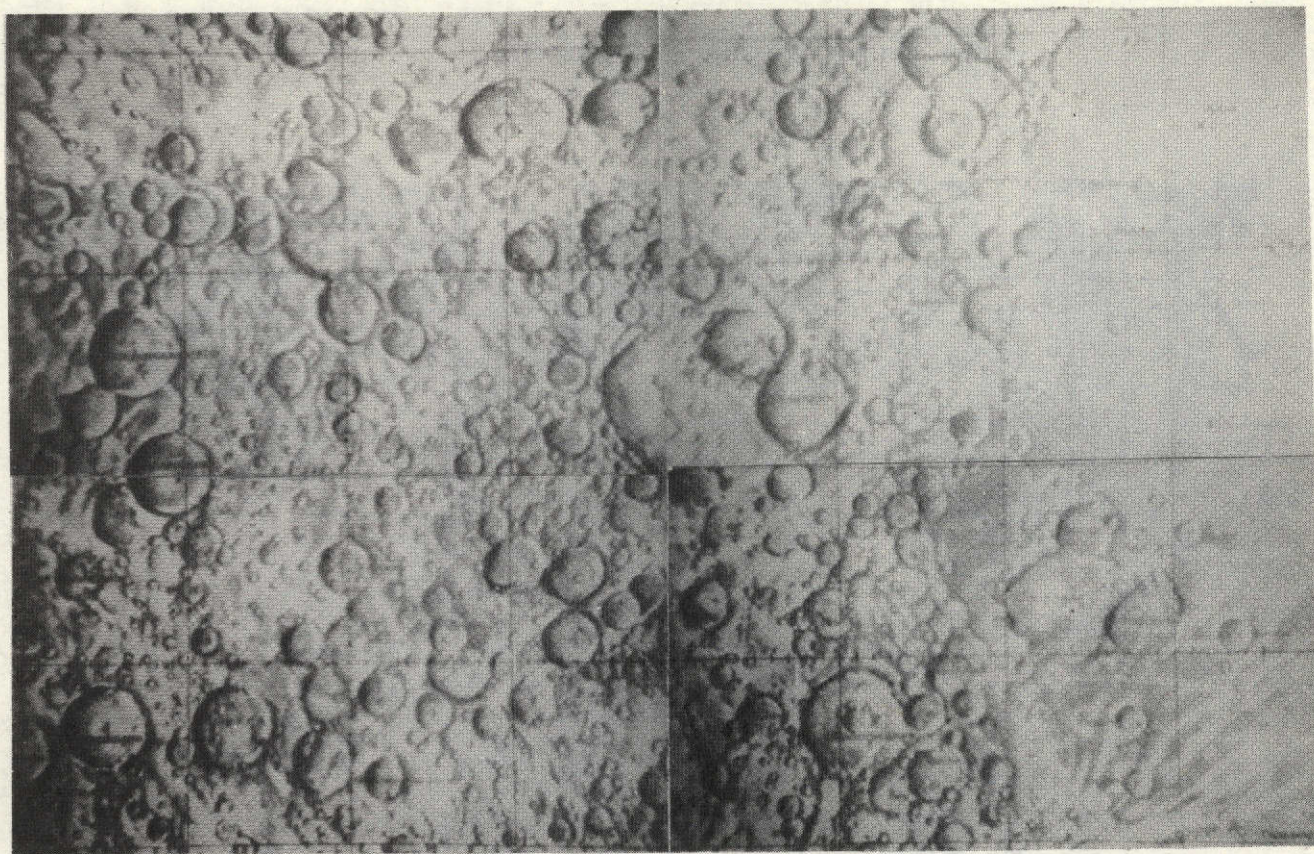


Figure 4. Fragment of Complete Lunar Map

Standardization of lunar place name nomenclature in the Russian language was particularly important. We can still find in the lunar literature two or three different forms of the same name. For example, the Sea of Crises is term the Sea of Hazards or the Sea of Shipwrecks. Such arbitrary translations can be encountered quite frequently. Different versions of the same features are also encountered in Latin. A catalog of lunar place names in the Russian and Latin languages was compiled by the Division of Lunar Physics of GAISH for the first edition of the Complete Lunar Map. This catalog was revised for the second edition with the aid of the bibliographic section of the Moscow State University library and specialists of the corresponding university departments.

All the lunar feature names approved by the International Astronomical Union are indicated on the second edition map, and the names on the eastern sector of the back side of the Moon, proposed by the commission of the Academy of Sciences of the USSR in 1967 and published in the Atlas of the Back Side of the Moon, Part 2, are also given. All the current names are shown in the place-name list on the map in the Russian and Latin transcription, and indexes are provided with the aid of which it is easy to find any feature. Some information on our natural satellite is presented in the reference data, provided separately.

⁵⁷⁰
A lunar globe to scale ~~1:10,000,000~~ was prepared along with the preparation of the Complete Lunar Map.) The scale of the globe, half that of the map, led to some selection and generalization of the relief forms. The advantages of the globe are well known. The globe permits maintaining simultaneously geometric similarity of contours, exact proportions of areas, and identical scales in all directions. Since the lunar globe depicts most accurately the outlines of the maria and continents and their positioning relative to one another, it serves as a visual aid in studying the natural satellite of the Earth

Preparation of the globe in two versions in the Russian and Latin languages is of great importance.

The Complete Lunar Map to scale 1 : 5,000,000, and the lunar globe to scale 1 : 10⁶, were prepared by GAISH together with the Topogeodesic Service of the USSR under the scientific guidance of Yu. N. Lipskiy.

The Complete Lunar Map is intended for the resolution of several scientific problems associated with study of the Moon and distribution of the formations on its surface.

The map navigational projection permits using it for plotting the traces of artificial lunar satellite trajectories and designing space experiments. The individual sheets covering the visible side of the Moon can be used successfully for telescopic observations. This map can serve as the basis for plotting thereon all sorts of additional information describing, for example, physical properties of the surface, parameters of the lunar medium, geological structure of the Moon, and so on.

References

1. Photographic Lunar Atlas. Kuiper (Ed.). University of Chicago Press, 1960.
2. Rectified Lunar Atlas, Suppl. N 2. University of Arizona Press, Tucson, 1963.
3. Lipskiy, Yu. N. Some Results of Global Study of the Lunar Surface. Vestnik AN SSSR, No. 4, 1968.
4. Lipskiy, Yu. N., and V. I. Chikmachev. Cartographic Tie-in of Zond 3 Pictures by Rectification Using Orienting Point. Astronomicheskii Zhurnal, No. 3, 1969.
5. Shevchenko, V. V. Use of the Earth for Selenographic Tie-in of Lunar Images Obtained from Space. Kosmicheskiye Issledovaniya, 4, No. 6, 1968.
6. Atlas of the Back Side of the Moon, Part 1, 1967; Part 2, 1969. Nauka Press, Moscow

IDENTIFICATION CHARACTERISTICS OF CERTAIN LUNAR
RELIEF FORMS ON PICTURES OBTAINED FROM
SPACECRAFT

V. I. Kravtsova

We have restricted our objectives to determining the recognitional characteristics of relief forms of a single type (dimple craters on the surface of maria), bearing in mind that this is one of the most common lunar surface relief forms. We shall arbitrarily consider craters as closed, negative relief forms, circular in plan-view, and symmetric relative to the center.

The phototone differences on lunar pictures are associated basically with the surface relief, and are caused either by the presence of shadows or the peculiarities of the illumination of surface irregularities, which leads to a unique distribution of image brightness in craters of different profile. These two factors — shadow and the nature of image brightness distribution — will be used as the relief form recognitional characteristics. Since forms having diameter/depth ratio $d/h = 10$ and more, i.e., with average slope angles less than 11° , are the dominant lunar crater form, there is a shadow image only on pictures taken with very low sun altitudes. Therefore, although the shadow is a more definite characteristic, indicating more exactly the nature of the form profile, the use of this characteristic is limited to pictures taken with low sun altitudes. Moreover, in the presence of shadows, it is impossible to identify surface details in the area occupied by the shadow. Brightness differences are a more stable characteristic, and appear on pictures taken with various sun altitudes. However, the edges of spots of different brightness are considerably less sharp than the shadow edges; therefore, their configuration is comparatively less definite than that of the shadow, so that it is more difficult to determine visually the nature of the relief form profile from the

brightness. In this case, it is possible to identify surface details over the entire formation area.

Shadows as crater identification characteristics. In order to use the shadow image as a relief form identification characteristic, it is necessary to know what shadow configuration is typical of the various formations under different lighting conditions. This has led to the preparation of a Shadow Atlas, indicating the shadow configuration for a definite set of relief forms with different profile and diameter-depth ratio for different lighting conditions (with sun altitudes from 10 to 45°).

The set of relief forms used in the Atlas included 40 shapes, representing various combinations of spherical and conical surfaces (Figure 1). Two groups of forms with ratio $d/h = 4$ and 10 were included. Forms with pointed and flat bottom were used. The basic primary forms with pointed bottom were the cone, spherical segment, and the shape formed by rotation of a convex arc. The forms with flat bottom were the truncated cone, truncated segment, and a circular half-barrel formed by rotation of a quarter circle. Further elaboration involved making these basic shapes more complicated by adding additional shapes, which included positive and negative conical and spherical shapes embedded into the basic shapes. The set also includes complex shapes formed by combining conical and spherical surfaces.

Two techniques were used to determine the shadow configuration in the craters — experimental determination of the shadow edge by illuminating the models of different profile shapes with a parallel light beam and geometric construction of the shadow edge using vertical section of the formation in the direction of the solar rays. /171

For all the shapes, we first constructed five vertical sections (through 0.6 R). By drawing through the edge of each section a line parallel to the solar rays, we obtained on the superposed vertical sections a series of points lying on the shadow edge; the ensemble /171

of such points on the horizontal projection of the shape yields the shadow contour.

The graphical constructions were supplemented by analytic determination of the position of certain points of the shadow edge, particularly the edge shadow points (on the lips of the forms), which are not well defined graphically. We also calculated the location of the shadow boundary points on the bottom of the flat-bottom relief forms and on the walls of the positive supplementary forms. These calculations facilitate the graphical constructions and provide a check on the latter.

Analysis of the shadow configuration of the 40 shapes presented in the Atlas shows that all the examined varieties of relife have their own characteristic shadow configuration peculiarities. Figure 2 shows six shapes in which those with pointed bottom differ markedly from the shapes with flat bottom. The former have a convex shadow boundary (except for the spherical shapes at high Sun angles); in the latter the convex shadow boundary near the edges of the shapes is replaced by a concave boundary on the flat bottom.

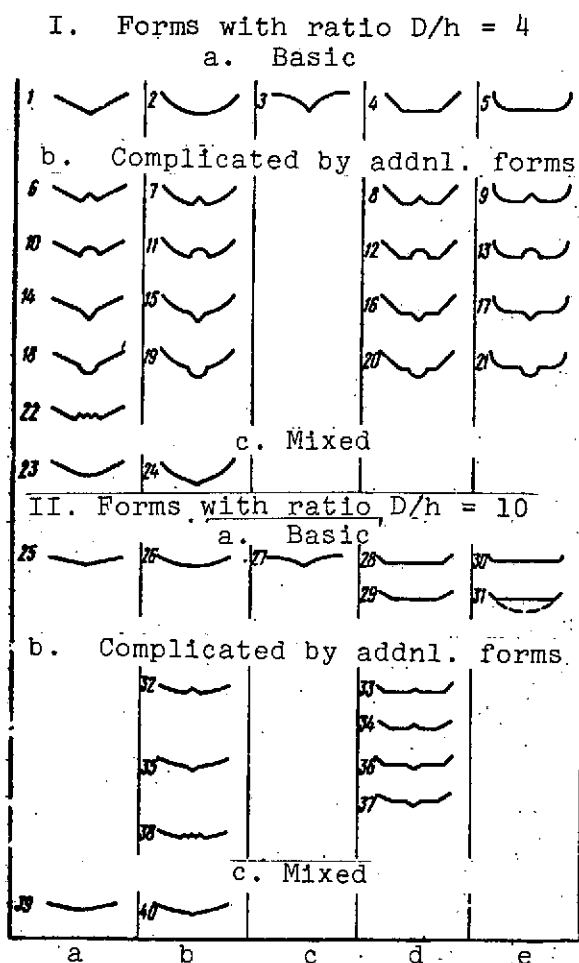


Figure 1. Set of relief shapes used in Shadow Atlas

Forms with pointed bottom: a — with conical walls; b — with spherical walls; c — formed by rotation of an arc. Forms with flat bottom: d — with conical walls; e — with spherical walls

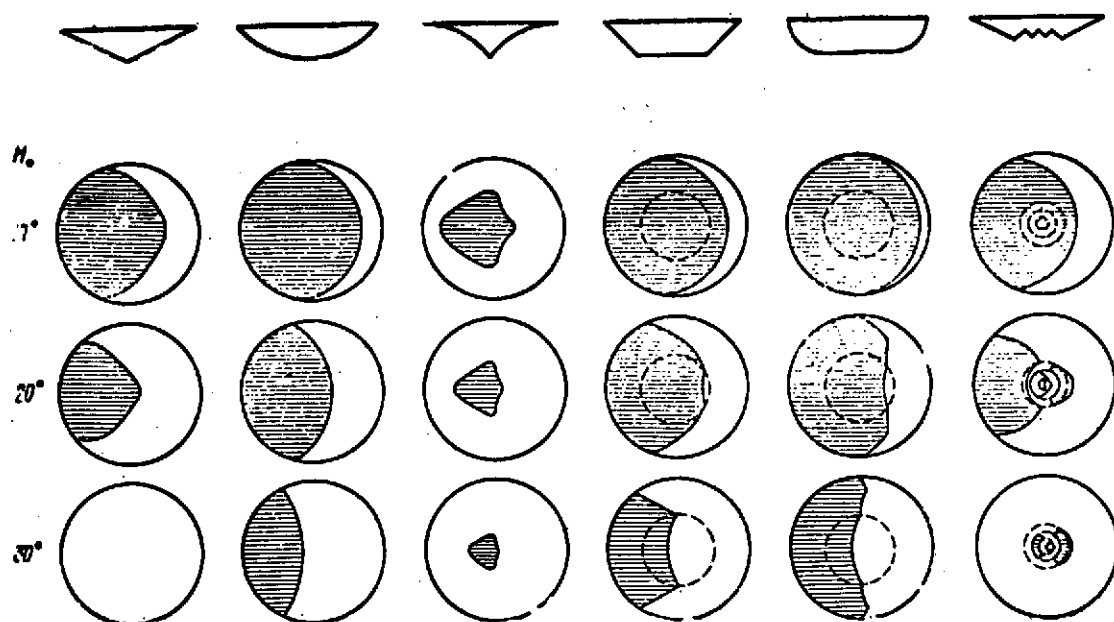


Figure 2. Shadow configuration in certain relief forms for different Sun altitudes

The conical shapes have a shadow boundary in the form of a parabola, as the sun altitude decreases the shadow narrows: the spherical shapes have an arc-shaped boundary, and as the sun altitude decreases, the shadow remains broad. The shapes formed by rotation of a convex arc have a leaf-shaped shadow located in the center of the formations and slightly elongated in the direction of the light source, which makes it possible to identify shapes of this profile reliably, but does not indicate the position of the formation boundaries.

The flat-bottom shapes — truncated cone and the circular half-barrel — are easily differentiated on the basis of their shadow; characteristic of the former is a crescent-shaped or trapezoidal shadow with sharp breaks of the boundaries upon transition from the flat bottom to the walls and nearly straight lines of the boundaries on the walls; characteristic for the latter are smooth shadow boundaries having a convex shape for low Sun heights, convex-concave (in

the center) for intermediate sun heights, and a concave shape for high Sun angles. The shadow in the truncated spherical segment is similar in configuration to that in the truncated cone, although the abruptness of the breaks in the boundaries upon transition from the flat bottom to the walls is less.

In most cases, the presence of the supplementary complicating shapes is well reflected in the shadow configuration; however, the identifiability of the positive supplementary shapes is poorer than that of the negative shapes. The combined relief shapes have unique shadow spot patterns.

The location of the edge shadow points, exactly definable mathematically for each shape, cannot be used as a shape profile identifying characteristic or for determining the wall slopes (because of the small change of point angular position with change of wall steepness). /173

In addition to the relief shape profile nature, the shadow can also be used to determine the shape diameter-depth ratio — d/h . This can be done quite accurately for the flat-bottom shapes (on the basis of shadow length), and also on the basis of the portion of the diameter occupied by the shadow. Tables, nomograms, and templates have been prepared which make it possible to determine both d/h and formation depth.

It is advisable that the problems of determining the relief shape profile, d/h , h , and the wall slopes be solved jointly. For this purpose, we prepared, on the basis of the Shadow Atlas, gaging templates (Figure 3) on which were displayed the shadow configuration of seven basic shapes with different ratio $d/h = 4 - 20$, and different d (3 - 30 mm). The templates were prepared for working with pictures taken with Sun altitudes of 10 and 15°.

Pictures taken with sun altitudes of 10 - 20° are optimum for identifying lunar relief forms from their shadows. It is true that pictures taken with very low Sun altitudes (on the order of 5 - 10°)

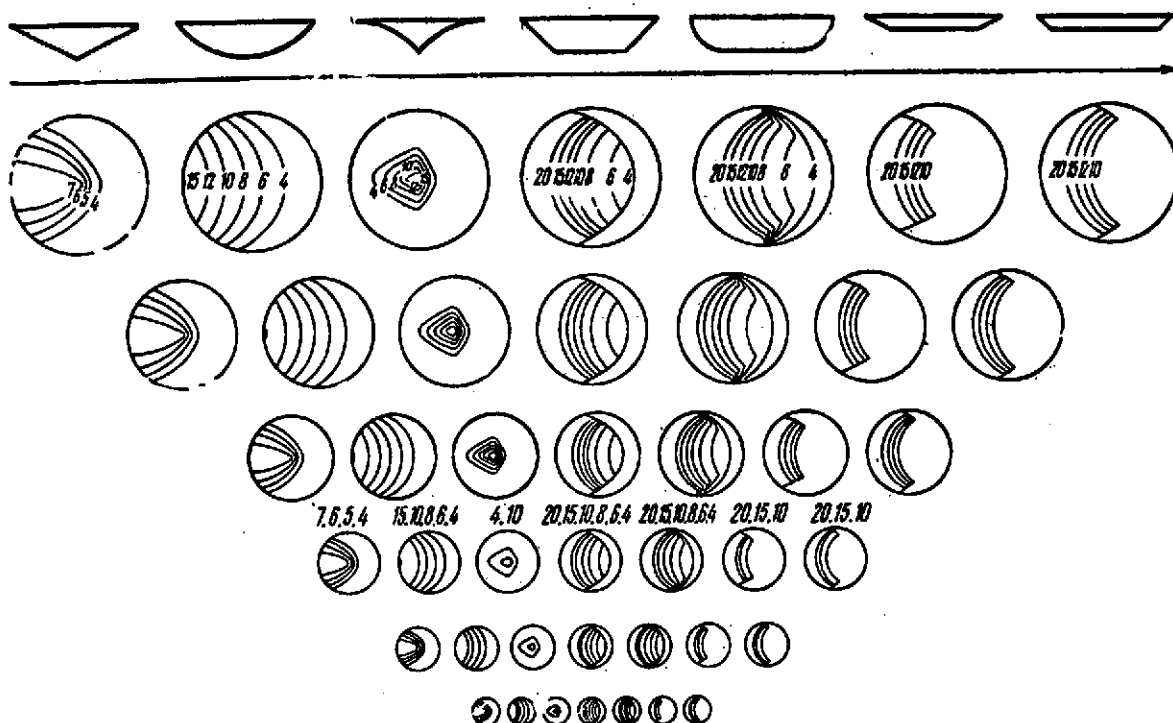


Figure 3. Template for determining relief shape profile and ratio d/h from shadow configuration on pictures taken with Sun height 15°

are best from the viewpoint of number of shadows generated. However, for these altitudes, the shadow configurations of different shapes may be similar to one another; moreover, the nature of the bottom — pointed or flat — is not reflected in the shadow pattern on such pictures, and the supplementary forms are not visible.

Image brightness distribution as crater identification characteristic. Because of the unique nature of light reflection from the lunar surface (elongated, pear-shaped scattering indicatrix), its brightness depends not only on the incident light flux and surface albedo but also on the photometric function Φ , which can be defined as each point by two angles (Figure 4): g is the angle between the line of sight and the solar ray, and α is the angle between the normal to the surface and the line of sight projected onto the g plane.

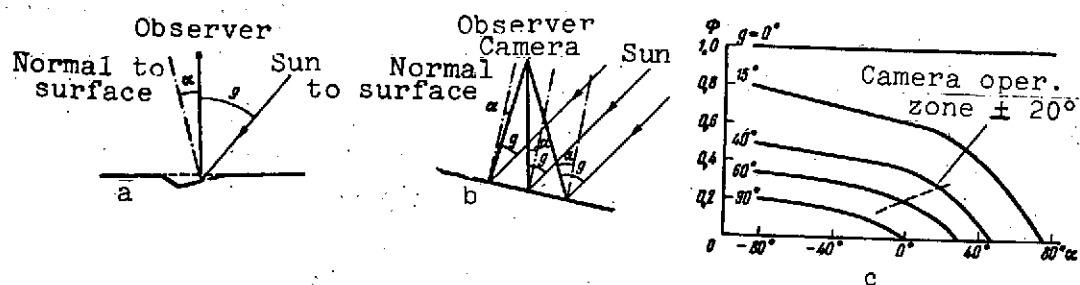


Figure 4. Illustration for determining the photometric function ϕ :

a — for the case of planview photography of surface point;
 b — for the case of planview photography of sloping surface segment; c — graph for determining variation of the magnitude of the photometric function ϕ as function of surface slope α for different sun phase angles g

For a constant angle g (within the limits of the central part of a single vertical picture), the photometric function becomes a function of the angle α , i.e., the surface slope in the direction of the solar rays. This situation is the basis of the photometric method for determining relief from pictures. We shall use it for other purposes — to identify craters of different profile on the basis of the configuration of spots with different brightness of the image on the pictures. Spots with different brightness are separated by isolines of the photometric function ϕ .

To construct the ϕ isolines, we used the technique of vertical sections (for spherical forms), and radial sections (for conical forms). After determining α on the section lines in the projection on the g plane, we then find the values of ϕ for the same points. The results of the construction for some forms are shown in Figure 5. The constructions of the ϕ isolines were performed for sun altitudes of 20 and 30°.

In the spherical relief forms, the ϕ isolines are arc-shaped; the arc in the hemisphere diverge from its poles, the values of ϕ (for $H_0 = 30^\circ$) vary from $\phi_{\max} = 0.35$ at the edge of the hemisphere to $\phi = 0.27$ at the shadow boundary; in the other spherical forms,

the arcs are less steep, do not converge at the poles, and the maximum values of ϕ reach magnitudes less than 0.35 (for $d/h = 4$, $\phi_{\max} = 0.304$; for $d/h = 10$, $\phi_{\max} = 0.252$); therefore, the values of ϕ decrease somewhat near the shadow boundary.

In the conical relief forms, the ϕ isolines coincide with the generators of the cones. The values of ϕ vary from $\phi_{\max} = 0.295$ for $d/h = 2$, $\phi_{\max} = 0.262$ for $d/h = 4$ and $\phi_{\max} = 0.232$ for $d/h = 10$ to $\phi = 0.2$ on the initial diameter, and $\phi = 0$ on the edge shadow points. As a result of this last situation, the apparent shadow boundary is distorted in the conical forms.

In the relief forms with flat bottom, the values of ϕ are the same on the entire bottom surface (on the horizontal surface, $\phi = 0.20$). The form of the isolines on the walls depends on the surface used to form the walls: on spherical walls the isolines are arched, on conical walls they are radial. A combination of the arched and radial ϕ isolines is characteristic for the mixed shapes, while for the relief shapes complicated by supplementary forms, the characteristic pattern is the superposing of one isoline pattern on the other, and the isolines may terminate within the forms and not continue one another.

Thus, characteristic for all the relief forms studied is a unique pattern of the ϕ isolines, which favors use of the configuration of spots of different brightness as the relief form profile identifying characteristic. /

The connection found by F. M. Truskov between the ϕ values and image optical density on our pictures, valid under several assumptions, makes it possible to transfer from the ϕ isolines to the isolines of the picture image, density D expected for various relief forms. Considering the density intervals discernible by the eye, we obtained the configuration of the brightness spots which can be seen by the eye for the different relief forms and, using prepared /

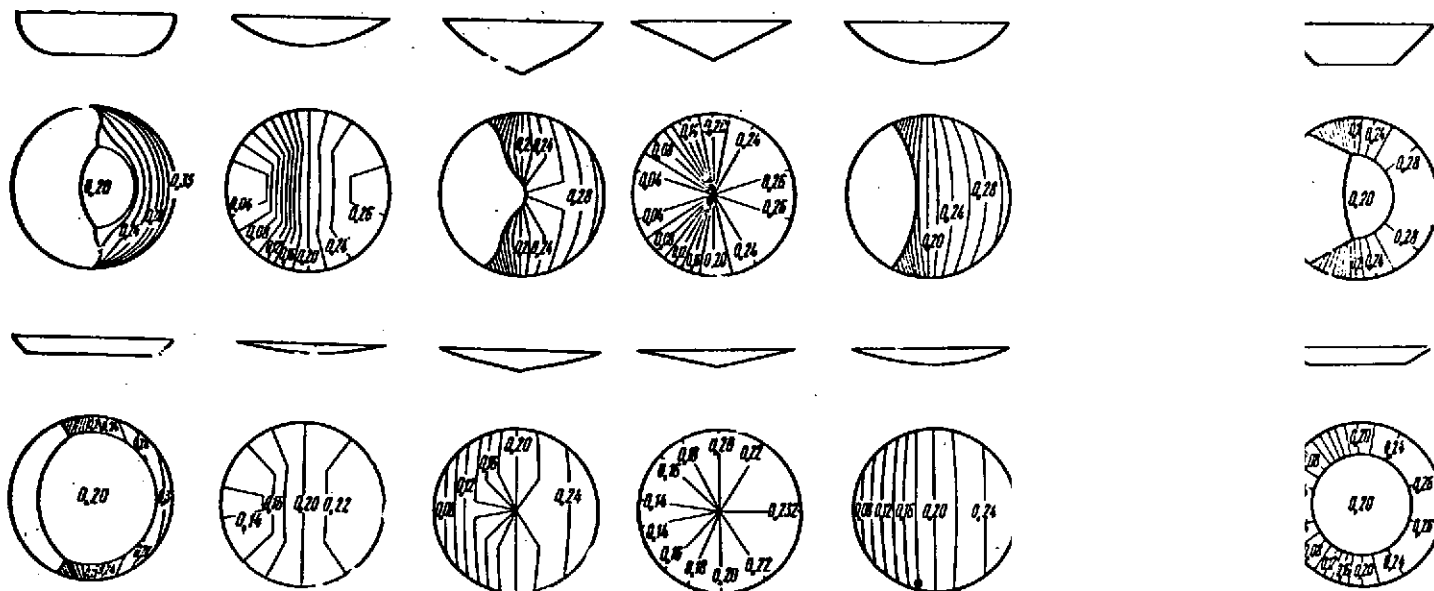


Figure 5. Isolines of photometric function ϕ in certain relief

altitude 30°

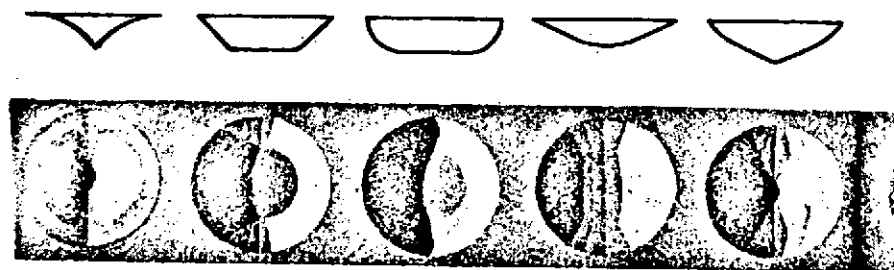


Figure 6. Models of photographic image of certain relief and constructed using isolines of the photometric function ϕ and density D for pictures taken with Sun altitude 30°

lated
den-

densities from differently exposed photographic paper, we made models of the photographic image of these forms (Figure 6) for the specific picture with which we were to work. Master curves for identifying the forms on the basis of image brightness distribution were prepared using these materials.

In order to verify the possibility of using the proposed technique, we conducted experiments involving interpretation of Lunar Orbiter pictures. We selected two reference areas, one of which is covered by pictures from two orbits made with approximately the same Sun altitude (30 and 28.5°), as a result of which stereoscopic analysis of the area is possible as a check of the interpretation. For the other area, we have pictures taken with different sun altitude (10 and 20°), which makes it possible to interpret these pictures independently by two methods: on the basis of shadow configuration using the "shadow template" (for the picture with $H_0=10^\circ$), and on the basis of brightness distribution using the "brightness template". Both forms of interpreting template were specially prepared for these pictures. The pictures of the reference areas were interpreted independently by several analysts. The following characteristics were determined during the interpretation: crater diameter, ratio of diameter to depth, sharpness of the lip, and nature of the crater profile. The experimental verification showed adequate reliability of the determination of these characteristics. Craters of seven different types (based on profile nature) were identified on the reference areas with the discrepancies in crater form for the different analysts and when using the different methods amounting to no more than 1%. The ratio d/h is determined with somewhat greater ambiguity.

A morphological map of the surface which includes the following factors can be compiled using the proposed identification technique: crater profile nature, crater diameter, ratio of diameter and depth, sharpness of the lip, and distribution density of the forms.) Several conditions were assumed in developing the interpretive templates. We assumed that the operation was carried out using a planview picture

and constant angles g within the limits of the picture, and we also assumed that the craters are on a horizontal surface. Therefore, for further use of the proposed identification technique, it is necessary to analyze how picture obliquity, variation of the angle g in the limits of the picture, particularly at the edges, and the general slope of the surface into which the forms are cut affect the configuration of the ϕ isolines.

ON THE DETERMINATION OF CERTAIN ASTRONOMICAL, SELENODESIC,
AND GRAVITATIONAL PARAMETERS OF THE MOON

Ye. P. Aleksashin, Ya. L. Ziman, I. V. Isavnina,
V. A. Krasikov, B. V. Nepoklonov,
B. N. Rodionov, A. P. Tishchenko

Problem formulation. We examine a method for joint construction /1' of a selenocentric fundamental system which can be realized by a coordinate catalog of reference contour points uniformly positioned over the entire lunar surface, and determination of the parameters characterizing the gravitational field, rotation, and orbital motion of the Moon.

Characteristic of the problem formulation is the introduction of a new complex of iconometric measurements which can be made using pictures obtained from an artificial lunar satellite (ALS) ~~[1, 2, 4]~~. The proposed method can be used to solve similar problems on any other planet for which surface images can be obtained from a spacecraft.

Iconometric determinations are an effective technique for studying planets from spacecraft. Their accuracy is independent of the distance between the planet being photographed and the Earth. With

proper selection of the orbit of the vehicle carrying the camera equipment, iconometric observations can be made at practically any points of circumplanetary space. An important advantage to iconometric determinations is the fact that they permit solving the posed problem and finding all the elements mentioned above, with the exception of the orbital parameters of the planet being photographed, without the use of any measurements from the earth. It will be possible to construct on the Moon, in the very near future, a global reference grid and correlate it directly with the gravitational field parameters, only on the basis of iconometric observations from spacecraft.

Characteristic of the proposed technique for solving the problem is the joint statistical analysis of all forms of measurements: orbital iconometric, Earth-based trajectory, and also a priori information on the parameters in question which is known from Earth-based astronomical studies.

Coordinate systems, parameters being determined, and basic data.
We introduce the following right-hand rectangular coordinate systems.

Vehicle-fixed system with origin at the mass center of the ALS; the axes lie in the direction of the satellite structural axes. The positions of the images of the photographed points are specified in this system by the vectors \bar{r} .

Selenocentric system with origin at the mass center of the Moon; \angle the abscissa and applicate axes coincide with the longest and shortest axes of the lunar ellipsoid of inertia, respectively. The position of points in this system are specified by the vectors \bar{r}' .

Inertial system with origin at the mass center of the Moon; the abscissa axis is directed toward the midpoint of the vernal equinox of the Earth to epoch T_0 , the applicate axis is directed toward the ecliptic pole. We denote the point position vectors in this system by \bar{R} .

Geocentric system with origin at the Earth's mass center; the abscissa and applicate axes are directed, respectively, toward the midpoint of the vernal equinox and along the mean axis of rotation of the Earth to epoch T_0 . Point locations in this system are specified by the vectors \bar{R}^\oplus .

We define the orientation of the vehicle, selenocentric, and geocentric systems, respectively, in the inertial system by the matrixes Θ, \mathfrak{M} , and H . Then

$$\bar{r} = \frac{|\bar{r}|}{|\bar{R} - \bar{R}_\Delta|} \Theta (\bar{R} - \bar{R}_\Delta), \quad (1)$$

$$\bar{R}' = \mathfrak{M} \bar{R}, \quad (2)$$

$$\bar{R}^\oplus = \bar{R}_\zeta^\oplus = H^T \bar{R}, \quad (3)$$

where \bar{R}_Δ is the inertial vector of ALS position; \bar{R}_ζ^\oplus is the geocentric vector of lunar mass center position.

We express all the parameters being determined in the inertial coordinate system at the instant t_0 , and form the estimate vector \bar{Q}_0

$$\bar{Q}_0 = (\bar{R}_\Delta, \bar{V}_\Delta, \bar{R}_\oplus, \bar{V}_\oplus, \bar{\mu}, c, \bar{L}, \bar{\lambda}_0, \bar{\psi}_i, \bar{R}_j)^T, \quad (4)$$

where $\bar{R}_\Delta, \bar{V}_\Delta$ and $\bar{R}_\oplus, \bar{V}_\oplus$ are the phase coordinates of the ALS and the Earth; $\bar{\mu}$ are the lunar gravitational parameters field; c is the maximum moment of inertia of the Moon, \bar{L} is the kinetic moment of the moon; $\bar{\lambda}$ are the Rodrigues-Hamilton parameters describing rotation of the Moon (they define the elements of the matrix \mathfrak{M})*; $\bar{\psi}_i$ ($i=1, 2, \dots, p$) are the Euler angles defining Θ_1 at the instant of photography t_{p1} ; \bar{R}_j ($j=1, 2, \dots, q$) are the coordinates of the lunar surface points which form the reference selenocentric grid.

* The Rodrigues-Hamilton parameters make it possible to represent in more general form the differential equations of lunar rotation about the center of mass, and remove the singularities characteristic of the angular variables [3].

We shall consider that the estimate of the vector \bar{Q}_0 is made using the following measurement complex: \bar{r}_s, \bar{r}_{pl} are the position vectors of the star images and lunar surface points in the vehicle-fixed coordinate system, referred to the photographing times t_p , where \bar{r}_s and \bar{r}_{pl} are determined by the measured coordinates of the picture points, the iconometric parameters of the imaging cameras and the elements of their mounting on the spacecraft; D, \dot{D} are the ALS distances relative to the Earth-based measurement stations and their rates of change, referred to the observation times, and D and \dot{D} are measured by radiotechnical means at Earth-based measurement stations. /181

The measurement complex can be broadened. We can measure from the Earth the ALS azimuth A and elevation γ , and their rates $\dot{A}, \dot{\gamma}$. We can measure from the ALS the distance d to definite points of the lunar surface, the ALS ground speed W , and other elements.

The basic data not subject to estimation include: t_t and t_p are the trajectory measurement and photography times, \bar{R}_s are the inertial coordinates of the stars, \bar{R}_{IS}^0 are the geocentric coordinates of the measurement stations; \bar{R}_i^0, \bar{V}_i^0 are the geocentric phase coordinates of the Sun, Jupiter, and other planets; M_ξ are the masses of the Sun, Earth, and other planets; H is the matrix of orientation of the inertial system in the geocentric system.

In solving the problem, we assume that all the measurements and a priori information on the parameters being determined, obtained from astronomical studies, obey the normal law with known second moment matrixes.

Coupling equations and problem solution algorithm. We write the equations coupling the current values of the estimate vector with the measured quantities in the form:

$$\bar{r}_{pl} = \begin{pmatrix} \bar{r}_{1l} \\ \dots \\ \bar{r}_{il} \\ \dots \\ \bar{r}_{pl} \end{pmatrix}, \quad \bar{r}_{il} = \frac{|\bar{r}_{il}|}{|\mathfrak{M}_i^T \bar{R}_j' - \bar{R}_{\Delta_l}|} (B_i \bar{R}_j' - \Theta_j \bar{R}_{\Delta_l}); \quad (5)$$

$$\bar{r}_s = \begin{pmatrix} \bar{r}_{1s} \\ \dots \\ \bar{r}_{is} \\ \dots \\ \bar{r}_{ps} \end{pmatrix}, \quad \bar{r}_{is} = \frac{1}{|\bar{r}_{is}|} \Theta_i \bar{R}_s; \quad (6)$$

$$\bar{D} = \begin{pmatrix} D_{11} \\ \dots \\ D_{kl} \\ \dots \\ D_{mn} \end{pmatrix}, \quad D_{kl} = \sqrt{(\bar{R}_{\Delta_k} - \bar{R}_{un_{lk}})(\bar{R}_{\Delta_k} - \bar{R}_{un_{lk}})}; \quad (7)$$

$$\bar{D} = \begin{pmatrix} \dot{D}_{11} \\ \dots \\ \dot{D}_{kl} \\ \dots \\ \dot{D}_{mn} \end{pmatrix}, \quad \dot{D}_{kl} = \frac{1}{D_{kl}} (\bar{V}_{\Delta_k} - \bar{V}_{un_{lk}})(\bar{R}_{\Delta_k} - \bar{R}_{un_{lk}}). \quad (8)$$

Here, $\xi=1,2,\dots,s$ are the numbers of the photographed stars; $k=1,2,\dots,m$ are the times of Earth-based trajectory measurement; $l=1,2,\dots,n$ are the numbers of the ground-based measurement stations; \bar{R}_ξ are the inertial coordinates of the photographed stars; $B_i=\Theta_i \mathfrak{M}_i^T$ is the orientation matrix of the body-fixed coordinate system in the selenocentric system.

In solving the problem, we assume the following conditions are satisfied:

1) on each picture of the lunar surface, we select no less than m images of points in the created reference grid; here $m \geq 3$ is determined by the picture overlap ratio;

2) each lunar surface reference point is represented on at least two pictures;

3) at least two stars are represented on each star picture;

4) the ground-based trajectory measurements are made from at least two measurement stations.

The first and second conditions permit constructing a triangulation grid, including the photographed lunar surface points and the observation points, and also permits determining in this grid system the orientation of the vehicle-fixed coordinate system at the exposure times. The third condition permits determining at each exposure time the orientation of the vehicle-fixed coordinate system in the inertial system.

We shall consider the vector \bar{Q} of current values of the parameters being determined as a function of the vector \bar{Q}_0 of estimates, which is the solution of the differential equations of the perturbed spacecraft motion relative to the lunar mass center, the differential equations of lunar rotation relative to its mass center, and the differential equations of the perturbed motion of the Earth relative to the lunar mass center.

We shall describe the ALS motion under the influence of perturbing accelerations arising from attraction of external bodies, noncentrality of the lunar gravity field, and solar radiation pressure. In the inertial system, the ALS equations of motion are written in the following form [5]:

$$\begin{aligned}\dot{\bar{R}}_s &= \bar{V}_s, \\ \bar{V}_s &= -\frac{\mu_c}{R_\Delta^3} \bar{R}_\Delta + \sum_{i=1}^n \mu_i \left(\frac{\bar{R}_i - \bar{R}_\Delta}{|\bar{R}_i - \bar{R}_\Delta|^3} - \frac{\bar{R}_i}{R_i^3} \right) + \nabla U + \kappa_{11} \frac{\bar{R}_\Delta - \bar{R}_\odot}{(R_\Delta - R_\odot)^3},\end{aligned}\quad (9)$$

where μ_i, \bar{R}_i are the gravitational parameters and inertial position vectors of the disturbing bodies; μ_c is the gravitational parameter of the moon; ∇U is a vector whose components are the partial derivatives of the lunar force function U with respect to the ALS phase coordinates; κ_{11} is the coefficient of light pressure, defined by

/183

the relation

$$\kappa_{11} = \frac{KA_{\Delta}}{m_{\Delta}}. \quad (10)$$

Here K is a coefficient characterizing the emittance of the sun and reflective properties of the object surface [6]; A_{Δ} is the ALS photo-metric cross section; m_{Δ} is the ALS mass.

The lunar force function is defined in terms of ALS selenocentric coordinates by the expression:

$$U = \frac{\mu_{\odot}}{R_{\Delta}} \left\{ 1 + \sum_{n=1}^{n_1} \left(\frac{a}{R_{\Delta}} \right)^n c_{n0} P_{n0}(\sin \varphi_{\Delta}) + \right. \\ \left. + \sum_{n=1}^{n_2} \sum_{m=1}^{n_2} \left(\frac{a}{R_{\Delta}} \right)^n [c_{nm} \cos m\lambda_{\Delta} + d_{nm} \sin m\lambda_{\Delta}] P_{nm}(\sin \varphi_{\Delta}) \right\}, \quad (11)$$

where a is the semimajor axis of the Moon, n_1 and n_2 are the numbers of sectoral and tesseral harmonics, respectively; $P_{nm}(\sin \phi)$ are the Legendre associated polynomials; ϕ_{Δ} , λ_{Δ} are the ALS selenocentric latitude and longitude; c_{nm} , d_{nm} are the coefficients of the force function series expansion in spherical harmonics, defined by the expressions [7]:

$$c_{nm} = \frac{v_{nm}}{Ma^n} \iiint_{(\mathbb{C})} (R')^n P_{nm}(\sin \varphi) \cos m\lambda dM, \\ d_{nm} = \frac{v_{nm}}{Ma^n} \iiint_{(\mathbb{C})} (R')^n P_{nm}(\sin \varphi) \sin m\lambda dM, \quad (12) \\ v_{n0} = 1; \quad v_{nm} = \frac{(n-m)!}{(n+m)!}.$$

We express the vector $\overline{\nabla U}$ in the form:

$$\overline{\nabla U} = \mathfrak{M} \cdot \eta \cdot \overline{g^2}, \quad (13)$$

where

$$\bar{g}^T = \begin{pmatrix} \frac{\partial U}{\partial R} \\ \frac{1}{R \cos \eta} \cdot \frac{\partial U}{\partial \lambda} \\ \frac{1}{R} \cdot \frac{\partial U}{\partial \eta} \end{pmatrix}$$

is a vector whose components are the projections of the lunar force function on the axes of the local horizontal coordinate system (z-axis along the radius vector, abscissa axis in the plane of the meridian); η is the orientation matrix of this system in the selenocentric system. /184

We write the differential equations of motion of the Earth in the inertial system in the form [8]:

$$\begin{aligned} \dot{\bar{R}}_0 &= \bar{V}_0, \\ \dot{\bar{V}}_0 &= -\frac{(\mu_c + \mu_0) \bar{R}_0}{R_0^3} + \sum_{i=1}^n \mu_i \left[\frac{\bar{R}_i - \bar{R}_0}{|\bar{R}_i - \bar{R}_0|^3} - \frac{\bar{R}_i}{R_i^3} \right]. \end{aligned} \quad (14)$$

We shall describe the dynamics of lunar rotation relative to its mass center using the general theory of motion of an absolutely rigid body. We express this motion by the elements of rotation of the selenocentric coordinate system in the inertial system. We write the differential equations of lunar rotation in the form [9]:

$$\begin{aligned} \dot{\bar{L}} &= \bar{M}, \\ \dot{\bar{\lambda}} &= \frac{1}{2} [\lambda_0 \bar{\omega} + \bar{\omega} \times \bar{\lambda}], \\ \lambda_0 &= -\frac{1}{2} \bar{\omega}^T \bar{\lambda}, \end{aligned} \quad (15)$$

where \bar{L} is the kinetic moment of the Moon; \bar{M} is the moment of the external forces; ω is the angular rate of lunar rotation; λ_0 and

$\bar{\lambda} = \begin{pmatrix} \lambda_1 \\ \lambda_2 \\ \lambda_3 \end{pmatrix}$ are the Rodrigues-Hamilton parameters.

We write the vector $\bar{\omega}$ in the form:

$$\bar{\omega} = (R^T I^{-1} R) \bar{L}, \quad (16)$$

where $I = \begin{pmatrix} A & -F & -E \\ -F & B & -D \\ -E & -D & C \end{pmatrix}$ is the lunar inertia tensor.

/185

We see from (12) that the lunar inertia tensor elements are connected with the gravity field expansion coefficients by the relations:

$$\begin{aligned} A &= C + a^2 M_C (c_{20} - 2c_{22}), \quad B = A + a^2 M_C 4c_{22}, \quad D = a^2 M_C d_{21}, \\ E &= a^2 M_C c_{21}, \quad F = a^2 M_C 2d_{22}. \end{aligned} \quad (17)$$

We shall discuss the geometric scheme for determining $\bar{\omega}$ from iconometric measurements. We take two pairs of synchronous pictures of the lunar surface and stars, obtained over the time interval t_{ij} , during which we can neglect $\bar{\omega}$ variations. From the lunar surface pictures, we find their mutual orientation in planetary space — the matrix B_{ij}^* . We determine from the star pictures the inertial orientation of the vehicle-fixed system at the exposure times — the matrixes θ_i and θ_j .

The rotation of the moon in the inertial system during the time t_{ij} is defined by the matrix E:

$$E = \theta_i B_{ij} \theta_j^T. \quad (18)$$

From the elements of this matrix, we find the average-over-the-time-segment t_{ij} vector $\bar{\omega}_{ij}$, its direction cosines l_{ij}^0 , m_{ij}^0 , n_{ij}^0 , and the angular velocity ω_{ij} in the inertial coordinate system [10]:

* The matrix B_{ij} may be found if the same five points of the lunar surface are represented on both pictures, or from three points in the triangulation grid.

$$\begin{aligned}
l_{ij}^* &= \cos \alpha_0 \cos \delta_0, & \omega &= l_{ij}^{-1} \arcsin \frac{l_{12} - l_{21}}{2l_{ij}^*}, \\
m_{ij}^* &= \sin \alpha_0 \cos \delta_0, & \alpha_0 &= \arctg \frac{l_{12} - l_{21}}{l_{12} - l_{21}}, \\
n_{ij}^* &= \sin \delta_0, & \delta_0 &= \arccos \sqrt{\frac{2(l_{12} - l_{21})}{\sin 2\alpha_0}}.
\end{aligned} \tag{19}$$

Construction of the selenocentric coordinate system is realized by shifting the origin to the point with coordinates

$$\begin{aligned}
X_0' &= ac_{11}, \\
Y_0' &= ad_{11}, \\
Z_0' &= ac_{10}
\end{aligned} \tag{20}$$

and rotation through the Euler angles [11]

/186

$$\begin{aligned}
\psi_1 &= \arctg \frac{c_{21}}{d_{21}}, \\
\psi_2 &= \frac{1}{2} \arctg \frac{d_{22}}{c_{22}} - \psi_1, \\
\psi_3 &= \frac{\sqrt{c_{21}^2 + d_{21}^2}}{-c_{20}}.
\end{aligned} \tag{21}$$

The direction cosines l_i', m_i', n_i' of the instantaneous lunar rotation vector in the selenocentric coordinate system (at the time t_1) are found from the expression:

$$\begin{pmatrix} l_i' \\ m_i' \\ n_i' \end{pmatrix} = \mathcal{R}_i \begin{pmatrix} l_{ij}^* \\ m_{ij}^* \\ n_{ij}^* \end{pmatrix}. \tag{22}$$

From the found coordinates X_j, Y_j, Z_j of the lunar surface points in the global reference grid, we can find the approximating geometric figure of the Moon — the reference surface — representing it by analogy with the gravity field in the form of the expansion of the radius vector in spherical functions [12], or by a three-axis ellipsoid. The dimensions of the latter, and its orientation in the selenocentric system are determined upon minimizing the functional

$$\Phi = \sum_{j=1}^q (a_{11}X_j^2 + a_{22}Y_j^2 + a_{33}Z_j^2 + a_{12}X_jY_j + a_{13}X_jZ_j + a_{23}Y_jZ_j + a_1X_j + a_2Y_j + a_3Z_j + 1). \quad (23)$$

The cited systems of differential equations and the equations coupling the measured quantities with the current values of the elements of the vector \bar{Q} make it possible to determine all the sought parameters of the problem.

1. The triangulation grid (5) is constructed from measurements of the lunar surface pictures.

2. The inertial orientation of the triangulation grid at the exposure times is determined using (6), from measurements of the star pictures.

3. The Quantities (18), (19) and the value of the lunar rotation vector are determined from the variations of the triangulation grid inertial orientation, and the inertia tensor and kinetic moment of the Moon are found from solution of (15), (16).

4. The triangulation grid scale*, the ALS phase coordinates, and the parameters of the lunar gravitational field are determined from the solution of (9), using the vectors of ALS location at the exposure times, found in constructing the triangulation grid. /187

5. The ALS phase coordinates and the lunar gravitational field parameters are also determined on the basis of Earth-based trajectory measurements from solution of (9) - (14); in so doing, the geocentric phase coordinates of the Moon are also found.

6. The selenocentric coordinate system is obtained (20), (21) using the resulting lunar gravitational field parameters (the positions of the photographed lunar surface points and the current values

*The scale can also be found from laser measurements of the altitude.

of the lunar rotation vector direction are determined in the selenocentric system).

7. The parameters of the reference ellipsoid are found (23) from the coordinates of the lunar surface points.

Algorithm for estimating vector of determined parameters. For evaluating the vector \bar{Q}_0 from the results of radiotechnical and iconometric measurements, we shall use one of the most effective statistical methods — the maximum likelihood method. The choice of this method is due to the simplicity of its numerical realization, and the fact that the estimates obtained are joint-efficient, consistent, unbiased, and asymptotically normal [13]*. Moreover, the inclusion of a priori information on the vector \bar{Q}_0 , when examining it as an additional measurement form, does not lead to change of the problem solution algorithm.

The amount of measurement information, the dimensions of the vector of estimates, and the impossibility of writing in explicit form the functional dependences of the measured quantities on the defining parameters made this problem extremely complex, even for computer realization. Therefore, optimization of the program and the measurement set and choice of the problem numerical solution algorithms are particularly important.

Estimation of the vector \bar{Q}_0 , in accordance with the maximum likelihood principle, leads to the necessity for minimizing the functional

$$\Phi(\bar{Q}_0) = \bar{n}^T K^{-1} \bar{n} + \bar{n}^{*T} \Gamma^{-1} \bar{n}^*, \quad (24)$$

where \bar{n} is the a posteriori information error vector; \bar{n}^* is the a priori information error vector, K and Γ are the correlation matrixes, respectively, of the a posteriori and a priori information.

*If the distribution law is other than normal, the estimates obtained will be the estimates of the generalized least squares method.

We obtain the estimate of the vector \bar{Q}_0 in accordance with (24) from solution of the system of likelihood equations

$$\frac{\partial \Phi}{\partial \bar{Q}_0} = A^T K^{-1} \bar{n} + \Gamma^{-1} \bar{n}^* = 0. \quad (25)$$

Here, the matrix

/188

$$A = A_1 A_2 = \frac{\partial \bar{n}(\bar{Q}_0)}{\partial \bar{Q}} \frac{\partial \bar{Q}}{\partial \bar{Q}_0} \quad (26)$$

is the matrix of partial derivatives of the measured quantities with respect to the parameters being determined.

Using (15) - (18), we can obtain the expressions for the elements of matrix A_1 in explicit form. The elements of matrix A_2 at the measurement times t_t , and the vector of theoretical values of the measured functions (5) - (8), will be obtained by numerical integration of the systems of differential equations describing ALS motion, motion and rotation of the Moon, and the variational equations for these bodies.

Since \bar{n} depends nonlinearly on \bar{Q}_0 and its value is known approximately, the system of equations (25) must be solved repeatedly by the Newton-Raphson method. At each step of the solution, we will have the likelihood equations linearized, relative to $\Delta \bar{Q}_0$, in the form

$$(A^T K^{-1} A + \Gamma^{-1}) \Delta \bar{Q}_0 + (A^T K^{-1} \bar{n} + \Gamma^{-1} \bar{n}^*) = 0, \quad (27)$$

where $\Delta \bar{Q}_0$ are the corrections in the iterations to the approximate values of the vector \bar{Q}_0 .

The structure of the coupling equations makes it possible to break the problem solution down into several stages without disturbing its rigor. We first determine from the star pictures their inertial orientation elements — the vector Θ and its correlation matrix Γ_Θ . The blocks of the Γ_Θ matrix are 3×3 and, consequently, their calculation does not present any difficulty. We introduce

the found elements of the vector $\bar{\theta}$ into the general system of equations as a priori information with their correlation matrix $\Gamma_{\bar{\theta}}$.

This makes it possible to exclude the vector \bar{r}_3 of measured values in the solution of the likelihood equations.

In the vector \bar{Q}_0 , the largest number of unknowns are the coordinates \bar{R}_{j0} of the planetary surface points. We shall solve the system of equations (27) without them. To do this, we represent the vector $\Delta\bar{Q}_0$ in the form of two subvectors $\Delta\bar{R}_j$ and $\Delta\bar{Q}'_0$. Then, (27) may be written as:

$$\begin{aligned} D_{11}\Delta\bar{R}_j + D_{12}\Delta\bar{Q}'_0 &= F_1, \\ D_{21}^T\Delta\bar{R}_j + D_{22}\Delta\bar{Q}'_0 &= F_2, \end{aligned} \quad (28)$$

where F_1 and F_2 are, respectively, subvectors of the free terms. Excluding $\Delta\bar{R}_j$, in (28), we obtain

$$[D_{22} - D_{21}^T D_{11}^{-1} D_{12}] \Delta\bar{Q}'_0 = F_2 - D_{21}^T D_{11}^{-1} F_1. \quad (29)$$

The matrix D_{11} is associated with the vector $\Delta\bar{R}_j$, and has the Jordan form with cell dimensions 3×3 ; therefore, its inversion does not present any problem. This makes it possible to formulate and solve the system of normal equations immediately in the form (29). Then by substitution of $\Delta\bar{Q}'_0$ into (28), we find $\Delta\bar{R}_j$, and the most likely values of the coordinates \bar{R}_j .

/189

In the iteration process, the selenocentric coordinate system is refined, in accordance with (20) and (21).

We obtain the error \bar{Q}_0 correlation matrix from the expression:

$$K_{\bar{Q}_0} = (A^T K^{-1} A + \Gamma^{-1})^{-1} (A^T K^{-1} K_u K^{-1} A + \Gamma^{-1}) (A^T K^{-1} A + \Gamma^{-1})^{-1}, \quad (30)$$

where K_u is the true correlation matrix of the measurement errors.

If the same matrix K is used in the analysis and in estimating the accuracy, then (30) takes the form

$$K_{\bar{Q}} = (A^T K^{-1} A + \Gamma^{-1})^{-1}. \quad (31)$$

Restricting ourselves to linear theory, we obtain the expression for the estimate of the accuracy of the function p of the parameters being determined:

$$K_p = H^T K_{\bar{Q}} H, \quad (32)$$

where H is the matrix of derivatives of the given functions with respect to the parameters being determined.

Expression (30) is used in synthesizing the optimum program and the measurement set for solving the posed problem. In this case, K_u is selected so as to obtain the maximum volume of the correlation ellipsoid of the errors of the sought vector \bar{Q}_0 .

Conclusion. For practical realization of the proposed technique it is necessary to create special space vehicles and inject them into definite orbits.

It is difficult to solve the posed problem from a single orbit. In principle, global photography of the Moon can be accomplished only from a high circumpolar orbit. On the other hand, to determine the parameters of the gravitational field, we require very low orbits, and with the greatest possible variety of inclinations.

The problem of determining the gravity field parameters imposes a limitation on the orientation system and the other equipment installed aboard the spacecraft with respect to the moments created by the equipment, which may affect the orbit. For lunar surface photography, the satellite must be oriented along the radius vector and the velocity vector. The gravity orientation system will probably be optimum. The effectiveness of the proposed technique will be determined to a great degree by the accuracy of the iconometric measurements and their disposition in time. Therefore, photographic equipment will be preferable as the imaging equipment, although it requires return of the exposed materials to the Earth.

/190

The parameters of the imaging apparatus determine the requirements on several other systems, particularly the time recording system.

All the listed requirements and many other requirements on the spacecraft itself — its orbit, orientation system, orbit monitoring system, imaging apparatus, and other elements of the onboard and ground-based complexes — can be obtained on the basis of the above analysis with numerical modeling and estimation of the problem accuracy.

References

1. Rodionov, B. N. Lunar Cartography. Geodeziya i kartografiya, Vol. 30, No. 7, 1967.
2. Aleksashin, Ye. P., Ya. L. Ziman, I. V. Isavnina, et al. Opredeleeniye nekotorykh geometricheskikh, dinamicheskikh i gravitatsionnykh parametrov po snimkam s KA nazemnym trayektornym i astronomicheskim nablyudeniym (Determination of Certain Geometric, Dynamic, and Gravitational Parameters from Spacecraft Pictures by Ground-Based Trajectory and Astronomical Observations). Moscow, Institute of Space Studies of the Academy of Sciences USSR, preprint VINITI (All Union Institute of Scientific and Technical Information), No. 2520 - 71.
3. Urmayev, N. A. Elementy fotogrammetrii (Elements of Photogrammetry). Geodezizdat, Moscow, 1941.
4. Brown, D. C. A Unified Lunar Control Network. Photogrammetric Engng., Vol. 34, No. 12, 1968.
4. Shapiro, I. I. The Prediction of Ballistic Missile Trajectories from Radar Observations. McGraw-Hill Co., New York, 1958.
5. Brouwer, D., and G. Clemence. Method of Celestial Mechanics. Acad. Press, N. Y. and London, 1961.
6. Radziyevskiy, V. V., and A. V. Artem'yev. Influence of Solar Radiation Pressure on Satellite Motion. Astronomicheskii Zhurnal, Vol. 38, No. 5, 1961.
7. Zhongolovich, I. D. Potential of the Earth's Attraction. Bull. Instituta teoreticheskoy astronomii, Akademii Nauk SSSR (ITA AN SSSR), 6, No. 8(81), 1957.

8. Duboshin, G. I. Nebesnaya mekhanika. Osnovnyye zadachi i metody (Celestial Mechanics. Basic Problems and Methods). Fizmatgiz, Moscow, 1963.
9. Chebotarev, G. A. Analiticheskiye i Chislennyye metody nebesnoy mekhaniki (Analytic and Numerical Methods of Celestial Mechanics). Nauka Press, Moscow, 1965.
10. Ziman, Ya. L., B. V. Nepoklonov, and B. N. Rodionov. Determining the Rotation Vector of Planets. Astronomicheskiy Zhurnal, 1277, 6, 1970.
11. Zhongolovich, I. D. Some Formulas Relating to the Motion of a Material Point in the Gravity Field of a Levelled Ellipsoid of Revolution. Bull. Instituta teoreticheskoy astronomii, Akademii Nauk SSSR (ITA AN SSSR), 6, No. 9(82), 1958.
12. Goudas, C. L. Development of Lunar Topography into Spherical Harmonics. Icarus, Vol. 2, No. 1, 1963.
13. Cramer, H. Mathematical Methods of Statistics. Princeton, 1954.
14. Faddeyev, D. K., V. N. Faddeyeva, Vychislitel'nye metody lineynoy algebry (Computational Methods of Linear Algebra). Fizmatgiz, Moscow-Leningrad, 1963.

EVALUATING THE ACCURACY OF SELENODESIC REFERENCE GRIDS

A. A. Koptev

Evaluation of the accuracy of lunar surface reference point coordinates given by the catalogs is a complex problem; therefore, the conclusions of scientists in regard to error magnitudes and their /191 distribution over the lunar disk are contradictory. The altitude errors are evaluated particularly inconsistently because of the low reliability of their determination. Specifically, Kopal [1] and Goudas [2] conclude that the altitudes of points are determined most accurately in the center of the lunar disk; the accuracy diminishes

toward the edges, and is an order of magnitude lower at the edges than in the center. Arthur [3] draws the opposite conclusion, stating that the altitude determination accuracy near the edge of the disk is at least 3.5 times higher than in the central region. Hapmann [4] takes an intermediate position on this question. He concludes that the altitudes are equally accurate everywhere.

Reference point coordinate accuracy can be evaluated by three techniques: on the basis of internal consistency, comparison of the catalogs, and calculation of the errors from theoretical analysis. The studies of Mills [5] showed that the accuracy evaluation on the basis of internal consistency yields satisfactory results only for a large number of photographs used (100 or more). Important factors are not taken into account when comparing catalogs with one another: accuracy of the telescope, number of photographs, and so on.

In the present article, we make an estimate of the accuracy of reference point grids using the third technique, where we take into consideration telescope accuracy, number of photographs, and libration amplitude.

Problem solution in general form. To solve the problem, we use the formulas for the relationship between the coordinates of lunar surface points and their images on the photograph [6]:

$$\xi - \xi_0 = (\zeta - \zeta_0) \frac{X'}{Z'}, \quad (1)$$

$$\eta - \eta_0 = (\zeta - \zeta_0) \frac{Y'}{Z'}, \quad (2)$$

where ξ , η , ζ are the lunar surface point coordinates in the selenocentric coordinate system, ξ_0 , η_0 , ζ_0 are the coordinates of the photograph center of projection in the same system; X' , Y' , Z' are the reduced picture point coordinates, obtained from the expressions:

$$\begin{aligned} X' &= a_1x + a_2y - a_3f, \\ Y' &= b_1x + b_2y - b_3f, \\ Z' &= c_1x + c_2y - c_3f. \end{aligned} \quad (3)$$

Here, x, y are the measured coordinates of the photograph points; f is the telescope focal length; a_1, b_1, c_1 are the direction cosines which convert the picture coordinate system into the selenocentric system. The quantities $\xi_0, \eta_0, \zeta_0, a_1, b_1, c_1$, the picture external orientation elements, are found from the picture orientation with respect to the reference points. The errors of the external orientation elements can be both systematic and random. The systematic part is due to the influence of the errors of the initial data if the same initial points were used for orienting all the pictures. The random part is due to the errors of point identification and measurement, and also the influence of the atmosphere. Different initial points may be used for orientation, which leads to the appearance basically of random errors; therefore, the least squares technique can be used for the solution of such problems. Thus, we convert from the exact equalities (1) and (2) to the equations of the corrections. Assume the unknowns ξ, η, ζ have the approximate values $\bar{\xi}, \bar{\eta}, \bar{\zeta}$, and the corrections to these values are $\delta_\xi, \delta_\eta, \delta_\zeta$. The equations of the corrections for each point, represented on n pictures, will have the form:

$$\delta_\xi - A\delta_\zeta + A_0 = \vartheta_\xi, \quad (4)$$

$$\delta_\eta - B\delta_\zeta + B_0 = \vartheta_\eta, \quad (5)$$

In (4) and (5), we have used the notation $A = X'/Z', B = Y'/Z',$

$$A_0 = (\bar{\xi} - \xi_0) - (\bar{\xi} - \xi_0)A; B_0 = (\bar{\eta} - \eta_0) - (\bar{\xi} - \xi_0)B. \quad (6)$$

The quantities A_0 and B_0 are free terms. The errors $\vartheta_\xi, \vartheta_\eta$ include not only the errors of the measured coordinates and the picture focal distance, but also the errors of the orientation elements, which also include the errors of the initial data.

We see from (4) and (5) that the unknowns $\delta_\xi, \delta_\eta, \delta_\zeta$ cannot be determined from a single picture, since there are two equations with three unknowns for each point. For their determination, we must have at least two pictures with different librations. In practice, more than two pictures are used, and, therefore, we obtain a large

number of redundant measurements, and the problem is solved by the least squares technique.

The normal equations, formulated on the basis of the correction equations, will have the form:

$$\begin{aligned} n\delta_z - \Sigma A\delta_z + \Sigma A_0 &= 0, \\ n\delta_\eta - \Sigma B\delta_z + \Sigma B_0 &= 0, \\ -\Sigma A\delta_z - \Sigma B\delta_\eta + (\Sigma A^2 + \Sigma B^2)\delta_z - \Sigma AA_0 - \Sigma BB_0 &= 0, \end{aligned} \quad (7)$$

where n is the number of pictures on which the given point is represented.

Accuracy evaluation. The weights of the unknowns are obtained using the well-known rules of the least squares technique. The formulas for their calculation have the form

$$\begin{aligned} \frac{1}{P_z} &= \frac{1}{n} + \frac{(\Sigma A)^2}{D}, \\ \frac{1}{P_\eta} &= \frac{1}{n} + \frac{(\Sigma B)^2}{D}, \\ \frac{1}{P_z} &= \frac{n^2}{D}, \end{aligned} \quad (8)$$

where D is the determinate of the System (7).

/193

The same rules were used to obtain the (altitude) function weight

$$h = \sqrt{\xi^2 + \eta^2 + \zeta^2} - R_0, \quad (9)$$

where R_0 is the radius of the levelled surface from which the altitudes are measured.

A formula having the following form was obtained for calculating the function weight:

$$\frac{1}{P_h} = \frac{1 - \zeta'^2}{n} + \frac{(\Sigma A\xi' + \Sigma B\eta' + n\zeta')^2}{D}. \quad (10)$$

In (10), the coordinates ξ' , η' , ζ' are expressed in fractions of the lunar radius, i.e., $\xi' = \xi/R_0$; $\eta' = \eta/R_0$; $\zeta' = \zeta/R_0$.

The use of (10) to analyze the accuracy of height determination on the Moon as a function of point location on the lunar surface is difficult. Therefore, in the further analyses, we shall take a pair of pictures as the basis. We divide all the pictures into pairs, so that the libration difference will be maximum between the pictures of each pair, while the librations themselves are approximately equal in absolute magnitude and opposite in sign.

For a picture pair, the determinant of (7) will have the value:

$$D = \frac{2}{p^0} (p^{0x} + q^{0y}). \quad (11)$$

Here, p^0 and q^0 are the longitudinal and transverse parallaxes of the horizontal picture, and are equal to

$$p^0 = \left(\frac{x'_2}{z'_2} - \frac{x'_1}{z'_1} \right) f, \quad q^0 = \left(\frac{y'_2}{z'_2} - \frac{y'_1}{z'_1} \right) f.$$

Moreover,

$$A_1 + A_2 = \frac{x'_2}{z'_2} + \frac{x'_1}{z'_1}, \quad B_1 + B_2 = \frac{y'_2}{z'_2} + \frac{y'_1}{z'_1}. \quad (12)$$

Let us now express the system determinant in terms of the libration magnitudes. We can write the approximate relations for the longitudinal and transverse parallaxes [6]:

/194

$$S = \frac{B_\xi f}{p^0}, \quad S = \frac{B_\eta f}{q^0}. \quad (13)$$

where S is the Earth-Moon distance; B_ξ , B_η are the projections of the photographic baseline on the ξ and η axes.

Expressing p^0 and q^0 from (13), we substitute them into (11):

$$D = 2 \left(\frac{B_\xi^2}{S^2} + \frac{B_\eta^2}{S^2} \right).$$

The terms B_ξ/S and B_η/S in this equality are the overall librations of the stereopair in longitude and latitude, i.e.,

$$\frac{B_1}{S} \approx \frac{l_1 + l_2}{\rho} = \frac{l}{\rho}, \quad \frac{B_2}{S} \approx \frac{b_1 + b_2}{\rho} = \frac{b}{\rho}.$$

Consequently,

$$D = \frac{2}{\rho^2} (l^2 + b^2). \quad (14)$$

For librations which are equal and opposite in sign, the values of $A_1 + A_2$ and $B_1 + B_2$ approach zero, since $A_1 \approx -A_2$, $B_1 \approx -B_2$. For a large number of stereopairs, the sums ΣA and ΣB will always be small quantities, because of compensation of the positive and negative librations, and can be neglected.

The point coordinates and heights are calculated for several stereopairs rather than for a single pair (in order to increase the accuracy of their determination). On the basis of (8), (10), (14), the weights of the unknowns ξ , η , ζ and their functions h , obtained from the stereopairs, will have the following values:

$$\frac{1}{P_\xi} = \frac{1}{P_\eta} = \frac{1}{2m}, \quad \frac{1}{P_\zeta} = \frac{2\rho^2}{m(l^2 + b^2)}, \quad \frac{1}{P_h} = \frac{1}{2m} \left(1 - \zeta'^2 + \frac{4\rho^2 \zeta'^4}{l^2 + b^2} \right). \quad (15)$$

After calculating the weights, the errors of the point coordinates and heights are calculated in accordance with the rule of the least squares technique, using the formulas:

$$m_\xi = m_\eta = \frac{\mu}{\sqrt{2m}}, \quad m_\zeta = \frac{\mu \rho \sqrt{2}}{\sqrt{m(l^2 + b^2)}}, \\ m_h = \mu \sqrt{\frac{1}{2m} \left(1 - \zeta'^2 + \frac{4\rho^2 \zeta'^4}{l^2 + b^2} \right)}. \quad (16)$$

where μ is the unit weight error.

We see from analysis of (16) that the coordinate and height errors depend on three parameters: libration magnitude, location of the points on the lunar surface (the coordinate ζ'), and the unit weight error. /195

Calculation of unit weight error. The unit weight error is usually calculated using the formula:

$$\mu^2 = \frac{\sum (\theta_i^2 + \theta_j^2)}{n-k}, \quad (17)$$

where n is the number of measurements; k is the number of unknowns (for the stereopair $n = 4$, $k = 3$).

Then,

$$\mu^2 = \theta_{\xi_0}^2 + \theta_{\eta_0}^2 + \theta_{\alpha}^2 + \theta_{\omega}^2 \approx 2(\theta_{\xi_0}^2 + \theta_{\eta_0}^2). \quad (18)$$

The errors θ_{ξ} and θ_{η} are functions of the linear and angular external orientation element errors, and the measured point coordinate errors. Consequently, we can write:

$$\theta_{\xi}^2 = \sum \left(\frac{\partial F}{\partial i} \right)^2 m_i^2, \quad \text{where } i = \xi_0, \zeta_0, \alpha, \omega, \kappa, x, y, f; \quad (19)$$

$$\theta_{\eta}^2 = \sum \left(\frac{\partial F}{\partial j} \right)^2 m_j^2, \quad \text{where } j = \eta_0, \zeta_0, \alpha, \omega, \kappa, x, y, f. \quad (20)$$

In these equations, α, ω, κ are the Euler angles. The following relations exist between the direction cosines and the Euler angles [6]:

$$\begin{aligned} a_1 &= \cos \alpha \cos \kappa - \sin \alpha \sin \omega \sin \kappa, & b_1 &= \cos \omega \sin \kappa, \\ a_2 &= -\cos \alpha \sin \kappa - \sin \alpha \sin \omega \cos \kappa, & b_2 &= \cos \omega \cos \kappa, \\ a_3 &= -\sin \alpha \cos \omega, & b_3 &= -\sin \omega, \\ c_1 &= \sin \alpha \cos \kappa + \cos \alpha \sin \omega \sin \kappa, & & \\ c_2 &= -\sin \alpha \sin \kappa + \cos \alpha \sin \omega \cos \kappa, & & \\ c_3 &= \cos \alpha \cos \omega. & & \end{aligned} \quad (21)$$

We obtain the partial derivatives appearing in (19), (20) after differentiating the basic equations (1), (2):

$$\begin{aligned} \left(\frac{\partial F}{\partial \alpha} \right)_1 &= S; \left(\frac{\partial F}{\partial \omega} \right)_1 = 0; \left(\frac{\partial F}{\partial \kappa} \right)_1 = 0; \left(\frac{\partial F}{\partial \xi_0} \right)_1 = S; \left(\frac{\partial F}{\partial \eta_0} \right)_1 = \frac{yS}{f}; \\ \left(\frac{\partial F}{\partial \alpha} \right)_2 &= -\frac{xS}{f} \left(\frac{\partial F}{\partial \xi_0} \right)_2 = -1; \left(\frac{\partial F}{\partial \omega} \right)_2 = -1; \left(\frac{\partial F}{\partial \kappa} \right)_2 = A = -\frac{x^0}{f}; \\ \left(\frac{\partial F}{\partial \alpha} \right)_3 &= B = -\frac{y^0}{f}; \left(\frac{\partial F}{\partial \omega} \right)_3 = -\frac{S}{f}; \left(\frac{\partial F}{\partial \kappa} \right)_3 = 0; \left(\frac{\partial F}{\partial \xi_0} \right)_3 = -\frac{S}{f}; \\ \left(\frac{\partial F}{\partial \eta_0} \right)_3 &= 0; \left(\frac{\partial F}{\partial \alpha} \right)_4 = \frac{xS}{f^2}; \left(\frac{\partial F}{\partial \omega} \right)_4 = \frac{yS}{f^2}, \end{aligned} \quad (22)$$

where $x^0 = -f \frac{X'}{Z'}$; $y^0 = -f \frac{Y'}{Z'}$ are the horizontal picture coordinates.

/196

Substituting the values of the partial derivatives into (19), (20) and then into (18), we obtain:

$$\mu^2 = 2 \left\{ m_{\omega}^2 + m_{\eta}^2 + \frac{(m_{\alpha}^2 + m_{\omega}^2)}{\rho^2} S^2 + (n_x^2 + m_y^2) \frac{S^2}{f^2} + \left[\frac{m_z^2}{S^2} r^0^2 + \left(\frac{m_x^2}{\rho^2} + \frac{m_f^2}{f^2} \right) r^2 \right] \cdot \frac{S^2}{f^2} \right\}, \quad (23)$$

where $r^2 = x^2 + y^2$, $r^0^2 = x^0^2 + y^0^2$. In (23), we then set $m_{\alpha} = m_{\omega} = m_{\alpha\omega}$, $m_{\omega} = m_{\eta} = m_{\omega\eta}$, $m_x = m_y = m_{xy}$, then

$$\mu^2 = 4 \left\{ \left(m_{\omega\eta}^2 + \frac{m_{\alpha\omega}^2 S^2}{\rho^2} \right) + \frac{m_{xy}^2}{f^2} S^2 + \left[\frac{m_z^2}{S^2} r^0^2 + \left(\frac{m_x^2}{\rho^2} + \frac{m_f^2}{f^2} \right) r^2 \right] \frac{S^2}{2f^2} \right\}. \quad (24)$$

We denote the constant error due to external orientation of the picture with respect to the reference points by $m_{\omega\eta}^2 + \frac{m_{\alpha\omega}^2}{\rho^2} S^2 = \delta^2$ and the variable error which depends on the picture point coordinates by

$$\left[\frac{m_z^2}{S^2} r^0^2 + \left(\frac{m_x^2}{\rho^2} + \frac{m_f^2}{f^2} \right) r^2 \right] \frac{S^2}{2f^2} = v^2.$$

With these notations, (24) will have the form:

$$\mu = 2 \sqrt{\delta^2 + v^2 + \frac{m_{xy}^2}{f^2} S^2}. \quad (25)$$

The external orientation elements are determined on the basis of the most reliable reference points, which should be distributed uniformly over the lunar disk. Unfortunately, the reference points contain significant errors which cannot be neglected. In order to reduce the influence of the reference data errors, it is necessary to orient each picture by using as many reference points as possible. Therefore, we require that

$$\sigma \ll \frac{m_{xy}}{f} S.$$

As for the magnitude of the error v , as a rule it is less than σ , but we also subject it to the condition $v \leq \frac{m_{xy} S}{l}$, assuming that this will compensate to some degree for the influence of the external conditions and the other ignored errors.

Considering the above remarks, the formula for calculating the unit weight error takes the form:

$$\mu = 2\sqrt{3} \frac{m_{xy}}{l} S. \quad (26)$$

We express the error m_{xy} due to accuracy of point coordinate measurement on the picture in terms of the telescope resolution, equal to $m_v = \frac{120''}{D_M} = \frac{0''.12}{D_M}$, where D_M is the telescope objective diameter in meters.

Thus, we set

$$\frac{m_{xy}}{l} = \frac{m_v}{p} = \frac{0''.12}{p D_M}. \quad (27)$$

Thus, the unit weight error with account for (27) has the value

$$\mu = 0.24\sqrt{3} \frac{S}{p D_M}. \quad (28)$$

Substituting the values of S and p into (28), we obtain the formula for the unit weight error in final form:

$$\mu = \left(\frac{0.84}{D_M} \right) kM. \quad (29)$$

The basic characteristics of the telescopes of the observatories whose pictures were used for lunar topography, and the corresponding unit weight errors, are shown in Table 1.

Here, the quantities m_{xy} characterize the metrological properties of the pictures, and m_v — the resolution of the telescopes.

TABLE 1

Observatory	f, cm	D, cm	Resolution		μ , km
			In angular measure, m_y	In linear measure on picture, m_{xy} , μ	
Lick (L)	1722	90	0.13	11.5	0.93
Pic-du-Midi (P)	1806	60	0.20	18.1	1.40
Goloseyevo (G)	550	40	0.30	8.2	2.10
Pulkovo (Pul)	1050	65	0.18	9.7	1.30

Modern instruments make it possible to measure picture point coordinates with accuracy on the order of 10 - 15 μ . Hence, it follows that the values of m_{xy} corresponding to the telescope resolution agree with the data of photogrammetric measurements, and may be taken as the basis for calculating the accuracy of the determination of lunar surface point coordinates. Also, in the resulting formulas, the values of m_{xy} were considered to be independent of the location of the features on the lunar surface. This is associated with the fact that, in deriving the formulas we considered point features of small dimensions, whose form does not influence the accuracy of their definition. When measuring real features (craters) on the pictures, their form changes from the center toward the edges of the Moon. For example, a crater which has a circular form in the center of the lunar disk is imaged on the picture in the form of an ellipse when it is located near the edge. Moreover, the different conditions of illumination of the features in different parts of the lunar disk influence the accuracy of the identification and measurement of the features. This is why the coordinates of points located in the limb zone are not determined when calculating the catalogs, and only the zone $\lambda = \beta \leq 70^\circ$ is considered. Tables 2 - 4 show the errors of the point coordinates and heights calculated using (16) and (29). The following factors were considered in calculating the errors: /198

TABLE 2 *

Number of stereo-pairs	$m_{\xi\eta}$, km			
	L	P	G	Pul
1	0,66 *	0,98	1,47	0,91
9	0,22	0,33	0,50	0,30
25	0,13	0,20	0,29	0,18
49	0,09	0,14	0,21	0,13

* Commas represent decimal points.

TABLE 3 *

$l = l_1 + l_2$	$b = b_1 + b_2$	No. of stereo-pairs m	m_{ξ} , km			
			L	P	G	Pul
6°	6°	1	8,9 *	13,2	20,0	12,3
		9	3,0	4,4	6,7	4,1
		25	1,8	2,6	4,0	2,5
		49	1,3	1,9	2,9	1,8
8	8	1	6,7	9,9	15,0	9,2
		9	2,2	3,3	5,0	3,1
		25	1,3	2,0	3,0	1,8
		49	1,0	1,4	2,1	1,3
10	10	1	5,3	7,9	11,9	7,3
		9	1,8	2,6	4,0	2,4
		25	1,1	1,6	2,4	1,5
		49	0,8	1,1	1,7	1,0

* Commas represent decimal points.

We see from the analysis of the data in Tables 2 - 4 that the errors in the ζ determination exceed by several fold the errors in the determination of ξ and η ;

/199

the accuracy of the determination of ζ and h increases with increase of the librations;

heights are determined more accurately toward the edges of the lunar disk than at its center;

/201

the higher the telescope resolution, the more accurately the point coordinates and heights are determined;

TABLE 4 *

$\begin{matrix} a_1 + b_1 = a_2 + b_2 \\ + \delta_1 = \delta_2 \end{matrix}$	No. of stereo- pairs m	$\zeta' = 1.0$				$\zeta' = 0.6$				$\zeta' = 0.2$			
		\overline{L}	\overline{P}	\overline{G}	$\overline{P_{11}}$	\overline{L}	\overline{P}	\overline{G}	$\overline{P_{11}}$	\overline{L}	\overline{P}	\overline{G}	$\overline{P_{11}}$
6°	1	9,9	13,2	20,0	12,3	5,3	7,9	11,9	7,3	1,9	2,8	4,2	2,6
	9	3,0	4,4	6,7	4,1	1,8	2,6	4,0	2,4	0,6	0,9	1,4	0,9
	25	1,8	2,6	4,0	2,5	1,1	1,6	2,4	1,5	0,4	0,6	0,8	0,5
	49	1,3	1,9	2,9	1,8	0,8	1,1	1,7	1,0	0,3	0,4	0,6	0,4
8	1	6,7	9,9	15,0	9,2	4,1	6,1	9,2	5,6	1,5	2,2	3,3	2,0
	9	2,2	3,3	5,0	3,1	1,4	2,0	3,1	1,9	0,5	0,7	1,1	0,7
	25	1,3	2,0	3,0	1,8	0,8	1,2	1,8	1,1	0,3	0,4	0,7	0,4
	49	1,0	1,4	2,1	1,3	0,6	0,9	1,3	0,8	0,2	0,3	0,5	0,3
10	1	5,3	7,9	11,9	7,3	3,3	4,8	7,3	4,5	1,2	1,8	2,7	1,7
	9	1,8	2,6	4,0	2,4	1,1	1,6	2,4	1,5	0,4	0,6	0,9	0,6
	25	1,1	1,6	2,4	1,5	0,7	1,0	1,5	0,9	0,2	0,4	0,5	0,3
	49	0,8	1,1	1,7	1,0	0,5	0,7	1,0	0,6	0,2	0,3	0,4	0,2

1 $m_{\lambda}, \text{ км}$

* Commas represent decimal points.

In order to improve the accuracy of coordinate and height determination, it is necessary to increase the number of pictures, selecting stereopairs with librations which are maximum in magnitude and opposite in sign.

In selenodesy and selenography, we use not only the (ξ, η, ζ) rectangular coordinate system, but also the selenographic coordinates: longitude λ , latitude β , and absolute heights h . These systems are connected with one another by the relations

$$\begin{aligned} -\xi &= (R+h) \cos \beta \sin \lambda, \\ \eta &= (R+h) \sin \beta, \\ \zeta &= (R+h) \cos \beta \cos \lambda. \end{aligned} \quad (30)$$

We obtain the inverse relation if we divide the first equation of the System (30) by the third equation:

$$\operatorname{tg} \lambda = \xi / \zeta. \quad (31)$$

We obtain the other coordinate β from the second equation:

$$\sin \beta = \frac{\eta}{R+h} = \frac{\eta}{\sqrt{\xi^2 + \eta^2 + \zeta^2}}. \quad (32)$$

Using (31) and (32), we find the mean square errors m_λ and m_β

$$m_\lambda = \frac{P}{R \cos \beta} \sqrt{\sin^2 \lambda \pi_c^2 + \cos^2 \lambda m_{\pi_c}^2} \quad (33)$$

$$m_\beta = \frac{P}{R} \sqrt{(1 - \sin^2 \beta \cos^2 \lambda) m_{\pi_c}^2 + \sin^2 \beta \cos^2 \lambda \pi_c^2} \quad (34)$$

The errors m_λ , m_β for $l = b = 8^\circ$, and $\lambda = 0^\circ$, $\beta = 60^\circ$ were calculated using (33) and (34). The calculation results are shown in Tables 5 - 7.

TABLE 5 *

($l = b = 8^\circ$)

β°	m	$\lambda = 0^\circ$				$\lambda = 60^\circ$			
		L	P	G	Pul	L	P	G	Pul
0	1	1',3	2',0	2',9	1',8	11',5	17',0	25',7	15',8
	9	0,4	0,7	1,0	0,6	3,8	5,7	8,6	5,3
	25	0,3	0,4	0,6	0,4	2,3	3,4	5,1	3,2
	49	0,2	0,3	0,4	0,3	1,6	2,4	3,7	2,2
60	1	2,6	4,0	5,8	3,6	23,0	34,1	51,1	31,7
	9	0,9	1,3	1,9	1,2	7,7	11,4	17,0	10,6
	25	0,5	0,8	1,2	0,7	4,6	6,8	10,2	6,3
	49	0,4	0,6	0,8	0,5	3,3	4,9	7,3	4,5

*Commas represent decimal points.

TABLE 6 *

($l = b = 8^\circ$)

β°	m	$\lambda = 0^\circ$				$\lambda = 60^\circ$			
		L	P	G	Pul	L	P	G	Pul
0	1	1',4	2',0	3',0	1',8	1',4	2',0	3',0	1',8
	9	0,5	0,7	1,0	0,6	0,5	0,7	1,0	0,6
	25	0,3	0,4	0,6	0,4	0,3	0,4	0,6	0,4
	49	0,2	0,3	0,4	0,3	0,2	0,3	0,4	0,3
60	1	11,6	17,2	26,0	16,0	5,9	8,8	13,3	8,1
	9	3,8	5,7	8,7	5,4	1,9	2,9	4,4	2,7
	25	2,2	3,5	5,2	3,1	1,2	1,8	2,7	1,6
	49	1,7	2,4	3,6	2,2	0,9	1,2	1,9	1,2

*Commas represent decimal points.

We see from analysis of the data in Tables 5 and 6 that:

the errors m_λ exceed the errors m_β by several fold, except for the central zone of the lunar disk;

the errors m_λ increase toward the edges of the lunar disk, and the errors in the edge zone are an order of magnitude larger than in the central zone;

the errors m_β increase with latitude increase, and change very little with longitude change.

For comparison with the theoretical calculations, we present the results of an evaluation of the errors m_λ , m_β , m_h of the Mills catalog [5]. The errors were calculated for two values of λ and β , equal to 0 and 60°. The Mills catalog was taken for comparison because the coordinates of the lunar features in this catalog were obtained from 120 photographs made at the Pic-du-Midi observatory. The use of a large number of photographs reduced the influence of random errors associated with atmospheric turbulence, identification of the points on the photographs, and so on. The errors of the Mills catalog for λ and β equal to 0° and 60° are shown in Table 7.

It follows from comparison of the theoretical calculations shown in Tables 4 - 6 (values underlined in the tables) with the results of the Mills catalog (Table 7) that not only are the laws of error variation over the lunar disk the same, but magnitudes of these errors are also in agreement with one another. The formulas and tables presented in this article can be used to evaluate the accuracy of catalogs compiled from photographic data of other observatories, and different numbers of pictures than used in the Mills catalog.

TABLE 7 *

β°	$\lambda=0^\circ$			$\lambda=60^\circ$		
	m_λ	m_β	m_h	m_λ	m_β	m_h
0	0',4	0',3	1,0	3',0	0',1	0,4
60	0,9	2,0	0,6	5,5	0,8	0,3

* Commas represent decimal points.

References

1. Kopal, Z. Topography of the Moon. Space Sci. Rev., Vol. 4, No. 3, 1965.
2. Goudas, C. L. The Selenodetic Control System of the U. S. Army Map Service. Icarus, Vol. 4, No. 2, 1965.
3. Arthur, D. W. G. The Computation of Selenodetic Coordinates Using the Librations. Commun Lunar and Planet. Lab, Vol. 4, No. 1, 1965.
4. Hapmann, I. Mitt. Univ.-Sternwarte Wien, Vol. 67, No. 12, 1965.
5. Mills, B. A., and P. V. Sudbury. Absolute Coordinates of Lunar Features III. Icarus, Vol. 9, No. 3, 1968.
6. Urmayev, N. A. Elementy fotogrammetrii (Elements of Photogrammetry). Geodezizdat, Moscow, 1941.

DETERMINATION OF DYNAMIC CORRECTIONS TO POINT
COORDINATES OF PHOTOGRAPHS OBTAINED BY THE
ZOND 6 AND ZOND 8 SPACECRAFT

V. V. Kiselev, B. N. Rodionov

The linear and angular motions of the Zond 6 and Zond 8 spacecraft imaging camera [1] during exposure cause displacements of the optical image points. In the case of instantaneous exposure of each individual point and nonsimultaneous exposure of the complete frame, this leads to finite geometric shifts of the points without causing blurring of the photographic image. Therefore, when measuring the resulting photographic pictures, the problem arises of reducing the picture point positions to a common instant of time. This reduction is performed by means of dynamic corrections to the measured picture point coordinates.

/204

These corrections are found using the formulas of dynamic photogrammetry [2]. Before using them in application to the spacecraft of the Zond 6 and Zond 8 type, let us turn to Figure 1. The following notations are used in the present report: L and R are the center and radius of the lunar sphere; S_1 , S is a segment of the spacecraft orbit; S_1 , ..., S is the position of the camera projection center at the instant of exposure; N_1 , ..., N are the subsatellite points (nadir points); N_1 , N are the projections of the orbit on the surface of the sphere; P is the plane tangent to the sphere at the nadir point (horizontal plane); p is the photographic picture; n is the nadir point on the picture; n_{SNL} is the local vertical; o and O are the principal points of the picture and the ground; no , NO are the principal verticals of the picture and the ground; $kSKK'$ is the projecting ray; K' , K , k are the ground point on the surface of the sphere; on the plane P , and its image on the picture; $H_N = SN$ is the vehicle flight altitude above the nadir point.

The following coordinate systems are shown in the figure.

$LX_L Y_L Z_L$ is the selenographic system with coordinate origin at the center of the Moon, the z -axis LZ_L coincides with the lunar axis of rotation, the abscissa axis LX_L is directed along the line of intersection of the lunar equator and zero meridian planes. The zero meridian plane passes through the center of the Earth at the instant when the mean longitude of the Moon on the ecliptic is equal to the mean longitude of the ascending node of its orbit. The ordinate axis LY_L lies in the plane of the equator and completes the right-hand frame, the position of a point is determined either by the three rectangular coordinates X_L , Y_L , Z_L , or by the spherical coordinates λ , ϕ , ρ : the longitude, latitude, and radius vector.

$ox'y'$ is the picture coordinate system fixed with the principal horizontal and principal vertical of the photographic picture.

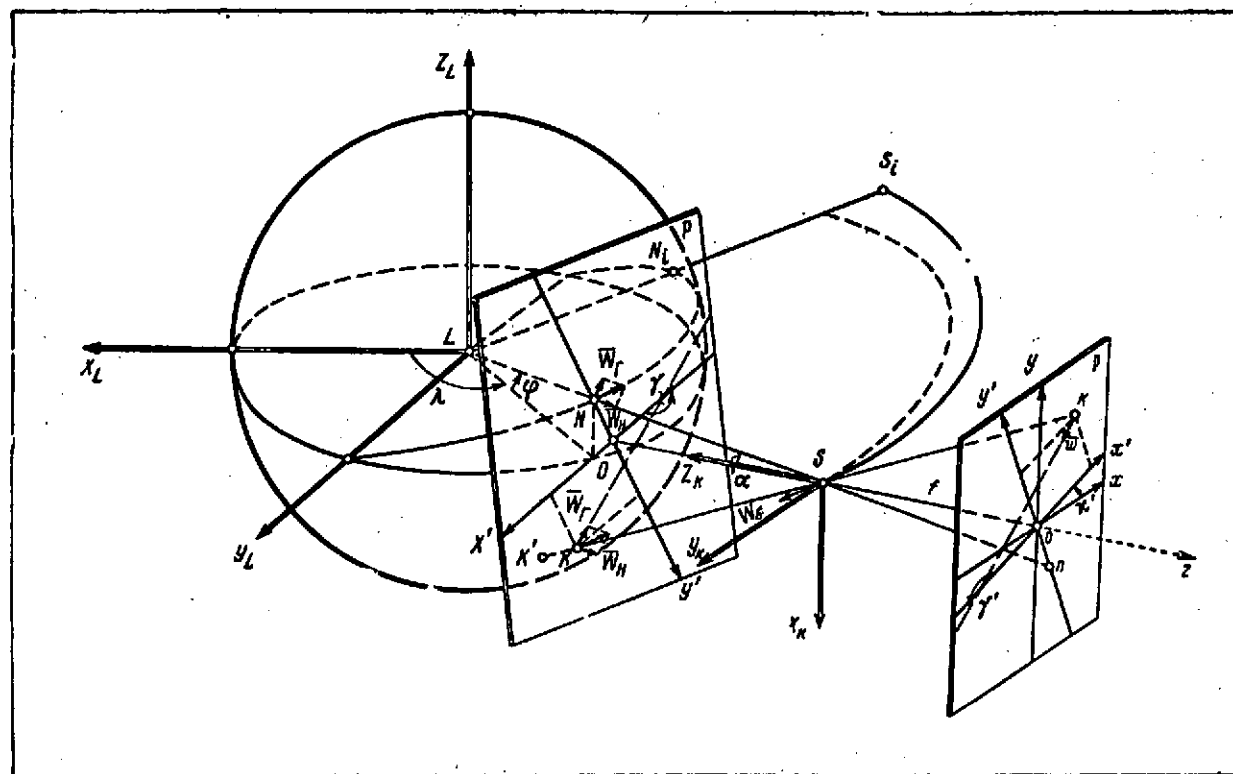


Figure 1. Diagram of Moon photography from Zond 6 and Zond 8 spacecraft, and the coordinate system used

oxy is the picture coordinate system specified by the coordinate marks.

$SX_k Y_k Z_k$ is the three-dimensional photogrammetric right-hand coordinate imaging camera system, whose origin is located at the center of projection. In this system, the SZ_k axis is directed along the camera optical axis toward the surface of the Moon, the SX_k and SY_k axes are parallel, respectively, to the oy and ox picture axes, and the SY_k axis can be directed either in or opposite the direction of flight.

$OX'Y'Z'$ is the ground coordinate system fixed with the principal horizontal and the principal vertical of the ground; in this system, the OX' and OY' axes lie in the P plane, the OZ' axis (not shown in the figure) completes the right-hand set. Also shown in the figure are the angles α — the angle between the camera optical axis and the local vertical or the absolute inclination of the picture; κ' is the angle of rotation of the $ox'y'$ picture coordinate system relative to the oxy coordinate system; \bar{W}_T is the horizontal velocity vector (in the plane P or a plane parallel thereto) of any point of the plane P or the ground (N, K, K', and so on); \bar{W}_H is the vertical velocity vector (perpendicular to the P plane) of any point of the plane P or the ground; γ is the angle between the horizontal velocity vector \bar{W}_T and the OX' axis of the $OX'Y'Z'$ coordinate system; \bar{W} is the velocity vector of a point of the optical image; γ' is the angle between the ox' picture axis and the vector \bar{w} .

/205

On the basis of the definitions made with the aid of Figure 1, we reduce the dynamic correction formulas to final form:

$$\Delta x'(W_r) = \frac{\frac{W_r}{H} t \left(\cos \gamma - \frac{x'}{f} \sin \gamma \sin \alpha \right) \left(\cos \alpha - \frac{y'}{f} \sin \alpha \right) t}{1 + \frac{W_r}{H} \sin \gamma \sin \alpha \left(\cos \alpha - \frac{y'}{f} \sin \alpha \right) t}, \quad (1)$$

$$\Delta y' (W_r) = \frac{\frac{W_r}{H} f \sin \gamma \left(\cos \alpha - \frac{y'}{f} \sin \alpha \right)^2 t}{1 + \frac{W_r}{H} \sin \gamma \sin \alpha \left(\cos \alpha - \frac{y'}{f} \sin \alpha \right) t}, \quad (2)$$

$$\Delta x' (W_H) = \frac{x' \left(e^{\frac{W_H}{H} t} - 1 \right) \cos \alpha \left(\cos \alpha - \frac{y'}{f} \sin \alpha \right)}{e^{\frac{W_H}{H} t} - \left(e^{\frac{W_H}{H} t} - 1 \right) \cos \alpha \left(\cos \alpha - \frac{y'}{f} \sin \alpha \right)}, \quad (3)$$

$$\Delta y' (W_H) = \frac{(y' + f \operatorname{tg} \alpha) \left(e^{\frac{W_H}{H} t} - 1 \right) \cos \alpha \left(\cos \alpha - \frac{y'}{f} \sin \alpha \right)}{e^{\frac{W_H}{H} t} - \left(e^{\frac{W_H}{H} t} - 1 \right) \cos \alpha \left(\cos \alpha - \frac{y'}{f} \sin \alpha \right)}, \quad (4)$$

$$\Delta x (\omega_x) = x \left[\frac{\sec (\omega_x f)}{1 - \frac{y}{f} \operatorname{tg} (\omega_x f)} - 1 \right] \quad (5)$$

$$\Delta y (\omega_x) = \frac{\left(f + \frac{y^2}{f} \right) \operatorname{tg} (\omega_x f)}{1 - \frac{y}{f} \operatorname{tg} (\omega_x f)}, \quad (6)$$

$$\Delta x (\omega_y) = \frac{\left(f + \frac{x^2}{f} \right) \operatorname{tg} (\omega_y f)}{1 - \frac{x}{f} \operatorname{tg} (\omega_y f)}, \quad (7)$$

$$\Delta y (\omega_y) = y \left[\frac{\sec (\omega_y f)}{1 - \frac{x}{f} \operatorname{tg} (\omega_y f)} - 1 \right], \quad (8)$$

$$\Delta x (\omega_z) = x [\cos (\omega_z f) - 1] - y \sin (\omega_z f), \quad (9)$$

$$\Delta y (\omega_z) = x \sin (\omega_z f) + y [\cos (\omega_z f) + 1], \quad (10)$$

where $\Delta x' (W_r)$, $\Delta y' (W_r)$ and $\Delta x' (W_H)$, $\Delta y' (W_H)$ are the corrections to the picture point coordinates in the $ox'y'$ system, caused by the horizontal and vertical spacecraft velocities relative to the ground point; $\Delta x (\omega_x)$, $\Delta y (\omega_x)$, $\Delta x (\omega_y)$, $\Delta y (\omega_y)$, $\Delta x (\omega_z)$, $\Delta y (\omega_z)$, are the corrections to the picture point coordinates in the oxy system caused by the angular rotation rates ω_x , ω_y , ω_z of the imaging camera about the axes of the $Sxyz$ coordinate system (not shown in Figure 1), beginning at the center of projection S and parallel to the oxy picture system; x' , y' and x , y are the measured picture point coordinates in the $ox'y'$ and oxy

systems, f is the focal length of the imaging camera; $t=(t_k-t_0)$ is the time interval between exposure times of the principal o and given k picture points.

Formulas (1) - (4) account for the linear motions of the imaging camera, and Formulas (5) - (10) account for the angular motions. For the angular rotation rates $\omega_x=\omega_y=\omega_z=1'.8 \text{ sec}^{-1}$ of the stabilized imaging camera of the Zond 6 and Zond 8 spacecraft, the change $0' 07$ of angular position relative to each axis during the complete frame exposure time 0.04 sec is less than the angular resolution $0'.2$ of the objective-photofilm system. Therefore, we can take $\omega_x=\omega_y=\omega_z=0$. This means that the dynamic correction calculation using (5) - (10) is not made in the present case.

Determination of input parameters for formulas of dynamic corrections to picture point coordinates. When using (1) - (4) to calculate the dynamic corrections to the picture point coordinates, we need to know the following quantities which appear in these equations: $\alpha, \kappa', H, W_r, W_H, \gamma$. Let us find their values.

To do this, we use the following basic data:

1) the selenographic rectangular coordinates $X_{L_S}, Y_{L_S}, Z_{L_S}$ of the spacecraft (center of projection)

2) the matrix of direction cosines of the photogrammetric coordinate system axes X_k, Y_k, Z_k relative to the selenographic system axes $LX_L Y_L Z_L$

$$A = \begin{pmatrix} a_{11} & a_{12} & a_{13} \\ a_{21} & a_{22} & a_{23} \\ a_{31} & a_{32} & a_{33} \end{pmatrix}, \quad (11)$$

at the moments of exposure (with orientation of the SY axis opposite the direction of flight, we denote the corresponding matrix by A'); /207

3) the modulus W_S and direction cosines $l_{WS1}, l_{WS2}, l_{WS3}$ of the vector \vec{W}_S of spacecraft orbital velocity relative to the axes selenographic coordinate system $\bar{X}_L \bar{Y}_L \bar{Z}_L$ at the moments of exposure.

Let us determine the angle α . The imaging camera optical axis SO coincides with the photogrammetric coordinate system axis SZ_k ; therefore, its direction in the $LX_L Y_L Z_L$ coordinate system is characterized by the direction cosines a_{31}, a_{32}, a_{33} (11) of the SZ_k axis. The angle α between the camera optical axis and the local vertical is found from the expression:

$$\cos \alpha = a_{31} l_{v1} + a_{32} l_{v2} + a_{33} l_{v3}, \quad (12)$$

where l_{v1}, l_{v2}, l_{v3} are the direction cosines of the local vertical nSNL (see Figure 1):

$$\begin{aligned} l_{v1} &= -X_{LS}(X_{LS}^2 + Y_{LS}^2 + Z_{LS}^2)^{-1/2}, \\ l_{v2} &= -Y_{LS}(X_{LS}^2 + Y_{LS}^2 + Z_{LS}^2)^{-1/2}, \\ l_{v3} &= -Z_{LS}(X_{LS}^2 + Y_{LS}^2 + Z_{LS}^2)^{-1/2}. \end{aligned} \quad (13)$$

To determine the angle κ' , we need to know the direction cosines of the oxy and ox'y' picture coordinate system axes in the $LX_L Y_L Z_L$ selenographic coordinate system. We add to the oxy planar picture coordinate system the third axis oz, which completes the right-hand system (see Figure 1). The matrix for converting from the $SX_k Y_k Z_k$ photogrammetric coordinate system to the oxyz picture coordinate system in accordance with the figure has the form:

$$B = \begin{pmatrix} 0 & -1 & 0 \\ -1 & 0 & 0 \\ 0 & 0 & -1 \end{pmatrix}. \quad (14)$$

We have the following matrix in place of B if the SY_k axis is oriented opposite the direction of flight:

$$B' = \begin{pmatrix} 0 & 1 & 0 \\ 1 & 0 & 0 \\ 0 & 0 & -1 \end{pmatrix}.$$

We obtain the matrix of direction cosines of the oxyz picture coordinate system relative to the axes of the $LX_L Y_L Z_L$ selenographic system from the product of the matrixes B (14) and A (11): /208

$$C = BA = \begin{pmatrix} 0 & -1 & 0 \\ -1 & 0 & 0 \\ 0 & 0 & -1 \end{pmatrix} \begin{pmatrix} a_{11} & a_{12} & a_{13} \\ a_{21} & a_{22} & a_{23} \\ a_{31} & a_{32} & a_{33} \end{pmatrix} = \begin{pmatrix} -a_{21} & -a_{22} & -a_{23} \\ -a_{11} & -a_{12} & -a_{13} \\ -a_{31} & -a_{32} & -a_{33} \end{pmatrix}. \quad (15)$$

The normal unit vector \bar{n}_v of the principal vertical plane SonSNO, whose trace on the picture is the oy' axis, determines the direction of the ox' picture axis, since the ox' axis is perpendicular to this plane.

The directions oSO and nSN, lying in the principal vertical plane, are characterized by the unit vectors \bar{v}_{SO} and \bar{v}_{SN} . The coordinates of the vector \bar{v}_{SO} in the system $LX_L Y_L Z_L$ are the direction cosines a_{31}, a_{32}, a_{33} (11) of the SZ_k axis of the photogrammetric coordinate system; the coordinates of the vector \bar{v}_{SN} are the direction cosines l_{v1}, l_{v2}, l_{v3} (13) of the local vertical. The coordinates n_{v1}, n_{v2}, n_{v3} of the vector \bar{n}_v and, consequently, the direction cosines of the ox' picture axis are found from the vector product $\bar{v}_{SO} \times \bar{v}_{SN}$, from which follows:

$$\begin{aligned} n_{v1} &= a_{32}l_{v3} - a_{33}l_{v2}, \\ n_{v2} &= a_{33}l_{v1} - a_{31}l_{v3}, \\ n_{v3} &= a_{31}l_{v2} - a_{32}l_{v1} \end{aligned} \quad (16)$$

In this case the vector \bar{n}_v and the ox' axis are pointed in the same direction.

Thus, from the known direction cosines of the ox , oy (15), and ox' (16) axes of the oxy and $ox'y'$ picture coordinate systems in the $LX_L Y_L Z_L$ selenographic coordinate system, we find the desired angle κ' , using the relations

$$\begin{aligned}\cos \kappa' &= -a_{11}n_{s1} - a_{21}n_{s2} - a_{31}n_{s3}, \\ \sin \kappa' &= -a_{11}n_{s1} - a_{12}n_{s2} - a_{13}n_{s3}.\end{aligned}\quad (17)$$

To find the flight height H_N above the nadir point, we need only subtract from the radius-vector length LS (Figure 1), the lunar sphere radius $LN = R$

$$H_N = (X_{LS}^2 + Y_{LS}^2 + Z_{LS}^2)^{1/2} - R. \quad (18)$$

But we are interested in the flight height above a given surface point. We proceed as follows. We find the direction cosines k_1, k_2, k_3 of the projecting ray $kSKK'$ in the $oxyz$ picture coordinate system (Figure 1), using the relations

$$\begin{aligned}k_1 &= -x(x^2 + y^2 + f^2)^{-1/2}, \\ k_2 &= -y(x^2 + y^2 + f^2)^{-1/2}, \\ k_3 &= -f(x^2 + y^2 + f^2)^{-1/2},\end{aligned}$$

and convert from them to the direction cosines l_{k1}, l_{k2}, l_{k3} of the same projecting ray in the $LX_L Y_L Z_L$ selenographic coordinate system, using the following matrix expression:

$$\begin{pmatrix} l_{k1} \\ l_{k2} \\ l_{k3} \end{pmatrix} = C^T \begin{pmatrix} k_1 \\ k_2 \\ k_3 \end{pmatrix}, \quad (19)$$

where C^T is the transposed matrix C (15)

$$C^T = \begin{pmatrix} -a_{21} & -a_{11} - a_{31} \\ -a_{22} & -a_{12} - a_{32} \\ -a_{23} & -a_{13} - a_{33} \end{pmatrix}. \quad (20)$$

On the basis of (19) and (20), we write

$$\begin{aligned}l_{k1} &= -a_{21}k_1 - a_{11}k_2 - a_{31}k_3, \\l_{k2} &= -a_{22}k_1 - a_{12}k_2 - a_{32}k_3, \\l_{k3} &= -a_{23}k_1 - a_{13}k_2 - a_{33}k_3.\end{aligned}\tag{21}$$

We determine the angle α' between the projecting ray $kSKK'$ and the local vertical $nSNL$, using their direction cosines (21), (13) in the $LX_L Y_L Z_L$ system, from the formula

$$\cos \alpha' = l_{v1}l_{k1} + l_{v2}l_{k2} + l_{v3}l_{k3}.$$

We obtain the sought height H on the basis of simple geometric arguments (Figure 2) from the relations:

$$\sin \beta = \left(1 + \frac{H_N}{R}\right) \cos \alpha', \quad H = H_N + R[\cos(\alpha' + \beta) + 1].\tag{22}$$

The correction to the height H for relief can be taken into account in the calculations using (18), (22) by varying the assumed radius R of the lunar sphere on the basis of picture interpretation results.

Let us determine the horizontal W_F and vertical W_H surface point velocities, and the angle γ . At the moment of exposure, the velocity vector \bar{W}_S is applied to the projection center S . By virtue of motion relativity, we can consider that the imaging camera is stationary and the velocity vector $\bar{W} = -\bar{W}_S$, equal in magnitude to W_S but having the opposite direction, is applied to each point of the surface being photographed. The modulus W_S and direction cosines $l_{W_S1}, l_{W_S2}, l_{W_S3}$ of the vector \bar{W}_S in the $LX_L Y_L Z_L$ selenographic coordinate system are known. The direction cosines of the vector \bar{W} are, respectively, $-l_{W_S1}, -l_{W_S2}, -l_{W_S3}$. The vector \bar{W} must be broken down into two components — parallel and perpendicular to the plane P (Figure 1) — or a plane parallel

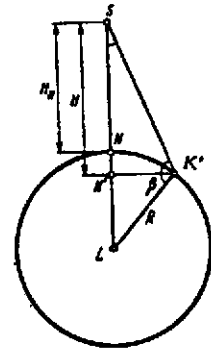


Figure 2. Diagram for determining flight height H above surface point K ($\alpha' = \angle LSK'$)

/210

thereto and passing through the given surface point K' . This objective will be accomplished if we resolve the vector W along the axes of the $OX'Y'Z'$ local coordinate system, whose axes OX' and OY' lie in the plane P and OZ' axis is perpendicular thereto.

Let us determine the direction cosines of the $OX'Y'Z'$ coordinate axes in the $LX_LY_LZ_L$ system. We find the direction cosines $l_{Y'1}, l_{Y'2}, l_{Y'3}$ of the OY' axis as the direction cosines of the line of intersection of the principal vertical plane $SonSNO$ with the plane P . The coordinates n_{v1}, n_{v2}, n_{v3} of the normal unit vector \bar{n}_v of the principal vertical plane are found from (16). The coordinates of the normal unit vector \bar{n}_p of the P plane are the direction cosines l_{v1}, l_{v2}, l_{v3} (13) of the local vertical.

We obtain the direction cosines $l_{Y'1}, l_{Y'2}, l_{Y'3}$ of the OY' axis from the vector product of the normal vectors $\bar{n}_p \times \bar{n}_v$, from which follows:

$$l_{Y'1} = n_{v3}l_{v2} - n_{v2}l_{v3},$$

$$l_{Y'2} = n_{v1}l_{v3} - n_{v3}l_{v1},$$

$$l_{Y'3} = n_{v2}l_{v1} - n_{v1}l_{v2}.$$

The direction cosines of the OZ' axis are

$$l_{Z'1} = -l_{v1}, l_{Z'2} = -l_{v2}, l_{Z'3} = -l_{v3},$$

and of the OX' axis:

$$l_{X'1} = -n_{v1}, l_{X'2} = -n_{v2}, l_{X'3} = -n_{v3}.$$

The direction cosines $\omega_1, \omega_2, \omega_3$ of the vector \bar{W} in the $OX'Y'Z'$ system are expressed by the relations:

$$\begin{aligned} \omega_1 &= -l_{X'1}l_{WS1} - l_{X'2}l_{WS2} - l_{X'3}l_{WS3}, \\ \omega_2 &= -l_{Y'1}l_{WS1} - l_{Y'2}l_{WS2} - l_{Y'3}l_{WS3}, \\ \omega_3 &= -l_{Z'1}l_{WS1} - l_{Z'2}l_{WS2} - l_{Z'3}l_{WS3}. \end{aligned}$$

The projections of the vector \bar{W} on the OX' , OY' , OZ' coordinate axes /211
will be

$$W_{X'} = -W_S \omega_1, W_{Y'} = -W_S \omega_2, W_{Z'} = -W_S \omega_3.$$

The sought magnitudes of the horizontal W_H and vertical W_V velocities of the surface point and the angle γ are found from the expressions:

$$\begin{aligned} W_H &= (W_{X'}^2 + W_{Y'}^2)^{1/2}, & \sin \gamma &= W_{Y'}/W_H, \\ W_V &= W_{Z'}, & \cos \gamma &= W_{Z'}/W_H. \end{aligned} \quad (23)$$

Sequence of introduction of dynamic corrections to picture point coordinates. The dynamic corrections to the picture point coordinates are introduced as follows. The point coordinates x, y in the oxy picture coordinate system are measured. Photogrammetric distortion is taken into account. Conversion to the x', y' coordinates of the point in the $ox'y'$ picture coordinate system is performed using the angle κ' , known from (17):

$$\begin{pmatrix} x' \\ y' \end{pmatrix} = \begin{pmatrix} \cos \kappa' & \sin \kappa' \\ -\sin \kappa' & \cos \kappa' \end{pmatrix} \begin{pmatrix} x \\ y \end{pmatrix}.$$

Using the Formulas (1) - (4) and the values (12), (17), (22), (23) found for their input parameters, we find the dynamic corrections $\Delta x'(W_H), \Delta y'(W_H), \Delta x'(W_V), \Delta y'(W_V)$, and then the corrected coordinate values:

$$\begin{aligned} x_u' &= x' + \Delta x'(W_H) + \Delta x'(W_V), \\ y_u' &= y' + \Delta y'(W_H) + \Delta y'(W_V). \end{aligned}$$

We convert from the corrected coordinates x_u', y_u' in the $ox'y'$ system to the corrected coordinates x_u, y_u in the oxy system:

$$\begin{pmatrix} x_u \\ y_u \end{pmatrix} = \begin{pmatrix} \cos \kappa' & -\sin \kappa' \\ \sin \kappa' & \cos \kappa' \end{pmatrix} \begin{pmatrix} x_u' \\ y_u' \end{pmatrix}.$$

The sequence of introduction of dynamic corrections to the coordinates of any picture point is analogous.

During photography from the Zond 8 spacecraft, the flight altitude above the moon was $H_N \approx 1100$ km, and the velocity — $W_S = 2.0$ km/sec. With resolution on the picture of 0.01 mm, and picture measurement accuracy 0.005 mm, the need arises for taking into account the dynamic errors, whose magnitudes reach ≈ 0.025 mm.

References

1. Rodionov, B. N., I. V. Isavnina, V. V. Kiselev, et al. New Data on the Figure and Relief of the Moon from Analysis of Photographs Obtained by Zond 6. Kosmicheskiye issledovaniya, No. 3, 1971. /212
2. Rodionov, B. N. Dynamic Photogrammetry. Geodeziya i kartografiya, No. 10, 1970.

REFINEMENT OF THE GOLOSEYEV CATALOG POINT COORDINATES IN THE LIMB ZONE AND DETERMINATION OF POINT COORDINATES ON THE BACK SIDE OF THE MOON

V. A. Krasikov

During the first session of lunar photography from the Zond 6 spacecraft, pictures were obtained which covered practically the entire western hemisphere [1]. The importance of these pictures lies in the fact that they cover a considerable portion of the lunar surface which is visible from the Earth, whose geometry has been quite thoroughly studied and is represented by point coordinates in lunar catalogs. These same pictures showed half the side of the Moon which is not visible from the Earth. This made it possible to

construct a photogrammetric grid encompassing the entire western hemisphere and referenced to points of the visible side, whose coordinates were taken from the Goloseyev catalog [2].

The problem was solved using two pictures taken during the flight approaching the Moon from an altitude of ~9000 km above the lunar surface. The position of the pictures made it impossible to use the familiar methods of photogrammetry in constructing the three-dimensional grid, since the angles of intersection of the projecting rays at the lunar surface points did not exceed $\sim 1^\circ$.

The photogrammetric grid was constructed as follows. The external orientation elements of the pictures were first determined by photogrammetric resection using the photographed catalog points of the visible side of the Moon, and the coordinates of the catalog points used were refined. The problem was solved by joint statistical analysis of the measurements of both pictures and the selenographic coordinates of the catalog points. For these purposes, we developed a special algorithm, and compiled a program realizing the maximum likelihood method which permitted working with up to 120 catalog points simultaneously.

Then we determined separately for each picture the selenographic coordinates of surface points on the back side of the Moon from the intersection of the projecting ray with a sphere of radius $R = 1738$ km. The final point coordinate value was taken as the arithmetic means of the coordinate values of the corresponding points for each picture. Since in this case the primary error in the coordinates is due to ignoring lunar surface relief, there was no basis for using an exact method for the problem solution. Therefore, the point coordinates on each picture were determined by the regressive gradient search method, which is far simpler in the program realization sense than the Newton method.

/213

Identification of points and measurement of pictures. Eighteen points on the visible side of the Moon were identified for determining the external orientation elements [2]. We selected as these

reference points the smallest possible craters, in order to minimize the error in identifying the crater centers (in our case they were observed in a different projection than when viewed from the Earth).

The picture measurements were made on a stereocomparator. To improve the accuracy of the initial measurement dispersion estimate, the observations were made six times using independent overlays with different orientation of the pictures. The estimate of the measurement dispersion for all the points except one, obtained on the basis of internal consistency, did not exceed ~ 0.030 mm. The corresponding estimate of the dispersion of the average of the six measurements was ~ 0.012 mm.

The measurements of fiducial crosses imaged on the pictures made it possible to conclude that deformation of the photographic material took place at the moment of measurement. The nature of the deformation was radial-annular; the deformation field is approximated well by a first-degree polynomial

Here, δx , δy are the corrections to the measured coordinates owing to photographic material deformation in mm; x , y are the measured coordinates referred to the center of the picture in mm; $a = b = 0.006$.

Determination of picture external orientation elements and refinement of point coordinates in the limb zone. For the solution of this problem, we used the well-known photogrammetric relationships between the point coordinates x_{1j} , y_{1j} measured on the pictures (selenographic coordinates X_1 , Y_1 , Z_1 of these points) and the picture external orientation elements

$$\begin{aligned} x_{1j} &= -f \frac{(X_1 - X_0) a'_{11} + (Y_1 - Y_0) a'_{12} + (Z_1 - Z_0) a'_{13}}{(X_1 - X_0) a'_{21} + (Y_1 - Y_0) a'_{22} + (Z_1 - Z_0) a'_{23}}, \\ y_{1j} &= -f \frac{(X_1 - X_0) a'_{31} + (Y_1 - Y_0) a'_{32} + (Z_1 - Z_0) a'_{33}}{(X_1 - X_0) a'_{21} + (Y_1 - Y_0) a'_{22} + (Z_1 - Z_0) a'_{23}}. \end{aligned} \quad (1)$$

Here, f is the camera focal length; a_{kl}^j are elements of the orthogonal transformation matrix, which are functions of the picture angular orientation elements.

Linearization of (1) in the vicinity of the approximate values of the parameters being determined leads to a system of linear equations of the form

$$AX + \Delta = l; \quad (2)$$

here A is the matrix of partial derivatives of the measurements with respect to the parameters being determined; X is the vector of corrections to the approximate values of the parameters being determined; Δ is the vector of measurement errors; l is the vector of deviations of the measured quantities from their calculated values.

Since it is assumed that the measurements are uncorrelated and equally accurate, we normalize (2) by the measurement dispersion

$$A_H = \left\| \frac{a_{pq}}{\sigma} \right\|, \quad \Delta_H = \left\| \frac{\Delta_p}{\sigma} \right\|, \quad l_H = \left\| \frac{l_p}{\sigma} \right\|; \quad (3)$$

$$A_H X + \Delta_H = l_H.$$

Since a priori data on certain components of the vector X are known (the selenocentric coordinates and dispersions of the catalog points), the maximum likelihood method makes it possible to obtain unconditional (Bayesian) estimates for the vector of unknowns and its correlation matrix [3]

$$\begin{aligned} \hat{X} &= (A_H^T A_H + K_x^{-1})^{-1} (A_H^T l_H + K_x^{-1} X^0), \\ K \hat{X} &= (A_H^T A_H + K_x^{-1})^{-1}. \end{aligned} \quad (4)$$

In our case, the matrix K_x is diagonal, and the dispersions of the point coordinates presented in the catalog are located along the diagonal.

The numerical realization of the algorithm for obtaining unconditional estimates by the maximum likelihood method was accomplished by solving the system of nonlinear equations (1) with account for the a priori information on the catalog point coordinates. The basic steps of the solution involved:

- 1) linearizing the system of nonlinear equations (1) in the vicinity of the approximate values of the parameters;
- 2) solving the linearized system of equations by the conjugate gradient method to obtain the corrections to the approximate values of the parameters x^0 ;
- 3) calculating the weighting coefficients to obtain estimates of the dispersions of the parameters being determined.

The form of the coefficient matrix of the normed linearized system, with account for the a priori information on the catalog point coordinates, is shown in Figure 1.

The upper part of the A_H matrix is the conventional matrix of derivatives of the measured functions with respect to the parameters, while the lower part is a diagonal matrix with elements $\sigma_0/\sigma x_i$, $\sigma_0/\sigma y_i$, $\sigma_0/\sigma z_i$ (where σ_0 is the estimate of the measurement dispersion; σx_i , σy_i , σz_i are the estimates of the dispersions of the corresponding coordinates of the i th catalog point). Norming of the matrix was performed so that the vector of differences had dimension in millimeters.

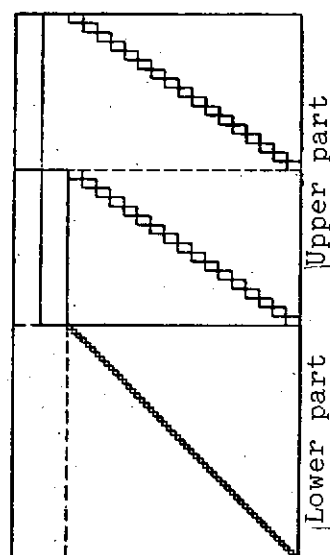


Figure 1. Structure of the A_H matrix

Processing of the measurements consisted of several stages. In the first stage, the measurement dispersion with account for possible inaccuracies in identifying the centers of the craters was taken equal to 0.020 mm. The coordinates of all 18 points were assumed to be known exactly. As a result of this solution, the measurement dispersion estimate based on the sum of the squares of the residual differences was found to be 0.150 mm. In view of the fact that the x and y picture axes nearly coincided in direction with the X and Z selenocentric coordinate system axes (Figure 2), it was advisable to perform the analysis of the residual difference vector V by grouping its components, respectively, with respect to the corrections to the abscissas V_x and ordinates V_y . The results of this analysis are shown in Table 1. The corrections V_x to

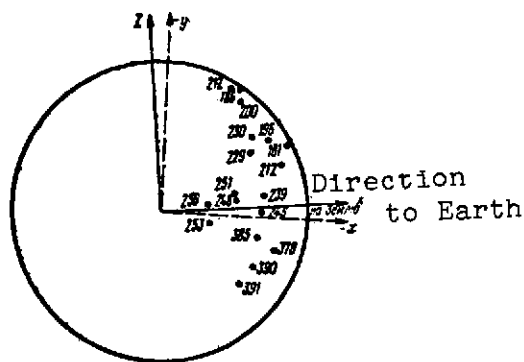


Figure 2. Diagram of point arrangement on the pictures

the measured values of the x picture point coordinates were larger by 4.5 times than the corrections V_y for the y picture point coordinates. For one of the points, the corrections to the measured coordinates exceeded 0.2 mm in both axes.

Analysis of the measurements of this point and of its image on the pictures makes it possible to conclude that, in this case, there is an inaccuracy in identification of the center of the crater. Therefore, this point was rejected and did not take part in the subsequent reduction stages. The distribution of the corrections with respect to the coordinate axes at the remaining 17 points can be explained by errors of the initial data, since the point X-coordinates presented in the catalogs are known more approximately by a factor of 4 - 5 times than the Y- and Z-coordinates. But the magnitude of these corrections does not agree at all with the magnitude of the x-coordinate dispersions. In fact, the measurement corrections reach a magnitude of 0.4 mm, which in the picture scale

/216

TABLE 1*

Point no. in. catalog [2]	V_x , mm	V_y , mm	Point no. in. catalog [2]	V_x , mm	V_y , mm
391	+0,028	+0,104	248	+0,173	+0,021
	+0,032	+0,095		+0,191	+0,018
253	-0,025	-0,040	251	+0,268	-0,005
	+0,003	-0,045		+0,263	+0,022
385	+0,117	+0,003	195	-0,038	+0,001
	+0,115	+0,014		-0,018	+0,003
181	0,000	-0,035	199	+0,020	-0,005
	+0,028	-0,028		-0,007	-0,011
212	+0,010	-0,011	186	-0,148	-0,007
	+0,020	-0,035		-0,124	-0,026
270	+0,055	+0,001	256	-0,453	-0,081
	+0,039	+0,029		-0,419	-0,099
378	+0,073	+0,059	239	+0,370	-0,015
	+0,072	+0,045		+0,336	+0,006
390	-0,250	+0,047	230	-0,139	-0,046
	-0,284	+0,055		-0,172	-0,043
246	-0,060	+0,008	Mean		
	-0,076	+0,003	square	0,182	0,042
			value		

* Commas represent decimal points.

corresponds to ~ 11 km, while the coordinate dispersions with respect to this axis do not exceed ~ 2 km.

In the second analysis stage, the X, Y, Z coordinates of the catalog points were used in the analysis with their dispersions. In this case, the estimate of the measurement dispersion based on the sum of the squares of the residual differences was found to be ~ 0.035 mm. The corrections δX and δZ to the catalog point coordinates obtained in this case are shown at the right side of Table 2. Analysis of these quantities and their comparison with the corresponding dispersions indicates that, while the corrections in the Y and Z coordinates agree with their catalog dispersions, the corrections to the X coordinates were significantly larger than the corresponding dispersions. Analysis of the vector of residual differences also showed that while the mean square magnitude of the correction to the

TABLE 2 *

Point no. in catalog	V_x, mm	V_x, mm	V_y, mm	V_z, mm	$\delta X, \text{mm}$	$\delta Z, \text{mm}$
391	0,000		+0,020			
	+0,006	+0,027	+0,009	+0,014	-1,95	-0,17
253	-0,013		-0,012			
	+0,013	-0,020	-0,015	-0,031	+1,88	+0,80
385	+0,009		-0,023			
	+0,004	+0,029	-0,012	-0,012	-2,90	+0,10
181	-0,012		-0,024			
	+0,020	+0,016	-0,018	-0,022	-2,20	+0,28
212	-0,004		+0,008			
	+0,008	+0,013	-0,016	-0,003	-1,11	+0,03
200	+0,009		0,000			
	-0,008	+0,008	+0,026	+0,008	-0,48	-0,06
378	+0,005		+0,010			
	+0,005	+0,038	-0,004	+0,002	-3,34	-0,02
390	-0,004		+0,010			
	-0,029	-0,077	+0,019	+0,024	+4,74	-0,43
246	+0,001		+0,024			
	-0,015	-0,025	+0,017	+0,015	+1,59	-0,13
248	0,000		+0,010			
	+0,012	+0,043	+0,007	+0,006	-3,10	-0,06
251	+0,017		-0,016			
	+0,004	+0,063	+0,010	-0,008	-4,85	+0,17
195	-0,014		+0,018			
	+0,008	+0,001	+0,020	+0,015	-0,05	-0,14
199	+0,014		0,000			
	-0,013	-0,004	-0,010	-0,005	+0,45	+0,08
188	-0,022		+0,008			
	+0,008	-0,051	-0,013	-0,001	+3,66	+0,01
256	-0,034		-0,003			
	+0,006	-0,128	-0,015	-0,015	+11,46	+0,037
239	+0,042		-0,030			
	0,000	+0,107	-0,011	-0,024	-7,70	+0,27
230	+0,009		0			
	-0,021	-0,044	+0,004	+0,004	+4,21	-0,06
Mean square value	0,015	0,053	0,015	0,015	-	-

* Commas represent decimal points.

measurement of the x and y point coordinates on the pictures and the mean square magnitude of the normed correction V_z to the Z coordinates was equal to ~ 0.015 mm, the mean square magnitude of the normed correction V_x to the X coordinate was equal to ~ 0.052 mm.

Such a situation can occur in the following four cases:

the measurements themselves were made more approximately than we have assumed; there was an error in crater center identification because of differences in the projection; the camera's photogrammetric parameters changed after calibration; the dispersions of the point coordinates with respect to the X axis presented in the catalogs are too low.

Let us examine all these cases in more detail.

Error of the measurements themselves is practically eliminated, /217 since the measurements were made using six independent overlays with different picture orientation.

More likely is error of crater center identification because of difference of the projections, although it is difficult to imagine that the identification error affects only the x coordinates of the picture points.

Nothing definite can be said concerning the errors which can occur as a result of change of the objective lens parameters, since the camera was not recalibrated after return to the Earth. It is difficult to imagine that this factor leads to random errors of large magnitude only in the picture x axis.

Most probable is the fourth factor, i.e., the catalog points have too low dispersion with respect to the X axis. In fact, as we have mentioned previously, this coordinate is determined more poorly from observations made from the Earth than are the Y and Z coordinates. Comparison of the corrections δX and δZ for the X and Z coordinates with their catalog dispersions yielded the following results (see Table 3). In four of the 17 cases, the corrections δ exceeded 3σ , and in four cases the corrections exceeded 4σ .

In the third analysis stage, the X-coordinates of all the catalog points were relaxed by the magnitude 3σ . The estimate of the measurement dispersion obtained was 0.017 mm. The corrections to the X and Z point coordinates and the data of the analysis of the residual difference vector are given in Table 4.

TABLE 3

Interval	No. of corrections in given interval	
	in X	in Z
$\sigma > \delta$	5	13
$2\sigma > \delta > \sigma$	5	4
$3\sigma > \delta > 2\sigma$	3	—
$4\sigma > \delta > 3\sigma$	2	—
$\delta > 4\sigma$	2	—
	17	17

Finally, a version was calculated in which the point X-coordinates were relaxed completely, i.e., they became definitive. The calculation results are shown in Table 5.

The last two versions yielded corrections δX and δZ , which nearly coincided in magnitude. The estimates of the dispersions of the vector of the parameters being defined were also calculated in the last version. The maximum magnitude of the estimate of the dispersion for the corrections to the X-coordinate amounted to ~ 0.7 km.

Combined analysis of the data shown in Tables 1, 2, 4, 5 gave the following results.

The mean square magnitude of the correction to the X-coordinates was ~ 5.2 km, while the mean square magnitude of the catalog dispersions of the coordinates with respect to the X axis was ~ 1.7 km. The mean square magnitude of the correction to the Z-coordinate was ~ 0.27 km, while the mean square magnitude of the catalog dispersions of the coordinates with respect to the Z axis was ~ 0.29 km.

On the basis of the analysis results, we can draw the tentative conclusion that the X-coordinates of the points presented in the catalog [2] are known more approximately by a factor of about three than the compilers assumed. As for the point Z-coordinates, their accuracy corresponds completely to the dispersions presented in the

TABLE 4 *

Point no. in catalog	$V_{x, MM}$	$V_{X, MM}$	$V_{y, MM}$	V_z, MM	$\delta X, KM$	$\delta Z, KM$
391	-0,003		+0,009			
	+0,003	+0,018	+0,001	+0,005	-3,95	-0,06
253	-0,012		-0,011			
	+0,017	+0,006	-0,015	-0,032	-1,99	+0,86
385	+0,006		-0,023			
	0,000	+0,017	-0,012	-0,012	-5,13	+0,10
181	-0,011		-0,030			
	+0,018	-0,008	-0,022	-0,027	+2,77	+0,35
212	-0,004		+0,007			
	+0,005	-0,003	-0,017	-0,004	+0,65	+0,04
200	+0,005		+0,004			
	-0,010	-0,012	+0,029	+0,001	+2,06	-0,06
378	+0,001		+0,009			
	-0,001	+0,016	-0,004	+0,002	-4,18	-0,02
390	+0,010		+0,007			
	-0,016	-0,017	+0,018	+0,019	+3,20	-0,33
246	+0,005		+0,028			
	-0,012	0	+0,020	+0,017	+0,001	-0,015
248	-0,007		+0,013			
	+0,006	+0,022	+0,009	+0,009	-5,8	-0,09
251	+0,008		-0,014			
	-0,004	+0,033	+0,010	-0,005	-7,65	+0,10
195	-0,013		+0,016			
	+0,007	+0,010	+0,018	+0,013	+2,48	-0,12
199	+0,013		+0,003			
	-0,013	-0,012	-0,007	-0,003	+3,64	+0,04
186	-0,017		+0,011			
	+0,012	-0,036	-0,009	+0,001	+7,66	-0,01
256	-0,022		+0,002			
	+0,021	-0,030	-0,012	-0,012	+8,16	0
239	+0,027		-0,029			
	-0,016	+0,043	-0,012	-0,021	-9,27	+0,25
230	+0,014		+0,003			
	-0,017	-0,018	+0,006	+0,006	+4,98	-0,07
Mean square value	0,012	0,021	0,015	0,015	—	—

* Commas represent decimal points.

TABLE 5 *

Point no. in catalog	V_x, mm	V_y, mm	V_z, mm	$\delta X, \text{mm}$	$\delta Z, \text{mm}$
391	-0,004 +0,003	+0,009 -0,002	+0,003	-4,37	-0,03
253	-0,012 +0,016	-0,012 -0,017	-0,034	-2,33	+0,87
385	+0,005 -0,001	-0,022 -0,012	-0,012	-5,40	+0,09
181	-0,011 +0,018	-0,029 -0,020	-0,025	+3,01	+0,33
212	-0,005 +0,005	+0,009 -0,015	-0,002	+0,77	+0,02
200	+0,006 -0,010	0 +0,023	+0,009	+2,36	-0,07
378	0,000 -0,001	+0,011 -0,003	+0,003	-4,45	-0,03
390	+0,011 -0,015	+0,008 +0,017	+0,018	+2,87	-0,32
246	+0,035 -0,012	+0,029 +0,021	+0,018	-0,12	-0,16
248	-0,008 +0,035	+0,013 +0,008	+0,009	-6,03	-0,09
251	+0,007 -0,006	-0,015 +0,010	-0,034	-7,80	+0,13
195	-0,013 +0,008	+0,017 +0,020	+0,014	+2,66	-0,14
199	+0,014 -0,012	-0,031 -0,038	-0,005	+3,99	+0,07
186	-0,014 +0,014	+0,007 -0,010	-0,001	+8,03	+0,01
256	-0,020 +0,022	+0,001 -0,013	-0,014	+7,97	+0,34
239	+0,026 -0,018	-0,028 -0,011	-0,020	-9,39	+0,24
230	+0,015 -0,016	+0,002 +0,007	+0,006	+5,14	-0,10
Mean square value	0,012	0,015	0,015	5,20	0,27

* Commas represent decimal points.

catalog. A final conclusion on the catalog accuracy can be drawn only after suitable analysis, using additional data and for a larger number of points.

Determination of selenographic coordinates of points on the back side of the Moon. We make the following transformation in order to solve this problem. In the Expression (1), for the measured picture point coordinates, replacing the value of the lunar surface point coordinates by their expressions in terms of B, L, and R = 1738 km, we obtain:

$$\begin{aligned} x_{ij} &= -f \frac{a_{11}^l (R \cos B_i \cos L_i - X_j) + a_{12}^l (R \cos B_i \sin L_i - Y_j) + a_{13}^l (R \sin L_i - Z_j)}{a_{21}^l (R \cos B_i \cos L_i - X_j) + a_{22}^l (R \cos B_i \sin L_i - Y_j) + a_{23}^l (R \sin L_i - Z_j)}, \\ y_{ij} &= -f \frac{a_{31}^l (R \cos B_i \cos L_i - X_j) + a_{32}^l (R \cos B_i \sin L_i - Y_j) + a_{33}^l (R \sin L_i - Z_j)}{a_{21}^l (R \cos B_i \cos L_i - X_j) + a_{22}^l (R \cos B_i \sin L_i - Y_j) + a_{23}^l (R \sin L_i - Z_j)}. \end{aligned} \quad (5)$$

Thus, we have a system of nonlinear equations with the two unknowns B and L. Here, B is the selenographic latitude, L is the selenographic longitude; X_j, Y_j, Z_j are linear picture external orientation elements (see Table 6).

The quantities a_{ki} in the orthogonal transformation matrix are calculated in terms of the known angular external orientation elements (see Table 6) using the formulas:

$$\begin{aligned} a_{11} &= -\sin A \sin \lambda - \cos A \cos \lambda \sin \varphi, \\ a_{12} &= \sin A \cos \lambda - \cos A \sin \lambda \sin \varphi, \\ a_{13} &= \cos A \cos \varphi, \\ a_{21} &= \cos A \sin \lambda - \sin A \cos \lambda \sin \varphi, \\ a_{22} &= -\cos A \cos \lambda - \sin A \sin \lambda \sin \varphi, \\ a_{23} &= \sin A \cos \varphi, \\ a_{31} &= \cos \varphi \cos \lambda, \quad a_{32} = \cos \varphi \sin \lambda, \quad a_{33} = \sin \varphi. \end{aligned} \quad (6)$$

The regressive gradient search method [5] was used to solve the nonlinear system of equations (5). As the functional to be minimized, we took the sum of the squares of the residual differences

TABLE 6 *

External orientation elements	Picture	
	12	19
A	278°23' ± 17'	278°42' ± 17'
λ	-92°33' ± 28'	-92°23' ± 15'
φ	2°12' ± 17'	1°43' ± 16'
X	-477,1 KM ± 8,1 KM	-588,1 KM ± 4,1 KM
Y	-10850,0 KM ± 2,5 KM	-10642,5 KM ± 2,5 KM
Z	525,9 KM ± 4,5 KM	531,7 KM ± 4,3 KM

* Commas represent decimal points.

$$\Phi = (x_{\text{meas}} - x_{\text{calc}})^2 + (y_{\text{meas}} - y_{\text{calc}})^2. \quad (7)$$

The gradient vector r was calculated by the finite difference method:

$$r = \begin{pmatrix} \frac{\Delta\Phi_B}{\delta B} \\ \frac{\Delta\Phi_\lambda}{\delta \lambda} \end{pmatrix}. \quad (8)$$

Here,

$$\begin{aligned} \Delta\Phi_B &= \Phi(B^0 + \delta B, L^0) - \Phi(B^0, L^0), \\ \Delta\Phi_L &= \Phi(B^0, L^0 + \delta L) - \Phi(B^0, L^0), \end{aligned} \quad (9)$$

are the changes of the Functional (7) for small variations of the parameters δB and δL .

The gradient step was selected so that, at each sequential point, the value of the functional became less than at the preceding point. Thus, at each step, the solution was improved, using the formulas

$$B_{i+1} = B_i + \alpha r_{i1}, \quad L_{i+1} = L_i + \alpha r_{i2}. \quad (10)$$

We took as the initial approximations the selenographic coordinates B and L of points identified on the Complete Lunar Map [4] to within a few degrees.

TABLE 7 *

Point no.	L, deg	B, deg	Point no.	L, deg.	B, deg
17	-84,2	-14,5	26	-105,9	40,8
18	-86,5	-32,0	27	-108,2	25,5
19	-91,1	4,0	23	-109,4	1,6
20	-93,8	12,0	29	-114,0	18,1
21	-93,8	-34,2	30	-118,8	-21,4
22	-94,2	33,5	31	-120,6	4,4
23	-94,0	-14,7	32	-126,3	37,9
24	-97,6	-3,7	33	-132,5	11,0
25	-103,2	-28,2			

* Commas represent decimal points.

The regressive gradient search method is simple in realization and has faster convergence than the steepest descent method [6]. The requirements on accuracy of selection of the initial approximations of the parameters are quite weak. The accuracy of the initial approximations should be such as to exclude ambiguity in the solution and may vary from a few tens of degrees in the central part of the disk to several degrees in the limb zone.

/224

The values of the selenographic coordinates B_1 and L_1 were determined from each of the pictures separately. Their arithmetic mean was taken as the final values of the coordinates. The values of the point coordinates obtained in this way are presented in Table 7. The location of the points is shown on the photomap of the back side of the Moon [1]. The error of these coordinates is due primarily to not accounting for the lunar surface relief.

References

1. Rodionov, B. N., I. V. Isavnina, V. A. Krasikov, et al. New Data on the Figure and Relief of the Moon From Results of Analysis of Photographs Obtained by Zond 6. Kosmicheskiye issledovaniya, No. 3, 1971.

2. Gavrilov, I. V., A. S. Duma, and V. S. Kislyuk. Catalog of Selenocentric Locations of 500 Basic Points on the Lunar Surface. Collection: Figura i dvizheniye luny (Figure and Motion of the Moon), Vol. 2. Naukova Dumka, Kiev, 1967.
3. Linnik, Yu. V. Metod naimen'shikh kvadratov i osnovy teorii obrabotki nablyudeniye (Least Squares Method and Bases of Observation Analysis Theory). Fizmatgiz, Moscow, 1962.
4. Polnaya karta luny (Complete Lunar Map), scientific editor Yu. N. Lipskiy. Nauka Press, Moscow, 1969.
5. Wilde, D. J. Optimum-Seeking Methods (Russian translation). Nauka Press, Moscow, 1969.
6. Faddev, D. K., and V. N. Gaddeva. Vychislitel'nyye metody lineynoy algebry (Computational Methods of Linear Algebra). Fizmatgiz, Moscow-Leningrad, 1964.

DETERMINATION OF SELENOGRAPHIC COORDINATES OF LUNAR
SURFACE POINTS FROM SINGLE PICTURES OB-
TAINED FROM ZOND 6

Ya. L. Ziman, V. F. Baratova,
I. V. Isavnina

Pictures of the lunar surface with an image of practically the entire lunar limb were obtained from the Zond 6 spacecraft. During the time of exposure, the entire lunar surface covered by these photographs was illuminated by the Sun [1]. Such single pictures were used to find the external orientation elements and selenographic coordinates of the photographed lunar surface points. The selenographic coordinate system was specified by the Golosev Catalog [2] and was realized by points of this catalog identified on the pictures and hereafter termed reference points*. Craters located on the

/225

* Any of the existing catalogs whose individual points are identified on the pictures can be used as the reference catalog.

invisible side of the Moon and also other points of the Goloseyev catalog, which can be used as control points, were taken as the points being determined. The problem was solved in the following sequence.

1. The picture tilt α and rotation κ angles and the selenocentric radius vector ρ of the spacecraft were found from the image of the limb edge.

2. The coordinates of the lunar surface point images were transformed, using the angles α and κ .

3. We calculated the auxiliary selenocentric coordinates of the photographed lunar surface points. The Z' axis of the auxiliary system (Figure 1) was aligned with the spacecraft selenocentric radius vector; the abscissa X' and ordinate Y' axes were aligned parallel to the corresponding x_T and y_T axes of the transformed picture. All the photographed points were referred to a sphere of given radius.

4. From the catalog and auxiliary reference point coordinates, we found the orientation elements of the auxiliary coordinate system in the catalog system. Using these elements, the coordinates of the photographed points and the picture external orientation elements were recomputed from the auxiliary system into the catalog system.

5. We calculated the coordinates on the picture of the selenographic meridian and parallel grid points.

The connection between the coordinates of the limb edge points of a planet, approximated by a three-axis ellipsoid, and their images in the picture, was examined in [3]. In the present case, the Moon is considered to be a sphere of constant radius R .

The following basic formula is used to determine the angles α , κ and the radius

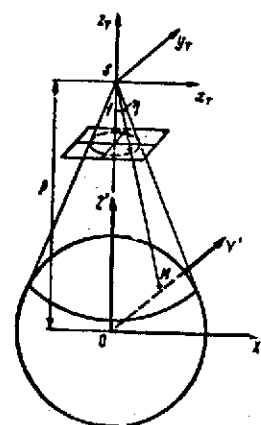


Figure 1. Auxiliary coordinate system

vector of the spacecraft:

$$\cos \eta = l_i l_0 + m_i m_0 + n_i n_0, \quad (1)$$

where η is the horizon dip angle (see Figure 1), l_i, m_i, n_i and l_0, m_0, n_0 are the direction cosines, respectively, of the limb points and its center in the picture coordinate system.

Expressing l_0, m_0, n_0 in terms of the angles α, κ and the angle η in terms of the lunar radius R and the radius vector ρ , we rewrite (1) as

$$\frac{1}{\cos \alpha} \sqrt{1 - \frac{R^2}{\rho^2}} = l_i \operatorname{tg} \alpha \cos \kappa + m_i \operatorname{tg} \alpha \sin \kappa - n_i. \quad (2)$$

Equation (2) can be solved provided neither R nor ρ are subject to refinement. In our case, as noted previously, the lunar radius R was specified. Expanding (2) into a Taylor series at the point $\alpha = \alpha_0, \kappa = \kappa_0$, and $\rho = \rho_0$, we obtain for the k limb points the system of error equations relative to the unknown corrections $\Delta \alpha, \Delta \kappa, \Delta \rho$ to the approximate values $\alpha_0, \kappa_0, \rho_0$:

$$\begin{aligned} a_1 \Delta \alpha + b_1 \Delta \kappa + c_1 \Delta \rho + \omega_1 &= v_1, \\ &\dots \dots \dots \\ a_k \Delta \alpha + b_k \Delta \kappa + c_k \Delta \rho + \omega_k &= v_k, \end{aligned} \quad (3)$$

where v_1 is the deviation of the left sides of the equations from zero because of measurement errors and random relief

$$\begin{aligned} a_i &= (l_i \cos \kappa_0 + m_i \sin \kappa_0) \cos \alpha_0 + n_i \sin \alpha_0, \\ b_i &= (-l_i \cos \kappa_0 + m_i \sin \kappa_0) \sin \alpha_0, \\ c_i &= -\frac{R_0^2}{\rho_0^2} \left(1 - \frac{R_0^2}{\rho_0^2}\right)^{-1/2}, \\ \omega_i &= (l_i \cos \kappa_0 + m_i \sin \kappa_0) \sin \alpha_0 - n_i \cos \alpha_0 - \left(1 - \frac{R_0^2}{\rho_0^2}\right)^{1/2}. \end{aligned}$$

The System (3) is solved by the iteration method under the condition:

$$\sum_{i=1}^k v_i^2 = \min. \quad (4)$$

The final values of the parameters being determined are obtained from the formulas

$$\begin{aligned}\alpha &= \alpha_0 + \Delta\alpha_1 + \Delta\alpha_2 + \dots, \\ x &= x_0 + \Delta x_1 + \Delta x_2 + \dots, \\ \rho &= \rho_0 + \Delta\rho_1 + \Delta\rho_2 + \dots\end{aligned}\quad (5)$$

For the case when we seek only α and κ , (1) is rewritten in the form

$$\cos \eta_i = l_i \frac{x_0}{r_0} + m_i \frac{y_0}{r_0} - n_i \frac{f}{r_0}, \quad (6)$$

where x_0, y_0 are the coordinates of the limb center image in the picture, f is the focal length of the imaging camera,

$$r_0 = \sqrt{x_0^2 + y_0^2 + f^2}.$$

We find the average value of $\cos \eta$ from (6):

227

$$(\cos \eta)_{\text{av}} = \frac{\sum_{i=1}^k \cos \eta_i}{k} = \frac{x_0}{r_0} \frac{\sum_{i=1}^k l_i}{k} + \frac{y_0}{r_0} \frac{\sum_{i=1}^k m_i}{k} - \frac{f}{r_0} \frac{\sum_{i=1}^k n_i}{k}. \quad (7)$$

Subtracting (7) from each Equation (6), we obtain

$$\begin{aligned}a'_1 x_0 + b'_1 y_0 + \omega'_1 &= v'_1, \\ &\dots\dots\dots \\ a'_k x_0 + b'_k y_0 + \omega'_k &= v'_k,\end{aligned}\quad (8)$$

where

$$\begin{aligned}a'_i &= \frac{1}{r_0} \left(l_i - \frac{\sum_{i=1}^k l_i}{k} \right), \quad b'_i = \frac{1}{r_0} \left(m_i - \frac{\sum_{i=1}^k m_i}{k} \right), \\ \omega'_i &= -\frac{f}{r_0} \left(n_i - \frac{\sum_{i=1}^k n_i}{k} \right)\end{aligned}$$

v'_1 are the deviations of the values of the left sides of (8) from zero because of measurement errors and random relief.

Solving (8) under the condition

$$\sum_{i=1}^k v_i' = \min,$$

we find x_0 and y_0 , and from them the angles α , κ or the direction cosines l_0 , m_0 , n_0

$$\alpha = \operatorname{arctg} \frac{\sqrt{x_0^2 + y_0^2}}{f}, \quad \kappa = \operatorname{arctg} \frac{y_0}{x_0}. \quad (9)$$

After finding x_0 , y_0 from (7), we can calculate the angle η_{av} and the radius vector ρ .

$$\rho = R \operatorname{cosec} \eta_{av}. \quad (10)$$

Transformation of the pictures is accomplished using the following formulas:

we calculate the picture rotation matrix M:

/228

$$M = \begin{pmatrix} \cos \alpha \cos \kappa & \cos \alpha \sin \kappa & \sin \alpha \\ -\sin \kappa & \cos \kappa & 0 \\ -\sin \alpha \cos \kappa & -\sin \alpha \sin \kappa & \cos \alpha \end{pmatrix}, \quad (11)$$

the coordinates of the lunar surface point images are multiplied by the matrix M:

$$\begin{pmatrix} x_j' \\ y_j' \\ z_j' \end{pmatrix} = M \begin{pmatrix} x_j \\ y_j \\ -f \end{pmatrix}; \quad (12)$$

then the transformed coordinates are calculated:

$$x_{Tj} = -f \frac{x_j'}{z_j'}, \quad y_{Tj} = -f \frac{y_j'}{z_j'}. \quad (13)$$

We express the auxiliary selenocentric coordinates of the photographed lunar surface points in terms of the found transformed coordinates of their images (see Figure 1):

$$X'_j = \frac{x_{Tj}}{-f} (p - Z'_j), \quad Y'_j = \frac{y_{Tj}}{-f} (p - Z'_j), \quad X_j'^2 + Y_j'^2 + Z_j'^2 = r_j^2. \quad (14)$$

We transform (14) to the form

$$AZ'^2 + BZ' + C = 0, \quad (15)$$

where

$$A = 1 + \frac{x_T^2 + y_T^2}{f^2}, \quad B = -2p \frac{x_T^2 + y_T^2}{f^2}, \quad C = -r^2 + p \frac{x_T^2 + y_T^2}{f^2}.$$

Solving (15), we find Z' ; substituting it into the first two equations (14) we find X' and Y' .

We define the connection between the coordinates in the X, Y, Z catalog system and the auxiliary system by the expression

$$\begin{pmatrix} X \\ Y \\ Z \end{pmatrix} = N \begin{pmatrix} X' - X'_0 \\ Y' - Y'_0 \\ Z' - Z'_0 \end{pmatrix}, \quad (16)$$

where X'_0, Y'_0, Z'_0 are the auxiliary coordinates of the catalog system; N is the rotation matrix. Using the reference points, we can find the solution of (16) X'_0, Y'_0, Z'_0 and the elements of the matrix N .

It is best to satisfy this solution under the condition

/229

$$\sum_{j=1}^p (\Delta X'_j + \Delta Y'_j + \Delta Z'_j) = \min.$$

where p is the number of reference points used in solving the problem, and

$$\begin{aligned} \Delta X'_j &= X_j - [n_{11}(X'_j - X'_0) + n_{12}(Y'_j - Y'_0) + n_{13}(Z'_j - Z'_0)], \\ \Delta Y'_j &= Y_j - [n_{21}(X'_j - X'_0) + n_{22}(Y'_j - Y'_0) + n_{23}(Z'_j - Z'_0)], \\ \Delta Z'_j &= Z_j - [n_{31}(X'_j - X'_0) + n_{32}(Y'_j - Y'_0) + n_{33}(Z'_j - Z'_0)]. \end{aligned}$$

After determining X'_0, Y'_0, Z'_0 and the elements of the matrix N , we convert the auxiliary coordinates of the lunar surface points into

the selenographic system of the catalog being used. The angular picture external orientation elements are defined by the matrix:

$$L = M^T N^T. \quad (17)$$

The coordinates X_s, Y_s, Z_s of the center of projection are calculated from (16) by the substitution $X' = 0, Y' = 0, Z' = \rho$.

The calculation of the selenographic meridian and parallel grid point coordinates on the picture is made in the following sequence:

1) we specify the selenographic longitudes λ_i and latitudes ϕ_i of the grid points;

2) we convert from the polar coordinates λ_i and ϕ_i to the rectangular coordinates X_i, Y_i, Z_i

$$X_i = R \cos \phi_i \cos \lambda_i, Y_i = R \cos \phi_i \sin \lambda_i, Z_i = R \sin \phi_i, \quad (18)$$

where R is the radius of the lunar sphere;

3) the resulting rectangular spatial grid point coordinates are /230 converted into the coordinates of the images of these points on the picture:

$$\begin{aligned} x &= -f \frac{(X_i - X_s) l_{11} + (Y_i - Y_s) l_{12} + (Z_i - Z_s) l_{13}}{(X_i - X_s) l_{21} + (Y_i - Y_s) l_{22} + (Z_i - Z_s) l_{23}}, \\ y &= -f \frac{(X_i - X_s) l_{31} + (Y_i - Y_s) l_{32} + (Z_i - Z_s) l_{33}}{(X_i - X_s) l_{21} + (Y_i - Y_s) l_{22} + (Z_i - Z_s) l_{23}}, \end{aligned} \quad (19)$$

where l_{ij} are elements of the matrix L (17).

* * *

Tables 1 - 3 show preliminary results of interpretation using the above described technique of two pictures of the Moon obtained from Zond 6. The selenographic coordinate system was realized by

TABLE 1. PICTURE EXTERNAL ORIENTATION ELEMENTS ***

Elements	Picture 12	Picture 19
α^*	$0^{\circ}34',4$	$1^{\circ}24',5$
κ	$97^{\circ}46',7$	$134^{\circ}12',1$
ρ	$10.905,7 \text{ KM}$	$10.712,3 \text{ KM}$
Matrix	$\begin{pmatrix} -0,0169 & 0,9939 & -0,0446 \\ -0,0439 & -0,0453 & -0,9939 \\ -0,9938 & -0,0149 & 0,0446 \end{pmatrix}$	$\begin{pmatrix} 0,5797 & 0,8132 & -0,0523 \\ -0,0692 & -0,0149 & -0,9975 \\ -0,8119 & 0,5313 & 0,0477 \end{pmatrix}$
N^{**}		
X_s^{**}	$-436,2 \text{ KM}$	$-560,6 \text{ KM}$
Y_s	$-10.893,8 \text{ KM}$	$-10.685,8 \text{ KM}$
Z_s	$+486,5 \text{ KM}$	$+510,6 \text{ KM}$

* α , κ , ρ were calculated for 60 limb points.

** The elements of the auxiliary system orientation matrixes N and the coordinates X_s , Y_s , Z_s of the centers of projection are given in the Goloseev catalog system.

*** Commas represent decimal points.

seven reference points. We calculated the coordinates of 12 points of the back side of the Moon and five points of the front side, which were used as control points. The location of the pictures of all these points, and also the selenographic coordinate grid points, is shown schematically in Figure 2; the reference points are denoted by triangles, the control points by squares, and the back side points are determined by circles.

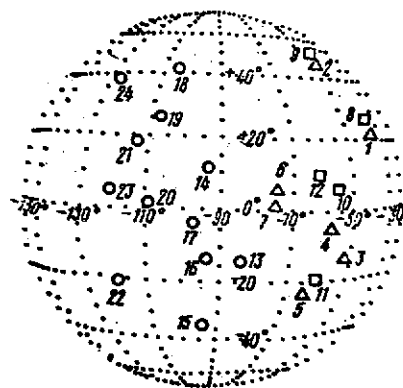


Figure 2. Location on the picture of selenographic grid of reference points and points being determined

All the calculations were made for the condition that the catalog and auxiliary coordinate system origins coincide, i.e., $X_0 = 0$, $Y_0 = 0$, $Z_0 = 0$.

TABLE 2. LUNAR SURFACE POINT COORDINATES*

Point no. in Fig. 2 (from catalog)	Picture 12			Picture 19			Aver. of pictures 12, 19	
	X, km	Y, km	Z, km	X, km	Y, km	Z, km	λ	ϕ
Visible side								
1 (212) ¹	+1298,7	-974,1	+620,8	+1298,4	-973,7	+620,8	-36°52'	+20°58'
2 (200)	+857,9	-795,3	+1283,8	+860,4	-793,2	+1283,1	-42°45'	+47°36'
3 (378)	+1077,5	-1298,5	-415,8	+1078,2	-1297,0	-415,0	-50°19'	-13°50'
4 (385)	+903,3	-1477,6	-158,8	+905,4	-1475,1	-158,1	-58°30'	-5°14'
5 (391)	+697,3	-1420,4	-725,8	+693,5	-1419,3	-724,5	-63°49'	-24°40'
6 (256)	+464,7	-1656,4	+204,4	+463,4	-1653,6	+206,4	-74°15'	+6°47'
7 (253)	+444,7	-1630,8	+31,1	+447,6	-1678,6	+33,0	-75°08'	+1°03'
8 (145) ²	+1273	-863,7	+807,3	+1273,5	-862,9	+806,5	-34°08'	+27°40'
9 (199)	+846,6	-707,2	+1339,4	+849,5	-703,0	+134,0	-39°45'	+50°25'
10 (246)	+936,0	-1414,7	+207,7	+994,2	-1411,2	+204,1	-55°01'	+6°48'
11 (390)	+809,2	-1417,5	-589,7	+812,5	-1414,3	-589,9	-60°12'	-19°50'
12 (248)	+774,5	-1524,3	+314,1	+778,4	-1520,8	+315,0	-62°59'	+10°26'
Back side								
13	+165,9	-1675,1	-438,1	+168,3	-1674,1	-435,6	-84°18'	-14°34'
14	-112,4	-1693,7	+357,3	-108,7	-1696,7	+360,4	-93°44'	+11°55'
15	-101,2	-1438,5	-971,9	-100,2	-1439,7	-968,4	-94°00'	-34°56'
16	-119,9	-1678,3	-441,1	-117,2	-1677,5	-439,3	-94°02'	-14°40'
17	-228,0	-1720,7	-115,1	-226,2	-1719,5	-112,5	-97°32'	-3°46'
18	-360,9	-1263,5	-1138,8	-357,2	-1261,6	+1140,7	-105°52'	+40°58'
19	-488,6	-1492,7	+746,8	-482,9	-1491,5	+750,2	-108°02'	+25°30'
20	-575,8	-1630,5	+45,8	-573,6	-1639,9	+48,7	-109°22'	+1°34'
21	-672,0	-1510,1	+541,2	-668,9	-1503,4	+545,7	-113°53'	+18°14'
22	-782,8	-1419,2	-630,2	-782,2	-1420,0	-623,3	-118°52'	-21°14'
23	-881,2	-1493,3	+135,0	-878,8	-1493,0	+133,4	-120°31'	+4°30'
24	-816,2	-1096,8	+1074,1	-812,0	-1095,3	+1077,8	-126°33'	+38°22'

¹1 - 7 are reference points²8 - 12 are control points

* Commas represent decimal points.

TABLE 3. ACCURACY CHARACTERISTICS OF LUNAR SURFACE POINT COORDINATES*

Point no. in Fig. 2 (from catalog)	Diff. of coordinates found from pictures 12 and 19, km			Diff. of aver. (from pictures 12 and 19) and catalog coor- dinates, km			
	$\Delta X'$	$\Delta Y'$	$\Delta Z'$	ΔX	ΔY	$\Delta Z'$	
1 (212)	+0.3	+0.4	0.0	+1.0	-0.5	-2.2	**
2 (200)	-2.5	+2.1	+0.1	+2.9	-2.2	-0.7	
3 (348)	-0.1	+0.1	+0.8	+4.8	-5.2	-1.2	
4 (385)	-2.1	+2.5	+0.7	+5.1	-3.7	-0.8	
5 (391)	-1.2	+1.1	+1.3	+3.5	0	-3.4	
6 (256)	-3.7	+2.8	-2.0	-7.8	+1.2	+2.4	
7 (253)	-2.1	+2.5	+0.7	+5.1	-3.7	-0.8	
8 (145)	-0.5	-0.8	+0.8	-0.7	+2.5	-2.0	
9 (199)	-2.1	+4.2	-0.1	+1.0	+2.0	-1.8	
10 (246)	-3.6	+6.4	+3.7	-2.4	+1.0	+4.2	
11 (390)	-3.3	+3.2	-0.2	-4.7	+4.0	-4.6	
12 (248)	-4.0	+4.4	-0.9	-7.1	-4.7	-1.7	
13	-2.4	+1.0	+2.5	—	—	—	
14	+3.7	+2.0	-3.1	—	—	—	
15	+1.0	-1.2	+3.5	—	—	—	
16	+2.7	+0.8	+1.8	—	—	—	
17	+1.8	+1.1	+2.5	—	—	—	
18	+3.7	+1.9	-1.9	—	—	—	
19	+5.7	+1.2	-3.4	—	—	—	
20	+2.2	-9.3	-2.9	—	—	—	
21	+3.1	+1.7	-4.5	—	—	—	
22	+0.6	-0.8	+3.9	—	—	—	
23	+2.4	+0.3	-3.4	—	—	—	
24	+4.2	+1.5	-3.7	—	—	—	

* Systematic θ and mean-square m differences:

$$\begin{aligned} \theta_X' &= \frac{\sum_{i=1}^{24} \Delta X_i'}{24} = -0.1 \text{ km}; & \theta_Y' &= \frac{\sum_{i=1}^{24} \Delta Y_i'}{24} = +1.1 \text{ km}; & \theta_Z' &= \frac{\sum_{i=1}^{24} \Delta Z_i'}{24} = -0.3 \text{ km}; \\ \theta_X &= \frac{\sum_{i=1}^{12} \Delta X_i}{12} = +0.2 \text{ km}; & \theta_Y &= \frac{\sum_{i=1}^{12} \Delta Y_i}{12} = -0.7 \text{ km}; & \theta_Z &= \frac{\sum_{i=1}^{12} \Delta Z_i}{12} = -0.8 \text{ km}; \\ m_X' &= \sqrt{\frac{\sum_{i=1}^{24} (\Delta X_i' - \theta_X')^2}{24}} = \pm 2.3 \text{ km}; & m_X &= \sqrt{\frac{\sum_{i=1}^{12} (\Delta X_i - \theta_X)^2}{12}} = \pm 4.0 \text{ km}; \\ m_Y' &= \sqrt{\frac{\sum_{i=1}^{24} (\Delta Y_i' - \theta_Y')^2}{24}} = \pm 2.0 \text{ km}; & m_Y &= \sqrt{\frac{\sum_{i=1}^{12} (\Delta Y_i - \theta_Y)^2}{12}} = \pm 2.9 \text{ km}; \\ m_Z' &= \sqrt{\frac{\sum_{i=1}^{24} (\Delta Z_i' - \theta_Z')^2}{24}} = \pm 1.7 \text{ km}; & m_Z &= \sqrt{\frac{\sum_{i=1}^{12} (\Delta Z_i - \theta_Z)^2}{12}} = \pm 2.4 \text{ km}. \end{aligned}$$

**Commas represent decimal points.

Therefore, in calculating the auxiliary coordinates using (14), values of r_{ij} for the points being determined were equated, as noted above, to the lunar radius, taken as $R = 1738$ km, and for the reference points to their selenographic radii vectors.

Comparison of the values obtained with the results of joint statistical interpretation of these same pictures [4] showed that the described technique can be used for determining the picture external orientation elements and photographed point coordinates when interpreting individual pictures of planets, and also as the first approximation in the statistical interpretation of stereophotos.

The authors wish to thank B. V. Nepolkonov, B. N. Rodionov, and A. P. Tishchenko for their valuable advice in discussions of the present article.

References

1. Rodionov, B. N., I. V. Isavnina, Ya. L. Ziman, et al. New Data on the Figure and Relief of the Moon from Analysis of Photographs Obtained by Zond 6. Kosmicheskiye issledovaniya, No. 3, 1971
2. Gavrilov, I. V., A. S. Duma, and V. S. Kislyuk. Catalog of Selenocentric Positions of 500 Basic Points on the Lunar Surface. Collection: Figura i dvizheniye Luny (Figure and Motion of the Moon), Vol. 2. Naukova Dumka Press, Kiev, 1967.
3. Nepoklonov, B. V. Determining the Orientation of Pictures From the Visible Horizon Line. Izv. vuzov, seriya geodeziya i aerofotos'yemka, No. 4, 1968.
4. Krasikov, V. A. Refinement of Goloseev Catalog Point Coordinates in the Limb Zone and Determination of Point Coordinates on the Back Side of the Moon. In present collection.

Translated for National Aeronautics and Space Administration under contract No. NASw 2483, by SCITRAN, P.O. Box 5456, Santa Barbara, California, 93108